



**UNIVERSITY OF
BIRMINGHAM**

**Non-Linear Analysis of Optical and Microwave
Sources**

By

Mohammad Afroozi Milani

A Thesis submitted to
University of Birmingham
For the degree of
DOCTOR OF PHILOSOPHY (PhD)

School of Electronic, Electrical and Systems Engineering
College of Engineering and Physical Sciences

February 16

UNIVERSITY OF
BIRMINGHAM

University of Birmingham Research Archive

e-theses repository

This unpublished thesis/dissertation is copyright of the author and/or third parties. The intellectual property rights of the author or third parties in respect of this work are as defined by The Copyright Designs and Patents Act 1988 or as modified by any successor legislation.

Any use made of information contained in this thesis/dissertation must be in accordance with that legislation and must be properly acknowledged. Further distribution or reproduction in any format is prohibited without the permission of the copyright holder.

ABSTRACT

Due to the ever increasing need for better and more capable communication systems, a large quantity of research is focused on the design and simulation of different sections of communication systems including the communication sources. Due to the massive cost of the fabrication involved in designing new communication sources, the accurate modelling and design of these sources using Computer Aided Design (CAD) is of great interest.

This thesis starts by reviewing the fundamentals of laser modelling and nonlinear microwave antenna design; followed by reviewing the most important works carried out by other researchers in these fields. The thesis continues by introducing a proposed, accurate model of the Vertical Cavity Surface Emitting Laser (VCSEL). The proposed model integrates the effects of the matching network as well as the parasitics, due to the VCSEL chip and the packaging mounting and the intrinsic VCSEL noise sources. Further in this thesis, a nonlinear Composite Right/Left Handed (CRLH) frequency doubler Leaky Wave Antenna (LWA) is designed which is capable of transmitting a signal in a direction that can be varied continuously from backfire to endfire, by varying the input frequency to the structure. The novelty of the proposed design is in the inclusion of nonlinear elements in the CRLH structure and also in the use of a quasi-lumped approach when designing the distributed structure. Finally, in this thesis a novel method of combining harmonic balance and EM analysis for the design and optimisation of nonlinear active antennas is developed. This method responds to the restriction of the CAD software in conveniently combining the analysis of nonlinear active antennas with advanced EM simulations such as radiation patterns. The proposed method enables the advanced EM analysis at the harmonic frequencies, generated within the nonlinear microwave structures when the structure is excited at the fundamental frequency, to be combined with full electromagnetic simulators.

To my beloved grandmother and parents

ACKNOWLEDGMENTS

I would like to say a special thank you to my supervisor Professor Peter Gardner for his excellent supervision and his continuous support throughout my studies. Without his support and encouragement I couldn't have successfully overcome the difficult moments during my research.

I would like to express my special thanks to Mrs Mary Winkles, for all her care during my studies. I would also like to thank all my friends and colleagues in the Communication Engineering Research Group for their support during my time as a researcher in this group. I would like to especially thank my friends Dr Oluwabunmi O. Tade, Dr Abubakar Tariq, Orod Haghghi, Yashar Haghghi, Morvarid Feizollahian, Farzad Hayati, Hasan Almahroug and Lewis Spencer for their friendship and their encouragement.

I wish to express my sincere gratitude to my family for their never ending support throughout my entire life. Their undoubted encouragement and belief in my ability paved the way to all my success. I would like to thank my grandmother, Haji, for all her prayers and her financial support throughout my life. Special thanks to my Mom, Zohreh, for her infinite love and thanks my Dad, Akbar, for being my idol and I hope that I have made them proud. I would like to thank my sisters, especially Ghazal for her infinite prayers and support; without her, my stay in the United Kingdom would not have been this enjoyable.

PUBLICATIONS UNDER REVIEW

- [1] M. Afroozi Milani and P. Gardner, "Integrated Vertical Cavity Surface Emitting Laser Model," *Optical and Quantum Electronics, Journal of*, 2015.

- [2] M. Afroozi Milani and P. Gardner, "Combining Harmonic Balance and EM Analysis for Design and Optimization of Nonlinear Active Antennas," *International Journal of RF and Microwave Computer-Aided Engineering*, 2015.

TABLE OF CONTENTS

ABSTRACT	i
ACKNOWLEDGMENTS	iii
PUBLICATIONS UNDER REVIEW	iv
TABLE OF CONTENTS	v
LIST OF FIGURES	x
LIST OF TABLES	xviii
LIST OF ABBREVIATIONS.....	xx
1 INTRODUCTION.....	1
1.1 Motivation	1
1.2 Thesis Objective.....	4
1.3 Thesis Layout.....	5
References	8
2 COMMUNICATION SOURCES: OPTICAL LASER AND MICROWAVE CRLH ANTENNAS' BASIC CONCEPTS AND APPLICATIONS	10
2.1 Introduction	10
2.2 Optical emission in semiconductor lasers	14
2.2.1 Essentials of optical generation	14

2.2.2	Optical radiation in semiconductors	17
2.3	Vertical Cavity Surface Emitting Lasers (VCSELs).....	22
2.4	VCSEL rate equations	25
2.5	VCSEL modelling	27
2.6	Microwave antennas.....	38
2.7	Basics of microstrip antennas.....	40
2.7.1	Patch antenna.....	41
2.7.2	Design procedure.....	43
2.7.2.1	Patch width calculation.....	44
2.7.2.2	Patch length calculation.....	45
2.7.2.3	Ground plane dimensions	45
2.7.2.4	Feed point location	46
2.8	Leaky wave antenna.....	48
2.8.1	Fundamental concepts	48
2.8.2	LWA classification.....	51
2.8.3	Recent advancement in LWAs	53
2.9	Composite Right/Left Handed (CRLH) metamaterial	62
2.10	Conclusion.....	65
	References	67
3	INTEGRATED VERTICAL CAVITY SURFACE EMITTING LASER MODEL BASED ON TRANSMISSION LINE MODELLING	75
3.1	Introduction	75

3.2	Proposed integrated VCSEL model overview	77
3.3	Intrinsic VCSEL model parameters derivation and analysis	79
3.3.1	Proposed lumped element VCSEL model	79
3.3.1.1	Small signal equivalent circuit model	82
3.3.2	Distributed intrinsic VCSEL model	97
3.3.3	Intrinsic VCSEL dynamic response	99
3.4	Electrical parasitics	101
3.4.1	Distributed electric parasitic model	104
3.5	Matching network	107
3.5.1	Design and analysis	108
3.6	Conclusion.....	113
	References	114
4	NONLINEAR COMPOSITE RIGHT/LEFT HANDED (NL-CRLH) FREQUENCY DOUBLER LEAKY WAVE ANTENNA DESIGN	118
4.1	Introduction	118
4.2	Proposed NL-CRLH leaky wave antenna specification and overview	120
4.3	CRLH design and simulation	122
4.3.1	CRLH design procedure	122
4.3.2	CRLH result analysis.....	125
4.4	Nonlinear CRLH design and simulation	127
4.4.1	Nonlinear CRLH design procedure	127
4.4.2	NL-CRLH result analysis	129

4.5	Distributed NL-CRLH leaky wave antenna model	130
4.5.1	Distributed NL-CRLH model design procedure	131
4.5.2	NL-CRLH distributed model results' analysis	132
4.5.3	EM analysis of CRLH leaky wave antenna.....	135
4.5.4	Radiation pattern analysis.....	138
4.6	Conclusion.....	140
	References	142
5	COMBINING HARMONIC BALANCE AND EM ANALYSIS FOR DESIGN AND OPTIMISATION OF NONLINEAR ACTIVE ANTENNAS	144
5.1	Introduction	144
5.2	Proposed harmonic balance simulation.....	145
5.3	Patch antenna design and simulation	147
5.3.1	Patch antenna specifications.....	147
5.3.2	Patch antenna result analysis	149
5.4	Frequency tripler patch antenna design.....	151
5.4.1	Frequency tripler design	153
5.4.2	Idler design	153
5.4.3	Feed line resonator design	156
5.4.4	Schottky diode location	157
5.5	Harmonic balance simulation.....	164
5.6	Harmonic Balanced Analysis of the NL-CRLH Leaky Wave Antenna.....	172
5.7	Conclusion.....	182

References	183
6 CONCLUSIONS AND FUTURE WORK.....	184
6.1 Conclusions	184
6.1.1 Integrated Vertical Cavity Surface Emitting Laser model based on transmission line modelling.....	186
6.1.2 Non-Linear Composite Right/Left Handed (NL-CRLH) frequency doubler leaky wave antenna design	187
6.1.3 Combining harmonic balance and EM analysis for design and optimisation of non-linear active antennas	188
6.2 Suggestions for possible future work.....	188
Appendix.....	190
A. Components Data Sheets	190
B. Microwave Simulation Software	208
B.1 OrCAD EE (PSpice) Designer	208
B.2 National Instruments AWR Design Environment.....	210
B.3 CST STUDIO SUITE	214
References	216

LIST OF FIGURES

Figure 1-1: Optical distribution of the phased array CRLH-LWA for 2-D scanning.....	4
Figure 2-1: General communication system architecture.	13
Figure 2-2: The electromagnetic spectrum range.	13
Figure 2-3: Fundamental optical process including (A) photon absorption, (B) spontaneous emission and (C) stimulated emission.	15
Figure 2-4: Schematic illustration of (A) material at the thermal equilibrium and (B) non-equilibrium known as population inversion.....	16
Figure 2-5: Energy band schematics of (A) intrinsic, (B) <i>n</i> -type and (C) <i>p</i> -type semiconductors.	18
Figure 2-6: Energy-wave vector diagram for (A) direct band gap semiconductors and (B) indirect band gap semiconductors.....	19
Figure 2-7: Heavily doped p-n homojunction (A) no biasing voltage (B) strongly forward biased.	20
Figure 2-8: Double Heterojunctions' (DH) semiconductor (A) layer and (B) energy band schematics [1].	22
Figure 2-9: Generic structure of vertical cavity surface emitting laser (VCSEL) [1].	24
Figure 2-10: Visual illustration of VCSEL rate equations.....	27
Figure 2-11: Proposed VCSEL equivalent circuits in [34]: (A) biased above threshold ($I_b > I_{th}$). (B) zero biased condition ($I_b = 0$).	28
Figure 2-12: Extraction and optimization algorithm suggested by [34].	29

Figure 2-13: Proposed equivalent circuit model [35]: (A) large signal equivalent circuit model and (B) small signal equivalent circuit model.	29
Figure 2-14: Comprehensive VCSEL model by [37]	30
Figure 2-15: Suggested VCSEL equivalent circuit model in [38].	31
Figure 2-16: Simulated results of [39]: (A) L-I characteristic of the VCSEL for different temperatures (B) transient response of the VCSEL.	33
Figure 2-17: The proposed VCSEL equivalent circuit model [41].	34
Figure 2-18: Comparison between the modulation response of the VCSEL measured in [42] (points) and simulated using the model presented in [40] (lines).	35
Figure 2-19: Proposed VCSEL model in [29]: (A) intrinsic VCSEL model and (B) VCSEL parasitic network.	37
Figure 2-20: Schematic of (A) typical microwave antenna based communication system and (B) a typical antenna transmitter equivalent circuit.	40
Figure 2-21: A side view of a typical microstrip transmission line including the electric E and magnetic H fields.	41
Figure 2-22: Microstrip patch antenna feeding methods: (A) microstrip inset feed line, (B) coaxial, (C) aperture coupling and (D) proximity coupling.	43
Figure 2-23: Microstrip patch antenna: (A) typical antenna geometry and (B) equivalent circuit model.	44
Figure 2-24: A typical LWA: a uniform waveguide with narrow leakage aperture.	50
Figure 2-25: Waveguide leaky wave antennas: (A) uniform structure, (B) periodic structure.	53
Figure 2-26: Geometry of quasi-uniform SIW-LWA [64].	54
Figure 2-27: Radiation pattern indicating the forward quadrant frequency scanning of the SIW LWA of [64].	55

Figure 2-28: Proposed structure of periodic LWA in [65] which includes quarter wave transformer to enable broadside radiation.....	56
Figure 2-29: Confirmation of broadside radiation for the structure presented in figure 2-28.	57
Figure 2-30: Proposed ferrite LWA [66].	58
Figure 2-31 Ferrite LWA radiation pattern confirming the space scanning for (A) fixed biased and (B) fixed frequency.	58
Figure 2-32: Dispersion diagram indicating the radiating (fast wave) and guiding (slow wave) regions for balanced and unbalanced CRLH transmission lines [69].....	60
Figure 2-33: Proposed CRLH-LWA schematics including the fabricated unit cell (adapted from [60]).....	60
Figure 2-34: A typical radiation pattern for the CRLH-LWA structure with 41 unit cells [68].	61
Figure 2-35: (A) CRLH waveguide LWA structure. (B) unit cell [71].	62
Figure 2-36: Lumped element equivalent circuit model of (A) RH, (B) purely LH and (C) CRLH transmission line.....	63
Figure 2-37: Dispersion diagram for the balanced and unbalanced CRLH structure presented in [73] using Equation 2-33.	65
Figure 3-1: Block diagram presentation of the proposed integrated VCSEL model.....	79
Figure 3-2: Typical Vertical Cavity Surface Emitting Laser (VCSEL) structure.	81
Figure 3-3: Small signal electrical equivalent circuit of intrinsic VCSEL.	83
Figure 3-4: Junction resistance R_j and capacitance C_j as a function of normalised bias current.	87
Figure 3-5: Photon storage L_0 and cavity losses R_0 as a function of normalised bias current.	87
Figure 3-6: Current noise spectral intensity (S_{ii}) as a function of normalised bias current. ...	90
Figure 3-7: Voltage noise spectral intensity (S_{vv}) as a function of normalised bias current..	91

Figure 3-8: Cross-spectral density of noise sources (S_{iv}) as a function of normalised bias current.	91
Figure 3-9: Frequency dependence of the VCSEL input impedance.	94
Figure 3-10: The impedance of an intrinsic VCSEL for various pump currents.....	94
Figure 3-11: Low frequency analysis of VCSEL, (a) relative intensity noise and (b) junction voltage noise spectrum as a function of normalized bias current ($f_{Lo} = 105 \text{ Hz}$).	96
Figure 3-12: Frequency dependence of (a) relative intensity noise and (b) junction voltage noise spectrum for various pump currents.	96
Figure 3-13: Intrinsic modulation response of the VCSEL for different biasing currents.	97
Figure 3-14: Distributed presentation of the intrinsic VCSEL model.	99
Figure 3-15: Transient response of intrinsic VCSEL for different biasing current.	100
Figure 3-16: VCSEL <i>toff</i> and the spatial hole burning phenomenon.....	101
Figure 3-17: The VCSEL parasitic network equivalent circuit model.	103
Figure 3-18: Schematic cross-section of VCSEL with the parasitic path included.....	103
Figure 3-19: Distributon model representation of lumped-element electric parasitic model of Figure 3-17.....	105
Figure 3-20: Intrinsic and extrinsic resonant frequency of the integrated VCSEL model. ...	106
Figure 3-21: Matching networks (A) lumped element L-Matching network. (B) single stub matching network for distributed model.....	108
Figure 3-22: Complex impedance of proposed integrated VCSEL model.....	109
Figure 3-23: S_{11} results (left: magnitude; right: Smith chart) of the matched lumped-element integrated VCSEL model at 4.5 GHz	110
Figure 3-24: S_{11} results (left: magnitude; right: Smith chart) of the matched TLM integrated VCSEL model at 4.5 GHz	111

Figure 3-25: Proposed integrated VCSEL model (A) lumped-element model. (B) Transmission line based equivalent.	111
Figure 3-26: Improvement in modulation response of the proposed integrated VCSEL due to the inclusion of a matching network at 4.5 GHz.....	112
Figure 4-1: Circuit level structure of symmetric 1-D CRLH unit cell.....	122
Figure 4-2: Dispersion diagram for the designed CRLH unit cell structure.....	126
Figure 4-3: Return loss ($S_{1,1}$) diagram for designed CRLH unit cell.....	127
Figure 4-4: SPICE model for varactor diode.	128
Figure 4-5: Circuit level structure of symmetric 1-D nonlinear CRLH unit cell.....	128
Figure 4-6: Comparison between linear and nonlinear CRLH unit cell dispersion diagram.	129
Figure 4-7: Harmonics generated in NL-CRLH unit cell structure.	130
Figure 4-8: Distributed NL-CRLH unit cell schematic.	132
Figure 4-9: The comparison between $S_{1,1}$ figure of linear, nonlinear and nonlinear distributed CRLH.....	133
Figure 4-10: Comparison between the dispersion diagram of the CRLH, NL-CRLH and distributed NL-CRLH.	134
Figure 4-11: The designed nonlinear CRLH leaky wave antenna layout.....	134
Figure 4-12: CRLH leaky wave antenna distributed model in CST.....	135
Figure 4-13: CST Studio Design $S_{1,1}$ result for the CRLH leaky wave antenna.....	136
Figure 4-14: Dispersion diagram for the distributed CRLH leaky wave antenna calculated using CST's $S_{1,1}$ results.	137
Figure 4-15: Cascaded CRLH leaky wave antenna ($N = 6$).....	138
Figure 4-16: Polar representation of CRLH leaky wave antenna's radiation pattern for four different frequencies. (Note that there are different dBi scales between backward radiation sections A, B and the forward radiation sections C and D).....	139

Figure 5-1: Proposed harmonic balance simulation technique.	146
Figure 5-2: Geometry of microstrip patch antenna with inset feed.	147
Figure 5-3: Simulated microstrip patch antenna using CST.	150
Figure 5-4: Return loss for designed patch antenna.	150
Figure 5-5: Patch antenna realised gain 2-D view.	151
Figure 5-6: Patch antenna directivity 3-D view.	151
Figure 5-7: Frequency tripler patch antenna prototype.	152
Figure 5-8: The effect of adding via to ground and Schottky diode connection ports on (A) realised gain and (B) power pattern.	152
Figure 5-9: Simple frequency tripler with idler circuit.	154
Figure 5-10: Power spectrum analysis for Schottky diode without the inclusion of idlers. ..	155
Figure 5-11: Power spectrum analysis for Schottky diode with idlers.	155
Figure 5-12: Feed line resonator design schematic.	156
Figure 5-13: Feed line resonator S-parameter characteristics.	157
Figure 5-14: Feed line network configuration to ensure the best location for the feed line resonator.	157
Figure 5-15: Realised gain and power field pattern of the frequency tripler patch antenna for different positions of the Schottky diode.	163
Figure 5-16: Measured and fitted trajectory for (A) realised gain and (B) power field.	164
Figure 5-17: Frequency tripler patch antenna without Schottky diode.	165
Figure 5-18: AWR Microwave Office circuit arrangement.	166
Figure 5-19: Proposed current network schematic.	167
Figure 5-20: Circuit configuration for generating the required current into the designed frequency tripler patch antenna.	168

Figure 5-21: Enforced currents (A) measured at the input feed line port; (B) measured at the intersection of the Schottky diode and patch antenna.....	169
Figure 5-22: (A) 2-D realised gain and (B) power pattern of the integrated nonlinear frequency tripler patch antenna.....	171
Figure 5-23: Power of the harmonics generated by the Schottky diode in the frequency tripler patch antenna.	171
Figure 5-24: NL-CRLH leaky wave antenna structure without varactor diodes.	173
Figure 5-25: AWR Microwave Office arrangement of the NL-CRLH leaky wave antenna.	174
Figure 5-26: Spice model for SKYWORKS SMV 1232 varactor.....	174
Figure 5-27: Capacitance verse Voltage plot to investigate the required biasing voltage.....	175
Figure 5-28: Power of the harmonics generated by the varactor diodes in the NL_CRLH leaky wave antenna (Figure 2-25).....	175
Figure 5-29: Current network schematic for current generation at the second harmonic to be injected to the NL-CRLH leaky wave antenna ports.....	178
Figure 5-30: Circuit configuration for injecting the required current into the NL-CRLH leaky wave antenna structure.....	179
Figure 5-31: Polar representation of NL-CRLH frequency doubler LWA's radiation pattern for three different frequencies.....	180
Figure B-1: OrCAD PSpice advanced part browser.....	209
Figure B-2: OrCAD PSpice analysis setup.....	209
Figure B-3: Microwave Office "Project Options" menu.	211
Figure B-4: Microwave Office "New Schematic" and "Elements" location.	211
Figure B-5: Microwave Office simulation.....	212
Figure B-6: Microwave Office optimisation and tuning tools.....	213
Figure B-7: CST MWS templates.....	215

Figure B-8: CST MWS window indicating the available 3-D shapes and the possible Boolean operators.....215

LIST OF TABLES

Table 2-1: Summary of the reviewed articles on VCSEL modelling.....	38
Table 2-2: Summary of the properties of the uniform and periodic LWAs.....	53
Table 3-1: 1300 nm VCSEL INTRINSIC PROPERTIES (Taken from [11, 15-17]).....	86
Table 3-2: Parameters of the VCSEL equivalent model for different normalised bias currents and 4.5 GHz operating frequency.	92
Table 3-3: The equivalence between lumped element and transmission line model components and dimensions of the distributed elements.	99
Table 3-4: VCSEL parasitic components value.....	104
Table 3-5: Equivalence between lumped element and transmission line model components and the dimension of distributed electric parasitic parameters' model.....	105
Table 3-6: Optimised L-matching network components.	109
Table 3-7: Optimised short single stub matching network dimensions.....	110
Table 4-1: Composite right/left handed design specifications.....	121
Table 4-2: Circuit level parameters of the designed balanced CRLH.	125
Table 4-3: Distributed model's dimensions.	133
Table 5-1: 3 GHz rectangular patch antenna design parameters.	149
Table 5-2: Measured realised gain and power corresponding to different Schottky diode locations.	163
Table 5-3: Complex current generated at the third harmonic at port 1 and 3.....	166
Table 5-4: Transconductance (gm) value of the voltage controlled current sources	168
Table 5-5: Complex current generated at the second harmonic at port 1 to 6.	176

Table 5-6: Transconductance value of the voltage controlled current sources..... 177

Table 5-7: Phase of the currents at port 3 and 6 of NL-CRLH leaky wave antenna (Figure 5-25) at the fundamental frequency (1.1 GHz) 182

LIST OF ABBREVIATIONS

AC	Alternating Current
ADS	Advanced Design System
CAD	Computer Aided Design
CRLH	Composite Right/Left Handed
DBR	Distributed Bragg Reflector
DC	Direct Current
DH	Double Heterojunction
EM	Electro Magnetic
EMI	Electro Magnetic Interference
HFSS	High Frequency Structural Simulator
IC	Integrated Circuit
LASER	Light Amplification by Stimulated Emission of Radiation
LED	Light Emitting Diode
LH	Left Handed
LWA	Leaky Wave Antenna
MAN	Metropolitan Area Network

MIM	Metal Insulator Metal
MQW	Multi Quantum-Well
NL	Non-Linear
RF	Radio Frequency
RH	Right Handed
RIN	Relative Intensity Noise
RoF	Radio-over-Fibre
SIW	Substrate Integrated Waveguide
TL	Transmission Line
TLM	Transmission Line Modelling
UHF	Ultra High Frequency
VCCS	Voltage Controlled Current Source
VCSEL	Vertical Cavity Surface Emitting Laser
VNA	Vector Network Analyser
WAN	Wide Area Network

1 INTRODUCTION

1.1 Motivation

Intense development of several technologies in recent decades has enabled rapid advancements in communications systems. In all communication systems, the information is modulated onto a carrier wave and then transmitted to the destination, where the modulated carrier is demodulated to extract the original information signal. The carrier varies significantly as for instance, in ancient communication systems the light of a fire or a light reflected from a mirror were used to transfer information. Continual increases in data transfer over recent years, due to the daily expansion of the Internet and broadband interactive services' usage requires the design of ever more efficient communication systems. In theory, as the frequency and bandwidth of the carrier waves increase, communication systems have larger information transfer capacities. Sophisticated techniques have been developed to convey information in different frequency ranges of electromagnetic waves, from radio to microwave and optical frequencies. Therefore there is intense research activity on the design

of stable and powerful optical and microwave sources which are also cost effective, with the potential to form the fundamental building blocks of future communication systems.

The design of optical and microwave sources obviously receives a great advantage from the availability of Computer Aided Design (CAD) tools. CAD based simulation of the optoelectronic sources enables the verification and optimisation of the required performance of the design prototype, before hugely investing in the fabrication. This will result in savings in the cost and duration of the design. Consequently, this thesis is largely concerned with the developments and analysis of the circuit based models of optical and microwave sources.

Vertical Cavity Surface Emitting Lasers (VCSELs) offer many benefits over the conventional laser diodes. These advantages include: submilliamp threshold current; very high speed modulations (over 25 Gbit/sec); easy integration with the other parts of communication systems without the need for expensive optical couplers; very low production costs and relatively simple chip testing due to the possibility of wafer level testing. The above mentioned advantages made the VCSELs a great candidate for medium to long haul communications and have attracted many research projects concerning the design and modelling of VCSELs [1].

On the other hand, directionality is a vital aspect of the microwave antennas. In some military and commercial applications, an antenna with the ability of changing its directivity to focus on a specific direction is of great interest. A Leaky Wave Antenna (LWA) can be used in such applications; since the direction of the radiation can be controlled in this type of antenna, by changing the frequency of the feeding wave [2]. However, conventional LWAs can only offer forward radiation and are unable to radiate at the broadside direction [3]. Composite Right/Left Handed (CRLH) metamaterials, due to their inherent simultaneous negative permittivity and permeability in certain frequency periods, enable both forward and

backward radiation [4]. The interesting properties of the CRLHs have attracted many researchers over recent years. One of the possible applications of the CRLH metamaterials is in the design of the LWAs [5]. This enables the seamless transition from backward to forward radiation by changing the frequency.

Radio-over-Fibre (RoF) is a technology in which a radio signal is being modulated on the light wave and being transmitted over the fibre optics to enable fast, low cost wireless access which is immune to Electro Magnetic Interference (EMI) [6]. This technology enables the ever-increasing users of the communication system to reliably benefit from modern telecommunication services. RoF system includes 3 parts; transmitter, optical link and receiver. In the transmitter, the laser beam is being modulated using RF signals and then carried over an optical link to be delivered to the receiver. At the receiver the photodiode detects the RF modulated data and passes it through the demodulator to convert it back to RF form.

There is an intense research interest in a variety of the RoF applications such as in mobile communications and wireless-over-fibre applications for the distribution of wireless over buildings and airports. Economical modules with reduced RF ranges to cover smaller areas are also possible with this technology [7-10]. Development of an improved RoF system such as an optical distribution of the phased array CRLH-LWA to achieve 2-D scanning is among the applications of the material developed in this thesis [11, 12]. The schematic of this system is illustrated in Figure 1-1. In this application, the appropriate RF signal that generates the required scanning angle in x-axis is being modulated on the VCSEL output beam in the control centre using the proposed integrated VCSEL model in this thesis, which takes into account the effects of the VCSEL noise sources as well as the VCSEL parasitic networks. The modulated light is then transmitted through an optical link to reach to the base station that can be as much as much as a thousand miles away. At the base station, using a

photodetector and the demodulator unit the modulated optical signal will be converted back to the RF form and will be used to drive the proposed nonlinear CRLH-LWA proposed later in this thesis that is capable of scanning from the backfire to endfire by varying the feeding frequency.

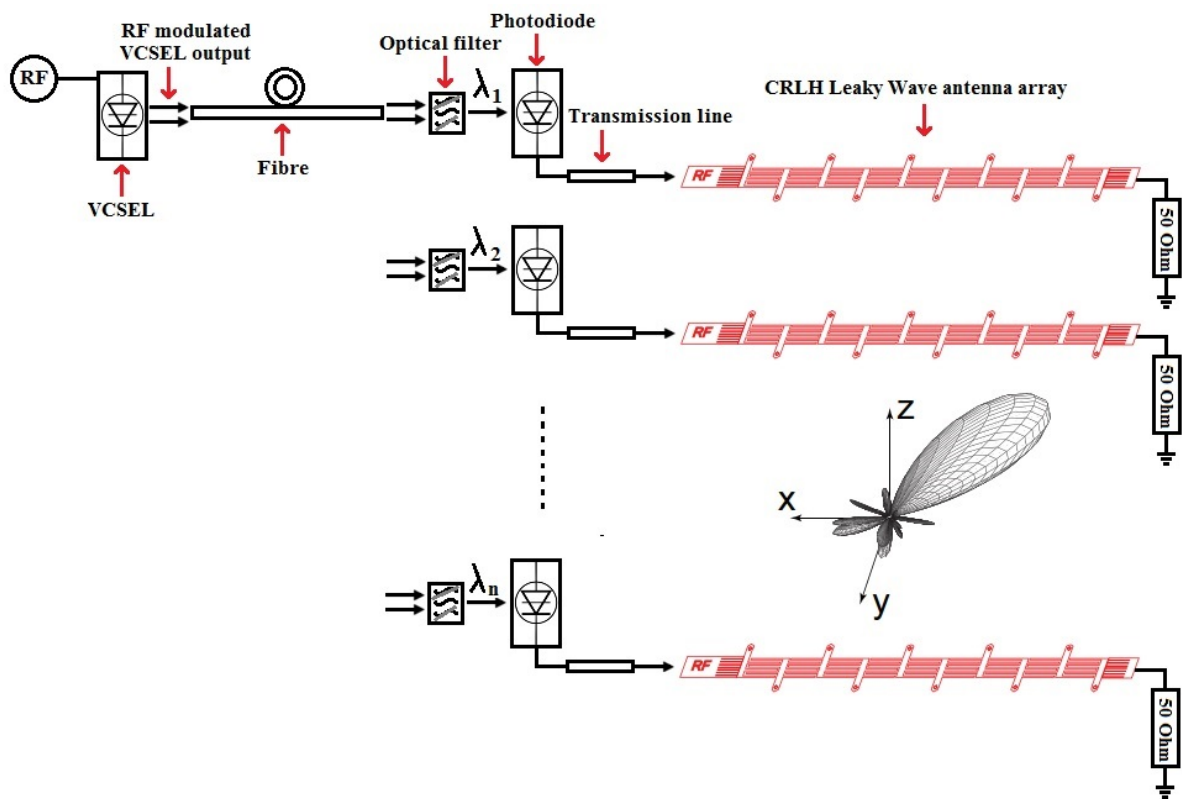


Figure 1-1: Optical distribution of the phased array CRLH-LWA for 2-D scanning.

1.2 Thesis Objective

The aim of this thesis is to better understand the nonlinear analysis of optical and microwave sources and to investigate a new circuit level model of the VCSEL and a design of the nonlinear CRLH-LWA. The knowledge from this thesis may be useful in allowing more accurate VCSEL models to be tested in optical communication system simulations; which may result in huge savings in the cost of designing these systems. The proposed nonlinear

CRLH frequency doubler LWA design offers simple but yet effective design techniques that can be of great interest in the millimetre wave region, where the generation of the fundamental wave sources is challenging. In addition, the developed method of combining harmonic balance and EM analysis is simple and yet effective, capable of being applied to any nonlinear active antenna. The main objectives of this thesis can be summarised as follows.

- Investigation of the vertical cavity surface emitting laser's structure by developing a novel VCSEL model capable of accurately simulating the VCSEL's intrinsic and extrinsic behaviours.
- Investigation of composite right/left handed metamaterials' properties including their applications in leaky wave antenna design.
- Design of a leaky wave antenna using nonlinear composite right/left handed metamaterials capable of seamless space scanning from backfire to endfire, including the broadside, by increasing the input frequency.
- Development of a method for combining harmonic balance and EM analysis for design and optimisation of nonlinear active antennas.

1.3 Thesis Layout

This thesis includes six chapters, which are organised as follows.

Chapter 1 includes the introduction and the motivation for the research on the topic of this thesis.

Chapter 2 contains the literature review discussing communication sources such as, optical and microwave sources. It includes the fundamentals of optical emission in semiconductor lasers by paying special attention to vertical cavity surface emitting lasers' structures. Brief discussions on microwave antennas by reviewing the microstrip patch antenna and leaky wave antenna are also included in this chapter. It also includes a review on the fundamentals of composite right/left handed metamaterials that show their exciting applications, including in the field of LWA design. It highlights some of the most important works carried out by other researchers in the field of VCSEL modelling and LWA design.

Chapter 3 contains the detailed analyses of the proposed integrated model for a VCSEL. It presents the intrinsic model derivation including the calculation of the model's parameters as well as the simulation of the VCSEL noise behaviours. It also includes the simulation results confirming the improving effects due to the inclusion of the electrical parasitic elements and the matching network in the VCSEL model. Furthermore, this chapter includes the distributed model of the proposed integrated VCSEL model designed using a quasi-lumped technique; which provides the feasibility of using the proposed model in the design of modulation port matching networks in the micro and millimetre wave region, where the lumped element model has inherent size restrictions.

Chapter 4 describes the proposed nonlinear CRLH frequency doubler LWA design method for low frequency regions. It includes the quasi-lumped element approach to design the distributed model of the proposed nonlinear structure. It also highlights the simulated radiation pattern of the structure when the harmonic frequencies are fed to the structure from the input port. However more realistic EM analysis of the structure could be achieved with

the second harmonics being generated by the varactor diode within the design. Unfortunately due to computational limitations, current CAD software is unable to perform all these analyses.

Chapter 5 provides a novel technique for combining harmonic balance and EM analysis for the design and optimisation of nonlinear active antennas. This chapter responds to the challenge raised in Chapter 4 for analysing the radiation pattern of the designed nonlinear CRLH frequency doubler LWA. This chapter verifies the proposed technique by analysing and optimising the radiation pattern of the nonlinear frequency tripler patch antenna. Further in this chapter the proposed method is used to analyse the radiation pattern for the unit cell of the designed NL-CRLH frequency doubler LWA.

Chapter 6 draws conclusion to the work in this thesis. It includes a review of the thesis' main works and highlights the significant achievements. Moreover, it provides a number of possible areas for further research in this field.

References

- [1] H. E. Li and K. Iga, *Vertical-cavity surface-emitting laser devices / H.E. Li, K. Iga (eds.)*. London: London : Springer, 2003.
- [2] A. A. Oliner and D. R. Jackson, "Leaky-Wave Antennas," in *Antenna Engineering Handbook*, J. Volakis, Ed., Fourth ed: McGraw-Hill Companies, Incorporated, 2007.
- [3] D. R. Jackson and A. A. Oliner, "Leaky-Wave Antennas," in *Modern Antenna Handbook*, C. A. Balanis, Ed., ed: Wiley-Interscience, 2008, pp. 325-368.
- [4] C. Caloz and T. Itoh, *Electromagnetic Metamaterials: Transmission Line Theory and Microwave Applications*: Wiley, 2006.
- [5] C. Caloz, T. Itoh, and A. Rennings, "CRLH metamaterial leaky-wave and resonant antennas," *Antennas and Propagation Magazine, IEEE*, vol. 50, pp. 25-39, 2008.
- [6] A. M. Zin, M. S. Bongsu, S. M. Idrus, and N. Zulkifli, "An overview of radio-over-fiber network technology," in *Photonics (ICP), 2010 International Conference on*, 2010, pp. 1-3.
- [7] V. Sittakul and M. J. Cryan, "A Fully Bidirectional 2.4-GHz Wireless-Over-Fiber System Using Photonic Active Integrated Antennas (PhAIAs)," *Lightwave Technology, Journal of*, vol. 25, pp. 3358-3365, 2007.
- [8] V. Sittakul and M. J. Cryan, "A 2.4-GHz Wireless-Over-Fibre System Using Photonic Active Integrated Antennas (PhAIAs) and Lossless Matching Circuits," *Lightwave Technology, Journal of*, vol. 27, pp. 2724-2731, 2009.
- [9] D. Wake, A. Nkansah, P. Assimakopoulous, N. Gomes, M. Violas, L. Zhansheng, S. Pato, F. Ferreira, G. De Valicourt, R. Brenot, and F. Van Dijk, "Design and

performance of radio over fibre links for next generation wireless systems using distributed antennas," in *Future Network and Mobile Summit, 2010*, 2010, pp. 1-9.

- [10] L. Tongyun, R. V. Penty, and I. H. White, "Novel digital radio over fibre for 4G-LTE," in *Communication Workshop (ICCW), 2015 IEEE International Conference on*, 2015, pp. 312-317.
- [11] P. R. Herczfeld, "Optically controlled phased array system and method," ed: Google Patents, 1989.
- [12] P. F. McManamon, T. A. Dorschner, D. L. Corkum, L. J. Friedman, D. S. Hobbs, M. Holz, S. Liberman, H. Q. Nguyen, D. P. Resler, R. C. Sharp, and E. A. Watson, "Optical phased array technology," *Proceedings of the IEEE*, vol. 84, pp. 268-298, 1996.

2 COMMUNICATION SOURCES: OPTICAL LASER AND MICROWAVE CRLH ANTENNAS' BASIC CONCEPTS AND APPLICATIONS

2.1 Introduction

In this chapter, the fundamental concepts of optical lasers and microwave CRLH antennas as an example of optical and microwave communication signal sources are reviewed. This chapter provides basic concepts for the understanding of Chapters 3 and 4. Further in this chapter, additional backgrounds are provided on harmonic balance generation on nonlinear structures and also the patch antenna properties, in order to achieve better understanding of the novel method of combining harmonic balance and EM analysis for design and optimisation of the nonlinear active antennas developed in Chapter 5.

The dramatic advancement of technology in recent decades has benefited from the progression in communications systems. The common aspect of all communication systems is that the information is modulated on the carrier and then transmitted to the destination,

where the modulated carrier is demodulated to use the original information signal. The architecture of a general communication system is summarised in Figure 2-1. The carrier in the communication system varies significantly as for instance, in ancient communication systems the light of a fire or a light reflected from a mirror were used to transfer information. In recent years the electromagnetic wave is commonly used to convey information. Theoretically the higher the frequency of the carrier waves, the larger the information carrier's ability. Sophisticated techniques have been developed to convey information in different frequency ranges of electromagnetic waves, from radio to microwave and optical frequencies [1]. The frequency range of different electromagnetic waves is demonstrated in Figure 2-2. Each of these frequency ranges has its own advantages and level of sophistication. Therefore depending on the application, a different communication system is developed.

The use of optical waves as a carrier in communication systems dates back to the ancient era; an example of these communication systems was mentioned previously. Although Alexander Graham Bell reported the transmission of voice over light in 1880 [2], there was a very limited use of optical waves before 1960 when the laser was invented based on a ruby rod by Maiman [3]. Semiconductor lasers are vital components in optical communications due to their small size, high-speed direct modulation and rather low manufacturing costs in comparison to gas lasers [4]. The first semiconductor based lasers were invented using the gallium arsenide (GaAs) and gallium arsenide phosphide (GaAsP) semiconductors by four groups of scientists directed by Nathan, Holonyak, Hall and Rediker [5]. In 1966 Kao and Hockam [6] and also Werts [7] developed an optical communication system via dielectric waveguides or glass based fibres, which alleviates the disadvantages such as high atmospheric degradation of the optical communication over free space. The idea of Vertical Cavity Surface Emitting Lasers (VCSELs) was first developed by Iga in 1977 [8] in order to

fabricate a monolithic semiconductor laser with short cavity length and dynamic single operating mode [9, 10]. The first VCSEL was manufactured in 1979 by Iga using $1.3 \mu\text{m}$ wavelength GaInAsP/InP as its active cavity [11]. This device was bulky and suffered from a high threshold current of 800 mA [4]. Threshold current, is the current in which the laser starts its stimulated emission and should be kept as low as possible to achieve a more efficient device. VCSELs attracted lots of research in the 1980s and 1990s, which resulted in the development of more compact VCSELs with high output power and below $200 \mu\text{A}$ threshold currents by the end of the 20th century [11]. The detailed history of the VCSEL developments was investigated in [4, 11, 12].

On the other hand, microwaves are also widely used in modern communication systems. The field of microwave engineering is founded on Maxwell's equations which were established in 1873 [13]. The first antenna for long haul communication was demonstrated by Marconi in 1901 [14]. The antenna technologies up to the 1940s were mainly based on wire radiating elements and frequencies as high as the UHF band. The era of microwave communications starts with the invention of microwave sources such as the klystron and magnetron, which enabled the generation of frequencies above 1 GHz [15]. Since then microwave based communication systems are in constant development with the design of different types of antennas and reflecting materials; as an example, widely used patch antennas and leaky wave antennas can be considered. A detailed historical review of this development was presented by Oliner in [16].

In 1967 Veselago theoretically predicted the existence of material with concurrent negative permittivity (ϵ) and permeability (μ) [17]. This was the starting point for the research on the new type of materials known as metamaterials. The first left handed (LH) metamaterial was designed in 2000 by Smith [18]. Following the design demonstrated by Smith in 2000, Caloz

and Itoh introduced in 2003 the concept of the composite right/left handed (CRLH) metamaterials [19]. Caloz proved in [20, 21] that the pure LH structure does not exist in reality even in a limited frequency region and the LH elements all necessarily include right handed (RH) properties. The inherent properties of the metamaterials lead to novel applications in the field of microwave and millimetre wave design; some of these applications were reviewed in [20, 22].

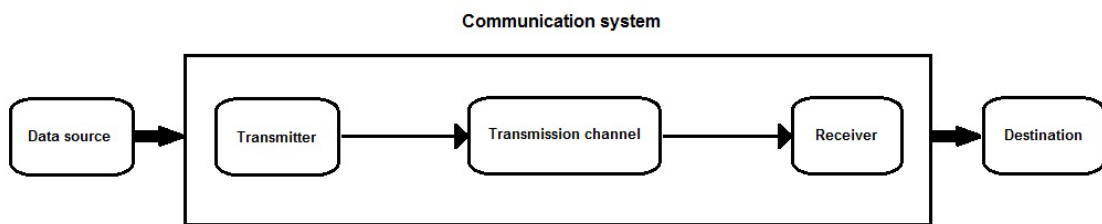


Figure 2-1: General communication system architecture.

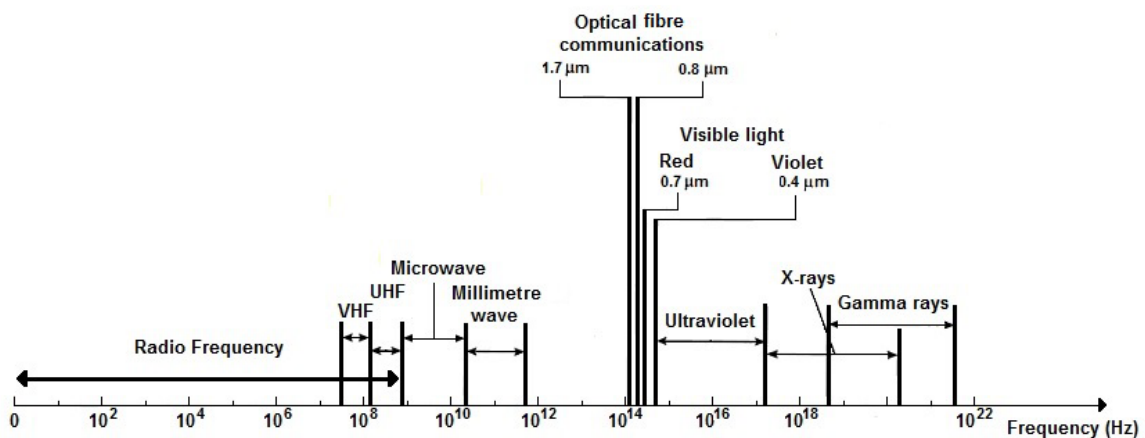


Figure 2-2: The electromagnetic spectrum range.

2.2 Optical emission in semiconductor lasers

In order to be able to model any type of laser, first a general understanding of the process in which the lasing action happens is necessary. In this section, the basic concepts of the light generation mechanism and optical emission from semiconductors will be briefly reviewed.

2.2.1 Essentials of optical generation

In optical communication systems, lasers are the main source of optical signals. Despite the different types of lasers which exist, such as gas, solid state or semiconductor lasers, the principle of optical generation is similar. The lasing action can be explained in three processes called photon absorption, spontaneous emission and stimulated emission [23]. These three processes are demonstrated in Figure 2-3. As quantum theory explains, electrons can only exist in discrete energy bands. It is seen in Figure 2-3 (A) that in the absorption process, the electron in the lower energy level (steady state level) will be excited by a photon with the required energy and moves to a higher energy level (unstable state). On the other hand in the spontaneous emission, the excited electron in the higher energy band emits the photon with the exact energy to move to more stable states. This process is illustrated in Figure 2-3 (B). As the electrons travel between these energy levels they absorb or emit radiation with the frequency f . Equation 2-1 illustrates the Planck's law used to calculate the frequency of the absorbed or emitted radiation [1]. The parameters E_1 and E_2 represent the lower and higher energy levels and h is the Planck constant.

$$E_2 - E_1 = hf \quad 2-1$$

As the name laser (light amplification by stimulated emission of radiation) suggests, the stimulated emission is one of the distinctive properties of a laser that makes it more appealing for optical fibre communications. In the stimulated emission, as shown in Figure 2-3 (C), a photon of energy hf will collide with an excited electron in the higher energy level. This will result in de-excitation of the electron to the lower energy level, which leads to the emission of a photon with same energy, phase and direction of the incident photon.

Another important phenomenon necessary to reach optical amplification in lasers is the population inversion. In room temperature, normal structures are in thermal equilibrium, where the number of electrons in the steady state energy level is greater than the number of electrons in the higher energy state. In order to achieve lasing action it is necessary to create a non-equilibrium condition in the structure, so that the population of the excited electrons in the higher energy band is greater than the number of electrons in the steady state level. This non-equilibrium condition is called population inversion. In Figure 2-4 a representation of the population inversion is demonstrated.

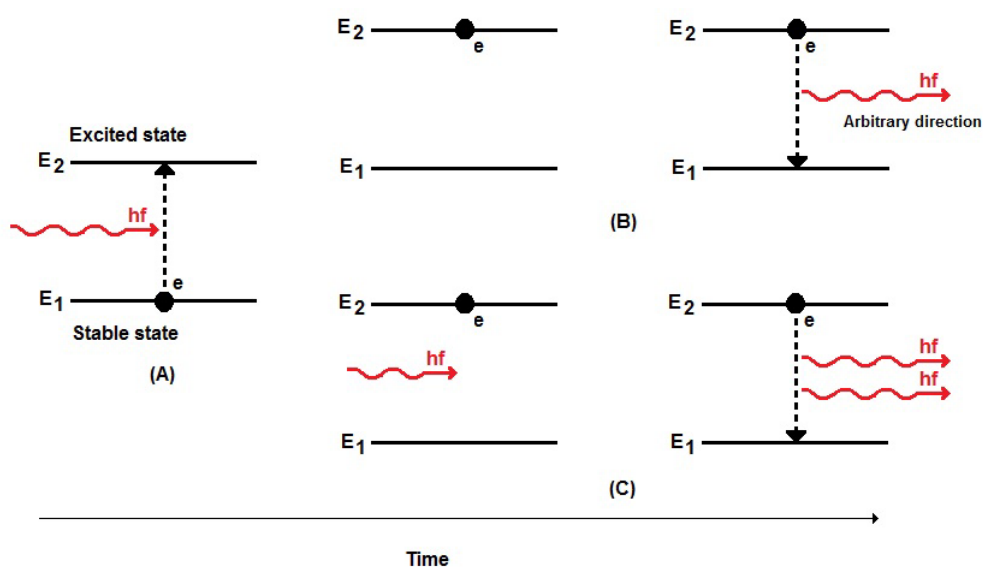


Figure 2-3: Fundamental optical process including (A) photon absorption, (B) spontaneous emission and (C) stimulated emission.

Non-equilibrium scattering of electrons can be only reached with the aid of an external source of energy. It should be noted that, according to the Einstein relation, population inversion is not possible in double state materials [1]. However population inversion can happen in materials with three or four energy state levels. In these types of materials the electrons would be pumped to the highest energy level and as this is a very unstable state, the electrons rapidly fall to the lower energy levels. These middle energy levels that are more stable than the highest energy level are called metastable states. In the metastable state it takes more time for electrons to fall to the more stable level and therefore the population inversion can occur. A more detailed explanation of the optical processes can be found in [1, 24].

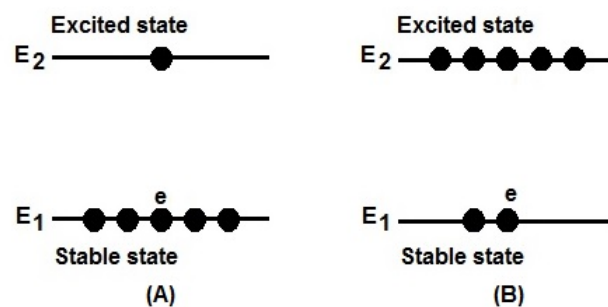


Figure 2-4: Schematic illustration of (A) material at the thermal equilibrium and (B) non-equilibrium known as population inversion.

Another key aspect of the laser, which makes it preferable for optical communications, is the coherence of the output beam. Since the length of the optical medium is rather small, if the stimulated photons are able to escape out as they reach the end of the active region for the first time, the amplification and coherence of the output beam cannot be obtained. Therefore in the lasers' structures, both ends of the active region are covered by material with very high reflectivity so that it stops the photon escaping the active region, causing it to reflect back

inside this region to generate more stimulated photons. If one of the reflective ends is fabricated to be able to partially transmit, the generated stimulated photons can radiate when the power exceeds a certain threshold. The constant output is only obtained when the amplification gain within the active region equates the losses in the active region. The sources of losses in the active region are mainly due to the scattering, absorption and impurities of the amplifying medium, as well as diffraction due to the reflecting ends.

2.2.2 Optical radiation in semiconductors

Most materials can emit a visible spectrum if the non-equilibrium thermal condition of the material is satisfied. However, only a few materials are capable of monochromatic emission, while most have a broad frequency range emission such as ordinary lamps. Semiconductors, on the other hand, can be used as a suitable candidate for the emission of a narrow band with a small divergence light beam at room temperature [25]. Intrinsic semiconductors at room temperature have few electrons at the upper energy level (known as the conduction band); therefore few holes in the more stable energy level (also known as the valance band). In this condition the Fermi energy level (E_F) which indicates the distribution of carriers in the conduction band and the corresponding holes in the valance band, is at equal distance from both the conduction and valance band. In order to fabricate $p - n$ junctions, the intrinsic semiconductors have to be doped with impurities. The n -type semiconductors can be achieved by doping the intrinsic semiconductors with the donor impurities and therefore will result in the conduction band having a considerable number of free carriers. The p -type semiconductors are fabricated by doping the intrinsic semiconductors with the acceptors impurities which results in more holes in the valance band than the carriers in the conduction band. Doping the semiconductors changes their Fermi level by moving it near to the

conduction band in the case of n -type semiconductors and near to the valance band in p -type semiconductors. The intrinsic, n -type and p -type semiconductors' energy band schematic is illustrated in Figure 2-5.

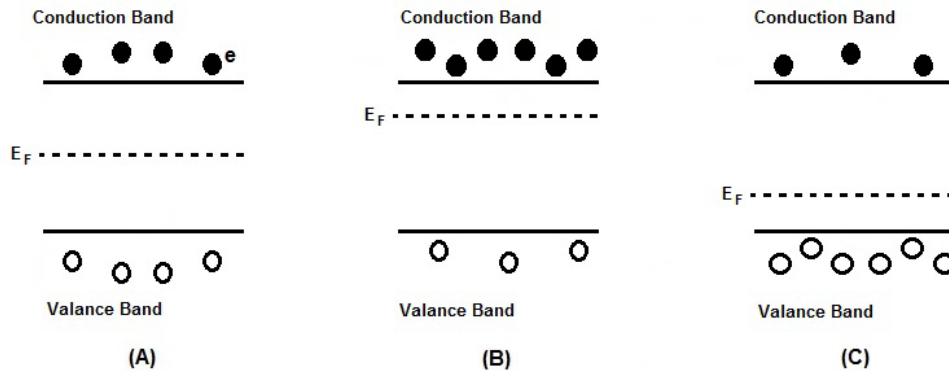


Figure 2-5: Energy band schematics of (A) intrinsic, (B) n -type and (C) p -type semiconductors.

The $p - n$ junction diodes are formed by joining together p -type and n -type semiconductors. This will result in the generation of a depletion layer between the n -type and p -type material. This layer is free of any moving charge and will only consist of the donor and acceptor impurities. The depletion layer in the absence of external voltage works as a potential barrier that prevents the inter-diffusion of the majority carrier from either side of the junction.

The semiconductors can be categorised into two types according to their wave vectors (k), called direct and indirect semiconductors. In the direct semiconductors the wave vector of the excited carriers in the conduction band is the same as the corresponding holes in the valance band. In the indirect semiconductors the carriers have a higher wave vector than the holes in the valance band [25]. Figure 2-6 illustrates the direct and indirect semiconductors' energy band versus the wave vector.

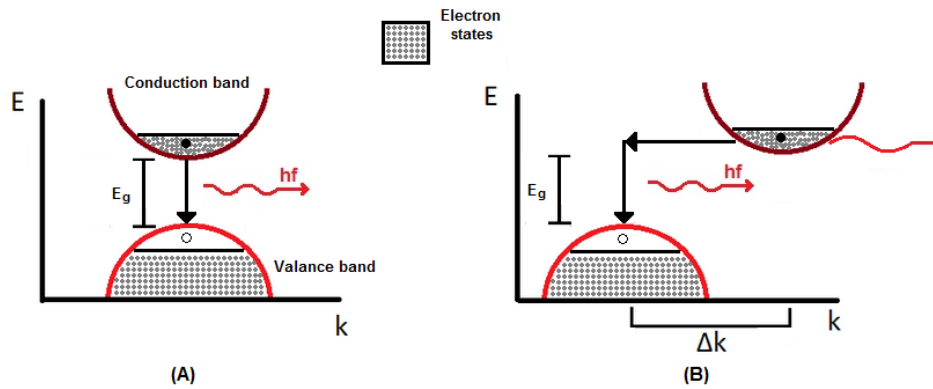


Figure 2-6: Energy-wave vector diagram for (A) direct band gap semiconductors and (B) indirect band gap semiconductors.

The main two emission types in semiconductors, known as spontaneous and stimulated emission, are highly dependent on the selection of the appropriate type of semiconductor. The spontaneous emission mostly happens in the LEDs and the stimulated emission is the distinguishing feature of the semiconductor lasers. In the spontaneous emission, the forward biased $p - n$ junction reduces the depth of the depletion layer and therefore the majority carriers of each side can travel to either side of the $p - n$ junction. The augmented concentration of the minority carriers in the opposite type sections will result in the recombination of the carriers across the band gap. This may result in the generation of the non-radiative recombination where the released energy will be dissipated in the form of heat and lattice vibrations; or it can result in the photon generation and therefore radiative recombination, which in this case is the generation of spontaneous emission. Since in the direct band gap semiconductors the electron-hole recombination occurs, the wave vector of the electron remains almost unaffected. Therefore this type of semiconductor provides an efficient mechanism for photon generation. On the other hand, in the indirect band gap semiconductors, as the maxima and minima of the valance and conduction band have

different wave vectors, therefore electron-hole recombination can only happen if the electrons lose momentum first. This three particle process in the indirect band gap semiconductors is much slower than the two particle process in the direct band gap semiconductors; which will improve the probability of the non-radiative process.

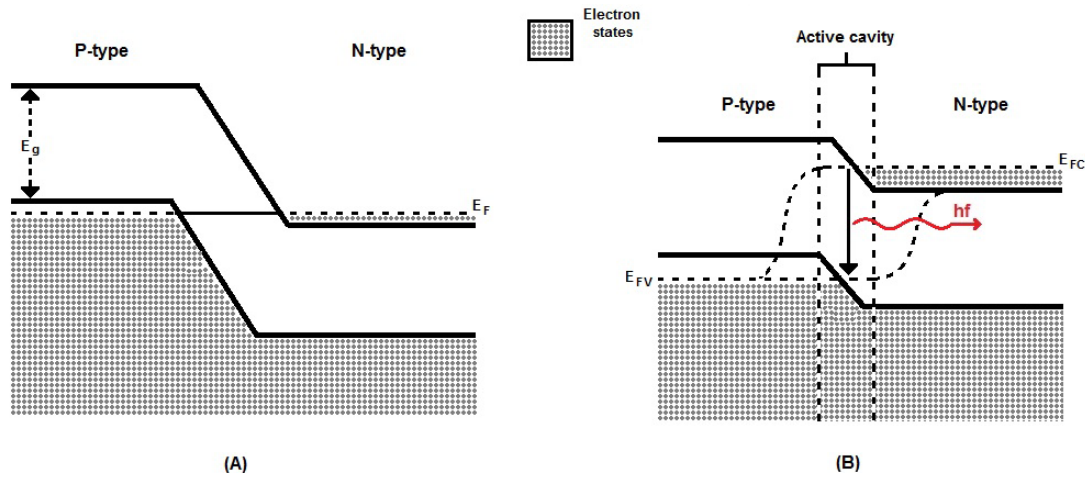


Figure 2-7: Heavily doped p-n homojunction (A) no biasing voltage (B) strongly forward biased.

In semiconductor lasers, to achieve the stimulated emission, population inversion should be achieved first. In order to reach the population inversion, the intrinsic $p - n$ junction semiconductor should be heavily doped with donors or acceptors as appropriate on each side of the junction (p -type with acceptor and n -type by donor impurities). The heavily doped acceptor impurities in the p -type region will lower the Fermi level to below the valance band. On the other hand, the heavily doped donor impurities in the n -type region will increase the Fermi level to above the conduction band. In the absence of the external potential energy the Fermi level of the $p - n$ junction is along the same line as can be seen in Figure 2-7 (A). To obtain the stimulated emission in the second step, the heavily doped $p - n$ junction has to be forward biased. This will result in the generation of the small region called the active region,

near to the depletion layer, where the free populations of the electrons and holes exist concurrently. In the active region the condition for the stimulated emission, as explained earlier in this chapter, is fulfilled. Hence the density of photons that are restricted in the active region will be amplified. The schematic of the forward biased heavily doped $p - n$ junction semiconductor is illustrated in Figure 2-7 (B). It should be noted that in order for the $p - n$ junction to start the lasing action the optical cavity should be shaped by cleaving and roughening the sides of the junction to form the optical feedback and therefore prevent any unwanted emission.

It is important to point out that the homojunction structure is considered above, where only one semiconductor was used to form the $p - n$ junction structure. Conversely the junctions can be formed by joining the semiconductors with different band gap energies, which can result in the improvement of the radiative properties of the semiconductors. These types of junctions are widely known as heterojunctions. The heterojunctions can be categorised as isotype and anisotype junctions. The isotype heterojunctions which are $n-n$ or $p-p$ structures are useful for confinement of the minority carriers in the active region. The anisotype heterojunctions which are $p - n$ structures, due to the large difference between their band gap energies, improve the injection efficiency of the carrier in order to achieve the population inversion. The energy band and the layer structure of the double heterojunction (DH) injected laser is illustrated in Figure 2-8 [1]. The use of a DH structure in the design of the semiconductor lasers reduces the threshold current by a factor of 100.

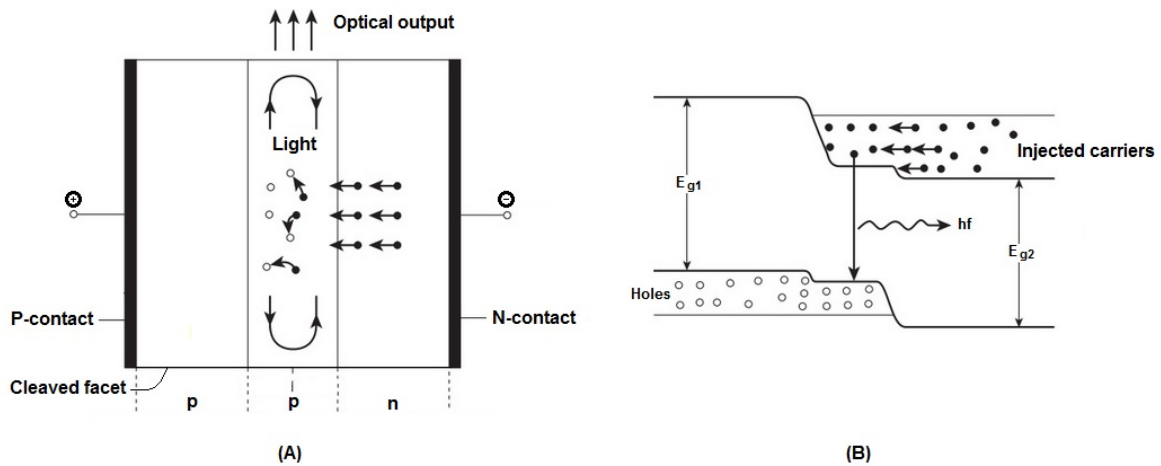


Figure 2-8: Double Heterojunctions' (DH) semiconductor (A) layer and (B) energy band schematics [1].

2.3 Vertical Cavity Surface Emitting Lasers (VCSELs)

The vertical cavity surface emitting laser is an evolutionary generation of the semiconductor laser diode, which radiates a coherent optical signal vertical to the device substrate. In contrast to the conventional edge emitting lasers, VCSELs have a rather different structure since a short vertical cavity is formed by the surfaces of the epitaxial layers and the optical output is emitted from one of the mirror faces [1]. The VCSEL structures have a number of advantages in comparison to the conventional edge emitting lasers. These advantages include: very low threshold current and ultrahigh bit rate modulation, due to a small active region volume; high relaxation oscillation frequency due to the short photon lifetime; high coherence with low divergence and circular output beam; and ease of integration with optical fibres and other optical devices, due to good mode matching [11]. VCSELs have the ability to function over a wide range of temperatures with minimum change in performance, which enables unmonitored operation[26]. The last, but maybe one of the most important merits of the VCSELs, are the simple testing procedures, which is due to the on-wafer testing ability of

the VCSELs in comparison with the facet emitting lasers. It should also be noted that the compact size of the VCSELs in comparison with conventional lasers results in the fabrication of more devices per wafer, which reduces the cost of productions in large scale [27]. Similar to any other devices, VCSELs suffers from a number of shortcomings. These include: difficulty of obtaining highly reflective distributed Bragg reflector (DBR); relatively high Auger recombination [27]; restricted optical emission performance due to the small active cavity dimensions which limits the output power to a few milli-watts; relatively long transverse cavity length resulting in multiple transverse optical modes; and also large frequency chirp of VCSELs that curbs the fibre transmission speed and distance [28].

The structure of a typical VCSEL is illustrated in Figure 2-9. It is observed in Figure 2-9 that despite the difference between VCSELs and conventional semiconductor lasers, the VCSEL structure includes the *p*-type and *n*-type semiconductors, the active region and the top and bottom contacts. As can be seen in Figure 2-9, the Fabry-Pérot active cavity consists of a multi quantum-well (MQW) material between two multi-layered distributed Bragg reflector (DBR) mirrors of a quarter of the laser wavelength thick, with alternately high and low refractive index. Quantum wells occur in thin-layered semiconductor structures in which the carrier movement normal to the active region in these devices is strictly limited. This results in quantisation of the energy into discrete energy levels. Quantum wells have state diagrams which exhibit step-like state density, resulting in quantum well lasers having an inherent benefit of higher gain at the low carrier density and therefore causing significantly smaller threshold currents [1]. The number of Bragg gratings on each side of the active region dictates the facets' reflectivity. The number of DBR layers typically varies between 10 and 30 in order to provide the required reflectivity in the top and bottom facet. It should be noted that the exact number of Bragg grating layers depends on the semiconductor material used in the structure [26]. The use of the DBR structure results in reflectivity of above 99% that is

needed for VCSELs. The high reflectivity needed in VCSELs is due to their small cavity length of around a wavelength of the emitted light. The small cavity dimension of VCSELs means that in a single pass of the cavity a photon has a small chance of starting a stimulated emission. Therefore VCSELs require highly reflective mirrors to provide efficient feedback that is needed to build-up the required optical power within the cavity. The other advantage of DBR mirrors in the design of the VCSELs is that any light reflected back towards the laser cannot re-enter the cavity. Hence the VCSELs are efficiently isolated against any other optical signal entering the active cavity.

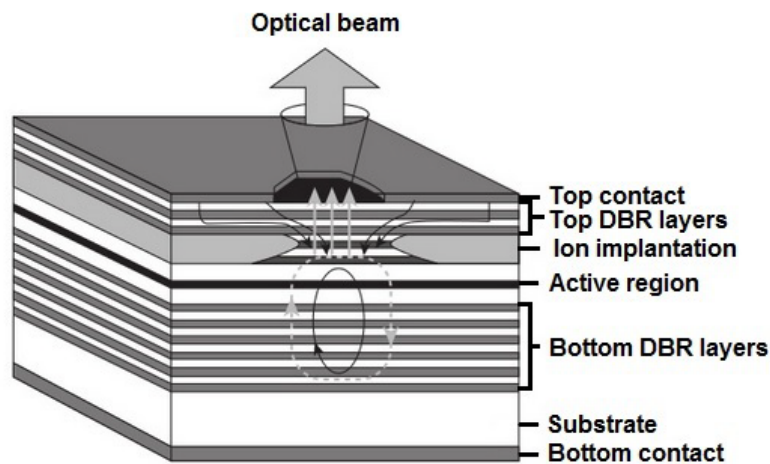


Figure 2-9: Generic structure of vertical cavity surface emitting laser (VCSEL) [1].

It is observed from Figure 2-9 that the top and bottom layers form a $p - n$ junction and the flow of the electric current is from the top contact to the $p - n$ junction. The current confinement and short cavity is typically achieved in the VCSELs by ion implantation, which is the method of injecting a non-conducting substance around the active region. The circular dotted line in Figure 2-9 represents the optical power generated and reflected by the DBR

layers through the active region, to provide necessary power for the generated optical signal to enable the emission of the optical beam from the top of the structure.

2.4 VCSEL rate equations

Rate equations in VCSELs, like any other type of laser diode, describe the exchange of energy between the input current and the output power, by considering the rate of exchange of the three principal optical processes; known as: spontaneous emission, stimulated emission and photon absorption. The large and small signal analyses of the VCSEL rate equations aid the understanding of VCSEL's high-speed modulation.

The exchanges between the photons and carriers are generically presented in Figure 2-10. The VCSEL rate equations are expressed based on Figure 2-10 and can be reviewed in Equations 2-2 and 2-3 [29]: where N and S are the carrier and photon concentrations in the VCSEL's active layer; η_i is the quantum efficiency; I is the injected current; q is the electron charge; V_{act} is the volume of the VCSEL's active cavity; A , B and C are the non-radiative, radiative and Auger recombination coefficients, respectively. Langevin noise sources F_N and F_S account for the fluctuations of carrier and photon densities; Γ is the current confinement factor; β is the spontaneous emission coefficient; τ_s is the photon life time and G is the modal gain which is the function of both carrier and photon densities and expressed in Equation 2-4. The variables v_g , a_0 , N_{tr} and ε in Equation 2-4 are the group velocity, differential gain coefficient, transparency carrier density and nonlinear gain factor respectively.

$$\frac{dN}{dt} = \frac{\eta_i I}{qV_{act}} - (A + BN + CN^2)N - G \cdot S + F_N \quad 2-2$$

$$\frac{dS}{dt} = \Gamma \cdot \beta \cdot B \cdot N^2 + \Gamma \cdot G \cdot S - \frac{S}{\tau_s} + F_s \quad 2-3$$

$$G = v_g \cdot a_0 \cdot \frac{N - N_{tr}}{1 + \epsilon S} \quad 2-4$$

In the carrier rate of Equation 2-2, the first term on the right hand side of the equation defines the electrons pumped into the active region that then recombine gradually with the holes during the spontaneous and stimulated emission, as accounted for in the second and third terms of Equation 2-2 respectively. On the other hand, in Equation 2-3 the first term represents the build-up of the photon population due to spontaneous emission and the second term represents the number of simultaneously emitted photons with the required direction that couple into the lasing mode. The third term in this equation represents dissipation of the photons due to the absorption [23].

The VCSEL's rate equation above is an accurate model of the carrier-photon exchange within the active region; as it includes the Langevin noise sources and also the gain compression effects, due to the hole burning and carrier diffusion [30]. Spectral hole burning is the photo-induced changes in the absorption spectrum which leads to gain compression of the semiconductor lasers [31, 32]. Spectral hole burning specifically increases the damping rate of relaxation oscillations and leads to single mode instability [32, 33].

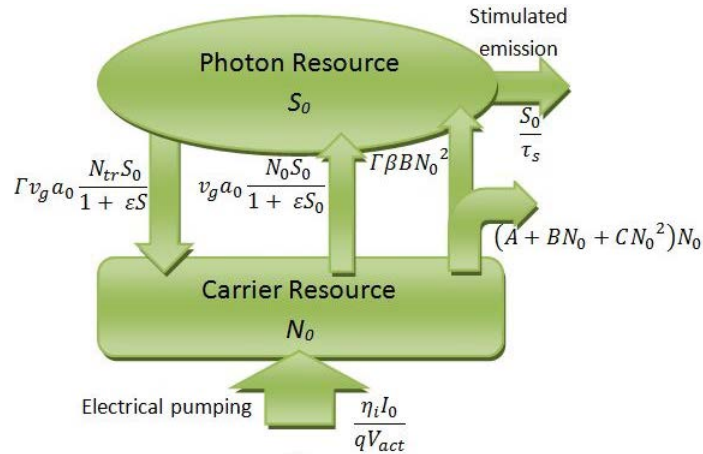


Figure 2-10: Visual illustration of VCSEL rate equations.

2.5 VCSEL modelling

There have been lots of attempts to present an accurate model for VCSELs over the last decade. These can be broadly divided into two categories: VCSEL modelling using parameter extraction, which combines an analytical and empirical optical optimisation process; and the VCSEL modelling using laser diode rate equations, in which the physical properties of the VCSEL are included using the analytical rate equations. In this section the most important works carried out in the literature are briefly reviewed.

The author in [34] presents two equivalent circuit models for a VCSEL. One represents the VCSEL in the lasing condition where the bias current is above the threshold current and the other represents the case when the injection current is set to zero. The suggested VCSEL equivalent circuits are illustrated in Figure 2-11. The initial values of the equivalent circuit model parameters were calculated using the extraction method based on the analytical approach by introducing the set of formulae derived from the presented equivalent circuits. The initial parameter values were then optimised in order to achieve the required error criteria.

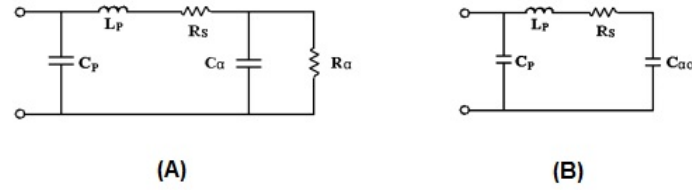


Figure 2-11: Proposed VCSEL equivalent circuits in [34]: (A) biased above threshold

($I_b > I_{th}$). (B) zero biased condition ($I_b = 0$).

Jianjun applied the extraction and optimisation technique that is summarised in Figure 2-12 for an actual VCSEL operating at 850 nm and the threshold current of $I_{th} = 0.6\text{ mA}$ to find the required model parameters. It should be noted that Jianjun, in the proposed model neglects the optical characteristics of the VCSELs, as he is assumed that optical characteristics of the VCSELs do not affect the input impedance of the model. This model considered the intrinsic VCSEL as a simple resistance R_a . However later Jianjun in [35] completed the proposed equivalent circuit model, by adding the rate equation driven model developed earlier by him in [36] for the conventional semiconductor laser diode. The proposed equivalent circuit model in [35] for the small signal and large signal analysis is presented in Figure 2-13. This work however mainly focuses on the calculation of the model parameters and does not give realistic and in depth knowledge of the VCSEL optical properties.

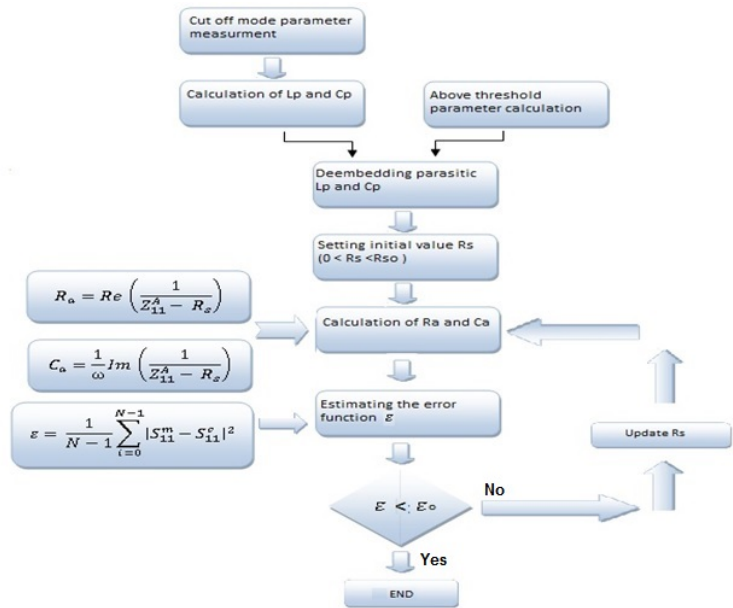


Figure 2-12: Extraction and optimization algorithm suggested by [34].

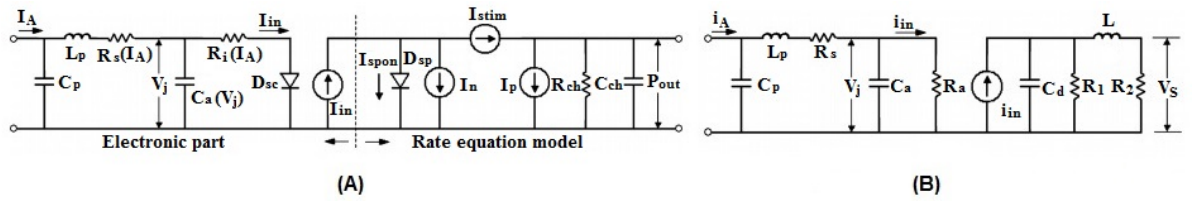


Figure 2-13: Proposed equivalent circuit model [35]: (A) large signal equivalent circuit model and (B) small signal equivalent circuit model.

Reference [37] presents a more detailed nonlinear model that includes the test fixture, parasitic network and the intrinsic VCSEL model. The proposed VCSEL model in [37] is illustrated in Figure 2-14. In this model the test fixture provides the connection to the measurement equipment. The next part of the suggested equivalent circuit model, is the parasitics network due to the wire bonds and packaging. The intrinsic VCSEL was modelled by series resistance R_a , which represents the access resistance of the VCSEL, $V(I, T)$; this

signifies the voltage fluctuation in the active cavity with respect to temperature and a shunt nonlinear capacitor C_j , representing the overall capacitance of the VCSEL structure including the $p - n$ junction diode capacitance, DBR capacitance and oxide layer capacitance.

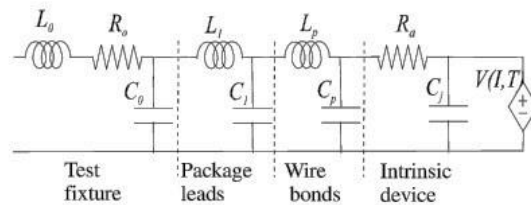


Figure 2-14: Comprehensive VCSEL model by [37] .

The authors in [37] introduced a number of semi-empirical equations in order to calculate the parameters of the intrinsic VCSEL model. It was suggested that the parameters of the empirical equations could be extracted using the measured DC current-light-voltage (I-L-V) characteristics at different temperatures and the measured small signal reflection coefficient of the VCSEL package.

The proposed two step extraction technique was then applied on two different commercialised VCSELs with an oxide aperture structure, operating at 850 nm , packaged on TO-46 and both capable to run at 2 Gb/s . The extracted parameters were then optimised in order to achieve an acceptable accuracy between the measured and simulated reflection coefficient and $I - V$ curves. Although this work provides an accurate model for the parasitic networks, it indicates that the suggested model is not capable of providing any realistic estimation of the optical properties of the VCSEL and can only be used to estimate the electrical characteristic of the VCSEL IC.

The same authors later in reference [38] present the modified VCSEL equivalent circuit model by using the same test fixture and combining the wire bonds and packaging parasitic

networks into a single LC structure. This work improved the VCSEL intrinsic model's ability to explain the optical VCSEL characteristic by proposing the equivalent circuit model based on the VCSEL rate equations. The proposed VCSEL equivalent circuit is illustrated in Figure 2-15. The VCSEL intrinsic in this work is modelled by a series resistance R_a and a shunt nonlinear capacitance C_j representing the access resistance and intrinsic capacitance of the VCSEL respectively. In addition, the intrinsic VCSEL model includes the internal resistance R_{int} , ideal diode D_{VCSEL} and a temperature dependent voltage controlled voltage source E_{inp} .

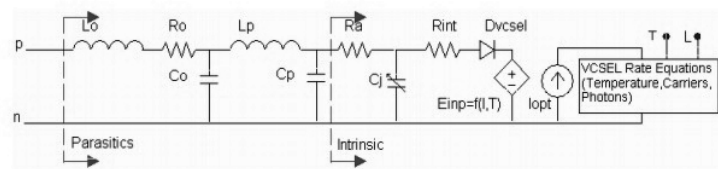


Figure 2-15: Suggested VCSEL equivalent circuit model in [38].

In this work, a semi-empirical equation relates the presented model based on VCSEL rate equations to VCSEL thermal effects using a temperature dependent voltage controlled voltage source E_{inp} . This equation can be reviewed in [38]. Since the calculation of parameters for this model requires finding 16 elements for the input circuit and 25 for the rate equation model, the authors proposed a three stage parameter extraction technique. In the first step, the DC dependent parameters of the input circuit including R_{int} and R_a were estimated based on the DC current-light (I-L) characteristics. Then, by using the optimisation software, the estimated values were tuned to achieve the required accuracy with the measured VCSEL current-voltage (I-V) curve. In the next step, the remaining parameters of the input circuit, which include the parasitics and test fixture parameters, were calculated using the

optimisation tool and tuning to achieve the acceptable accuracy between the measured and optimised S_{11} vector. Finally in the last step, the carrier and photon related parameters in the rate equations were estimated by optimising the parameters to achieve the measured DC I-L VCSEL characteristics. It is clear from the explanation that although in this work a more comprehensive model of the VCSEL is developed, the complication of the model requires sophisticated extraction and optimisation techniques. Furthermore, in this work the proposed equivalent circuit is only capable of following the VCSEL characteristic that is already measured and is not able to predict its characteristics based on the physical structure of the VCSEL.

Reference [39] is another article that tried to use the VCSEL rate equations to model the VCSEL behaviour. In this work the VCSEL rate equations' model includes the basic spatial and thermal behaviour of the VCSEL. Although the authors did not clearly illustrate the VCSEL's equivalent circuit model, but by following the analysis in this work it is indicated that the presented circuit level model is capable of modelling the optoelectronic characteristics of the VCSEL, such as L-I characteristics and transient response of the VCSEL (Figure 2-16). The parameters of the model presented in this work were calculated using the VCSEL parameters taken from [40]. Although the model proposed is capable of modelling the intrinsic characteristics of the VCSELs with modest computational requirements, the model does not take into account the effects of the parasitics and the test fixture in the simulation of the VCSEL characteristics. Furthermore, the presented model in this work is not capable of predicting the VCSEL's optical characteristics. These weaknesses make this a non-realistic model.

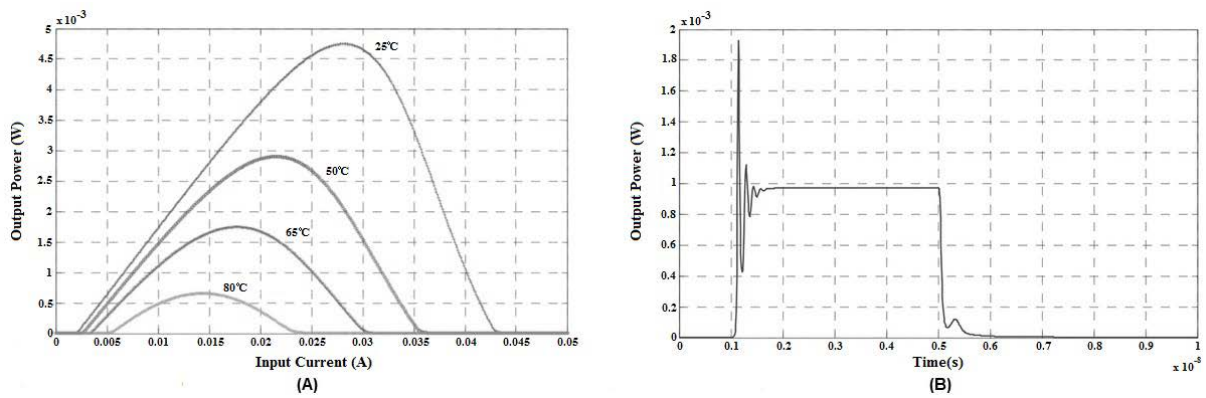


Figure 2-16: Simulated results of [39]: (A) L-I characteristic of the VCSEL for different temperatures (B) transient response of the VCSEL.

Reference [41], is another example of VCSEL modelling based on the rate equations. This work presents a comprehensive VCSEL equivalent circuit model that takes into account the dependence on VCSEL temperature of the threshold current and the optical output power rollover by presenting the empirical offset current in the VCSEL rate equations. The proposed model in this work is only capable of analysing the VCSEL's AC and transient behaviour over a limited range of temperature, due to the empirical nature of the thermal behaviour of the VCSEL model.

The equivalent circuit model suggested in this work is shown in Figure 2-17. In this model pd and nd represent the electrical ports of the VCSEL; the voltage node related to port po represents the output power P_o and device temperature T is modelled using the td terminal. Further information on how to calculate the equivalent circuit elements can be found in the literature. It should be noted that as seen in Figure 2-17, the VCSEL equivalent circuit is modelled by three mutually related sections. This makes the model less useful for computer aided design (CAD) in optical system simulations composed of many photonic and electronic elements. The results of modelling three different VCSELs using the model proposed in this

work indicates that the model over-calculates the thermal attributes at high temperature; which can be the result of simplistic assumptions in the rate equations used in this model, such as neglecting the spatial hole burning.

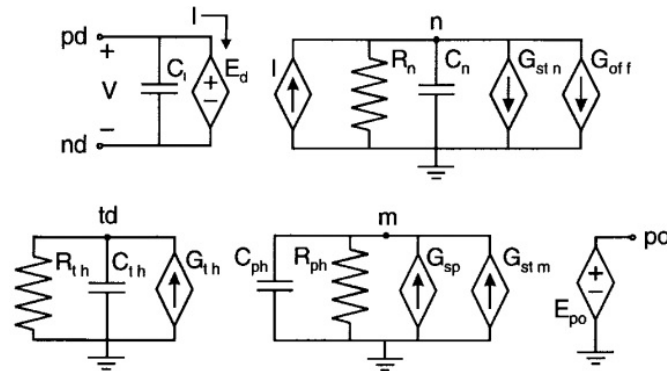


Figure 2-17: The proposed VCSEL equivalent circuit model [41].

The same authors in [40] introduced a more comprehensive version of the model developed in [41], which enables the modelling of the multimode VCSEL structures. In this work the rate equations used to model the VCSEL include the thermal dependence of the active cavity's gain; thermal leakage of the carriers out of the active cavity; as well as the spatial properties of the VCSEL, including the transverse profile of optical modes and lateral diffusion of carriers in the active cavity. The authors claim that although spatially independent multimode rate equations were used, which results in a model with less computational difficulties, the rate equations still implicitly model VCSEL's spatial properties. In this work, the same equivalent circuit used in reference [41] was used as illustrated in Figure 2-17.

The efficiency of the suggested equivalent circuit model of [40] was verified by first simulating typical single and two mode VCSEL properties, which include thermally dependent threshold current and small signal analysis with respect to the transient

phenomena, multimode operation and temperature. The equivalent model was then simulated against the measured characteristics of four VCSEL structures. The results indicate that although the simulated and measured results showed a similar trend, the simulated results did not exactly match the measured data. This mismatch can be explained based on the nature of the suggested model in this work, as a relatively large number of the model's parameters were tuned to match few experimental data. Therefore it is rather difficult to make sure all the model's parameters were correctly related to the corresponding physical parameters of the particular VCSEL structure. Figure 2-18 indicates the comparison between the modulation response of the simulated results and the measured data at the ambient temperature of 22 °C for the thin oxide aperture VCSEL presented in reference [42]. One of the shortfalls of the demonstrated equivalent circuit model in [40, 41] is that the authors did not take into account neither the VCSEL intrinsic noise sources, nor the realistic parasitic and the matching network for the VCSEL model.

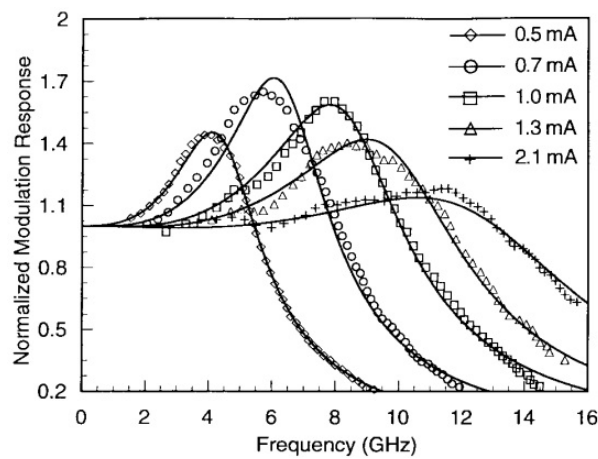


Figure 2-18: Comparison between the modulation response of the VCSEL measured in [42] (points) and simulated using the model presented in [40] (lines).

Another interesting example of VCSEL modelling, which includes a model of the VCSEL's parasitic network as well as an intrinsic VCSEL model can be found in [29]. The authors used a methodology which was first introduced in [43, 44], to model conventional lasers. In this model the small signal electrical equivalent circuit was derived based on comprehensive rate equations that include the nonlinear gain term and covers the spatial related properties of the VCSELs. One of the unique features of the equivalent circuit model in this work is that each element of the model represents a physical optical cavity entity. Another distinctive feature of this model is that the elements of the equivalent circuit are calculated following an analytical process based on basic theorems such as Kirchhoff's circuit laws and the optical rate equations. This analytical process resulted in equivalent circuit element values that do not require any numerical tuning. The proposed equivalent circuit model of the intrinsic VCSEL is shown in Figure 2-19 (A). Further in this work the authors used the method developed in [45] to calculate the parasitic network as a separate equivalent circuit, which is shown in figure 2-19 (B). It is important to point out that the proposed model in this work does not need any complicated intrinsic parameters extraction. Therefore by using the physical and structural dependent parameters of the VCSEL the model is capable of predicting the VCSEL's behaviour with good accuracy. However the model in this work does not take into account the effects of the intrinsic noise sources related to the carrier and photon population that are vital for a realistic model of a VCSEL. The authors in this work did not also take into account the mismatch between the proposed combined model of the VCSEL and the parasitic network and the vector network analyser (VNA). It should be also noted that in [29] the authors made a mistake in the derivation of the formulas for intrinsic VCSEL model parameters.

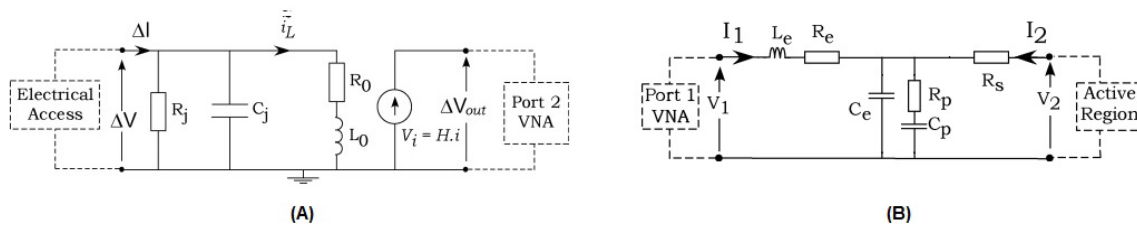


Figure 2-19: Proposed VCSEL model in [29]: (A) intrinsic VCSEL model and (B) VCSEL parasitic network.

From the above review of the models suggested for a VCSEL in the literature, there are a number of issues that have limited the application of the proposed models. The use of the empirical equations for the calculation of the model's parameters limits the proposed model to specific types of VCSEL. Only a few of the proposed models take into account the effect of the parasitics on the VCSEL characteristics. Furthermore, none of the proposed models include the quantum noise arising from the fluctuation of the carrier and photons inside the intrinsic VCSEL structure that may significantly reduce the VCSEL's signal to noise ratio. In addition, due to the high frequency operating range of the VCSELs, a matching network needed to be included in the VCSEL model to minimise the reflection towards the signal generator. A high level of RF power is required to overcome the ohmic losses related to electrical parasitics, bias tee and electrical cables. Table 2-1 shows a summary of the reviewed articles on the VCSEL modelling, detailing the key model features: the type of model, which indicates whether an empirical or analytical based model is suggested; whether the proposed model is capable of predicting the VCSEL optical characteristics or just modelling the VCSEL chip electrical properties; the inclusion of the parasitic network in the VCSEL model and the presence of noise effects in the VCSEL intrinsic model. Also included in the table are the details about the inclusion of the thermal effects and matching network in

the suggested model. For comparison the model proposed in this thesis as explained in chapter 3 is also included in the Table 2-1.

Table 2-1: Summary of the reviewed articles on VCSEL modelling.

Reference	Type of VCSEL model	Optical or electrical properties	VCSEL's thermal effects	Inclusion of parasitic network	Noise effects	Matching network
[34]	Empirical	Electrical	No	Yes	No	No
[35]	Analytical	Electrical	No	Yes	No	No
[37]	Empirical	Electrical	Yes	Yes	No	Yes
[38]	Analytical	Both	Yes	Yes	No	Yes
[39]	Analytical	Electrical	Yes	No	No	No
[41]	Semi-analytical	Both	Yes	Yes	No	No
[40]	Semi-analytical	Both	Yes	Yes	No	No
[29]	Analytical	Both	No	Yes	No	No
This thesis	Analytical	Both	No	Yes	Yes	Yes

2.6 Microwave antennas

In this subsection, we now turn our attention to background research in the other main area of research in this thesis, namely microwave antennas. An antenna is defined as a section of a communication system aimed to send or receive electromagnetic waves carrying the modulated information [46]. It should be noted that, as illustrated in Figure 2-20 (A), antennas are generally connected to other elements of the communication system using a

transmission line or waveguide. A typical equivalent model of a transmitter antenna is shown in Figure 2-20 (B). The antenna impedance is represented in Equation 2-5, where R_A and X_A represent the antenna's resistance and reactance. The antenna's resistance, R_A in this model, includes the radiation resistance R_r and the loss resistance R_L which denotes the conduction and dielectric losses.

$$Z_A = R_A + jX_A \quad 2-5$$

$$R_A = R_r + R_L \quad 2-6$$

Since different properties are expected from antennas in different communication systems, the field of antenna design has been in constant development since it was first introduced in the last century. There are different types of antenna structures, each having unique merits for a particular application. For instance, some antennas are more directional, meaning that they are capable of propagating most of the signal power in specific directions, such as log-periodic and horn antennas; whereas some other antennas may provide wider bandwidth, like spiral antennas. In this work two different antenna structures called microstrip patch antennas and leaky wave antennas are reviewed.

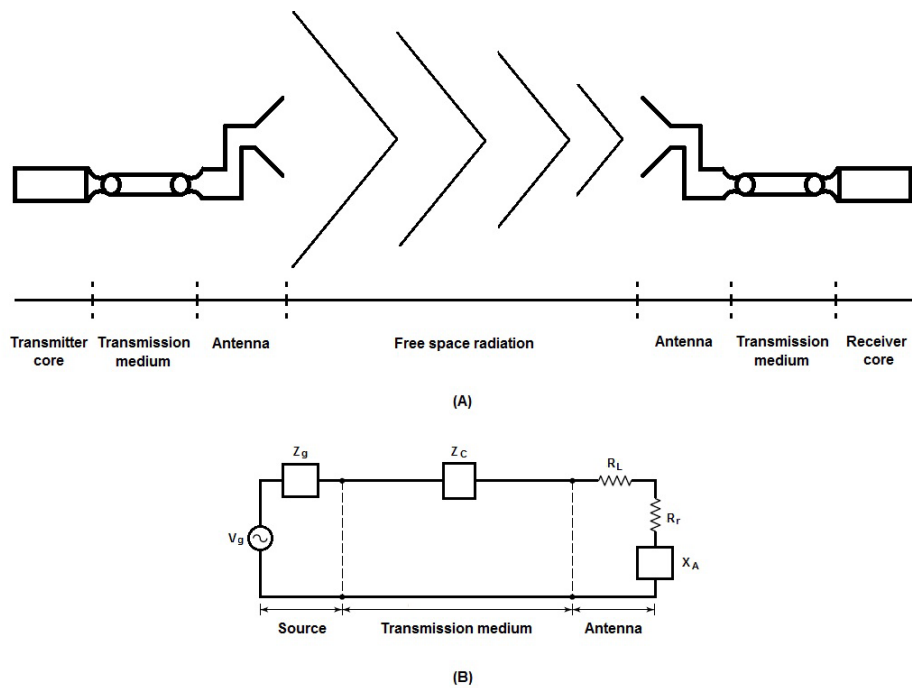


Figure 2-20: Schematic of (A) typical microwave antenna based communication system and (B) a typical antenna transmitter equivalent circuit.

2.7 Basics of microstrip antennas

Microstrip antenna is perhaps one of the most well-known examples of planar antenna. Planar structures are typically unbalanced, consisting of uniform conductors on a dielectric substrate [47]. The majority of planar structures were designed using microstrip transmission lines. Microstrip transmission lines consist of conducting strips on one side and the ground plane on the other side of the dielectric substrate. A side view of a typical microstrip transmission line including the electric and magnetic field lines is illustrated in Figure 2-21. A detailed explanation of microstrip transmission lines including characteristic properties, effective dielectric constant and losses within the microstrip structures was presented in [48, 49].

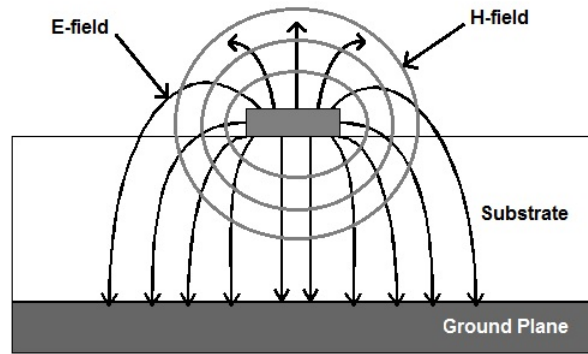


Figure 2-21: A side view of a typical microstrip transmission line including the electric E and magnetic H fields.

The microstrip antenna, due to its modest design complexity, low manufacturing cost and performance, is a popular candidate for satellite, missile, mobile and wireless applications. However, microstrip antennas suffer from low efficiency and power, low scanning ability and narrow frequency bandwidth; which need to be considered and compensated in the design process.

2.7.1 Patch antenna

The patch antenna is perhaps the most well-known microstrip antenna. This group of antennas consists of a microstrip patch on top of the substrate and a ground plane on the other side. The patch, which is the radiating element of the antenna, can take different geometry such as, rectangular, circular, elliptical, whole or portion of circular rings. The specific geometry is chosen depending on the radiation and bandwidth required in a specific application. A variety of substrate materials are used in the design of microstrip patch antennas. Thick substrates with low dielectric constants (ϵ_r) (around 2.2) are more desirable

for applications where the size of the antenna is not of great interest and instead, a larger bandwidth and higher efficiency are required. In contrast, a thin substrate with high dielectric constant (ϵ_r) (around 12) results in a compact design that is desirable for microwave circuitry at the expense of sacrificing the bandwidth and efficiency [50].

As seen in Figure 2-20, the signal has to be transferred to the antenna structure. As a result of the inherent low gain of microstrip patch antennas' structures, a suitable feeding method that ensures most of the signal power is coupled to the structure is necessary. Furthermore, the feeding method directly influences the impedance matching, surface waves and operating modes of the microstrip patch antenna [51]. There are different feeding techniques, including microstrip inset, coaxial, aperture coupling and proximity coupling. Each of these feeding methods has its own merits and drawbacks. The microstrip inset feed is the most common feeding method used in microstrip patch antenna design, due to its ease of modelling and fabrication. It should be noted that this feeding method introduces high surface waves and spurious feed radiation in thick substrates. Coaxial feeding however is more difficult to model and not suitable for microstrip arrays as it leads to lots of soldering and coaxial lines. Coaxial feeding generates less spurious radiation. On the other hand, aperture and proximity coupling methods are more difficult to fabricate but will result in reduced surface waves and larger bandwidth [51, 52]. Figure 4.22 shows the schematic of the four commonly used feeding methods for typical microstrip patch antenna structure.

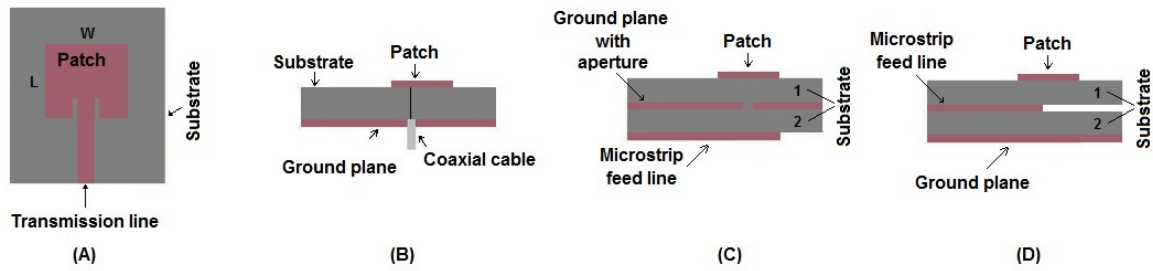


Figure 2-22: Microstrip patch antenna feeding methods: (A) microstrip inset feed line, (B) coaxial, (C) aperture coupling and (D) proximity coupling.

2.7.2 Design procedure

In order to design the patch antenna, first the length (L) and width (W) of the patch should be calculated. These values are then used to calculate the inset feed location and feed line dimensions using the formulae explained in the following sections. A simple patch antenna and the parameters needed to design the microstrip patch antenna are illustrated in Figure 2-23 (A). The equivalent circuit model of the two radiating slots of the microstrip patch antenna is shown in Figure 2-23 (B). The numbers in Figure 2-23 (B) indicate the first and second radiation slot equivalent circuit model parameters.

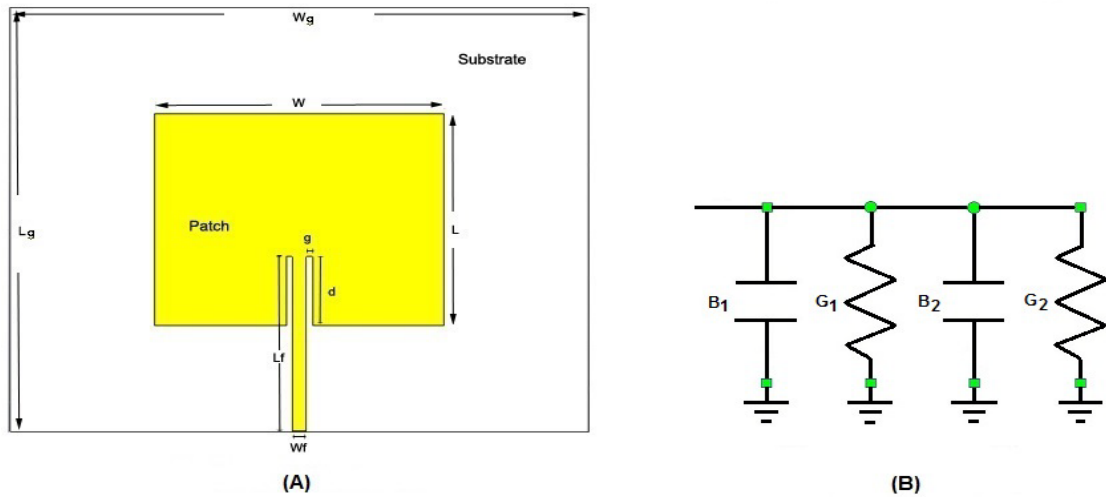


Figure 2-23: Microstrip patch antenna: (A) typical antenna geometry and (B) equivalent circuit model.

2.7.2.1 Patch width calculation

Microstrip patch antenna width can be calculated as follows [15, 53, 54]:

$$W = \frac{c}{2f_o \sqrt{\frac{(\epsilon_r + 1)}{2}}} \quad 2-7$$

It is important to point out that the width of the patch antenna will largely affect input resistance, bandwidth and antenna gain and have very little effect on resonant frequency and radiation pattern. Equation 2-7 gives a practical width for the patch, which results in good radiation efficiencies.

2.7.2.2 Patch length calculation

The length of the patch antenna mainly dominates the patch resonant frequency and plays a vital role in design. This is due to the narrow bandwidth nature of patch antenna. Length (L) can be approximated using Equation 2-8 [50].

$$L = L_{eff} - 2\Delta L \quad 2-8$$

The effective length of the patch is L_{eff} and ΔL is the extension length on either side of the patch. Equations 2-9 and 2-10 can be used to calculate the L_{eff} and ΔL respectively [50, 53, 55].

$$L_{eff} = \frac{c}{2f_0\sqrt{\epsilon_{reff}}} \quad 2-9$$

$$\Delta L = 0.412h \frac{(\epsilon_{reff} + 0.3) \left(\frac{W}{h} + 0.264\right)}{(\epsilon_{reff} - 0.258) \left(\frac{W}{h} + 0.8\right)} \quad 2-10$$

The effective dielectric constant (ϵ_{reff}) can be calculated using Equation 2-11 [15, 50].

$$\epsilon_{reff} = \frac{\epsilon_r + 1}{2} + \frac{\epsilon_r - 1}{2} \left[1 + 12 \frac{h}{W}\right]^{-\frac{1}{2}} \quad 2-11$$

2.7.2.3 Ground plane dimensions

The calculation of patch dimensions above is based on an assumption of infinite ground planes. In practice only a finite ground plane can be realised. The effect of the infinite ground plane can be also achieved in a finite plane by satisfying the condition set out in Equations 2-12 and 2-13 [55].

$$L_g \geq 6h + L \quad 2-12$$

$$W_g \geq 6h + W \quad 2-13$$

2.7.2.4 Feed point location

After the calculation of patch and ground plane dimensions, it's important to evaluate the feed point location to maintain the best impedance match between the generator and the input impedance of the patch antenna [55]. There are different feeding techniques available, as reviewed in section 2.7.1, which result in different calculations. The microstrip inset feed line calculation is reviewed here to provide background for the patch antenna designed in Chapter 5. In this feeding method, in addition to the feed point position (x_f, y_f) , feed line width (W_f) and length (L_f) also need to be calculated.

The input resistance for the dominant mode TM_{10} can be calculated from Equation 2-14. The use of a 50Ω microstrip feed line is assumed for these equations. Therefore the inset point should be located where the patch antenna's input impedance $(R_{f,in}(d))$ would match the 50Ω inset line. The inset feed distance (d) from the first radiating edge can be seen in Figure 2-23 (A). The radiation resistance $(R_{p,in})$ at the patch can be approximated using Equation 2-15 [15]. This equation determines the input resistance assuming that there are no mutual coupling effects between the patch radiating slots.

$$R_{f,in}(d) = R_{p,in}(0) \cos^2 \left(\frac{\pi d}{L} \right) \quad 2-14$$

$$R_{p,in} = \frac{1}{2G_1} \quad 2-15$$

The conductance G_1 can be calculated from Equation 2-16 [15]; I_1 can be calculated from Equation 2-17 [15].

$$G_1 = \frac{I_1}{120\pi^2} \quad 2-16$$

$$I_1 = \cos(k_0W) + (k_0W)S_i(k_0W) + \frac{\sin(k_0W)}{(k_0W)} - 2 \quad 2-17$$

Wave vector k_0 can be calculated using Equation 2-18.

$$k_0 = \frac{2\pi}{\lambda} \quad 2-18$$

In the feed line design, it is usual to select the feed line to be in the middle of the rectangular patch width in order to prevent the unwanted modes $TM_{1n}(n \text{ odd})$, hence:

$$y_f = \frac{W}{2}$$

The width of the microstrip inset feed (W_f) can be found either using the characteristic impedance (Z_c) of the inset feed that can be calculated using Equation 2-19 [50], or using microstrip line calculator software such as TXLine tool within the AWR Microwave Office package.

$$Z_c = \begin{cases} \frac{60}{\sqrt{\epsilon_{reff}}} \ln \left[\frac{8h}{W_f} + \frac{W_f}{4h} \right], & \frac{W_f}{h} \leq 1 \\ \frac{120\pi}{\sqrt{\epsilon_{reff}} \left[\frac{W_f}{h} + 1.393 + 0.667 \ln \left(\frac{W_f}{h} + 1.444 \right) \right]}, & \frac{W_f}{h} > 1 \end{cases} \quad 2-19$$

2.8 Leaky wave antenna

Leaky wave antenna (LWA) is a type of antenna capable of radiation, by leaking input power along its waveguide structure. LWAs are profoundly different from the resonance antennas as they are based on travelling waves. In this section the fundamentals of the LWAs which include the basic physics and the core of the leaky wave process are reviewed. Further in this section a summary of recent advancements in this type of antenna, which enables the radiation through broadside and endfire, is revised.

2.8.1 Fundamental concepts

As the name leaky wave antenna implies, this type of antenna is traditionally a waveguide structure that can radiate by leaking the input energy from a type of aperture which exists along the structure into the free-space with the phase velocity greater than the speed of light. Therefore the dimensions of LWAs only affect the directivity of the antenna and not the operating frequency. LWAs offer the advantage of high directivity and the ability of space scanning by frequency variation without a sophisticated feeding network [56]. The first LWA was developed in 1940 by Hansen [57]. Since the introduction of the LWAs, this field is under constant development. A detailed review of the historical advancement of LWAs was presented in [58].

The wave above the LWA, in the free space, is described using Equation 2-20; where $\gamma(\omega)$ is the frequency dependent complex propagation constant, which is defined in Equation 2-21 and consists of the waveguide propagation constant (β) and leakage constant (α); k_y is the transverse wave number which is the function of propagation constant ($\beta(\omega)$) and therefore

frequency dependent, as defined in Equation 2-22 [59]. Free space wave number k_0 is defined using Equation 2-23. Figure 2-24 illustrates a typical waveguide LWA.

$$\psi(r) = \psi_0 e^{-\gamma z} e^{-jk_z z} \quad 2-20$$

$$\gamma(\omega) = \alpha(\omega) + j\beta(\omega) \quad 2-21$$

$$k_y \cong \sqrt{k_0^2 - \beta^2(\omega)} \quad 2-22$$

$$k_0 = \frac{\omega}{c_0} \quad 2-23$$

It is observed in Equation 2-22 that the transverse radiation constant (k_y) can be imaginary when $\beta(\omega) > k_0$, which indicates that the phase velocity (v_p) (Equation 2-24) of the propagated wave is slower than the speed light (c), resulting in a wave decaying exponentially in free space as it travels away from the structure. Therefore the structure is known to be in guided wave mode. Conversely, k_y can be purely real if $\beta(\omega) < k_0$; hence the phase velocity of the propagated wave is faster than the speed of light and therefore known as radiating mode.

$$v_p = \frac{\omega}{\beta} \quad 2-24$$

The direction (θ_0) and width ($\Delta\theta$) of the LWAs main beam are calculated using Equations 2-25 and 2-26 [20]. It is observed in these two equations that the main beam direction and consequently main beam width are directly related to the propagation constant $\beta(\omega)$. Therefore, the radiation direction and width are frequency dependent. This means that LWAs are capable of changing the beam direction by altering the frequency of the propagated wave within the structure [60].

$$\theta_0 = \sin^{-1} \left(\frac{\beta(\omega)}{k_0} \right) \quad 2-25$$

$$\Delta\theta \approx \frac{1}{(l/\lambda_0) \cos \theta_0} \quad 2-26$$

$$\lambda_0 = \frac{2\pi}{k_0} \quad 2-27$$

The l and λ_0 in Equation 2-26 are the length of the LWA and free space wavelength (Equation 2-27) respectively.

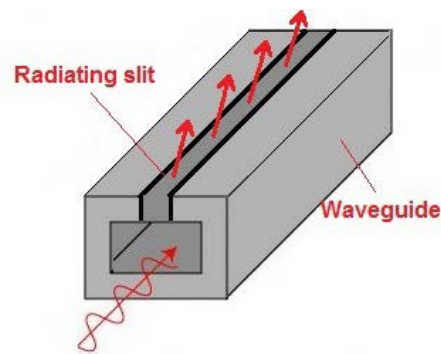


Figure 2-24: A typical LWA: a uniform waveguide with narrow leakage aperture.

The other important factor in LWAs is the leakage factor (α). The leakage factor represents the amount of radiation per unit length plus the ohmic and dielectric losses in the radiative structures such as LWAs. It should be noted that in the design of recent antennas, due to the use of high quality substrates, the ohmic and dielectric losses can be neglected. Therefore, the lower the leakage factor, the larger the structure can be made and hence the higher directivity can be achieved in LWAs. Practically the LWAs are designed long enough to achieve high radiation of around 90% of their input powers [61] and the remaining power dissipates in the matched termination at the end of the structure [59]. The approximate electrical length of the structure with 90% radiation efficiency can be found using Equation 2-28 [20].

$$\frac{l}{\lambda_0} \approx \frac{0.18k_0}{\alpha} \quad 2-28$$

2.8.2 LWA classification

LWAs can be classified based on their direction of propagation into a unidirectional or bidirectional LWA. In the unidirectional LWAs, the antenna is fed by a source at either end of the structure. Whereas in bidirectional LWAs the structure is generally fed by a source placed in the middle of the structure. On the other hand, the LWAs are divided into three categories based on their structure known as, uniform, quasi-uniform and periodic.

In the uniform LWAs, the antenna's transverse cross section does not change along the propagation axis. In these structures the propagation constant ($\beta(\omega)$) is always greater than zero and therefore these structures only support forward radiation. An example of a uniform LWA is shown in Figure 2-25 (A), where a rectangular waveguide with a narrow slit along its wall is presented. This structure supports the radiation of the dominant mode TE_{10} , which is a fast wave (the propagation constant is smaller than the free space wave number ($\beta < k_0$)). The uniform LWAs are capable of frequency scanning from near broadside to approximately endfire by increasing the input frequency of the structure. However the LWA's ability to radiate through the broadside and endfire strictly depends on the structure and material used in its design. For instance, the presented LWA in Figure 2-25 (A) can only scan the areas as close as 15° to both the broadside and endfire limits. This shortfall can be alleviated by filling half of the waveguide structure with dielectric material. This will result in the generation of the slow wave region ($\beta(\omega) > k_0$) as well as the fast wave region ($\beta(\omega) < k_0$) and therefore the transition between these two regions will result in near endfire radiation ($\beta \approx k_0$) [59].

Quasi-uniform LWA structures are very similar to the uniform LWAs, except that periodic structures are used as apertures for the radiation. It should be noted that the period of these structures must be significantly smaller than the guided wavelength (λ_g) to prevent the higher order space harmonics radiating within the operating frequency range of the LWA [62].

In periodic LWAs, the structure has a periodic variation in one of its features. This periodicity can happen in the metallisation, aperture, permeability or even permittivity of the structure. Such periodic variations can be represented using a Fourier series with an infinite series of spatial harmonics and associated propagation modes. In these structures, the fundamental mode is a non-radiating mode. Therefore the periodic LWAs support slow wave propagation ($\beta(\omega) > k_0$). Some of the propagation modes in these structures are fast and therefore radiating. One of the advantages of the periodic LWAs is that they enable both forward and backward radiation with positive and negative mode indices (n) [63]. This advantage makes them more appealing for practical applications. Figure 2-25 (B) illustrates a typical periodic LWA structure. The LWA illustrated in Figure 2-25 (B) consists of a waveguide filled with dielectric and periodic radiating cuts on its wall. In this structure, due to the presence of the dielectric, the fundamental space harmonic is associated with TE_{10} which is normally slow wave and therefore non-radiative. The fast mode which radiates in this structure is highly related to the LWA design of the radiating slits. These structures can be designed to radiate at fast mode related to $n = -1$ [63]. Table 2-2 summarises the main difference between the uniform and periodic LWA structures.

Table 2-2: Summary of the properties of the uniform and periodic LWAs.

	Space scanning	Dominant mode	Main leakage mode	Stopband
Uniform LWAs	Forward radiation only	Fast	β_0	No
Periodic LWAs	Both forward and backward radiation	Slow	β_{-1}	Yes

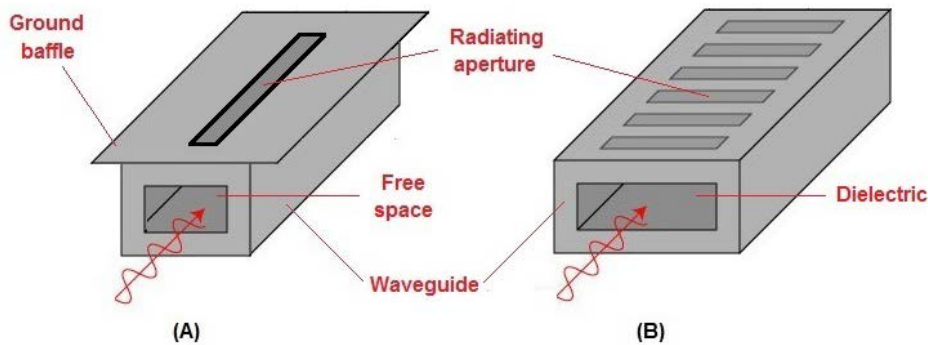


Figure 2-25: Waveguide leaky wave antennas: (A) uniform structure, (B) periodic structure.

2.8.3 Recent advancement in LWAs

In this section, some of the recent developments in the field of LWAs' design are reviewed. One of the weaknesses of conventional LWAs that restrict their application is their failure to scan through entire space from backfire to endfire. This fundamental drawback was alleviated by using CRLH metamaterials. The concept of CRLH is reviewed in section 2.9 in more detail.

The authors of [64] introduced the LWA design based on substrate integrated waveguide (SIW) which enables forward radiation up to very close proximity of endfire. In comparison with conventional rectangular waveguide LWAs, the SIW-LWA offers low production cost, small losses, lighter weight and better integrability with planar structures. Figure 2-26 represents the SIW-LWA structure proposed in [64]. It can be observed in Figure 2-26 that the SIW-LWA is similar to a rectangular waveguide. This SIW-LWA is designed by shorting the wide microstrip line, on the top of the substrate, to the ground plane on the other side of the substrate, through a number of reasonably spaced vias ($S \ll \frac{\lambda_g}{4}$). The leakage is achieved and controlled through a periodic set of apertures that perturb the current distribution on the top of the SIW. It should be noted that the SIW-LWA presented in this work can only scan through the forward quadrant. This structure is able to scan through the endfire with pencil beam radiation when the ground plane length is considered to be large. The LWA structure in this work maintained a small space between the leaking apertures and was therefore characterised as a quasi-uniform LWA working at fast TE_{10} mode.

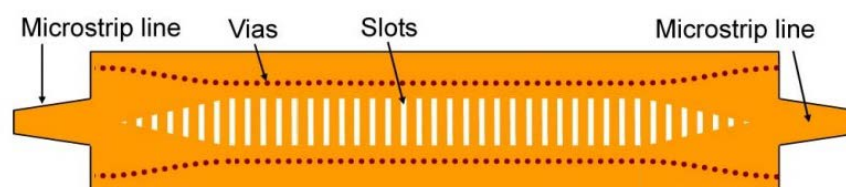


Figure 2-26: Geometry of quasi-uniform SIW-LWA [64].

The radiation pattern achieved by this structure is shown in Figure 2-27. It is observed in this figure that as the frequency increases from 10.2 GHz to 11.7 GHz, the main lobe direction of the radiation pattern moves from the near broadside to around endfire. The LWA in this work exhibits a small leakage factor due to the material loss and therefore indicates poor radiation

in the broadside direction. It should be noted that the radiation patterns achieved from the simulation of the finite ground plane structure can approach the infinite ground plane radiation pattern by increasing the size of the ground plane, although they will always exhibit 6 dB differences at the endfire due to diffraction.

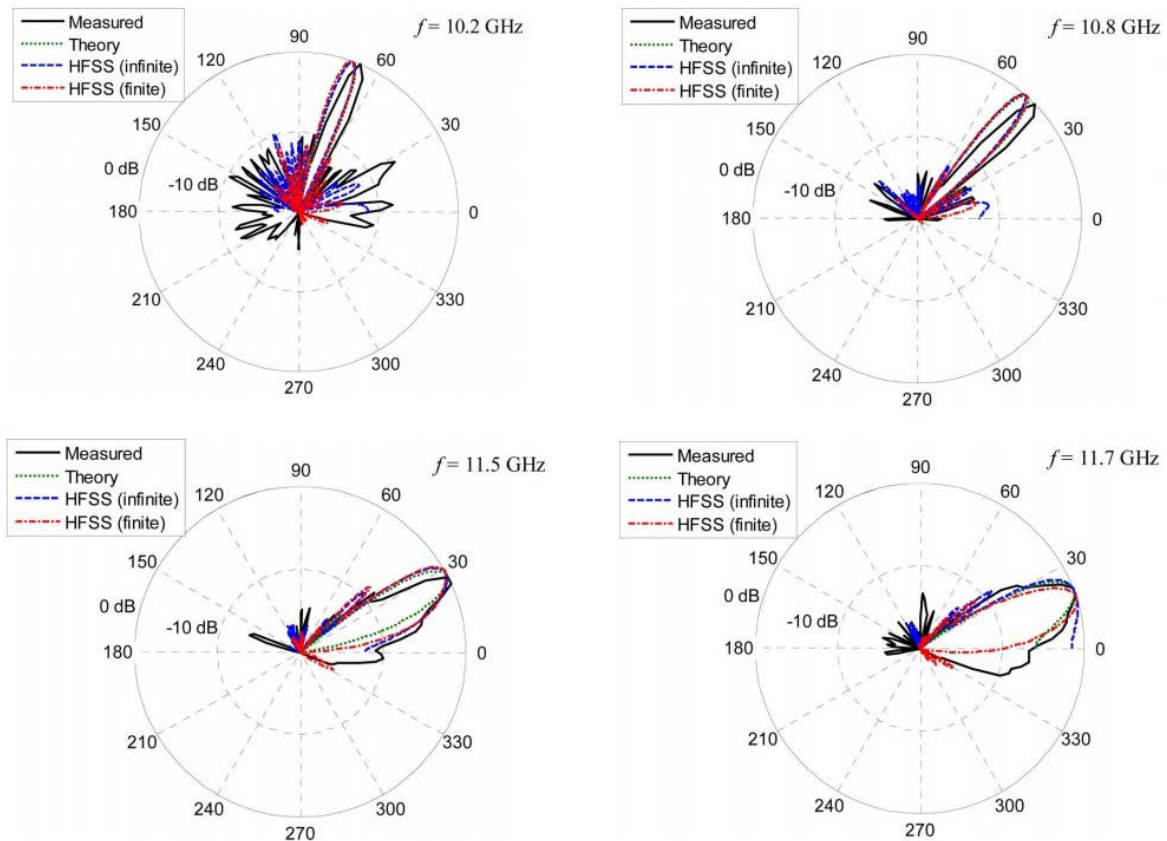


Figure 2-27: Radiation pattern indicating the forward quadrant frequency scanning of the SIW LWA of [64].

The authors of [65] provide a novel method to enable the broadside radiation of periodic LWAs. This method is based on the introduction of the quarter wave transformer within the unit cell of a periodic LWA to ensure real and nonzero Bloch impedance at the broadside frequency. Bloch impedance is a concept used in analysis of periodic structures, which represents the ratio of the voltage and current in the eigen-modes, as a generalisation of the

familiar characteristic impedance concept in transmission line. The proposed method was examined on two periodic microstrip LWAs with one and two radiating elements in the unit cell, resulting in elimination of the stopband at the broadside frequency. In order to design the quarter wave transformer first the broadside radiation frequency was extracted from the dispersion diagram of the unperturbed LWA. The input impedance of the unit cell, when looking to the right of the radiating element is assumed to be Z_{in}^R . The distance (d) on the left side of the radiating structure is calculated in order to achieve purely real input impedance (Z_d), when looking to the right from the left side of the LWA unit cell. The quarter wave matching transformer with the characteristic impedance of Z_T is replaced at distance d from the radiating element [65]. A schematic of the designed periodic LWA of this work is illustrated in Figure 2-28. Therefore the designed LWA structure, due to the inclusion of the quarter wave transformer within the structure, is always having the input impedance of Z_{in}^R when looking towards its right side. This structure prevents the open stopband at the broadside frequency. The broadside radiation of the structure is investigated in Figure 2-29 [65]. It should be noted that the proposed method is simple and can be generalised to any form of periodic structure. This method requires an iterative process to find the accurate broadside radiation frequency.

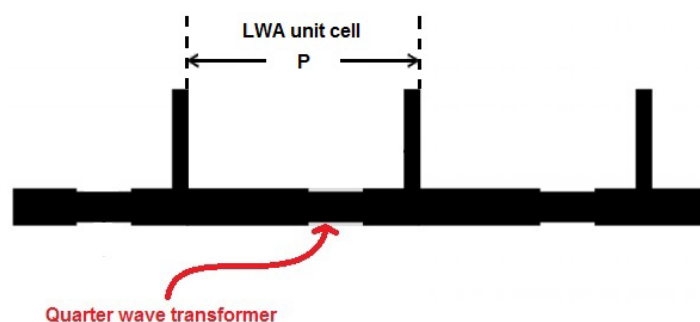


Figure 2-28: Proposed structure of periodic LWA in [65] which includes quarter wave transformer to enable broadside radiation.

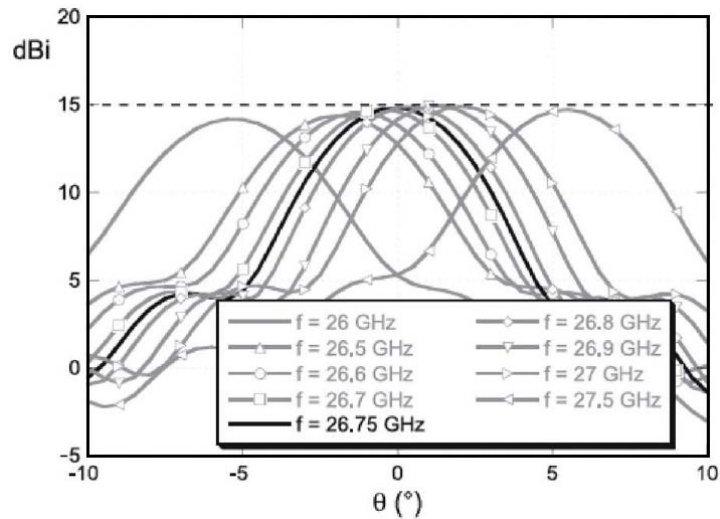


Figure 2-29: Confirmation of broadside radiation for the structure presented in figure 2-28.

A ferrite based LWA is another example of the recent breakthroughs in the field of LWA design. In [66], a uniform waveguide LWA is filled with ferrite material in order to enable the bidirectional beam leakage. The LWA structure is biased by the magnetic field H_0 perpendicular to the width of the waveguide structure and the leakage happens from the open wall of the waveguide. The LWA designed in this work is presented in Figure 2-30. It should be noted that due to high permittivity of the ferrite material only a small portion of the propagating wave inside the waveguide structure leaked out. This structure is capable of space scanning both by steering the frequency, where the biasing magnetic field is constant and by varying the biasing field keeping the input frequency constant. The radiation pattern shown in Figure 2-31 (A) and (B) illustrates the beam scanning by changing the frequency and the biasing field respectively. The structure in this work is filled with the material offered by muRata as a ferrite material. It should be noted that the designed structures in this work suffer from a number of weaknesses including, low gain, as a result of using a high loss

ferrite material and degradation of the radiation pattern by changing the radiation direction; due to the narrow bandwidth input matching network used in this design. Although the proposed design in this work clearly presents the bidirectional radiation, however due to the waveguide nature of this design, it is unable to radiate at the backfire and endfire.

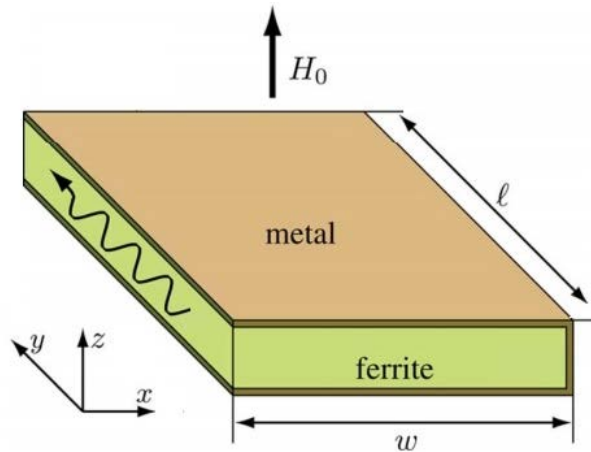


Figure 2-30: Proposed ferrite LWA [66].

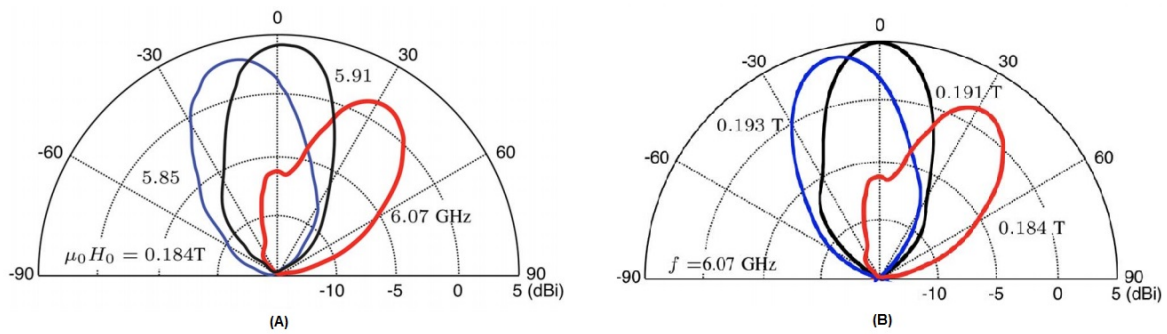


Figure 2-31 Ferrite LWA radiation pattern confirming the space scanning for (A) fixed biased and (B) fixed frequency.

Another revolutionary development in the field of LWA design is the use of metamaterial that enables scanning from the backfire to endfire continuously even through the broadside

without any radiation degradation. CRLH metamaterials, discussed in more detail in the next section, have an unusual dispersion diagram that is shown in Figure 2-32. The dispersion diagram of the CRLH structures, unlike natural materials, includes both positive and negative propagation constants. This unusual property of the CRLH structures makes them a great candidate for planar LWA design. The first CRLH-LWA was introduced in [67] where the left handed (LH) properties were generated using interdigital capacitors and stub inductors; and the right handed (RH) properties came from the magnetic flux, generated by the current following through the interdigital capacitor and the capacitance due to the parallel plate voltage gradients between the trace and the ground plane [60]. The proposed CRLH-LWA in [67] is illustrated in Figure 2-33. It can be seen in this figure that CRLH-LWA is structurally periodic, but due to its small unit cell length with respect to the LWA, the structure is assumed to be quasi-uniform and therefore operating in dominant $n = 0$ space harmonic. The full wave radiation pattern of the planar CRLH-LWA of Figure 2-33 with 41 unit cells is shown in Figure 2-34 [68]. It is observed from the radiation pattern that the CRLH based LWA is capable of space scanning from the backward radiating region (LH properties), through broadside ($\beta = 0$) and to the forward radiating region (RH properties) by increasing the operating frequency. It should be noted that the radiation in the broadside direction can only happen if the open stopband in the dispersion diagram is prevented in the design procedure. This can be achieved by designing the balanced CRLH structure, where the resonance frequency of the LH and RH elements are the same.

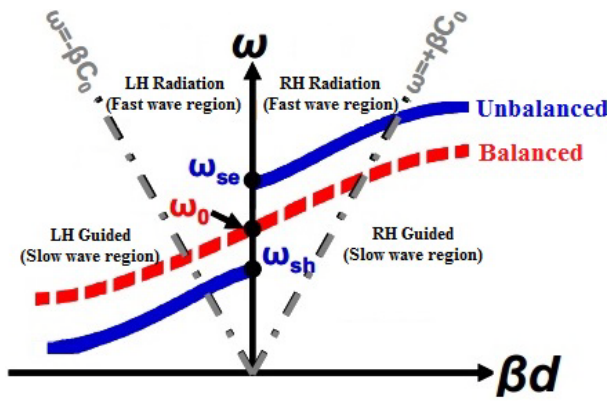


Figure 2-32: Dispersion diagram indicating the radiating (fast wave) and guiding (slow wave) regions for balanced and unbalanced CRLH transmission lines [69].

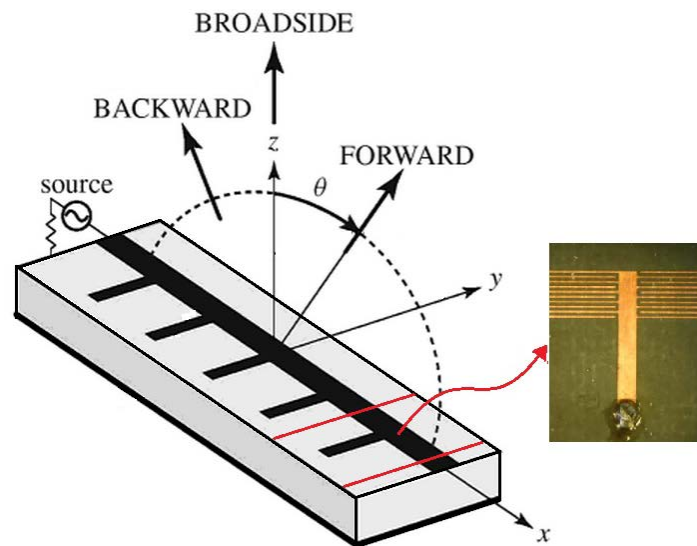


Figure 2-33: Proposed CRLH-LWA schematics including the fabricated unit cell (adapted from [60]).

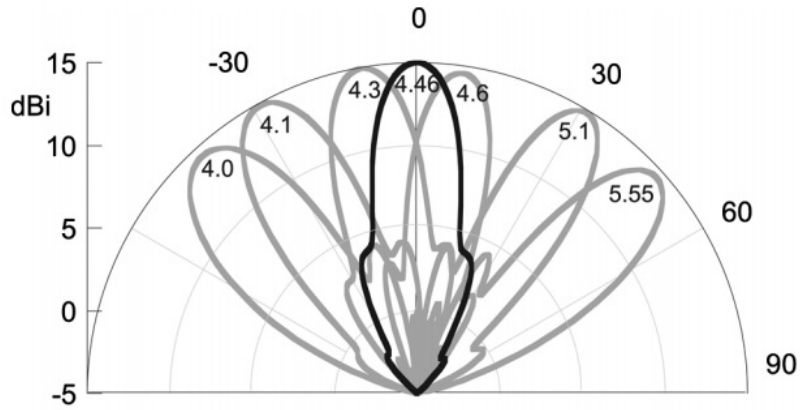


Figure 2-34: A typical radiation pattern for the CRLH-LWA structure with 41 unit cells [68].

The application of CRLH-LWA is not bounded to the planar structures. Waveguide structures were also reported in [70, 71] that exhibit CRLH properties. The authors of [70] designed a LH waveguide structure by operating the waveguide under the cut off frequency of the fundamental mode, so that the waveguide exhibits its shunt inductor behaviour and dielectric filled corrugation to provide the series capacitor nature to the structure [70]. Although the proposed waveguide LWA in this work is capable of backward radiation, it presents a bandgap between the fundamental LH mode and the RH radiation mode and therefore the structure is incapable of broadside radiation. Conversely, the authors of [71] presented a balanced CRLH waveguide LWA which is capable of space scanning from -61° to 78° including the broadside radiation. The CRLH-LWA proposed in this work is a simple cut off waveguide structure backed by periodic short circuited stubs that makes the waveguide apertures capacitive. The schematic of the proposed CRLH waveguide LWA of this work is shown in Figure 2-35 [71].

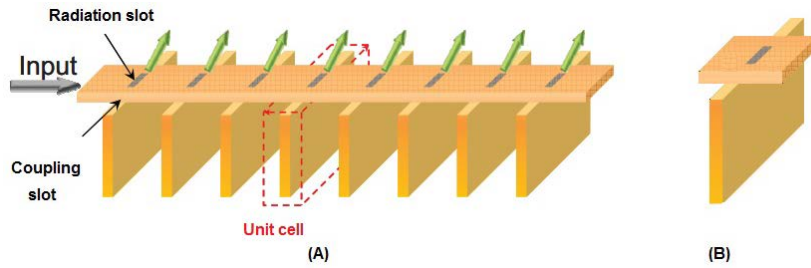


Figure 2-35: (A) CRLH waveguide LWA structure. (B) unit cell [71].

2.9 Composite Right/Left Handed (CRLH) metamaterial

CRLH transmission line was first introduced by Caloz et al in [19]. This type of material consists of RH and LH transmission lines. The RH transmission line is a conventional transmission line that can be modelled by a series inductor (L'_R) and a shunt capacitor (C'_R). The equivalent circuit model of RH-TL with the length (Δz) is illustrated in Figure 2-36 (A). The pure LH transmission line, on the other hand, exhibits an unusual simultaneous negative permittivity and permeability and therefore a negative refractive index, which results in backward propagation in a radiating application. The pure LH transmission line is modelled by a series capacitor (C'_L) and a shunt inductor (L'_L) as seen in Figure 2-36 (B). It should be noted that purely LH transmission lines do not exist, since in the distributed realisation of the LH transmission line, as the wave propagates in the structure, the voltage and currents generated will induce RH counterparts of the LH elements in the design. The attribute of the RH parasitic increases as the frequency increases. This phenomenon introduces the concept of the CRLH transmission line, where both RH and LH properties coexist in the same structure. The equivalent circuit model of the CRLH-TL is shown in Figure 2-36 (C). CRLH structures at low frequencies behave as a LH transmission line and at higher frequencies as a RH transmission line.

CRLH-TLs are categorised into two groups, known as balanced and unbalanced CRLH-TLs. In the balanced CRLH-TL, the dispersion diagram does not indicate any discontinuity along the frequency axis. In order to achieve a balanced CRLH structure the resonant frequency of the series (ω_{se}) and shunt (ω_{sh}) elements should be designed to be the same ($\omega_{se} = \omega_{sh}$). The series and shunt resonant frequency can be calculated using Equations 2-29 and 2-30 respectively [20]. On the other hand, an unbalanced CRLH structure exhibits a discontinuity along the frequency axis of its dispersion diagram. The transition frequency (ω_0) between the LH and RH region is calculated using Equation 2-31 [19].

$$\omega_{se} = \frac{1}{\sqrt{L'_R C'_L}} \quad 2-29$$

$$\omega_{sh} = \frac{1}{\sqrt{L'_L C'_R}} \quad 2-30$$

$$\omega_0 = \sqrt[4]{L'_R C'_R L'_L C'_L} \quad 2-31$$

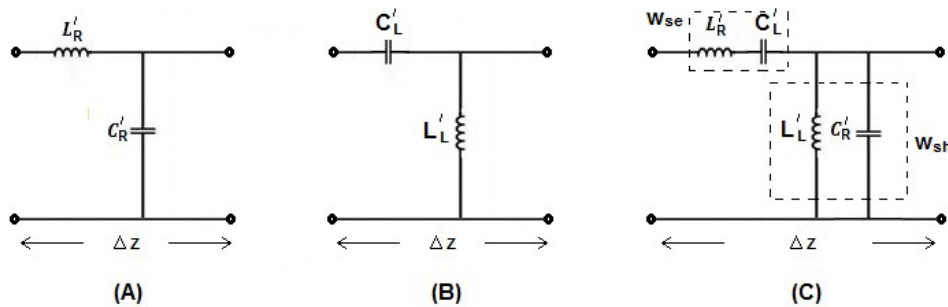


Figure 2-36: Lumped element equivalent circuit model of (A) RH, (B) purely LH and (C) CRLH transmission line.

It should be mentioned that the above formulation is for the homogenous CRLH transmission line, where the transmission line is assumed to have a constant cross section along the propagation direction. However the homogeneity can only be maintained when the length of the unit cell (Δz) is much smaller than the guided wavelength (λ_g). The practical effective homogeneity condition is illustrated in Equation 2-32 [20].

$$\Delta z < \frac{\lambda_g}{4} \quad 2-32$$

By assuming the effectively homogenous structure and using periodic boundary conditions, Equation 2-33 for the complex propagation constant was derived for the CRLH structure of Figure 2-36 (C) [72].

$$\beta(\omega) = \frac{1}{\Delta z} \cos^{-1} \left(1 + \frac{ZY}{2} \right) \quad 2-33$$

The series impedance (Z) and shunt admittance (Y) of the CRLH unit cell is defined in Equations 2-34 and 2-35 respectively [72]. The dispersion diagram for the work presented in [73] is simulated using Equation 2-33 for both balanced and unbalanced CRLH transmission lines and is illustrated in Figure 2-37.

$$Z(\omega) = j(\omega L_R - \frac{1}{\omega C_L}) \quad 2-34$$

$$Y(\omega) = j(\omega C_R - \frac{1}{\omega L_L}) \quad 2-35$$

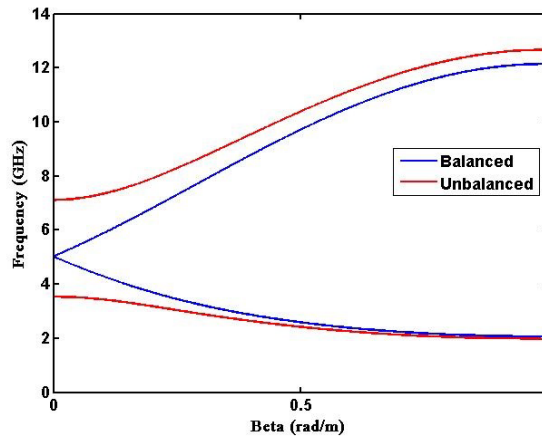


Figure 2-37: Dispersion diagram for the balanced and unbalanced CRLH structure presented in [73] using Equation 2-33.

2.10 Conclusion

In this chapter, the concepts of some of the most interesting communication signal sources in the microwave and optical wave regions were reviewed. Special attention in the sections related to the optical wave sources was paid to the vertical cavity surface emitting lasers (VCSELs), as a promising alternative for the conventional edge emitting lasers. This provides the necessary background information for understanding the novel integrated VCSEL model proposed in Chapter 3. In the sections related to the microwave communication sources, the fundamentals of leaky wave antennas (LWAs) and composite right/left handed (CRLH) metamaterials were reviewed to establish the necessary knowledge required for understanding the proposed design for a nonlinear CRLH frequency doubler LWA in Chapter 4. Furthermore, in this chapter, the design procedures for microstrip patch antennas were reviewed to support the understanding of the proposed method of combining the harmonic balance and EM analysis for the design and optimisation of the nonlinear active antennas developed in Chapter 5.

Some of the most significant work in the modelling of the VCSELs has been reviewed in this chapter. A summary of this work is provided in Table 2-1. The common problem with all these works is that the effect of the noise sources within the intrinsic VCSELs has not been taken into account. Among all the works reviewed in this field there is only one, [38], that presents an integrated VCSEL model capable of predicting the effect of the parasitic and matching network within the same model. However this work did not introduce a very accurate intrinsic VCSEL model.

On the other hand, recent developments in the field of leaky wave antenna design indicate that the CRLH based LWA presents an easy design with the capability of space scanning from backfire through the broadside to the endfire with no beam degradation and without the need for sophisticated feeding techniques. However the interesting properties of the nonlinear CRLH are far away from being fully investigated. Nonlinear CRLH structures can be used to design the structures with even more interesting applications than the linear CRLH reviewed in this chapter.

References

- [1] J. M Senior and Y. Jamro, *Optical Fiber Communications: Principles and Practice*: Financial Times/Prentice Hall, 2009.
- [2] A. G. Bell, "Selenium and the Photophone," *The Electrician*, 1880.
- [3] T. H. Maiman, "Stimulated Optical Radiation in Ruby," *Nature*, vol. 187, pp. 493-494, 1960.
- [4] Y. Suematsu and K. Iga, "Semiconductor Lasers in Photonics," *Lightwave Technology, Journal of*, vol. 26, pp. 1132-1144, 2008.
- [5] N. Holonyak, "The semiconductor laser: a thirty-five-year perspective," *Proceedings of the IEEE*, vol. 85, pp. 1678-1693, 1997.
- [6] K. C. Kao and G. A. Hockham. (1966, Dielectric-fibre surface waveguides for optical frequencies. *Proceedings of the Institution of Electrical Engineers* 113(7), 1151-1158. Available: <http://digital-library.theiet.org/content/journals/10.1049/piee.1966.0189>
- [7] A. Werts, "Propagation de la lumiere coherente dans les fibre optiques," *L'Onde Electronique*, pp. 967-980, 1966.
- [8] K. Iga, F. Koyama, and S. Kinoshita, "Surface emitting semiconductor lasers," *Quantum Electronics, IEEE Journal of*, vol. 24, pp. 1845-1855, 1988.
- [9] K. Iga, "Vertical cavity surface emitting lasers photonics," *Japanese Journal of Applied Physics*, vol. 45, p. 6541, 2006.
- [10] K. Iga, "Surface-emitting laser-its birth and generation of new optoelectronics field," *Selected Topics in Quantum Electronics, IEEE Journal of*, vol. 6, pp. 1201-1215, 2000.

- [11] H. E. Li and K. Iga, *Vertical-cavity surface-emitting laser devices / H.E. Li, K. Iga (eds.)*. London: London : Springer, 2003.
- [12] Y. H. Lee, J. L. Jewell, A. Scherer, S. L. McCall, J. P. Harbison, and L. T. Florez, "Room-temperature continuous-wave vertical-cavity single-quantum-well microlaser diodes," *Electronics Letters*, vol. 25, pp. 1377-1378, 1989.
- [13] J. C. Maxwell, *A Treatise on Electricity and Magnetism: 2*: Clarendon Press, 1873.
- [14] J. D. Kraus, "Antennas since Hertz and Marconi," *Antennas and Propagation, IEEE Transactions on*, vol. 33, pp. 131-137, 1985.
- [15] C. A. Balanis, *Antenna Theory: Analysis and Design*, 3rd ed.: Wiley-Interscience, 2005.
- [16] A. A. Oliner, "Historical Perspectives on Microwave Field Theory," *Microwave Theory and Techniques, IEEE Transactions on*, vol. 32, pp. 1022-1045, 1984.
- [17] V. G. Veselago, "THE ELECTRODYNAMICS OF SUBSTANCES WITH SIMULTANEOUSLY NEGATIVE VALUES ϵ AND μ ," *Physics-Uspekhi*, vol. 10, pp. 509-514, 1968.
- [18] D. R. Smith, W. J. Padilla, D. Vier, S. C. Nemat-Nasser, and S. Schultz, "Composite medium with simultaneously negative permeability and permittivity," *Physical Review Letters*, vol. 84, p. 4184, 2000.
- [19] C. Caloz and T. Itoh, "Novel microwave devices and structures based on the transmission line approach of meta-materials," in *Microwave Symposium Digest, 2003 IEEE MTT-S International*, 2003, pp. 195-198 vol.1.
- [20] C. Caloz and T. Itoh, *Electromagnetic Metamaterials: Transmission Line Theory and Microwave Applications*: Wiley, 2006.

- [21] A. Sanada, C. Caloz, and T. Itoh, "Characteristics of the composite right/left-handed transmission lines," *Microwave and Wireless Components Letters, IEEE*, vol. 14, pp. 68-70, 2004.
- [22] C. Caloz, "A personal perspective on CRLH antennas," in *Electromagnetic Theory (EMTS), Proceedings of 2013 URSI International Symposium on*, 2013, pp. 882-884.
- [23] W. M. WONG, "Microwave Circuit Models of Semiconductor Laser," Doctor of Philosophy Dynamic Modelling of Semiconductor Laser Devices using Microwave Circuit Techniques, Faculty of Engineering, University of Birmingham, Birmingham, 2001.
- [24] G. Keiser, *Optical Fiber Communications*: McGraw-Hill Education, 2010.
- [25] H. J. Queisser and U. Heim, "Optical Emission From Semiconductors," *Annual Review of Materials Science*, vol. 4, pp. 125-145, 1974.
- [26] A. Larsson, "Advances in VCSELs for Communication and Sensing," *Selected Topics in Quantum Electronics, IEEE Journal of*, vol. 17, pp. 1552-1567, 2011.
- [27] S. F. Yu, *Analysis and design of vertical cavity surface emitting lasers / S.F. Yu*. Hoboken, N.J.: Hoboken, N.J. : Wiley-Interscience, 2003.
- [28] C. Rumelhard, C. Algani, and A.-L. Billabert, *Microwaves Photonic Links: Components and Circuits*: John Wiley & Sons, 2013.
- [29] A. Bacou, A. Hayat, V. Iakovlev, A. Syrbu, A. Rissons, J. Mollier, and E. Kapon, "Electrical Modeling of Long-Wavelength VCSELs for Intrinsic Parameters Extraction," *Quantum Electronics, IEEE Journal of*, vol. 46, pp. 313-322, 2010.
- [30] A. Fiore and A. Markus, "Differential Gain and Gain Compression in Quantum-Dot Lasers," *Quantum Electronics, IEEE Journal of*, vol. 43, pp. 287-294, 2007.

- [31] H. Trommsdorff, A. Corval, and L. Von Laue, "Spectral hole burning: Spontaneous and photoinduced tunneling reactions in low temperature solids," *Pure and applied chemistry*, vol. 67, pp. 191-198, 1995.
- [32] G. P. Agrawal, "Spectral hole-burning and gain saturation in semiconductor lasers: Strong-signal theory," *Journal of Applied Physics*, vol. 63, pp. 1232-1235, 1988.
- [33] R. F. Kazarinov, C. H. Henry, and R. A. Logan, "Longitudinal mode self-stabilization in semiconductor lasers," *Journal of Applied Physics*, vol. 53, pp. 4631-4644, 1982.
- [34] J. Gao, "An Analytical Method to Determine Small-Signal Model Parameters for Vertical-Cavity Surface Emitting Lasers," *Lightwave Technology, Journal of*, vol. 28, pp. 1332-1337, 2010.
- [35] J. Gao, "High Frequency Modeling and Parameter Extraction for Vertical-Cavity Surface Emitting Lasers," *Lightwave Technology, Journal of*, vol. 30, pp. 1757-1763, 2012.
- [36] J. Gao, X. Li, F. J., and B. G., "Direct parameter-extraction method for laser diode rate-equation model," *Lightwave Technology, Journal of*, vol. 22, pp. 1604-1609, 2004.
- [37] K. Minoglou, E. D. Kyriakis-Bitzaros, D. Syvridis, and G. Halkias, "A compact nonlinear equivalent circuit model and parameter extraction method for packaged high-speed VCSELs," *Lightwave Technology, Journal of*, vol. 22, pp. 2823-2827, 2004.
- [38] K. Minoglou, G. Halkias, and E. D. Kyriakis-Bitzaros, "VCSEL device modeling and parameter extraction technique," in *Electronics, Circuits and Systems, 2007. ICECS 2007. 14th IEEE International Conference on*, 2007, pp. 14-17.

- [39] X. Shi, C. Qi, G. Wang, and J. Hu, "Rate-equation-based VCSEL model and simulation," in *Computer-Aided Design and Computer Graphics, 2009. CAD/Graphics '09. 11th IEEE International Conference on*, 2009, pp. 503-507.
- [40] P. V. Mena, J. J. Morikuni, S. M. Kang, A. V. Harton, and K. W. Wyatt, "A comprehensive circuit-level model of vertical-cavity surface-emitting lasers," *Lightwave Technology, Journal of*, vol. 17, pp. 2612-2632, 1999.
- [41] P. V. Mena, J. J. Morikuni, S. M. Kang, A. V. Harton, and K. W. Wyatt, "A simple rate-equation-based thermal VCSEL model," *Lightwave Technology, Journal of*, vol. 17, pp. 865-872, 1999.
- [42] B. J. Thibeault, K. Bertilsson, E. R. Hegblom, E. Strzelecka, P. D. Floyd, R. Naone, and L. A. Coldren, "High-speed characteristics of low-optical loss oxide-apertured vertical-cavity lasers," *Photonics Technology Letters, IEEE*, vol. 9, pp. 11-13, 1997.
- [43] C. Harder, J. Katz, S. Margalit, J. Shacham, and A. Yariv, "Noise equivalent circuit of a semiconductor laser diode," *Quantum Electronics, IEEE Journal of*, vol. 18, pp. 333-337, 1982.
- [44] J. Katz, S. Margalit, C. Harder, D. Wilt, and A. Yariv, "The intrinsic electrical equivalent circuit of a laser diode," *Quantum Electronics, IEEE Journal of*, vol. 17, pp. 4-7, 1981.
- [45] A. Bacou, A. Hayat, A. Rissons, V. Iakovlev, A. Syrbu, J. Mollier, and E. Kapon, "VCSEL Intrinsic Response Extraction Using T-Matrix Formalism," *Photonics Technology Letters, IEEE*, vol. 21, pp. 957-959, 2009.
- [46] "IEEE Standard Definitions of Terms for Antennas," *IEEE Std 145-1983*, pp. 1-31, 1983.
- [47] S. A. Maas, *The RF and Microwave Circuit Design Cookbook*: Artech House, 1998.

- [48] I. J. Bahl and D. K. Trivedi, "A Designer's Guide to Microstrip Line," *Microwaves*, pp. 147-182, May 1977.
- [49] D. M. Pozar, *Microwave Engineering, 3Rd Ed*: Wiley India Pvt. Limited, 2009.
- [50] C. A. Balanis, *Advanced Engineering Electromagnetics* vol. 20. New York: John Wiley & Sons, 1989.
- [51] Z. N. Chen and M. Y. W. Chia, *Broadband planar antennas: design and applications*: John Wiley & Sons, 2006.
- [52] M. I. Nawaz, H. Zhao, M. S. Sultan Nawaz, K. Zakim, S. Zamin, and A. Khan, "A review on wideband microstrip patch antenna design techniques," in *Aerospace Science & Engineering (ICASE), 2013 International Conference on*, 2013, pp. 1-8.
- [53] Z. I. Dafalla, W. T. Y. Kuan, A. M. A. Rahman, and S. C. Shudakar, "Design of a rectangular microstrip patch antenna at 1 GHz," in *RF and Microwave Conference, 2004. RFM 2004. Proceedings*, 2004, pp. 145-149.
- [54] M. Kara, "Formulas for the computation of the physical properties of rectangular microstrip antenna elements with various substrate thicknesses," *Microwave and Optical Technology Letters*, vol. 12, pp. 234-239, 1996.
- [55] R. Garg, P. Bhartia, I. Bahl, and A. Ittipiboon, *Microstrip antennas design handbook*: Artech House, 2001.
- [56] C. Caloz and S. Otto, "A tour on recent developments and discoveries of crucial practical importance in leaky-wave antennas," in *Microwave Conference (EuMC), 2013 European*, 2013, pp. 495-498.
- [57] W. W. Hansen, "Radiating electromagnetic waveguide," U.S. Patent 2.402.622, 1940.
- [58] D. R. Jackson and A. A. Oliner, "Leaky-Wave Antennas," in *Modern Antenna Handbook*, C. A. Balanis, Ed., ed: Wiley-Interscience, 2008, pp. 325-368.

- [59] A. A. Oliner and D. R. Jackson, "Leaky-Wave Antennas," in *Antenna Engineering Handbook*, J. Volakis, Ed., Fourth ed: McGraw-Hill Companies, Incorporated, 2007.
- [60] C. Caloz, T. Itoh, and A. Rennings, "CRLH metamaterial leaky-wave and resonant antennas," *Antennas and Propagation Magazine, IEEE*, vol. 50, pp. 25-39, 2008.
- [61] X. Feng and W. Ke, "Understanding Leaky-Wave Structures: A Special Form of Guided-Wave Structure," *Microwave Magazine, IEEE*, vol. 14, pp. 87-96, 2013.
- [62] D. R. Jackson, C. Caloz, and T. Itoh, "Leaky-wave antennas," *Proceedings of the IEEE*, vol. 100, pp. 2194-2206, 2012.
- [63] F. Gross, *Frontiers in Antennas: Next Generation Design & Engineering*: McGraw-Hill Education, 2011.
- [64] J. Liu, J. D. R., and Y. Long, "Substrate Integrated Waveguide (SIW) Leaky-Wave Antenna With Transverse Slots," *Antennas and Propagation, IEEE Transactions on*, vol. 60, pp. 20-29, 2012.
- [65] S. Paulotto, P. Baccarelli, F. Frezza, and D. R. Jackson, "A Novel Technique for Open-Stopband Suppression in 1-D Periodic Printed Leaky-Wave Antennas," *Antennas and Propagation, IEEE Transactions on*, vol. 57, pp. 1894-1906, 2009.
- [66] T. Kodera and C. Caloz, "Uniform Ferrite-Loaded Open Waveguide Structure With CRLH Response and Its Application to a Novel Backfire-to-Endfire Leaky-Wave Antenna," *Microwave Theory and Techniques, IEEE Transactions on*, vol. 57, pp. 784-795, 2009.
- [67] L. Liu, C. Caloz, and T. Itoh, "Dominant mode leaky-wave antenna with backfire-to-endfire scanning capability," *Electronics Letters*, vol. 38, pp. 1414-1416, 2002.
- [68] S. Paulotto, P. Baccarelli, F. Frezza, and D. R. Jackson, "Full-Wave Modal Dispersion Analysis and Broadside Optimization for a Class of Microstrip CRLH Leaky-Wave

- Antennas," *Microwave Theory and Techniques, IEEE Transactions on*, vol. 56, pp. 2826-2837, 2008.
- [69] M. R. M. Hashemi, B. S. Williams, and T. Itoh, "Leaky wave antennas based on transmission line metamaterials," in *Infrared, Millimeter and Terahertz Waves (IRMMW-THz), 2011 36th International Conference on*, 2011, pp. 1-4.
- [70] I. A. Eshrah, A. A. Kishk, A. B. Yakovlev, and A. W. Glisson, "Rectangular waveguide with dielectric-filled corrugations supporting backward waves," *Microwave Theory and Techniques, IEEE Transactions on*, vol. 53, pp. 3298-3304, 2005.
- [71] D. Taema, A. Sanada, and H. Kubo, "Composite right/left-handed waveguide beam-steering leaky-wave antennas using a cut-off waveguide and short-ended stubs," in *Microwave Conference, 2008. APMC 2008. Asia-Pacific*, 2008, pp. 1-4.
- [72] A. Lai, T. Itoh, and C. Caloz, "Composite right/left-handed transmission line metamaterials," *Microwave Magazine, IEEE*, vol. 5, pp. 34-50, 2004.
- [73] C. Caloz, A. Sanada, and T. Itoh, "A novel composite right-/left-handed coupled-line directional coupler with arbitrary coupling level and broad bandwidth," *Microwave Theory and Techniques, IEEE Transactions on*, vol. 52, pp. 980-992, 2004.

3 INTEGRATED VERTICAL CAVITY SURFACE EMITTING LASER MODEL BASED ON TRANSMISSION LINE MODELLING

3.1 Introduction

Using visible light as a means of communication has always been attractive for human beings. In recent communication systems, optical fibres have been used as a low loss, high bandwidth and very fast alternative to traditional coaxial lines and waveguides for conveying microwave or millimetre wave signals.

Lasers as the major source of generating optical signals have attracted lots of interest in recent decades. Laser diodes are divided into two different types, based on their direction of emission: conventional edge emitting laser diodes; and vertical cavity surface emitting laser diodes (VCSELs). Vertical Cavity Surface Emitting Lasers (VCSELs) were first proposed and manufactured by K. Iga and his colleagues at the Tokyo Institute of Technology in the 1970s [1]. VCSELs have vertical emission, orthogonal to those of conventional facet mirror emitting lasers [2]. This simple orientation difference of the VCSELs' cavity, dramatically improves the fabrication complexities and the output performance of the VCSELs in

comparison to the conventional semiconductor lasers [3, 4]. Compared to the edge emitting semiconductor lasers, VCSELs offer many advantages. Single longitudinal mode behaviour, low threshold current, high modulation bandwidth, small divergence angle of the output beam, capability of ultrahigh bit rate modulation, circular light beam, increased ability to integrate with other optoelectronic components, negligible temperature dependence around room temperature, cheap testing and packaging cost, are among the most important advantages offered by VCSELs [5-7]. Developments in the double fusion of GaAs/AlAs distributed Bragg reflectors (DBRs) to the AlGaInAs/InP QW active layer for the 1300 nm long-wavelength VCSELs, improves the drawbacks of the early stage InP-based materials used in the long-wavelength VCSELs. As an example of such drawbacks, high Auger recombination coefficient and complications in the achievement of a very high reflectivity (>99.9%) in the InP-based VCSEL can be mentioned [1]. Hence, VCSELs are good candidates for long-haul optical based computer networks such as metropolitan area networks (MAN) and a wide area network (WAN).

In order to be able to investigate the optical communication systems before investing heavily in manufacturing, an accurate system model has to be developed. An accurate small signal model of a VCSEL is necessary to realise the device's physical behaviour and its optimised performance. The lumped-element VCSEL model proposed in this chapter is based on the rate equations that gave a great insight into the physical features within the VCSEL's structure. However, the model cannot claim to accurately portray the physical behaviour and the performance of the VCSEL unless it includes an accurate model of noises within the structure. Therefore the rate equation-based model proposed in this work takes into account the effects of intrinsic noise sources and noise arising from the electrical parasitic and the packaging.

One of the advantages of the proposed VCSEL lumped-elements model is that it can be easily modelled with circuit simulator software such as OrCAD PSpice. However lumped elements have a practical complexity of fabrication for the work in higher frequencies. In order to overcome this limitation, the distributed model of the VCSEL was introduced using quasi-lumped technique.

In this chapter an integrated transmission line based model for the VCSEL is proposed. The proposed integrated VCSEL model consists of three different sections; matching network, electrical parasitic model, which includes the effect of wire bonding and packaging; and intrinsic laser model that also includes intrinsic noise sources. The proposed model in this work is a realistic microwave optoelectronics model since it involves both practical microwave parameters such as the matching network and electrical parasitic, as well as the intrinsic laser characteristics using rate equations.

The originality of this work is the use of accurate rate equations without any simplifying assumptions [8-11] and also the inclusion of intrinsic noise sources within the intrinsic VCSEL model. Furthermore, the integration of the matching network in the integrated model has never been reported for VCSEL modelling.

3.2 Proposed integrated VCSEL model overview

The integrated VCSEL model proposed in this work consists of three sections. The first section is the intrinsic model of the VCSEL. The proposed model for the VCSEL's core is based on the rate equations. The rate equation-based model was used successfully in modelling conventional edge-emitting lasers [12]. The effects of the noise sources within the active layer and cavity of the VCSEL were included in the VCSEL model, which leads to

more realistic and practical applications. The proposed VCSEL model also takes into account the effect of the VCSEL's nonlinearities, radiative and non-radiative recombination and Auger recombination within the VCSEL's structure. The second section in the proposed integrated VCSEL model represents the electrical parasitics. The electrical parasitics produce high frequency roll-off in the input drive current of the intrinsic VCSEL; which in the time domain results in slowing down the fast transients of the VCSEL's drive current waveform [13]. The electrical parasitics' circuit used in this work takes into account the effects of parasitics arising from the packaging and the semiconductor chip. Finally the last section of the proposed integrated VCSEL model is the matching network. Similar to the system design in microwave applications, in optoelectronic devices such as lasers, the reflection towards the signal generator due to the impedance mismatch should be minimised. Matching networks also have vital importance in the modelling of the VCSELs as they provide better power transfer between the signal generator and the laser diode. A high level of RF power is needed to feed to the structure in order to overcome the losses related to electrical cable, bias tees and the packaging and bonding. Figure 3-1 represents the block diagram of the proposed integrated VCSEL model. Further in this chapter, to overcome the limitation of the lumped elements such as an inherent low frequency nature, a transmission line VCSEL model was proposed. The detailed design procedure of different parts of the integrated VCSEL model developed in this work, including the development of the distributed VCSEL model, is explained in separate sections of this chapter.

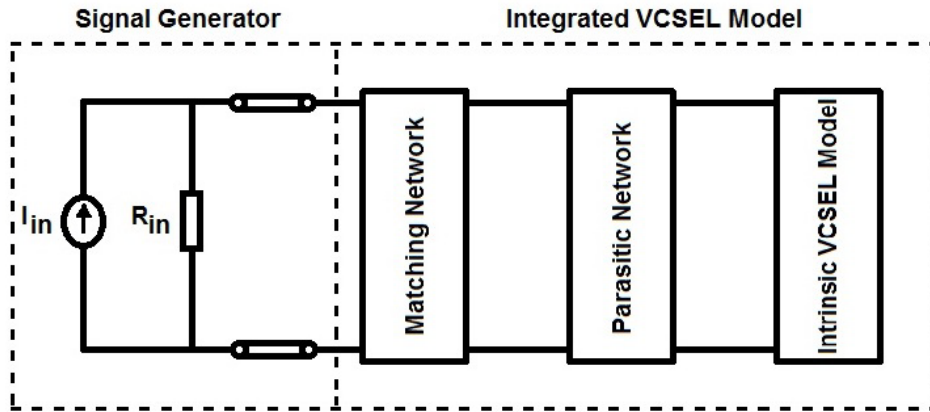


Figure 3-1: Block diagram presentation of the proposed integrated VCSEL model.

3.3 Intrinsic VCSEL model parameters derivation and analysis

In this section the proposed small signal intrinsic model of a VCSEL is investigated by reviewing the derivation of the proposed VCSEL model's parameters. Further in this section the noise characteristics of the VCSEL are analysed by calculating the spectral and cross-spectral intensity of the intrinsic noise sources. Then the relative intensity noise (RIN) of the proposed VCSEL model is analysed in order to define the instability in the power of the VCSEL. Finally in this section, a distributed model of a VCSEL is developed using microstrip transmission lines; then the direct modulation and transient response of the modelled VCSEL is simulated.

3.3.1 Proposed lumped element VCSEL model

In order to model any type of laser diode a close understanding of the laser structure is of great importance. A 1300 nm intra-cavity-contacted VCSEL is considered in this work. The

structural configuration of this VCSEL can be seen in Figure 3-2. The structure in Figure 3-2 was selected for this work to serve as an example when developing the effects of VCSEL parasitics, which are structure dependent, further in this chapter. The VCSEL structure of Figure 3-2 consists of an InAs/InGaAs multiple quantum-well active region with a selectively oxidised current aperture of AlO, grown on an AlAs/GaAs substrate, sandwiched between two multilayer GaAlAs/AlAs DBRs [14]. The top and bottom layers have 21 and 35 pairs of quarter wavelength thick DBRs, with alternating high and low refractive indices. The VCSEL's rate equations define the relationship between optical output power and the VCSEL drive current through three primary optical processes namely: (i) spontaneous emission, (ii) stimulated emission and (iii) absorption by taking into account the VCSEL structure. The single-mode VCSEL's rate equations are expressed in Equations 3-1 and 3-2 [15]. The VCSEL rate equations were reviewed in more detail in Chapter 2.

$$\frac{dN}{dt} = \frac{\eta_i I}{qV_{act}} - (A + BN + CN^2)N - G.S + F_N \quad 3-1$$

$$\frac{dS}{dt} = \Gamma \cdot \beta \cdot B \cdot N^2 + \Gamma \cdot G \cdot S - \frac{S}{\tau_s} + F_s \quad 3-2$$

$$G = v_g \cdot a_0 \cdot \frac{N - N_{tr}}{1 + \epsilon S} \quad 3-3$$

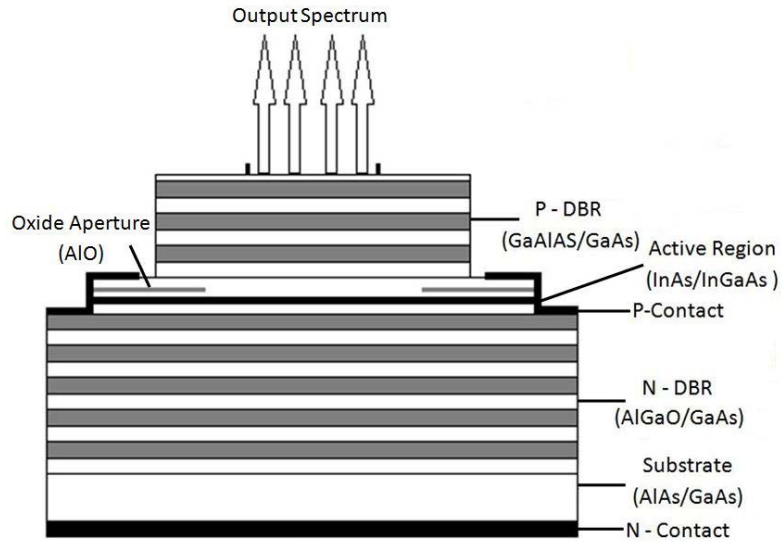


Figure 3-2: Typical Vertical Cavity Surface Emitting Laser (VCSEL) structure.

In order to solve the rate equations, firstly steady state analysis is performed. In the steady state condition, the average change in carrier and photon spectral intensities and therefore intrinsic noise sources, $\langle F_N \rangle$ and $\langle F_S \rangle$ are assumed to be zero. The steady state analysis enables the calculation of the average carrier and photon densities, N_0 and S_0 respectively. The VCSEL rate equations in the steady state are given in Equations 3-4 and 3-5; where I_0 is a DC pump current.

$$0 = \frac{\eta_i I_0}{q V_{act}} - (A + B N_0 + C N_0^2) N_0 - G \cdot S_0 \quad 3-4$$

$$0 = \Gamma \cdot \beta \cdot B \cdot N_0^2 + \Gamma \cdot G \cdot S_0 - \frac{S_0}{\tau_s} \quad 3-5$$

In order to calculate the VCSEL's small signal circuit model parameters, Equations 3-4 and 3-5 were linearised. Thus, the injected current $I(t)$, the carrier density $N(t)$ and the photon density $S(t)$ were expressed in Equations 3-6 to 3-8. Looking at Equations 3-1 and 3-2 it can be observed that the rate of change in carrier density (\dot{N}) depends on I, N, S ; while the rate of

change in photon density (\dot{S}) only depends on N and S . Therefore to continue the linearisation process the derivatives of Equations 3-4 and 3-5 were calculated.

$$N(t) = N_0 + \Delta N(t) \quad 3-6$$

$$S(t) = S_0 + \Delta S(t) \quad 3-7$$

$$I(t) = I_0 + \Delta I(t) \quad 3-8$$

$$\Delta \dot{N} = \frac{\partial \dot{N}}{\partial I} \Delta I + \frac{\partial \dot{N}}{\partial N} \Delta N + \frac{\partial \dot{N}}{\partial S} \Delta S \quad 3-9$$

$$\Delta \dot{S} = \frac{\partial \dot{S}}{\partial N} \Delta N + \frac{\partial \dot{S}}{\partial S} \Delta S \quad 3-10$$

Using Equations 3-9 and 3-10, the linearised rate equations were derived as follows.

$$\begin{aligned} \Delta \dot{N} = & \frac{\eta_i}{qV_{act}} \Delta I - \left(v_g a_0 \frac{S_0}{1 + \varepsilon S_0} + A + 2BN_0 + 3CN_0^2 \right) \Delta N \\ & - v_g a_0 \frac{N_0 - N_{tr}}{(1 + \varepsilon S_0)^2} \Delta S \end{aligned} \quad 3-11$$

$$\begin{aligned} \Delta \dot{S} = & \left(2 \cdot \Gamma \cdot \beta \cdot B \cdot N_0 + \Gamma \cdot v_g \cdot a_0 \cdot \frac{S_0}{1 + \varepsilon \cdot S_0} \right) \cdot \Delta N \\ & + \left(\Gamma \cdot v_g \cdot a_0 \cdot \frac{N_0 - N_{tr}}{(1 + \varepsilon \cdot S_0)^2} - \frac{1}{\tau_S} \right) \cdot \Delta S \end{aligned} \quad 3-12$$

3.3.1.1 Small signal equivalent circuit model

The electrical equivalent circuit model of a conventional laser diode, which is based on the rate equations, was first introduced by Katz [12]. In this work a similar equivalent circuit schematic for the VCSEL is adopted as shown in Figure 3-3, where the elements L_0 , R_0 , C_j and R_j represent the photon storage, damping resonance, the laser diode junction capacitance

and resistance, respectively. Moreover, $\overline{i_n^2}$ and $\overline{v_n^2}$ represent the current and voltage noise sources, respectively.

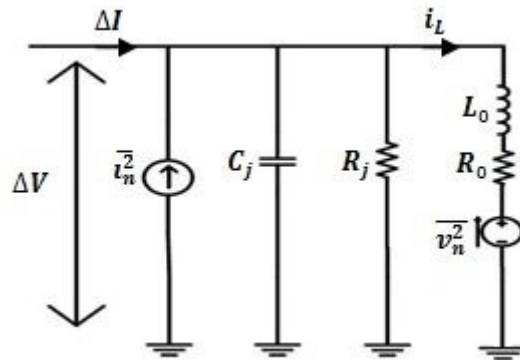


Figure 3-3: Small signal electrical equivalent circuit of intrinsic VCSEL.

The input to this circuit model is a small sinusoidal voltage $\Delta V(t)$ which produces a small sinusoidal current $\Delta I(t)$. In order to fully implement this equivalent model, the circuit elements of Figure 3-3 were calculated in terms of VCSEL's intrinsic parameters. In order to do so the equivalent circuit model was analysed by applying Kirchhoff's voltage and current law, resulting in Equations 3-13 and 3-14. The i_L in these equations represents the stimulated current. On the other hand, the relationship between the small signal fluctuating diode voltage ΔV , carrier density ΔN and injected current ΔI can be seen in Equation 3-15 [11].

$$\frac{d\Delta V}{dt} = \frac{\Delta I}{C_j} - \frac{\Delta V}{R_j \cdot C_j} - \frac{i_L}{C_j} + \frac{i_n}{C_j} \quad 3-13$$

$$\frac{di_L}{dt} = \frac{\Delta V}{L_0} - \frac{R_0 \cdot i_L}{L_0} - \frac{V_n}{L_0} \quad 3-14$$

$$\frac{\Delta V}{m \cdot V_T} = \frac{\Delta I}{I_0} = \frac{\Delta N}{N_0} \quad 3-15$$

Equation 3-16 was generated by differentiating Equation 3-15 with respect to time. Replacing Equation 3-16 in 3-11 and comparing the resulting equation (3-17) with Equation 3-13, the expressions for the junction capacitor and resistor (C_j, R_j) and stimulated current (i_L) were calculated as seen in Equations 3-18 to 3-20 respectively.

$$\frac{1}{m \cdot V_T} \frac{d\Delta V}{dt} = \frac{1}{I_0} \frac{d\Delta I}{dt} = \frac{1}{N_0} \frac{d\Delta N}{dt} \quad 3-16$$

$$\begin{aligned} \Delta \dot{V} = \frac{m \cdot V_T}{N_0} \cdot & \left(\frac{\eta_i}{q \cdot V_{act}} \Delta I \right. & 3-17 \\ & - \left(v_g a_0 \cdot \frac{S_0}{1 + \varepsilon \cdot S_0} + A + 2 \cdot B \cdot N_0 + 3 \cdot C \cdot N_0^2 \right) \cdot \frac{N_0}{m \cdot V_T} \cdot \Delta V \\ & \left. - v_g a_0 \cdot \frac{N_0 - N_{tr}}{(1 + \varepsilon \cdot S_0)^2} \cdot \Delta S \right) \end{aligned}$$

$$C_j = \frac{N_0 \cdot q \cdot V_{act}}{m \cdot V_T \cdot \eta_i} \quad 3-18$$

$$R_j = \frac{m \cdot V_T \cdot \eta_i}{N_0 \cdot q \cdot V_{act} \cdot \left(v_g a_0 \cdot \frac{S_0}{1 + \varepsilon \cdot S_0} + A + 2 \cdot B \cdot N_0 + 3 \cdot C \cdot N_0^2 \right)} \quad 3-19$$

$$i_L = \frac{v_g a_0 \cdot q \cdot V_{act}}{\eta_i} \cdot \frac{(N_0 - N_{tr})}{(1 + \varepsilon \cdot S_0)^2} \cdot \Delta \dot{S} \quad 3-20$$

Expressions for photon storage (L_0) and resonance damping (R_0) were found in a similar manner by replacing 3-16 in 3-12 and comparing the resulting equation (3-21) with Equation 3-14.

$$i_L = \frac{v_g a_0 \cdot q \cdot V_{act}}{\eta_i} \cdot \frac{(N_0 - N_{tr})}{(1 + \varepsilon \cdot S_0)^2} \cdot \left(\left(2 \cdot \Gamma \cdot \beta \cdot B \cdot N_0 \right. \right. \quad 3-21$$

$$\left. \left. + \Gamma \cdot v_g \cdot a_0 \cdot \frac{S_0}{1 + \varepsilon \cdot S_0} \right) \cdot \frac{N_0}{m \cdot V_T} \cdot \Delta V \right.$$

$$\left. + \left(\Gamma \cdot v_g \cdot a_0 \cdot \frac{N_0 - N_{tr}}{(1 + \varepsilon \cdot S_0)^2} - \frac{1}{\tau_S} \right) \cdot \Delta S \right)$$

$$L_0 = \frac{1}{C_j \cdot v_g \cdot a_0 \cdot \frac{(N_0 - N_{tr})}{(1 + \varepsilon \cdot S)^2} \cdot (2 \cdot \Gamma \cdot \beta \cdot B \cdot N_0 + \Gamma \cdot v_g \cdot a_0 \cdot \frac{S_0}{1 + \varepsilon \cdot S_0})} \quad 3-22$$

$$R_0 = L_0 \left(\frac{1}{\tau_S} - \Gamma \cdot v_g \cdot a_0 \cdot \frac{N_0 - N_{tr}}{(1 + \varepsilon \cdot S_0)^2} \right) \quad 3-23$$

Equations 3-18 to 3-20, 3-22 and 3-23 indicate that the parameters of the VCSEL are all functions of both N_0 and S_0 , which were obtained from the steady state rate Equations 3-4 and 3-5. The authors of [15] used a similar approach but in the course off the work described in this thesis, some errors have been revealed in the derivation of their intrinsic model parameters equation. In order to calculate the parameters of the intrinsic VCSEL equivalent model using the equations calculated above, the VCSEL's intrinsic parameters in Table 3-1 were used. Table 3-1 summarises the required parameters of the VCSEL used in this work. The values of the proposed VCSEL equivalent circuit model were calculated for different normalised bias currents (i_0/i_{th}). It was observed in Figures 3-4 and 3-5 as the bias current increases above the threshold current and the VCSEL approaches its stimulated photon emission, the values of the junction resistance (R_j), photon storage (L_0) and cavity losses (R_0) decrease to reach steady state; whereas the junction capacitance (C_j), which according to its definition directly relates to bias voltage, increases to achieve its stimulated steady state. Although the values of the results in Figure 3-4 and 3-5 are different from the results in [11], due to inherent difference between the edge emitting lasers and the VCSEL structures used in

this thesis, both results indicate the same trend of behaviour with changes in the biasing currents.

Table 3-1: 1300 nm VCSEL INTRINSIC PROPERTIES (Taken from [11, 15-17])

Symbol	Value	Description
η_i	0.8	Internal quantum efficiency
m	2	Diode ideality factor
N_{tr}	$3.22 \times 10^{18} \text{ cm}^{-3}$	Transparency electron number
A	$1.1 \times 10^8 \text{ s}^{-1}$	Non-radiative recombination coefficient
B	$1 \times 10^{-10} \text{ cm}^{-3} \text{ s}^{-1}$	Bimolecular recombination coefficient
C	$3.57 \times 10^{-29} \text{ cm}^{-6} \text{ s}^{-1}$	Auger recombination coefficient
ε	$2.09 \times 10^{-17} \text{ cm}^3$	Nonlinear gain coefficient
a_0	$4.8 \times 10^{-16} \text{ cm}^2$	Differential gain coefficient
Γ	0.06	Confinement factor
v_g	$7.7 \times 10^9 \text{ cm s}^{-1}$	Group velocity
β	7×10^{-3}	Spontaneous emission gain
V_{act}	$4 \times 10^{-12} \text{ cm}^3$	Active layer volume
I_{th}	$2.2 \times 10^{-3} \text{ A}$	Threshold current
τ_S	$6.4 \times 10^{-12} \text{ s}$	Photon lifetime
τ_N	$6.9 \times 10^{-10} \text{ s}$	Carrier lifetime
q	$1.602 \times 10^{-19} \text{ C}$	Electron charge

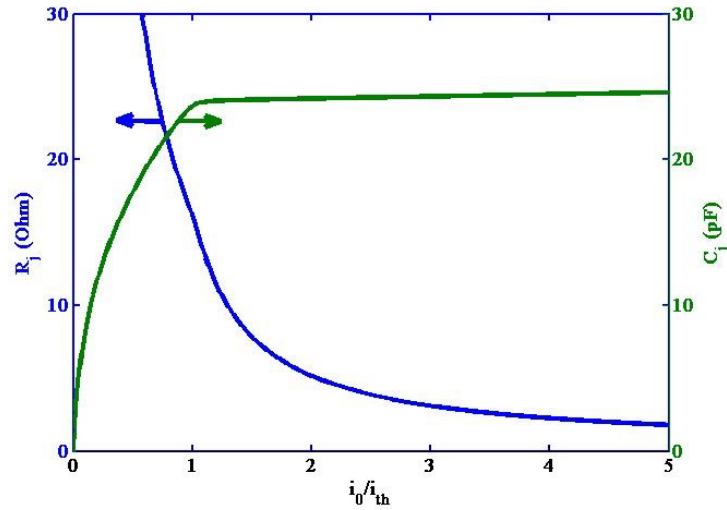


Figure 3-4: Junction resistance R_j and capacitance C_j as a function of normalised bias current.

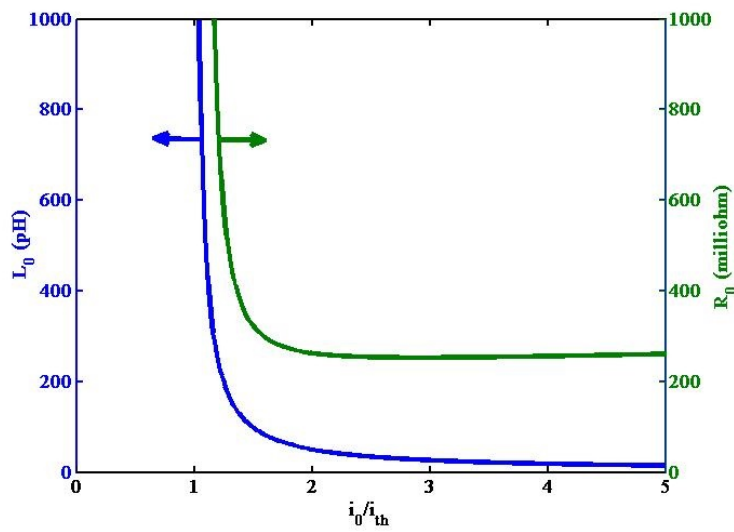


Figure 3-5: Photon storage L_0 and cavity losses R_0 as a function of normalised bias current.

The effects of Langevin noise sources F_N and F_S were taken into account by calculating the spectral intensities and inter correlation of the noise sources. According to the McCumber analysis, changes in photon and electron densities in the semiconductor lasers are due to the noise impulse of unit integrated intensity [18]. The VCSEL's spectral intensities, $\langle F_N^2 \rangle$, $\langle F_S^2 \rangle$

and the cross spectral intensity $\langle F_N F_S \rangle$ of Langevin noises were obtained from the frequency of the carrier and photon entering and leaving the sources [11]. Following the rate of entering and leaving the photon and carrier sources (Figure 2-10) and the steady state rate Equations 3-4 and 3-5, the following expressions were derived for the VCSEL Langevin noise sources in terms of I_0 and S_0 .

$$\langle F_N^2 \rangle = \sum f_{Carrier}^{Enter} + \sum f_{Carrier}^{Leave}$$

$$\langle F_N^2 \rangle = (A + BN_0 + CN_0^2)N_0 + v_g a_0 \frac{N_0 S_0}{1 + \epsilon S_0} + \Gamma v_g a_0 \frac{N_{tr} S_0}{1 + \epsilon S_0}$$

Steady state rate Equation 3-4 was used to simplify the above equation.

$$0 = \frac{\eta_i i_0}{qV_{act}} - (A + BN_0 + CN_0^2)N_0 + v_g a_0 \frac{N_{tr}}{1 + \epsilon S} \cdot S_0 - v_g a_0 \frac{N_0}{1 + \epsilon S} \cdot S_0$$

$$(A + BN_0 + CN_0^2)N_0 + v_g a_0 \frac{N_0}{1 + \epsilon S} \cdot S_0 = \frac{\eta_i i_0}{qV_{act}} + v_g a_0 \frac{N_{tr}}{1 + \epsilon S} \cdot S_0$$

$$\langle F_N^2 \rangle = \frac{\eta_i i_0}{qV_{act}} + v_g a_0 \frac{N_{tr} S_0}{1 + \epsilon S_0} + \Gamma v_g a_0 \frac{N_{tr} S_0}{1 + \epsilon S_0}$$

$$\langle F_N^2 \rangle = \frac{\eta_i I_0}{qV_{act}} + (1 + \Gamma) v_g a_0 \frac{N_{tr} S_0}{1 + \epsilon S_0} \quad 3-24$$

$$\langle F_S^2 \rangle = \sum f_{Photon}^{Enter} + \sum f_{Photon}^{Leave}$$

$$\langle F_S^2 \rangle = \Gamma \beta B N_0^2 + v_g a_0 \frac{N_0}{1 + \epsilon S} \cdot S_0 + \Gamma v_g a_0 \frac{N_{tr} S_0}{1 + \epsilon S_0} + \frac{S_0}{\tau_s}$$

Steady state rate Equation 3-5 was used to simplify the above equation.

$$0 = \Gamma \beta B N_0^2 + \Gamma v_g a_0 \frac{N_0}{1 + \epsilon S} \cdot S_0 - \Gamma v_g a_0 \frac{N_{tr} S_0}{1 + \epsilon S_0} - \frac{S_0}{\tau_s}$$

$$\Gamma \cdot \beta \cdot B \cdot N^2 = -\Gamma \cdot v_g \cdot a_0 \cdot \frac{N_0}{1 + \varepsilon S} \cdot S_0 + \Gamma \cdot v_g \cdot a_0 \cdot \frac{N_{tr} S_0}{1 + \varepsilon \cdot S_0} + \frac{S_0}{\tau_s} \quad 3-25$$

$$\langle F_S^2 \rangle = 2 \frac{S}{\tau_s} + 2 \cdot \Gamma \cdot v_g \cdot a_0 \cdot \frac{N_{tr} S_0}{1 + \varepsilon \cdot S_0} + (1 - \Gamma) \cdot v_g \cdot a_0 \cdot \frac{N_0 \cdot S_0}{1 + \varepsilon S_0} \quad 3-26$$

$$\langle F_N F_S \rangle = - \left[\sum f_{N-S} + \sum f_{S-N} \right]$$

$$\langle F_N F_S \rangle = - \left[\Gamma \cdot \beta \cdot B \cdot N_0^2 + v_g \cdot a_0 \cdot \frac{N_0}{1 + \varepsilon S_0} \cdot S_0 + \Gamma \cdot v_g \cdot a_0 \cdot \frac{N_{tr} S_0}{1 + \varepsilon \cdot S_0} \right]$$

Using Equation 3-25, the cross spectral intensity $\langle F_N F_S \rangle$ was calculated as follows:

$$\langle F_N F_S \rangle = - \left[\frac{S}{\tau_s} + 2 \cdot \Gamma \cdot v_g \cdot a_0 \cdot \frac{N_{tr} S_0}{1 + \varepsilon \cdot S_0} \right] \quad 3-27$$

The spectral intensities of the current (S_{ii}), voltage (S_{vv}) noise sources and their cross spectral intensity (S_{iv}) were calculated by comparing the small signal rate Equations 3-1 and 3-2 with the electrical circuit equivalent Equations 3-13 and 3-14 and using Equation 3-16.

$$\frac{i_n}{C_j} = \frac{m V_T}{N_0} F_N$$

$$i_n = \frac{N_0 \cdot q \cdot V_{act}}{m \cdot V_T \cdot \eta_i} \cdot \frac{m V_T}{N_0} \cdot F_N$$

$$S_{ii} = \frac{\overline{i_n^2}}{\Delta f} = 2 \cdot \left(\frac{q \cdot V_{act}}{\eta_i} \right)^2 \cdot \langle F_N^2 \rangle \quad 3-28$$

$$- \frac{V_n}{L_0} = \frac{v_g a_0 \cdot q \cdot V_{act}}{\eta_i} \cdot \frac{(N_0 - N_{tr})}{(1 + \varepsilon \cdot S_0)^2} \cdot F_S$$

$$V_n = - \frac{m \cdot V_T \cdot \eta_i}{N_0 \cdot q \cdot V_{act} \cdot v_g \cdot a_0 \cdot \frac{(N_0 - N_{tr})}{(1 + \varepsilon \cdot S_0)^2} \cdot (2 \cdot \Gamma \cdot \beta \cdot B \cdot N_0 + \Gamma \cdot v_g \cdot a_0 \cdot \frac{S_0}{1 + \varepsilon \cdot S_0})} \cdot \frac{v_g a_0 \cdot q \cdot V_{act}}{\eta_i} \cdot \frac{(N_0 - N_{tr})}{(1 + \varepsilon \cdot S_0)^2} \cdot F_S$$

$$S_{vv} = \frac{\overline{v_n^2}}{\Delta f} = \frac{2 \cdot m^2 \cdot V_T^2}{N_0^2 \cdot (2 \cdot \Gamma \cdot \beta \cdot B \cdot N_0 + \Gamma \cdot v_g \cdot a_0 \cdot \frac{S_0}{1 + \epsilon \cdot S_0})^2} \cdot \langle F_S^2 \rangle \quad 3-29$$

$$S_{iv} = \frac{\overline{i_n v_n}}{\Delta f} = \frac{2 \cdot m \cdot V_T \cdot q \cdot V_{act}}{N_0 \cdot \eta_i \cdot (2 \cdot \Gamma \cdot \beta \cdot B \cdot N_0 + \Gamma \cdot v_g \cdot a_0 \cdot \frac{S_0}{1 + \epsilon \cdot S_0})} \cdot \langle F_N \cdot F_S \rangle \quad 3-30$$

It is important to mention that a factor 2 was added to Equations 3-28 to 3-30 to achieve a more commonly used single-sided noise spectrum rather than the double-sided spectrum. It was observed from Equation 3-28 that the current noise source i_n is mostly responsible for the Langevin noise in the carrier density and according to Equation 3-29 the variation in photon density is mainly due to the voltage noise source v_n . The noise sources i_n and v_n are mutually dependent due to the coupled rate equations and cross spectral intensity equation as observed in Equations 3-1, 3-2 and 3-30. Figures 3-6 to 3-8 indicate the spectral intensities of Langevin noise sources S_{ii}, S_{vv} and their cross spectral intensity S_{iv} given in Equations 3-28 to 3-30 as a function of normalised bias current. Comparing the spectral intensities of Langevin noise sources for the edge emitting laser used in [11] and the simulated results in Figure 3-6 to 3-8 indicate the same trend as the value of the normalised bias current increases.

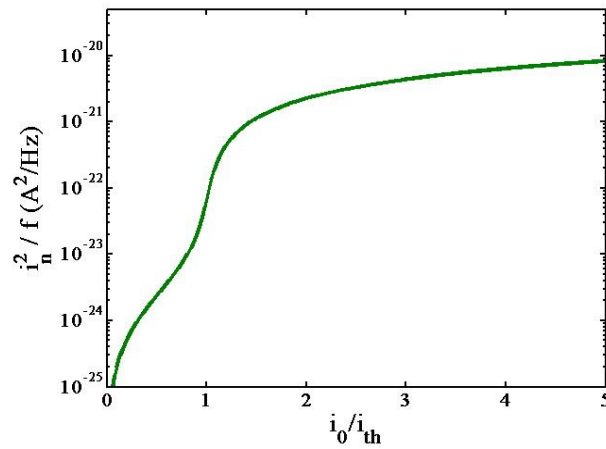


Figure 3-6: Current noise spectral intensity (S_{ii}) as a function of normalised bias current.

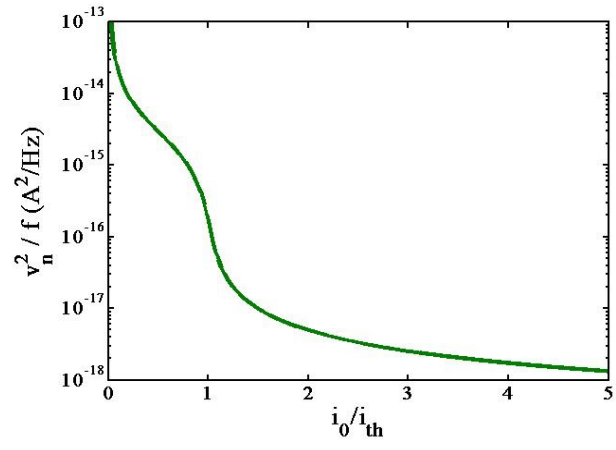


Figure 3-7: Voltage noise spectral intensity (S_{vv}) as a function of normalised bias current.

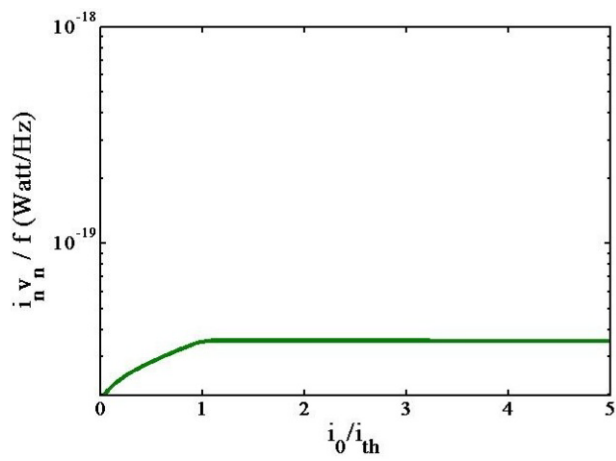


Figure 3-8: Cross-spectral density of noise sources (S_{iv}) as a function of normalised bias current.

It can be observed from Figure 3-6 that S_{ii} increases significantly when $0 < i_0/i_{th} < 2$ but as $i_0/i_{th} > 2$ the rate of increase slows down and gradually approaches its steady state value. Similarly, in Figure 3-7 the voltage noise spectral intensity decreases significantly when $0 < i_0/i_{th} < 2$ and then approaches to its steady state value when $i_0/i_{th} > 4$. In contrast with the trend of the spectral intensities in Figures 3-6 and 3-7, it is observed in Figure 3-8 the cross spectral intensity S_{iv} reached its steady state value much faster as the bias current just passed its threshold value. Table 3-2 summarises the intrinsic VCSEL's equivalent circuit model elements for different normalised bias currents.

Table 3-2: Parameters of the VCSEL equivalent model for different normalised bias currents and 4.5 GHz operating frequency.

I_0/I_{th}	C_j (pF)	R_j (Ω)	R_0 (Ω)	L_0 (pH)	$\overline{i_n^2}$ (A)	$\overline{v_n^2}$ (V)
1	23.66	16.03	1.11	1050	$2.9e^{-13}$	$7.4e^{-6}$
2	24.18	5.16	0.26	50.14	$1.0e^{-11}$	$2.2e^{-8}$
3	24.33	3.11	0.25	26.34	$1.9e^{-11}$	$1.1e^{-8}$
4	24.47	2.25	0.26	18.49	$2.8e^{-11}$	$7.7e^{-9}$

Since the VCSEL equivalent circuit model's elements were fully calculated, the extrinsic characteristics of the VCSEL such as; input impedance ($Z(\omega)$), photon modulation transfer function ($H(\omega)$), junction voltage noise spectrum ($\overline{v_1^2}/\Delta f$) and the relative intensity noise ($RIN(\omega)/\Delta f$) were analysed. The input impedance ($Z(\omega)$) was calculated by analysing the total impedance of the equivalent circuit as seen in the derivation of Equation 3-31. Figure 3-9 illustrates good agreement between input impedance of the VCSEL,

calculated using Equation 3-31 and simulating the equivalent circuit model in Figure 3-3 and the parameter set in Table 3-2 for $I_0/I_{th} = 2$ using AWR Microwave Office. This agreement in Figure 3-9 indicates that the calculation of $Z(\omega)$ in Equation 3-31 is correct. The agreement between Figure 3-9 and published works such as in reference [1] indicates that the element values in Tables 3-1 and 3-2 are accurate and valid. Since the elements of the VCSEL equivalent circuit depend on the biasing current, therefore the input impedance of the VCSEL also changes with the changes in the bias current. The behaviour of the input impedance of the VCSEL for different normalised bias currents is illustrated in Figure 3-10.

$$Z_p = \frac{-jR_0}{\omega R_j C_j + j}$$

$$Z_s = R_0 + j\omega L_0$$

$$Z(\omega) = Z_p \parallel Z_s = \frac{(R_0 + j\omega L_0)}{\left(1 + \frac{(R_0 + j\omega L_0) \cdot (\omega R_j C_j - j)}{-jR_j}\right)}$$

$$Z(\omega) = \frac{V_1(\omega)}{I_1(\omega)} = \frac{(R_0 + j\omega L_0)}{1 + j\omega C_j R_0 + \frac{R_0}{R_j} - \omega^2 L_0 C_j + j\omega \frac{L_0}{R_j}}$$

$$Z(\omega) = \frac{V_1(\omega)}{I_1(\omega)} = \frac{(R_0 + j\omega L_0)}{L_0 C_j D} \tag{3-31}$$

$$D = -\omega^2 + j\omega \left(\frac{R_0}{L_0} + \frac{1}{R_j C_j} \right) + \frac{1}{L_0 C_j} \left(1 + \frac{R_0}{R_j} \right)$$

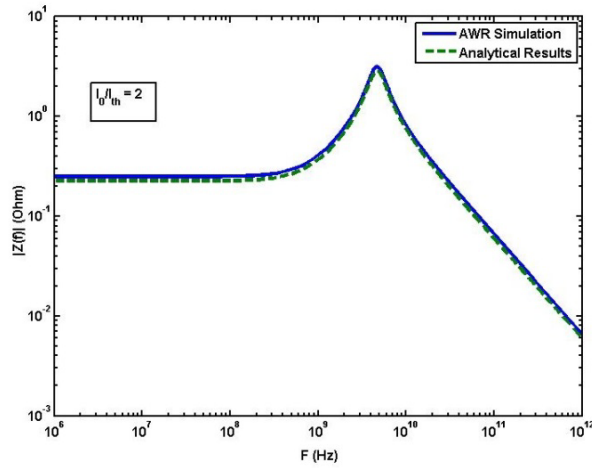


Figure 3-9: Frequency dependence of the VCSEL input impedance.

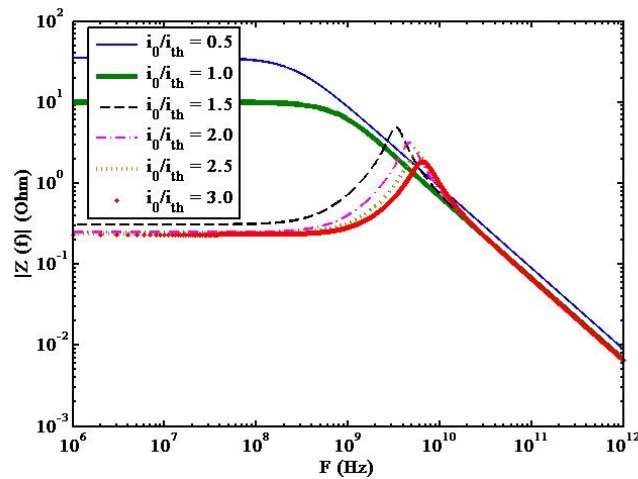


Figure 3-10: The impedance of an intrinsic VCSEL for various pump currents.

It is observed in Figure 3-10 that at a given frequency below the relaxation oscillation of the VCSEL, the VCSEL impedance decreases from 35Ω to 0.23Ω when the bias current changes from $i_0 = 0.5i_{th}$ to $i_0 = 3i_{th}$. The junction voltage noise spectrum ($\overline{v_1^2}/\Delta f$) and relative intensity noise ($RIN(\omega)$) are essential semiconductor laser characteristics as they

illustrate the laser capability of high-speed modulation in a communication system [7]. Equations 3-32 and 3-33 were derived to calculate junction voltage noise spectrum and relative intensity noise, using the method outlined in [7, 11, 19] for conventional semiconductor laser diodes.

$$\frac{\overline{v_1^2}(\omega)}{\Delta f} = \frac{\overline{i_n^2} \left((R_0^2 + (\omega L_0)^2) \right) + \overline{v_n^2} + 2\overline{v_n i_n} R_0}{(L_0 C_j)^2 D D^*} \cdot \frac{1}{\Delta f} \quad 3-32$$

$$\frac{RIN(\omega)}{\Delta f} = \frac{\langle \delta S^2 \rangle}{S_0^2} = \left(\frac{\eta_i \cdot (1 + \varepsilon \cdot S_0)^2}{v_g a_0 \cdot q \cdot V_{act} (N_0 - N_{tr})} \right)^2 \cdot \frac{|Z_p|^2 \cdot \overline{i_n^2} + \overline{v_n^2} - \frac{2R_j \overline{v_n i_n}}{1 + \omega^2 C_j^2 R_j^2}}{|Z_p|^2 + |Z_S|^2 + \frac{R_j(2R_0 - 2R_j \cdot L_0 \cdot C_j \cdot \omega)}{1 + \omega^2 C_j^2 R_j^2}} \cdot \frac{1}{S_0^2} \cdot \frac{1}{\Delta f} \quad 3-33$$

The small signal VCSEL relative intensity noise and junction voltage noise low frequency behaviour were analysed for the normalised biasing current when $F_{Lo} = 10^5 \text{ Hz}$. It is observed in Figure 3-11 (a) and (b) that both relative intensity noise and junction voltage noise present a maximum at the onset of stimulated emission ($i_0/i_{th} = 1$). Figure 3-12 (a) and (b) illustrates the spectra of both relative intensity noise and junction voltage noise, for different VCSEL normalised bias currents respectively. It can be seen in Figure 3-12 (a) and (b) when VCSEL is at stimulated emission ($i_0 > i_{th}$), a resonance at the VCSEL relaxation oscillation frequency (Ω_R) is observed. The value of relaxation oscillation frequency increases with an increase in i_0 . Both spectra remain constant when $F \ll \Omega_R$ however, the value of this constant decreases as the bias current increases.

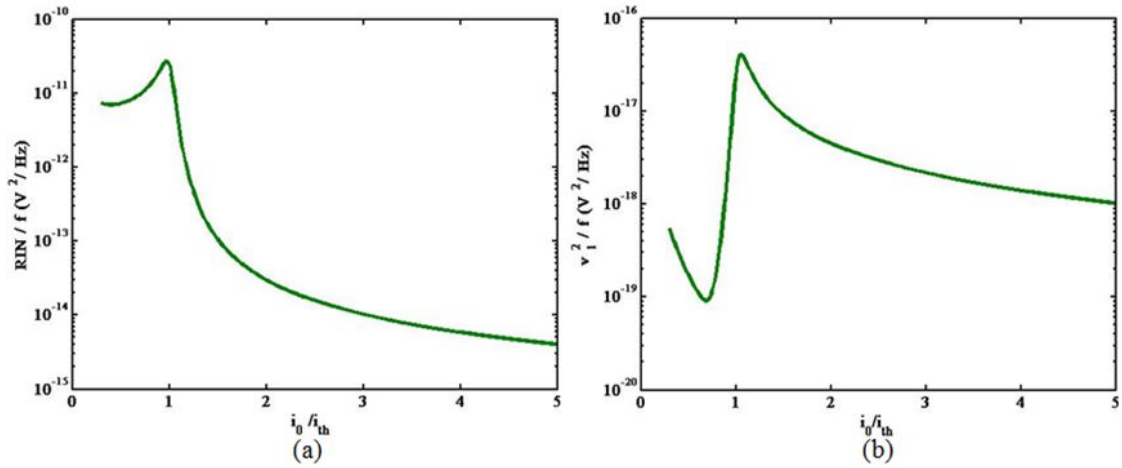


Figure 3-11: Low frequency analysis of VCSEL, (a) relative intensity noise and (b) junction voltage noise spectrum as a function of normalized bias current ($f_{Lo} = 10^5$ Hz).

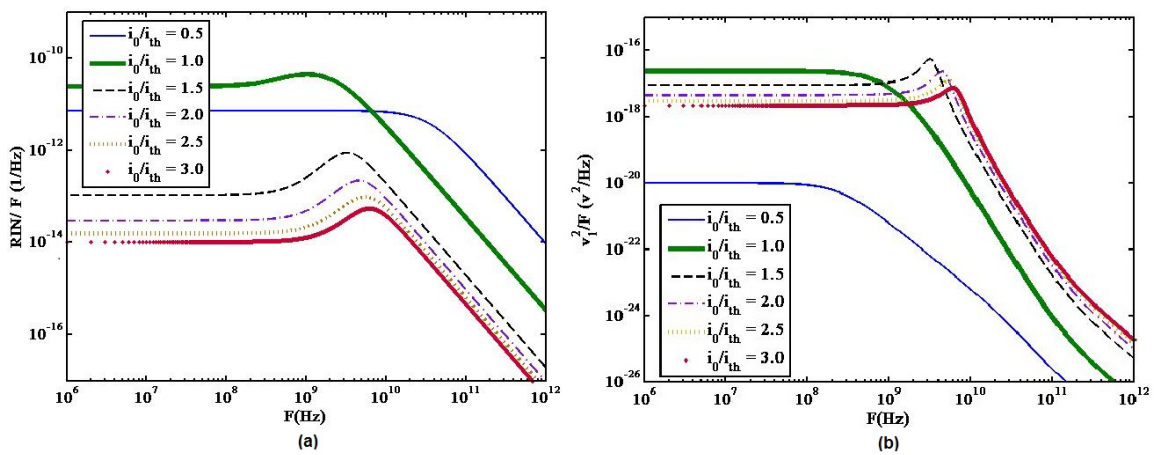


Figure 3-12: Frequency dependence of (a) relative intensity noise and (b) junction voltage noise spectrum for various pump currents.

Another application of the small-signal VCSEL equivalent circuit model is that by using this model, the modulation response of the VCSEL can be analysed directly from the equivalent circuit model. In Figure 3-13 the modulation response of the VCSEL used in this work was investigated for different bias currents. It is detected from Figure 3-13 that the resonant peak

of the modulation response moves to higher frequencies as the biasing current increases; whereas the resonant peak magnitudes decrease. It is important to mention that in practice the electrical parasitics have large and limiting effects on the VCSEL's modulation bandwidth. The effects of the electrical parasitics on the VCSEL's modelling are investigated in detail in section 3.4.

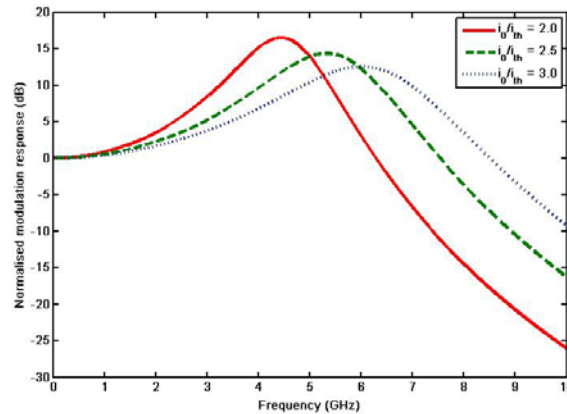


Figure 3-13: Intrinsic modulation response of the VCSEL for different biasing currents.

3.3.2 Distributed intrinsic VCSEL model

The lumped-element circuit model proposed earlier in this section has proven to have lots of advantages over the numerical models of VCSELs developed in the literature. The advantages of the lumped-element model enabled the integration of the parasitics and matching networks which yields accurate and realistic results. Furthermore, the lumped-element VCSEL model enabled the use of circuit simulator software to analyse the advanced VCSEL properties such as; RIN, input impedance and modulation response of the VCSEL, with high accuracy. However, the lumped-element model has an inherent size limitation in the micro and millimetre wave region. Therefore, a distributed intrinsic VCSEL model is proposed based on the lumped-element model.

In order to convert the elements of the lumped-element VCSEL model (Figure 3-3) to the distributed model, the quasi-lumped method was used [20]. In this method, the lumped element will be replaced by the microstrip line with a specific width and length. In this method a shunt capacitor is modelled by a wide microstrip and the inductor with a floating short circuit series stub. Figure 3-14 represents the transmission line equivalent model of the intrinsic VCSEL model of Figure 3-3. In Table 3-3 the equivalence between the lumped elements and the transmission line model components is defined. The lengths of the inductor and capacitor in Table 3-3 are calculated using Equations 3-34 and 3-35 respectively.

$$l_{shcap} = v_p Z_0 C \quad 3-34$$

$$l_{Ind} = \frac{\lambda_g}{2\pi} \tan^{-1} \left(\frac{\omega L}{Z_0} \right) \quad 3-35$$

The phase velocity (v_p) and guided wavelength (λ_g) are defined as follows: the variables c and λ_0 are the speed of light and free space wavelength respectively. The effective dielectric constant (ϵ_{eff}) is defined in section 2.7.2.2. The effective dielectric constant of Equation 2-11 is defined for the structures with the larger width of the microstrip line, than the height of the substrate ($W/h > 1$) [20]. The structure in this work satisfies the above condition.

$$v_p = \frac{c}{\sqrt{\epsilon_{eff}}}$$

$$\lambda_g = \frac{\lambda_0}{\sqrt{\epsilon_{eff}}}$$

The width of the microstrip lines for both shunt inductance and capacitance were calculated using Equation 3-36.

$$w = \sqrt{\frac{\mu}{\epsilon_{eff}} \frac{h}{Z_0}} \quad 3-36$$

Table 3-3: The equivalance between lumped element and transmission line model components and dimentions of the distributed elements.

Lumped element	Equivalent TLM	Dimension (mm)/Impedance (Ω)
C_j	Z_{C_j}	$l = 53.8 \quad w = 9.2$
L_0	Z_{L_0}	$l = 0.6 \quad w = 9.2$
R_j	R_j	5.16
R_0	R_0	0.26

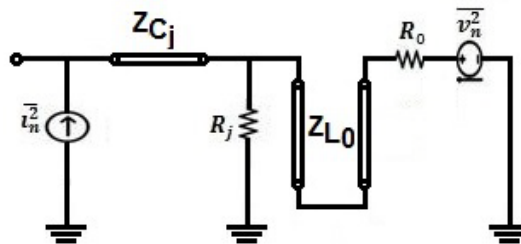


Figure 3-14: Distributed presentation of the intrinsic VCSEL model.

3.3.3 Intrinsic VCSEL dynamic response

Since one of the common applications of any semiconductor laser including the VCSEL is to be used as a source of optical signal in high-speed fibre communications, the dynamic behaviour analysis of the VCSEL becomes extremely crucial. The transient response phenomena such as: switch-on (turn-on) delay (t_{on}) and relaxation oscillation frequency

(Ω_R), will distort the pulse shape in high frequencies; therefore it is desirable to reduce these phenomena [21].

The effect of biasing current on the transient response of the VCSEL used in this work was analysed in Figure 3-15 by feeding the step waveform current ($I_{step} = 2 \text{ mA}$) into the intrinsic VCSEL model (Figure 3-14). It is observed in Figure 3-15 that a higher equilibrium power level is achieved by increasing the biasing level. Furthermore, it is detected in Figure 3-15 that turn on delay (t_{on}) and the overshoot of the relaxation oscillation decreases as the biasing level increases.

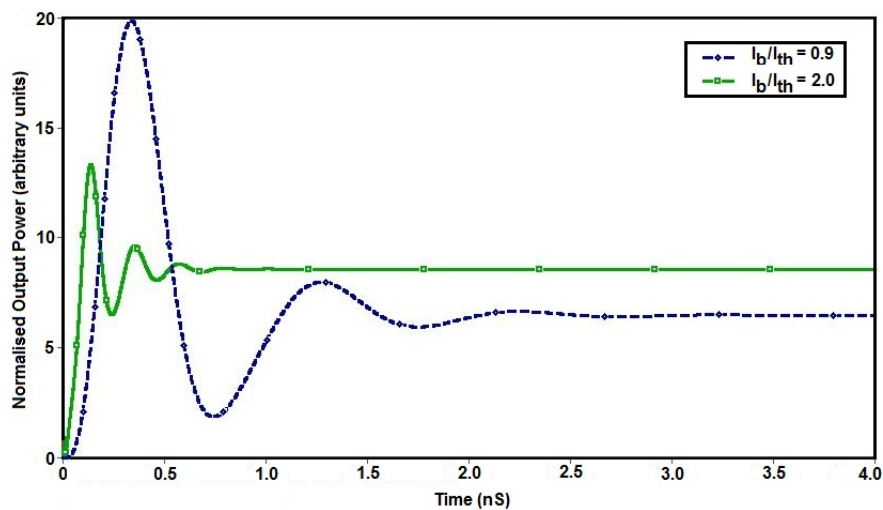


Figure 3-15: Transient response of intrinsic VCSEL for different biasing current.

In Figure 3-16, the VCSEL transient response to a square pulse input current with a delay of 1 ns and pulse width of 5 ns , the low and high level of 0 and 5 mA , is illustrated. It is observed from Figure 3-16 that the second pulse, occurring after the current magnitude changed to zero, is smaller than the first pulse at the onset of emission; this is due to spatial hole burning. This phenomenon indicated that once the step current reduced below the

threshold value for the short period of time (t_{off}), the number of carriers in the active region exceeds the threshold values and results in a small secondary transient pulse. This increase in the carrier happened as the carriers diffused to the active region intersecting the optical mode to replace those that were lost to spatial hole burning [22].

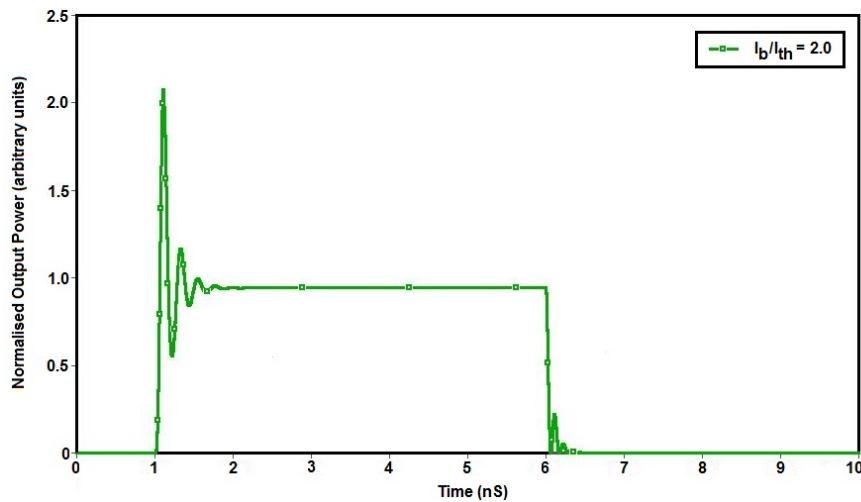


Figure 3-16: VCSEL t_{off} and the spatial hole burning phenomenon.

3.4 Electrical parasitics

The precise bandwidth evaluation of the source has vital importance in any communication system. The modulation bandwidth of the VCSEL and its constraining factors are of great importance in determining the applications of the VCSEL in broadband optical fibre communication systems. Electrical parasitics introduce a high frequency roll-off in the frequency domain of the VCSEL derived current. This high frequency roll-off slows down the fast transient of the VCSEL drive current waveform and therefore reduces the modulation bandwidth [23].

In order to include the effects of the electrical parasitics, the equivalent circuit of the parasitic network is added to the proposed VCSEL model. The parasitic network of the VCSEL can be

modelled as a cascade of the package or mount parasitics, which mainly include the bond wire series inductance and resistance and standoff shunt capacitance between the input package ports and parasitics linked with the VCSEL chip, which mainly includes the extrinsic parameters of the VCSEL. This method of modelling parasitics was also reported for conventional laser models [13]. Figure 3-17 illustrates the parasitic network used in the proposed VCSEL model.

Hypothetically, parasitics linked with the VCSEL chip provide a shunt DC path draining the biasing current away from the VCSEL's active region, which can be estimated with a simple shunt resistor [24]. However during high-speed modulation, the parasitic DC path related to the VCSEL chip is highly frequency and structure dependent and cannot be modelled with only a simple shunt resistor.

In order to demonstrate VCSEL chip parasitics, the parasitic paths introduced within the VCSEL structure of Figure 3-2 can be observed in Figure 3-18. The series resistance (R_s) in the VCSEL chip parasitic circuit model arises from substrate resistance (R_{SS}) below the VCSEL active region and the resistance between the P-contact and the active region (R_{SP}), which in the structure used in this work is very small ($\approx m\Omega$). The $p - n$ junction which is formed by sandwiching the active layer is modelled as the junction diodes (D_L) and the corresponding capacitors (C_L). A large resistance R_Q exists between the active region and the junction diode (D_L). Resistance R_Q limits the escape of current from the VCSEL active region to the junction diode (D_L). In series with the C_L is a substrate resistance (R_{SUB}) [10, 13, 23, 25].

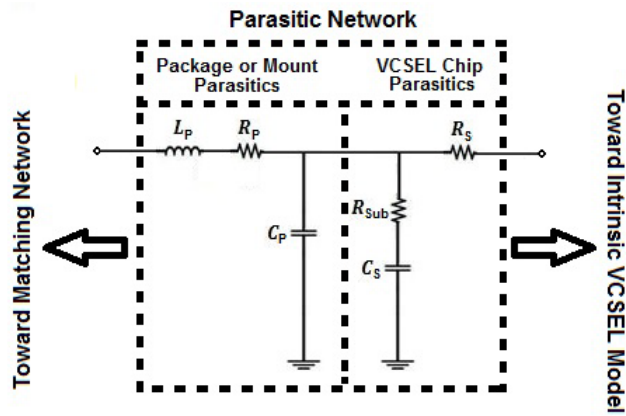


Figure 3-17: The VCSEL parasitic network equivalent circuit model.

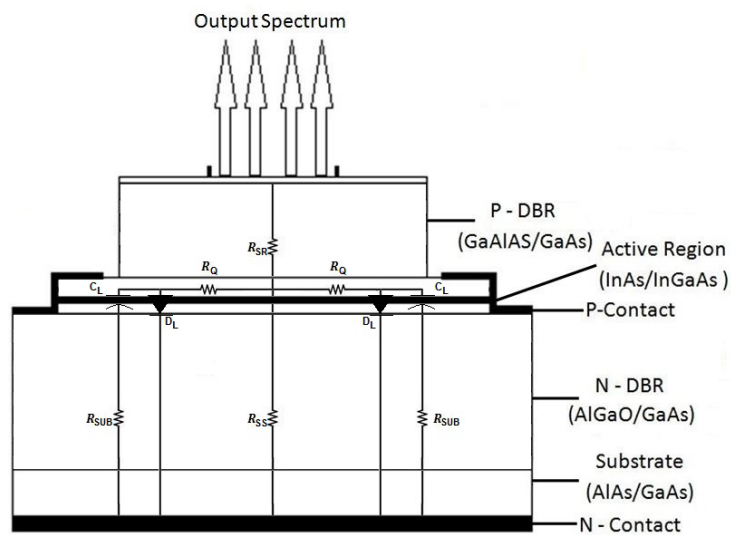


Figure 3-18: Schematic cross-section of VCSEL with the parasitic path included.

The value of parasitic network parameters can be calculated by fitting the experimentally measured S-parameters of the VCSEL to the equivalent circuit model using optimisation

software such as AWR Microwave Office [26]. The value of the parasitic parameters of Figure 3-17 are summarised in Table 3-4 [25].

Table 3-4: VCSEL parasitic components value.

Symbol	Value	Description
R_p	14 Ω	Bondwire resistance
L_p	49.6 pH	Bondwire inductance
C_p	0.84 pF	Standoff shunt capacitance
R_{SUB}	64.6 Ω	Chip substrate resistance
C_S	0.58 pF	Shunt parasitic capacitance
R_S	57.7 Ω	Chip series resistance
R_{in}	50 Ω	Generator resistance

3.4.1 Distributed electric parasitic model

In order to convert the lumped-element electrical parasitic model in Figure 3-17 to the distributed model, the same method used in designing the distributed intrinsic VCSEL was used. The lumped-element electrical parasitic model includes shunt capacitors and a series inductor. The conversion process of shunt capacitor to distributed counterpart was discussed earlier in section 3.3.2; therefore in this section the conversion procedure and equivalent distributed model of the series inductor are only reviewed.

In the quasi-lumped method, a series inductance is modelled using a rather long microstrip line. The length of this microstrip line (l_{Sind}) was calculated using Equation 3-37. The width of the microstrip line was calculated using Equation 3-36. Table 3-5 represents the

equivalence between the lumped element and distributed electric parasitic model and the dimensions of the distributed elements. A distributed model of the VCSEL electrical parasitic network is presented in Figure 3-19.

$$l_{\text{ind}} = \frac{v_p L}{Z_0} \quad 3-37$$

Table 3-5: Equivalence between lumped element and transmission line model components and the dimension of distributed electric parasitic parameters' model.

Lumped element	Equivalent TLM	Dimension (mm)/Impedance (Ω)
L_p	Z_{Lp}	$l = 0.56$ $w = 9.2$
C_p	Z_{Cp}	$l = 1.89$ $w = 9.2$
C_s	Z_{Cs}	$l = 1.29$ $w = 9.2$
R_p	R_p	14Ω
R_{SUB}	R_{SUB}	64.6Ω
R_s	R_s	57.7Ω

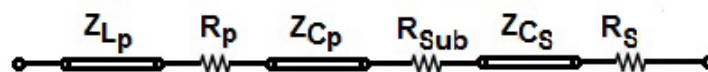


Figure 3-19: Distributed model representation of lumped-element electric parasitic model of Figure 3-17.

In order to analyse the effects of a parasitic network on the proposed VCSEL model, the small signal frequency response of the VCSEL was compared for both with and without the inclusion of a parasitic network in the VCSEL model. The intrinsic and extrinsic relaxation

oscillation frequencies were calculated to be 4.8 GHz and 4.1 GHz, respectively as illustrated in Figure 3-20. The results in Figure 3-20 were found by simulating the current flowing across the intrinsic VCSEL model with and without the inclusion of the parasitic network using OrCAD PSpice Design Environment. It is observed in Figure 3-20 that the inclusion of the parasitic reduces the magnitude of the frequency response at the relaxation frequency (f_r) by approximately 8 dB. It is important to mention that the existence of the large electrical parasitics can dramatically reduce the f_{-3dB} point to under f_r . It is also observed in Figure 3-20, that the VCSEL modelled in this work exhibits a dip before resonance frequency when the parasitic network was included and this is due to the rather large $R_S C_S$ product. The dip in the frequency response of the VCSEL indicates that the VCSEL model in this work has similar behaviour to that of an etched mesa buried heterostructure (EMBH) laser [10].

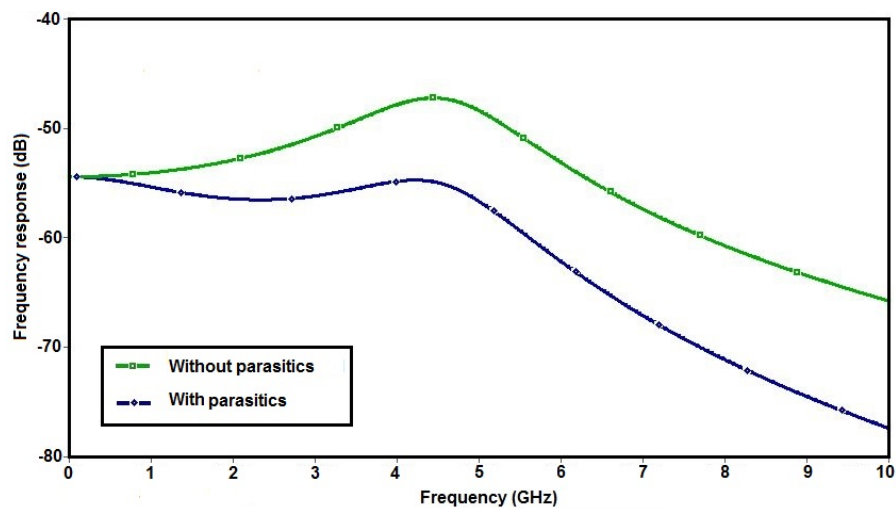


Figure 3-20: Intrinsic and extrinsic resonant frequency of the integrated VCSEL model.

3.5 Matching network

Semiconductor lasers can be used as a source of microwave or millimetre wave signals. The optical signal processing techniques for microwave and millimetre wave signal generation was studied in [27]. In these high frequency applications the matching network is necessary first to minimise the reflections towards the signal generator due to impedance mismatch [28]; and secondly, due to the high level of RF power required to overcome the ohmic losses related to electrical parasitics, bias tee and electrical cables. It is important to point out that at high frequencies, parasitics introduce a roll-off in laser modulation response and therefore, it is important to include parasitic effects in the design of the matching network [13].

There are a number of matching techniques available, such as: the conventional method of connecting the series chip resistor between the signal generator and the laser model[29]; or using matching networks. Matching networks are widely preferred in laser diode matching [8, 30-32], as they provide better power transfer from the signal generator to the VCSEL model. In the proposed integrated VCSEL model, a simple L-matching network [20], as illustrated in Figure 3-21 (A), was used to match the lumped element VCSEL model with the signal generator. However realising lumped elements in the Gigahertz region is rather difficult as they have to be very small with respect to the operating wavelength. As illustrated in [33] a passive lumped-element matching network was implemented at 5.6 GHz using spiral inductors and monolithically integrated Metal Insulator Metal (MIM) capacitors to minimise the physical dimension. In order to overcome the size and bandwidth limitation of an L-matching network, a shunt stub matching network (Figure 3-21 (B)) was designed in the distributed model of the proposed integrated VCSEL model.

3.5.1 Design and analysis

The matching network can be designed for different frequencies, depending on the application for which the integrated VCSEL model will be used. Based on the frequency at which the L-network will be matched, the circuit structure in Figure 3-21 (A) can be modified by moving the inductor L_m towards the signal generator, just before the shunt capacitor C_m . Detailed matching considerations are investigated in [20]. In this work, the matching network was designed to match at 4.5 GHz. Since the modulation bandwidth of the intrinsic VCSEL model when it is biased at twice the VCSEL threshold current ($I_b = 2I_{th}$) (see Figure 3-13) is 5.12 GHz and that is greater than 4.5 GHz, therefore efficient direct modulation at this frequency is possible.

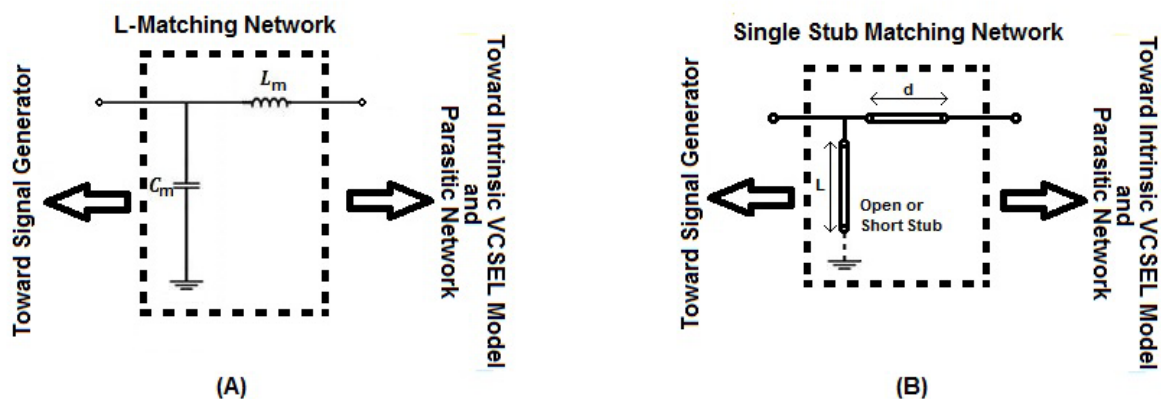


Figure 3-21: Matching networks (A) lumped element L-Matching network. (B) single stub matching network for distributed model.

To determine the L-matching network components, first the early values of the matching components were calculated using the Smith chart. These values were then optimised, using the AWR Microwave Office software to achieve insertion loss of about -58 dB. Table 3-6 summarises the tuned values of the L-matching network designed at 4.5 GHz. In Table 3-6,

Z_{Load} is the complex impedance representing the parasitic network and intrinsic VCSEL model equivalent impedance. Figure 3-22 indicates the impedance of the integrated VCSEL model across the frequency range. The plot of reflection coefficient (S_{11}) of the designed integrated VCSEL model is illustrated in Figure 3-23.

Table 3-6: Optimised L-matching network components.

Frequency (GHz)	L_m (nH)	C_m (pF)	Z_{Load} (Ω)	Z_{Gen} (Ω)
4.5	1.52	0.59	$29.42 - j18.31$	50

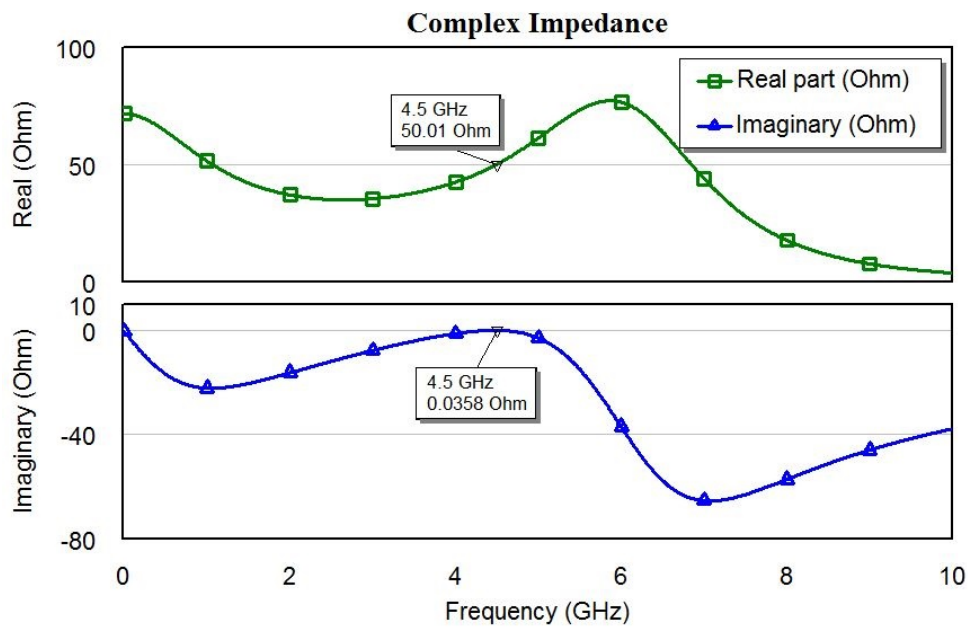


Figure 3-22: Complex impedance of proposed integrated VCSEL model.

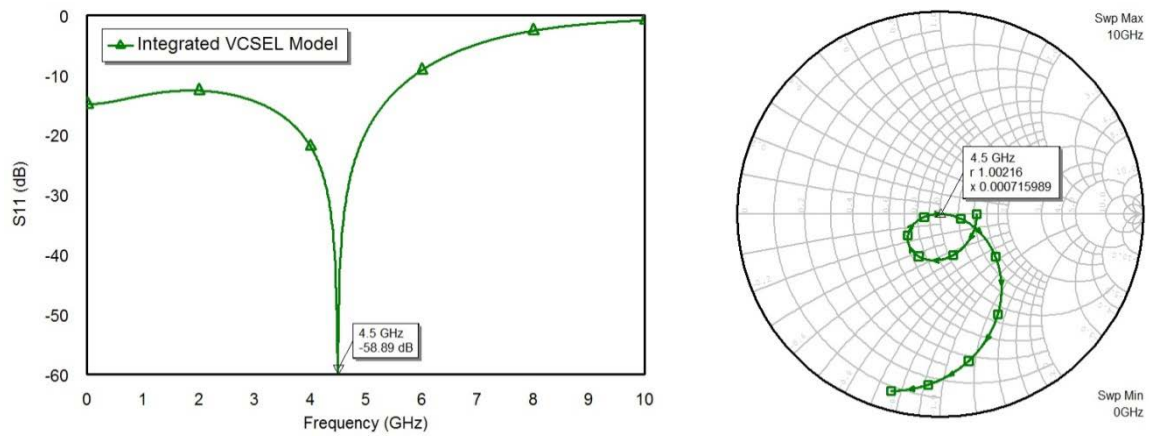


Figure 3-23: S_{11} results (left: magnitude; right: Smith chart) of the matched lumped-element integrated VCSEL model at 4.5 GHz.

In order to design the single stub matching network for the distributed model, first the initial values for the length of the microstrip lines were calculated analytically for the 50 Ω microstrip line. The analytical values were then optimised using the AWR Microwave Office package to achieve the return loss of around -60 dB at 4.5 GHz. Table 3-7 summarises the dimension of the designed short circuit single stub matching network. Figure 3-24 represents the reflection coefficient (S_{11}) plot of the integrated TLM VCSEL model. It is observed from Figure 3-24 that the TLM based integrated VCSEL model is finely matched at 4.5 GHz.

Table 3-7: Optimised short single stub matching network dimensions.

Matching Network Elements	Length (mm)	Width (mm)
Short stub	13.9	1.7
Series microstrip line	7.1	1.7

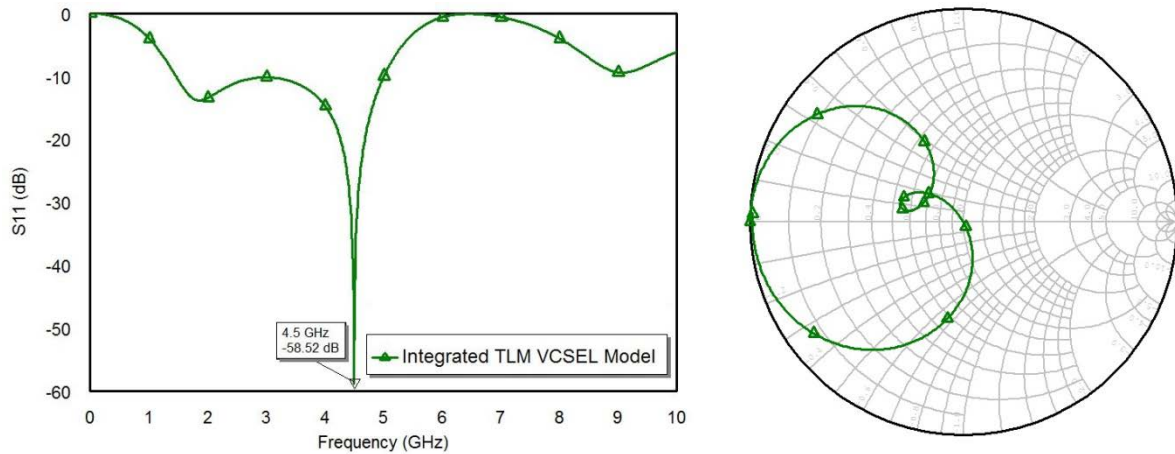


Figure 3-24: S_{11} results (left: magnitude; right: Smith chart) of the matched TLM integrated VCSEL model at 4.5 GHz.

The finalised integrated VCSEL model schematic proposed in this work is illustrated in Figure 3-25 (A) and (B) for both lumped-element and transmission line based models, respectively.

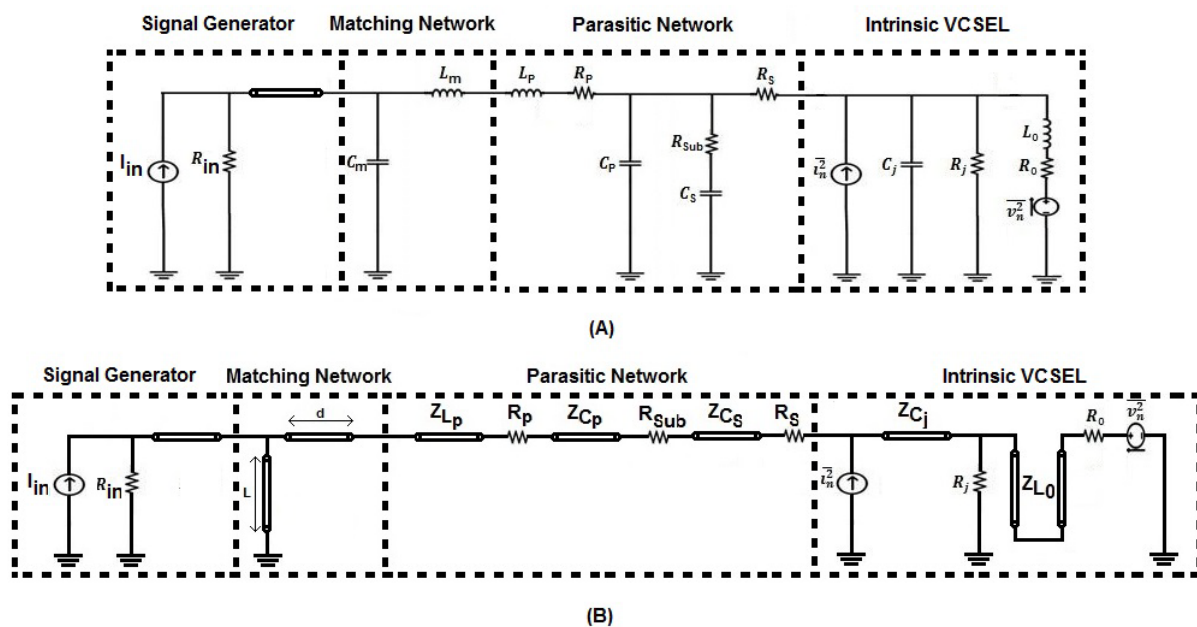


Figure 3-25: Proposed integrated VCSEL model (A) lumped-element model. (B)

Transmission line based equivalent.

The small signal modulation response of the proposed integrated VCSEL model was simulated for both the matched and unmatched versions, in order to analyse the effects of the matching network as indicated in Figure 3-26. This result was calculated by performing the FFT on the impulse response of the proposed VCSEL model both in the presence and the absence of the matching network using OrCAD PSpice Design Environment. It is observed from Figure 3-26 that the inclusion of the matching network improved the emitted signal by just above 3 dB. This is in line with the results of [10] for the improvements, due to the matching for conventional lasers.

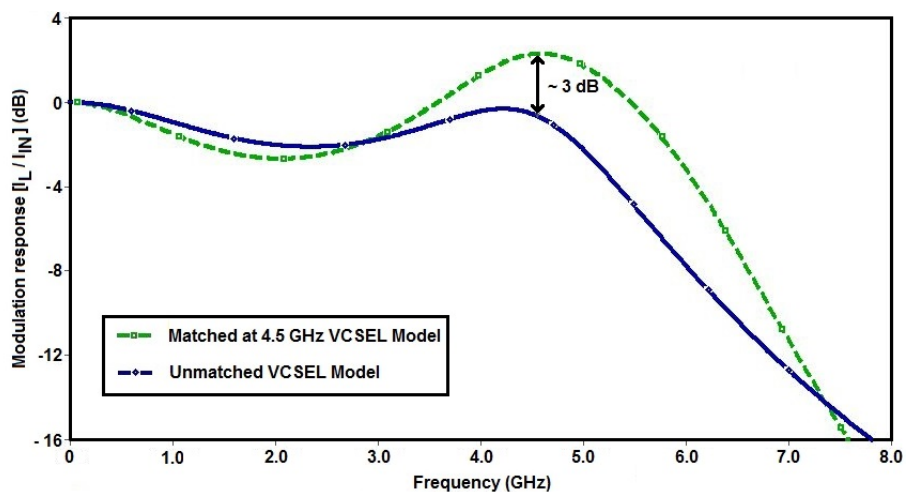


Figure 3-26: Improvement in modulation response of the proposed integrated VCSEL due to the inclusion of a matching network at 4.5 GHz.

3.6 Conclusion

In this chapter, an accurate intrinsic equivalent VCSEL model was proposed by using the VCSEL rate equation and taking into account the effect of the VCSEL Langevin noise sources. Different characteristics of the VCSEL were analysed by simulating the proposed intrinsic VCSEL model. These characteristics include: intrinsic VCSEL transient behaviour; direct modulation response; and small signal characteristics such as: input impedance ($Z(\omega)$); photon modulation transfer function ($H(\omega)$); junction voltage noise spectrum ($\overline{v_1^2}/\Delta f$); and the relative intensity noise ($RIN(\omega)/\Delta f$). Further to the optical characteristics of the VCSEL, the electrical aspect of the modelling such as electrical parasitics was also considered in the proposed VCSEL model, by including both parasitics arising from the VCSEL chip and packaging. Furthermore in this work, the effect of the matching network was also considered by including an L-matching network in the proposed integrated VCSEL model. It was observed from the simulation of the proposed integrated VCSEL model that inclusion of the matching network improves the direct modulation response by 3 dB.

On the other hand, due to the inherent practical limitations of the lumped-elements in high frequency regions, a distributed equivalent model of the proposed integrated VCSEL model was also developed in this work. The proposed distributed model of the VCSEL is designed based on the quasi-lumped method, where each element in the lumped-element model was replaced by a microstrip line with specific dimensions. The proposed distributed VCSEL model has an application for microwave signal generation, such as: harmonic generation by frequency switching, that has been reported in [10] for conventional lasers. However this is beyond the scope of this research and can be suggested as future work.

References

- [1] S. F. Yu, *Analysis and design of vertical cavity surface emitting lasers / S.F. Yu.* Hoboken, N.J.: Hoboken, N.J. : Wiley-Interscience, 2003.
- [2] J. M and Y. Jamro, *Optical Fiber Communications: Principles and Practice*, Third ed.: Financial Times/Prentice Hall, 2009.
- [3] T. Marozsak, A. Kovacs, E. Udvary, and T. Bercei, "Direct modulated lasers in radio over fiber applications," in *Microwave Photonics, 2002. International Topical Meeting on*, 2002, pp. 129-132.
- [4] C. Carlsson, H. Martinsson, R. Schatz, J. Halonen, and A. Larsson, "Analog modulation properties of oxide confined VCSELs at microwave frequencies," *Lightwave Technology, Journal of*, vol. 20, pp. 1740-1749, 2002.
- [5] J. Gao, "An Analytical Method to Determine Small-Signal Model Parameters for Vertical-Cavity Surface Emitting Lasers," *Lightwave Technology, Journal of*, vol. 28, pp. 1332-1337, 2010.
- [6] T. Marozsak, "Circuit model for multiple transverse mode vertical-cavity surface-emitting lasers," *Lightwave Technology, Journal of*, vol. 21, pp. 2977-2982, 2003.
- [7] H. E. Li and K. Iga, *Vertical-cavity surface-emitting laser devices / H.E. Li, K. Iga (eds.)*. London: London : Springer, 2003.
- [8] K. C. Sum and N. J. Gomes, "Integrated microwave-optoelectronic simulation of semiconductor laser transmitters," *Microwave and Optical Technology Letters*, vol. 14, pp. 313-315, 1997.

- [9] W. M. Wong and H. Ghafouri-Shiraz, "Integrated semiconductor laser-transmitter model for microwave-optoelectronic simulation based on transmission-line modelling," *Optoelectronics, IEE Proceedings* -, vol. 146, pp. 181-188, 1999.
- [10] W. M. WONG, "Microwave Circuit Models of Semiconductor Laser," Doctor of Philosophy Dynamic Modelling of Semiconductor Laser Devices using Microwave Circuit Techniques, Faculty of Engineering, University of Birmingham, Birmingham, 2001.
- [11] C. Harder, J. Katz, S. Margalit, J. Shacham, and A. Yariv, "Noise equivalent circuit of a semiconductor laser diode," *Quantum Electronics, IEEE Journal of*, vol. 18, pp. 333-337, 1982.
- [12] J. Katz, S. Margalit, C. Harder, D. Wilt, and A. Yariv, "The intrinsic electrical equivalent circuit of a laser diode," *Quantum Electronics, IEEE Journal of*, vol. 17, pp. 4-7, 1981.
- [13] R. Tucker, "High-speed modulation of semiconductor lasers," *Electron Devices, IEEE Transactions on*, vol. 32, pp. 2572-2584, 1985.
- [14] T. Asano, D. Feezell, R. Koda, M. H. M. Reddy, D. A. Buell, A. S. Huntington, E. Hall, S. Nakagawa, and L. A. Coldren, "InP-based all-epitaxial 1.3- μm VCSELs with selectively etched AlInAs apertures and Sb-based DBRs," *Photonics Technology Letters, IEEE*, vol. 15, pp. 1333-1335, 2003.
- [15] A. Bacou, A. Hayat, V. Iakovlev, A. Syrbu, A. Rissons, J. Mollier, and E. Kapon, "Electrical Modeling of Long-Wavelength VCSELs for Intrinsic Parameters Extraction," *Quantum Electronics, IEEE Journal of*, vol. 46, pp. 313-322, 2010.
- [16] C. W. Wilmsen, L. A. Coldren, and H. Temkin, *Vertical-cavity surface-emitting lasers : design, fabrication, characterization, and applications* Cambridge: Cambridge : Cambridge University Press, 1999.

- [17] A. Rissons and J. C. Mollier, *The Vertical-Cavity Surface Emitting Laser (VCSEL) and Electrical Access Contribution*: INTECH Open Access Publisher, 2011.
- [18] D. McCumber, "Intensity Fluctuations in the Output of cw Laser Oscillators. I," *Physical Review*, vol. 141, pp. 306-322, 1966.
- [19] J. Perchoux, A. Rissons, and J.-C. Mollier, "Multimode VCSEL model for wide frequency-range RIN simulation," *Optics Communications*, vol. 281, pp. 162-169, 2008.
- [20] D. M. Pozar, *Microwave Engineering*, 4th ed.: Wiley Global Education, 2011.
- [21] J. M Senior and Y. Jamro, *Optical Fiber Communications: Principles and Practice*: Financial Times/Prentice Hall, 2009.
- [22] X. Shi, C. Qi, G. Wang, and J. Hu, "Rate-equation-based VCSEL model and simulation," in *Computer-Aided Design and Computer Graphics, 2009. CAD/Graphics '09. 11th IEEE International Conference on*, 2009, pp. 503-507.
- [23] M. L. Majewski and D. Novak, "Method for characterization of intrinsic and extrinsic components of semiconductor laser diode circuit model," *Microwave and Guided Wave Letters, IEEE*, vol. 1, pp. 246-248, 1991.
- [24] P. A. Barnes and T. L. Paoli, "Derivative measurements of the current-voltage characteristics of double-heterostructure injection lasers," *Quantum Electronics, IEEE Journal of*, vol. 12, pp. 633-639, 1976.
- [25] A. Bacou, A. Hayat, A. Rissons, V. Iakovlev, A. Syrbu, J. Mollier, and E. Kapon, "VCSEL Intrinsic Response Extraction Using T -Matrix Formalism," *Photonics Technology Letters, IEEE*, vol. 21, pp. 957-959, 2009.
- [26] R. Tucker and D. Pope, "Microwave Circuit Models of Semiconductor Injection Lasers," *Microwave Theory and Techniques, IEEE Transactions on*, vol. 31, pp. 289-294, 1983.

- [27] A. J. Lowery and P. C. R. Gurney, "Comparison of optical processing techniques for optical microwave signal generation," *Microwave Theory and Techniques, IEEE Transactions on*, vol. 46, pp. 142-150, 1998.
- [28] P. Young, "MATCHING TECHNIQUES OPTIMIZE HIGH-SPEED LASER INTERFACES," *Microwaves & RF* vol. 33, 1994.
- [29] Mitsubishi Electric, *Optical semiconductor devices and optical-fiber communication systems*, 1992.
- [30] A. Ghiasi and A. Gopinath, "Novel wide-bandwidth matching technique for laser diodes," *Microwave Theory and Techniques, IEEE Transactions on*, vol. 38, pp. 673-675, 1990.
- [31] K. W. Ho and C. Shu, "Efficient gain switching of laser diodes with quarter-wave impedance transformer," *Electronics Letters*, vol. 29, pp. 1194-1195, 1993.
- [32] C. L. Goldsmith and B. Kanack, "Broad-band reactive matching of high-speed directly modulated laser diodes," *Microwave and Guided Wave Letters, IEEE*, vol. 3, pp. 336-338, 1993.
- [33] S. Maricot, J. P. Vilcot, D. Decoster, J. C. Renaud, D. Rondi, P. Hirtz, R. Blondeau, and B. de Cremoux, "Monolithic integration of optoelectronic devices with reactive matching networks for microwave applications," *Photonics Technology Letters, IEEE*, vol. 4, pp. 1248-1250, 1992.

4 NONLINEAR COMPOSITE RIGHT/LEFT HANDED (NL-CRLH) FREQUENCY DOUBLER LEAKY WAVE ANTENNA DESIGN

4.1 Introduction

Metamaterials are the general name given to the synthesised materials that cannot be found in nature. These materials exhibit electromagnetic properties that are not expected to be obtained in nature [1]. Metamaterials offer promising features specifically for radiating devices from low microwave frequency ranges to very high optical regions. These attractive features are due to the effectively homogenous structure of metamaterials that offers rather unusual concurrent negative permittivity (ϵ), permeability (μ) and therefore negative refractive index (n) [2, 3]. Left Handed (LH) materials, first introduced by Viktor Veselago, have simultaneous negative permittivity and permeability that cannot be seen in nature. Therefore LH materials are considered as metamaterials [4]. Caloz first brought together the idea of Composite Right/Left Handed (CRLH) which as the name suggests is the combination of conventional transmission line (RH-TL) and the artificial left handed

transmission line (LH-TL) [5, 6]. Depending on the driving frequency of the CRLH structure, it can exhibit both RH and LH properties. Conventional leaky wave antennas (LWA) are travelling wave structures capable of changing the direction of radiation by changing the operating frequency. The main drawback of conventional LWAs is that they are only capable of radiating in a forward direction and therefore they cannot scan from backfire to broadside without sophisticated biasing considerations [7]. CRLH based LWAs are capable of scanning at dominant mode from backfire to broadside when the frequency range is in the LH operating region and broadside to endfire when it's operating in the RH frequency region. If a balanced CRLH is used in the design of LWAs then the CRLH based LWA is capable of continuous backfire to endfire scanning. Replacing the LH capacitors with the varactor diodes will introduce the nonlinear effects into the CRLH that can lead to promising applications, such as subwavelength imaging, harmonic generation and soliton [2, 8, 9]. The wave propagation phenomena of the NL-CRLH transmission line were reviewed by Kozyrev in [10-12]. In this chapter novel integrated frequency doubler leaky-wave antenna design procedure based on nonlinear composite right/left handed (NL-CRLH) metamaterial is introduced. The novelty of this design includes the use of nonlinear elements in the CRLH structure and also the use of the quasi-lumped approach in designing the distributed structure. The limitation of Computer Aided Design (CAD) software means that the analysis of distributed nonlinear circuits cannot be conveniently combined with the advanced EM simulations, in order to produce radiation patterns at the harmonic frequencies which are generated within the nonlinear structure, when the structure is excited at the fundamental. Therefore the radiation patterns of the linear CRLH leaky wave antenna have been studied in this work which verifies backward to forward radiation from the left-handed region to the right handed region. Further in Chapter 5, a novel method of combining EM analysis and

harmonic balance simulation has been performed; which can be used to analyse the EM features of the nonlinear CRLH LWA designed in this chapter.

4.2 Proposed NL-CRLH leaky wave antenna specification and overview

To design the NL-CRLH leaky wave antenna, first the linear CRLH was designed with the specifications given in Table 4-1. The initial aim of this work was to be used in the millimetre wavelength region, where the harmonic frequency generation is of great interest since it is difficult to generate fundamental sources. The design involves the quasi-lumped element approach for designing the distributed structure. The required EM simulation is complex because of the need to analyse radiation patterns of the second harmonic generated within the structure. The approach required for this is developed in the next chapter. The work in this chapter is about proving the nonlinear CRLH antenna design technique in the low frequency region. The design of the Terahertz frequency doubler nonlinear CRLH can be suggested as further work. The number of unit cells (N) in Table 4-1, were selected as the minimum number needed to generate the reasonable radiation pattern and yet minimise the complexity of the design. In this work a substrate with rather low dielectric constant is used, as can be seen in Table 4-1; this is due to two important factors: first as the initial aim of the design was to scale up the operating frequency to the terahertz frequency region, a high relative permittivity is not desirable as it makes the structure very tiny. Secondly, a substrate with high relative permittivity increases the mismatch between the radiating element and free space, which makes the achievement of the required array properties rather challenging. To guarantee a seamless radiation and beam scanning in the transition from the left-handed to the right-handed region the balanced CRLH is used in the design of the NL-CRLH based leaky

wave antenna. After designing the CRLH in order to implement the nonlinearity to the designed structure, the appropriate varactor diode was selected. The varactor replaced the LH capacitor in order to design the NL-CRLH. In the next step, to design the distributed NL-CRLH leaky wave structure, the lumped elements in the designed circuit were replaced using the short stub, open stub and microstrip line model counterparts and the quasi-lumped element approach. The physical dimensions of the designed CRLH based leaky wave antenna have been calculated in AWR Microwave Office. Then the designed structure was remodelled in CST to analyse the radiation pattern and the beam scanning features of the designed CRLH based leaky wave antenna. At this point the limitation of the simulation software prevents the advanced EM analysis of the designed frequency doubler NL-CRLH based leaky wave antennas at the second harmonic frequency. Therefore a novel method of combining harmonic balance and EM analysis is proposed; it is described in detail in Chapter 5.

Table 4-1: Composite right/left handed design specifications.

Parameters	Value	Description
f_L	1 GHz	Left handed cut-off frequency
f_R	5 GHz	Right handed cut-off frequency
f_0	2.2 GHz	Transition frequency
N	6	Number of unit cell
Z_0	50 Ω	Line impedance
t	1.5 mm	Substrate's thickness
ϵ_r	2.2	Relative permittivity of the substrate

4.3 CRLH design and simulation

In this section, the designed CRLH is briefly investigated by reviewing the required CRLH parameter calculations. The simulation results are then analysed to ensure that the required performance set in Table 4-1 was met in the designed CRLH structure.

4.3.1 CRLH design procedure

As the CRLH structures described earlier in Chapter 2 suggest, in order to design 1-D CRLH, first the values of the series elements such as: left-handed capacitor and right-handed inductor; and also shunt elements such as: left-handed inductor and right-handed capacitor, have to be calculated. Figure 4-1 shows the lumped element circuit level model of the CRLH.

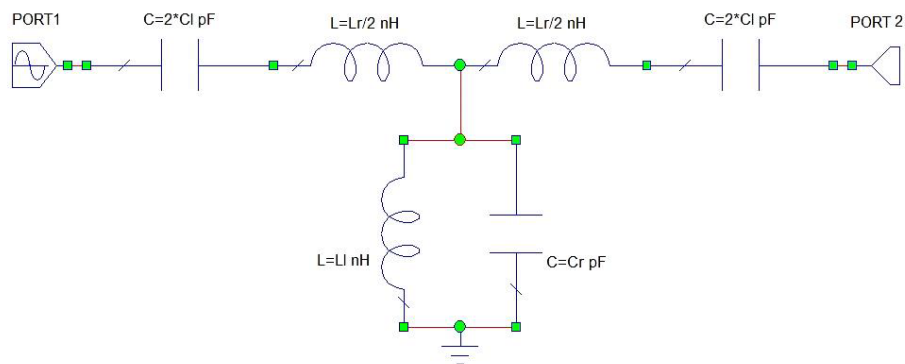


Figure 4-1: Circuit level structure of symmetric 1-D CRLH unit cell.

In order to find the four unknown elements of the CRLH structure (C_l , L_l , C_r , L_r), a system of four equations and four unknowns have to be solved. The four equations of this system are described as follows.

The balanced CRLH structure is designed in this work. Therefore to have a balanced structure, the condition in Equation 4-1 has to be satisfied. The resonant frequency of the

series (ω_{se}) and shunt (ω_{sh}) elements can be found using Equations 4-2 and 4-3. Substituting 4-2 and 4-3 in 4-1 generates the first equation used to solve the system of unknowns.

$$\omega_{se} = \omega_{sh} \quad 4-1$$

$$\omega_{se} = \frac{1}{\sqrt{C_l L_r}} \quad 4-2$$

$$\omega_{sh} = \frac{1}{\sqrt{C_r L_l}} \quad 4-3$$

The transient frequency (ω_0) of the CRLH can be calculated from Equation 4-4 [13]. Using the condition of the balanced CRLH in Equation 4-1 and replacing the resonant frequency of the series and shunt elements defined by 4-2 and 4-3 into Equation 4-4, generates the second equation needed to find the parameters of the balanced CRLH.

$$\omega_0 = \frac{1}{\sqrt[4]{C_l L_l C_r L_r}} \quad 4-4$$

$$\omega_0 = \frac{1}{\sqrt[4]{C_l L_l C_r L_r}} = \sqrt{\omega_{se} \omega_{sh}} = \omega_{se} = \omega_{sh} \quad 4-5$$

The matching condition of the CRLH structure can be found in Equation 4-6 [2]; where Z_L and Z_R are the purely left-handed and purely right-handed impedances respectively. Equations 4-7 and 4-8 can be used to calculate Z_L and Z_R . Replacing Equations 4-7 and 4-8 in 4-6 will generate the third equation needed to solve the system of unknowns.

$$Z_0 = Z_L = Z_R \quad 4-6$$

$$Z_R = \sqrt{\frac{L_r}{C_r}} = Z_0 \quad 4-7$$

$$Z_L = \sqrt{\frac{L_l}{C_l}} = Z_0 \quad 4-8$$

The last equation used to find the parameters of the CRLH is found using the bandwidth of the structure which extends from the left-handed cut-off frequency (ω_{cL}) to the right-handed cut-off frequency (ω_{cR}). The left and right handed cut-off frequencies can be found using Equations 4-9 and 4-10 respectively[2].

$$\omega_{cL} = \omega_R \left| 1 - \sqrt{1 + \frac{\omega_L}{\omega_R}} \right| \quad 4-9$$

$$\omega_{cR} = \omega_R \left(1 + \sqrt{1 + \frac{\omega_L}{\omega_R}} \right) \quad 4-10$$

Where ω_R and ω_L in Equations 4-9 and 4-10 are the resonance frequencies of the pure right handed and left handed structure. These two resonance frequencies were defined as seen below [2].

$$\omega_R = \frac{1}{\sqrt{L_r C_r}} \quad 4-11$$

$$\omega_L = \frac{1}{\sqrt{L_l C_l}} \quad 4-12$$

Equations 4-1 to 4-12 have been used to find the unknown variables C_l, L_l, C_r, L_r . The calculated values for the designed CRLH structure can be seen in Table 4-2.

Table 4-2: Circuit level parameters of the designed balanced CRLH.

Parameter	Value	Description
C_l	1.27 pF	Left-handed capacitor.
L_l	3.18 nH	Left-handed inductor.
C_r	1.59 pF	Right-handed capacitor.
L_r	3.98 nH	Right-handed inductor.

4.3.2 CRLH result analysis

The designed CRLH structure with the parameters calculated above was simulated using AWR Microwave Office software. To make sure that the designed structure performs as a CRLH, the dispersion diagram of the designed structure was generated by using the S-parameters of the simulated structure. S-parameters are the elements of a matrix which represents a network in terms of the linear relationships between normalised input and output voltage waves. An alternative representation such as the ABCD matrix can be used, based on terminal voltages and currents. Using the conversion equations from S-parameters to ABCD parameters for a transmission line section [14], the dispersion relation in Equation 4-13 can be derived. The dispersion diagram of the designed CRLH can be seen in Figure 4-2. Equation 4-13 was used to calculate the dispersion diagram from the S-parameters of the simulated structure [15, 16]. In this equation, p represents the length of the CRLH unit cell. It can be seen in Figure 4-2 that the structure has a left-handed characteristic from 1 GHz to the transient frequency at 2.23 GHz, then the CRLH structure has a right-handed characteristic up to the cut-off frequency at 5 GHz.

$$\beta = \frac{1}{p} \cos^{-1} \left(\frac{1 - S_{11}S_{22} + S_{12}S_{21}}{2S_{21}} \right) \quad 4-13$$

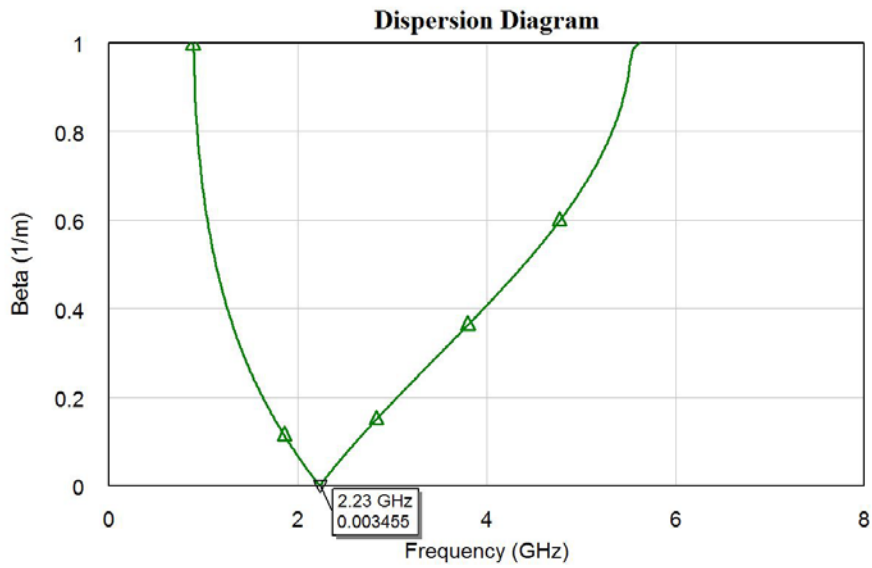


Figure 4-2: Dispersion diagram for the designed CRLH unit cell structure.

In order to confirm that the designed CRLH unit cell satisfies the bandwidth requirements set in Table 4-1, the return loss ($S_{1,1}$) of this structure is reviewed as seen in Figure 4-3. The simulated results verify that the designed structure of Figure 4-1 has a 10 dB bandwidth between 1 GHz to 4 GHz.

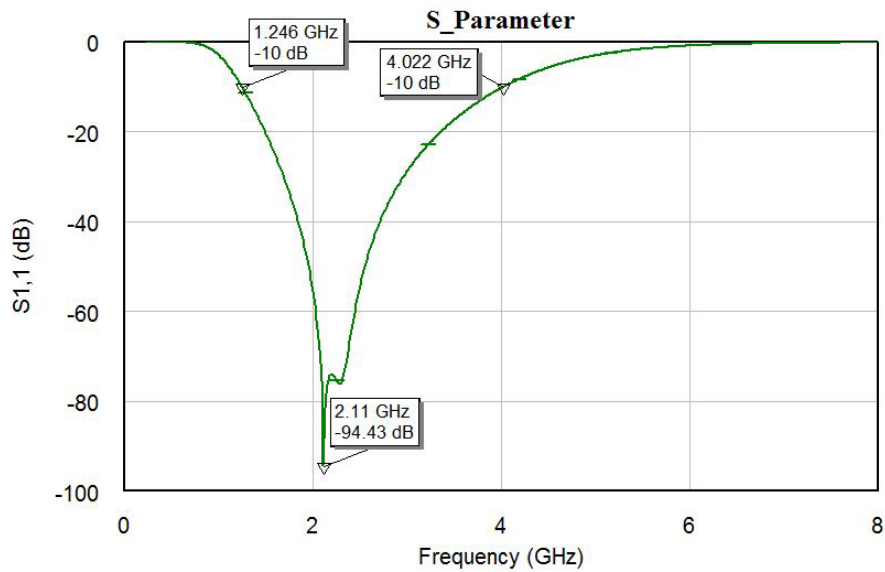


Figure 4-3: Return loss ($S_{1,1}$) diagram for designed CRLH unit cell.

4.4 Nonlinear CRLH design and simulation

In this section the design of the nonlinear CRLH (NL-CRLH) was studied by reviewing the selection of appropriate varactor diodes to induce the nonlinear effects within the designed CRLH structure. Further in this section the performance of the designed NL-CRLH structure was analysed by simulating the dispersion diagram and the power level of harmonics generated within the structure.

4.4.1 Nonlinear CRLH design procedure

The nonlinear effect which includes frequency doubling was added to the designed CRLH structure of Figure 4-1 by replacing the series (left-handed) capacitor with the varactor diode. In order to find the appropriate diode, the operating capacitance and frequency range of the varactor have to be taken into account. In this design, the Skyworks SMV1430 silicon abrupt

junction varactor was used. The appropriate reverse biasing voltage for this varactor diode was selected to make the varactor capacitance equal to that of the capacitor it was replacing. This is done by looking at the C-V characteristics of the varactor diode. The above information for the selected varactor diode can be found in its data sheet that is included in the appendix. The SPICE model for the selected varactor can be seen in Figure 4-4. The SPICE model in Figure 4-4 replaced the series capacitors in the CRLH structure to form the NL-CRLH structure that can be seen in Figure 4-5.

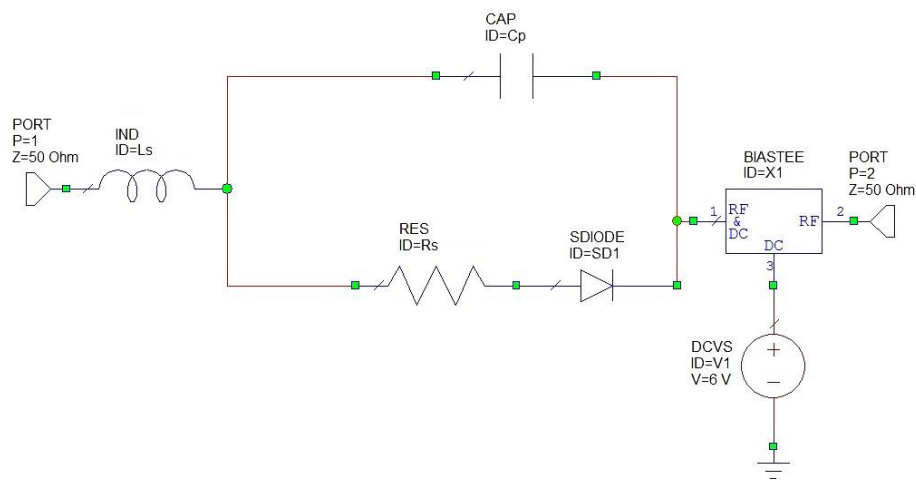


Figure 4-4: SPICE model for varactor diode.

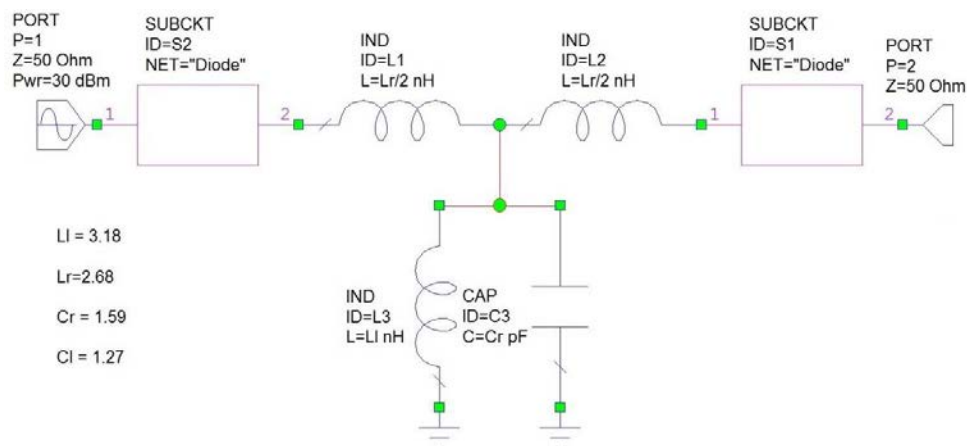


Figure 4-5: Circuit level structure of symmetric 1-D nonlinear CRLH unit cell.

4.4.2 NL-CRLH result analysis

In order to make sure that the new circuit model of Figure 4-5 still acts as a CRLH metamaterial, the dispersion diagram of the structure was simulated and compared with the dispersion diagram of the linear CRLH design. Figure 4-6 indicates that the designed structure in Figure 4-5 is the CRLH structure with exactly the same transient frequency as the linear CRLH structure. Figure 4-6 also indicates that the NL-CRLH structure has a wider bandwidth, extending from 0.9 GHz to 5.6 GHz. This increase in bandwidth of the dispersion diagram is due to the inductor and capacitor which are included in the SPICE model of the varactor structure (Figure 4-4) but they are not part of the linear CRLH model (Figure 4-1). It should be noted that in the varactor model in Figure 4-4, the diode bias (-6 V) is introduced via an ideal bias tee. In a real practical implementation, the bias needs to be introduced using a network of inductors and capacitors, and the second order effects of these on the RF performance would need to be taken into account in the modelling.

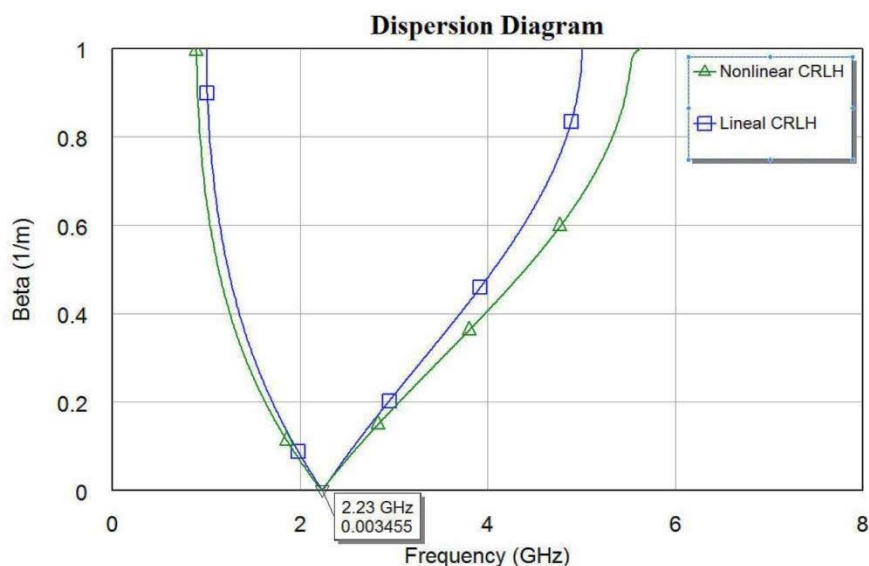


Figure 4-6: Comparison between linear and nonlinear CRLH unit cell dispersion diagram.

The inclusion of nonlinear elements in the CRLH structure results in the generation of the harmonics of the fundamental frequency with which the circuit is fed. In this research the generated second harmonic frequency will be used to excite the leaky wave antenna. Figure 4-7 indicates the power of different harmonics in the designed NL-CRLH structure. It can be seen in Figure 4-7 that the NL-CRLH structure has been fed with the fundamental frequency of 1.1 GHz with 30 dBm power; which results in the generation of the second harmonic with 19.2 dBm power that indicates good conversion efficiency at this harmonic.

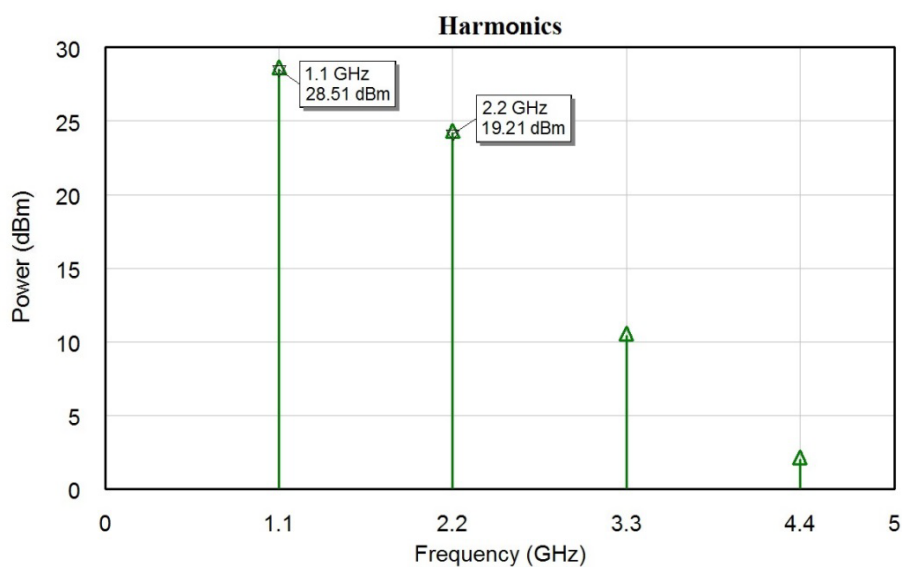


Figure 4-7: Harmonics generated in NL-CRLH unit cell structure.

4.5 Distributed NL-CRLH leaky wave antenna model

In this section, first the procedure to convert the lumped element model to the distributed structure is reviewed. The designed distributed model is then simulated to ensure the required performance is met. Finally the radiation pattern of the cascaded CRLH-LWA was analysed by confirming its leaky wave antenna properties.

4.5.1 Distributed NL-CRLH model design procedure

In order to study the EM characteristics of the designed NL-CRLH structure, such as the radiation pattern, the designed lumped element model was converted to the distributed model. To convert the lumped element model to the distributed model, the quasi-lumped element design method was used. In this method, shunt capacitors are replaced by wide microstrip lines ($w > l$), series inductors with rather long microstrip lines ($l > w$), series capacitor and shunt inductor with open and short stubs respectively. In order to calculate the dimensions of these microstrip lines, the impedance (Z_0) of each microstrip line was estimated. Using the estimated impedance the length and width of the microstrip lines were calculated. Equations 3-37 and 3-34 in Chapter 3 were used to calculate the length of the series inductor and shunt capacitor (l_{SInd}, l_{ShCap}) and Equations 3-35 and 4-14 were used to calculate the length of the shunt inductor and series capacitors (l_{Ind}, l_{Scap}). The widths of the microstrips (w) were calculated using Equation 3-36. The calculation of the microstrip lines' dimensions is an iterative process; since having deep changes in the width of adjacent elements generates unwanted parasitic capacitance and therefore should be avoided. Thus sometimes the process has to be repeated with different values of the microstrip's characteristic impedance, to ensure a smooth transaction between adjacent elements.

$$l_{Scap} = \frac{\lambda_g}{2\pi} \tan^{-1}(Z_0 \omega C) \quad 4-14$$

The distributed schematic of the designed NL-CRLH leaky wave antenna can be seen in Figure 4-8. In order to calculate a suitable length and width, a MATLAB program was written which is able to iterate the value of the microstrip characteristic impedance (Z_0) to find the optimum dimension of the microstrip lines. Good agreement has been achieved in

$S_{1,1}$ and the dispersion diagram, after tuning the dimensions of the microstrip lines obtained from the equations above. The return loss ($S_{1,1}$) and dispersion diagram are shown in Figures 4-9 and 4-10 respectively. The dimensions of the microstrip lines used in the simulations are summarised in Table 4-3.

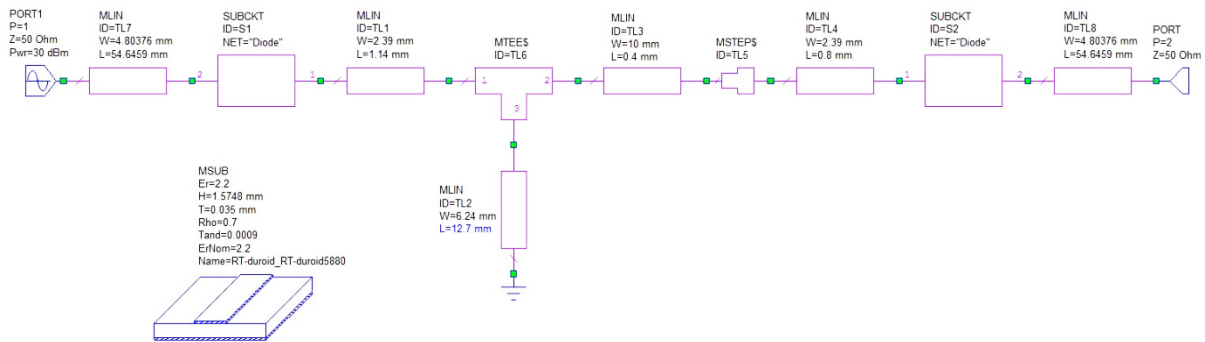


Figure 4-8: Distributed NL-CRLH unit cell schematic.

4.5.2 NL-CRLH distributed model results' analysis

In order to confirm that the designed distributed model is still a CRLH structure and satisfies the specifications set in Table 4-1, the $S_{1,1}$ parameters of the linear CRLH, NL-CRLH and distributed NL-CRLH were compared in Figure 4-9. It is observed from Figure 4-9 that the bandwidth and the minimum depth of the $S_{1,1}$ figure has slightly changed from linear CRLH to NL-CRLH and the distributed model, but still the designed structure satisfies the requirements of Table 4-1.

Table 4-3: Distributed model's dimensions.

Lumped Element Name	Width	Length
Varactor to 50 Ω Port connector	4.80 mm	54.64 mm
L_r	2.39 mm	1.14 mm
L_l	6.24 mm	12.7 mm
C_r	10 mm	0.4 mm

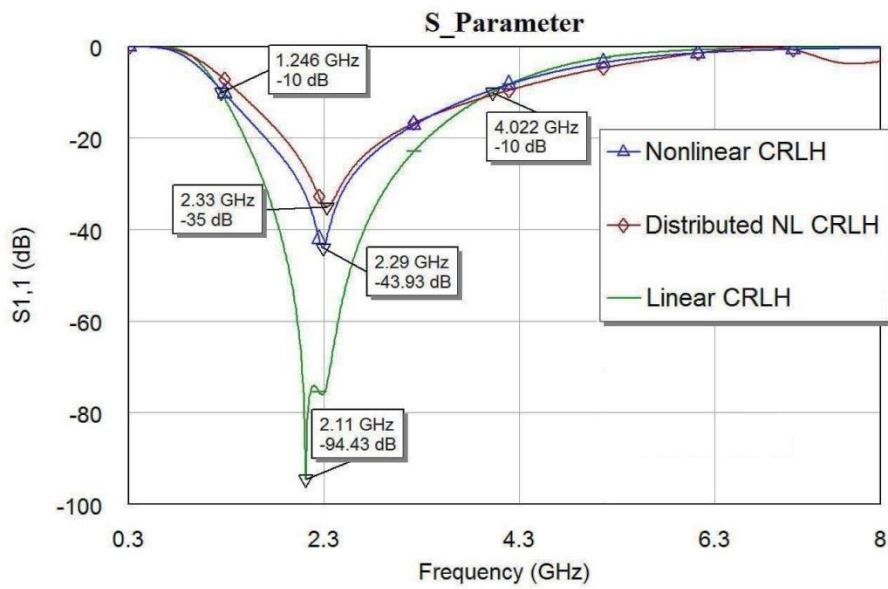


Figure 4-9: The comparison between $S_{1,1}$ figure of linear, nonlinear and nonlinear distributed CRLH.

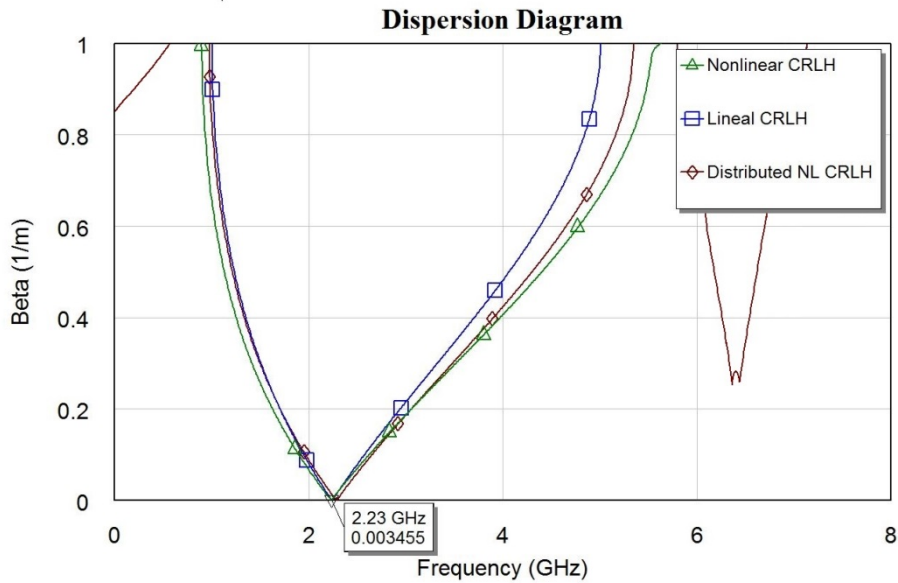


Figure 4-10: Comparison between the dispersion diagram of the CRLH, NL-CRLH and distributed NL-CRLH.

The dispersion diagram of the distributed model is compared with that of the CRLH and NL-CRLH structures, as shown in Figure 4-10. In this figure, the distributed NL-CRLH indicates both right-handed and left-handed regions and has the transient frequency slightly moved from 2.3 GHz to 2.35 GHz; this is still in acceptable proximity to the required specification in Table 4-1. Figure 4-11 indicates the layout representation of the distributed NL-CRLH leaky wave antenna structure (Figure 4-8).

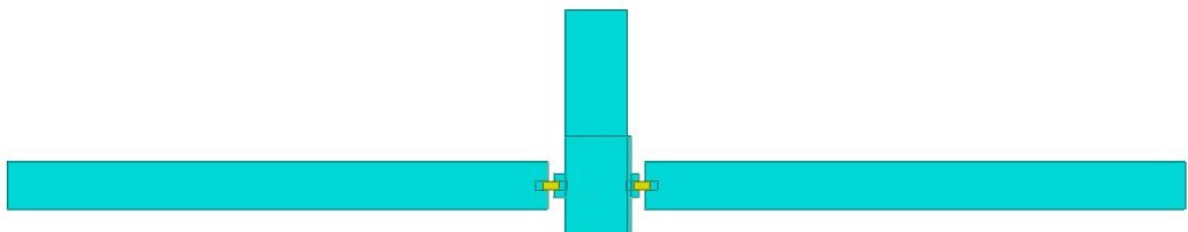


Figure 4-11: The designed nonlinear CRLH leaky wave antenna layout.

4.5.3 EM analysis of CRLH leaky wave antenna

In order to perform full wave EM simulation on the designed frequency doubler nonlinear CRLH leaky wave unit cell structure, the structure should be simulated with the second harmonics being generated by the varactor diode within the design. Unfortunately due to computational limitations, current CAD software is unable to perform all these analyses. Therefore to analyse the EM features of the leaky wave antenna in this work the designed structure has been changed to a linear CRLH leaky wave antenna, by replacing the varactor diodes with the corresponding capacitors, as outlined in section 4.3.1. Figure 4-12 indicates the designed CRLH leaky wave antenna in CST Design Studio. The design in this figure is reconstructed using the dimensions of the distributed NL-CRLH model in Figure 4-8. The blue parts in Figure 4-12 represent the lumped capacitors of the balanced CRLH which replaced the varactors of the NL-CRLH and its values are listed in Table 4-2.

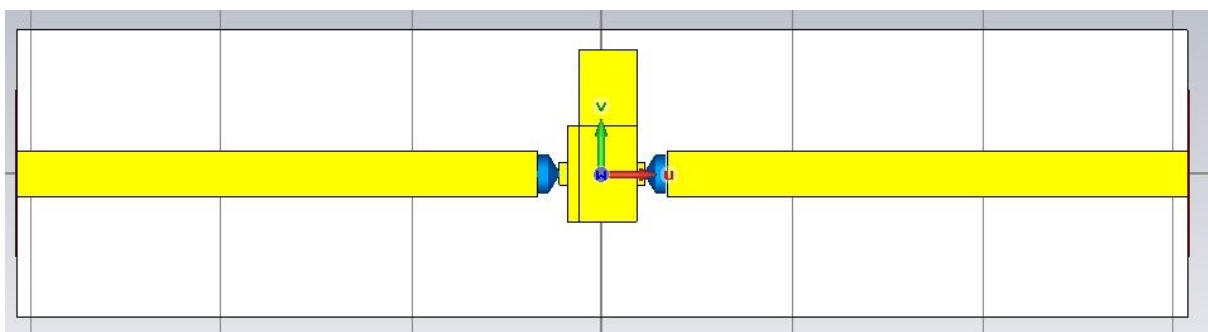


Figure 4-12: CRLH leaky wave antenna distributed model in CST.

To confirm that the modelled structure satisfies the requirements which have been set up in Table 4-1, the transmission line parameters and the dispersion diagram of this model were

investigated in Figures 4-13 and 4-14. It is observed that the $S_{1,1}$ results in Figure 4-13 did not match the circuit simulation results in Figure 4-9; since the maximum depth and the bandwidth have been slightly changed. These changes in the bandwidth and the maximum depth are due to parasitic resonance, coupling and fringing effects that were not included in the circuit simulations in previous sections.

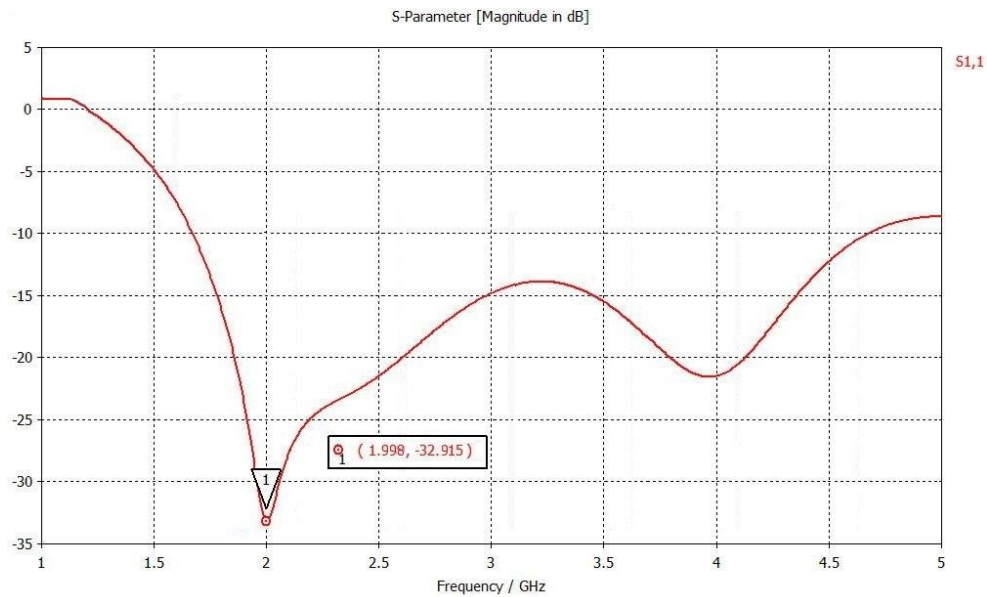


Figure 4-13: CST Studio Design $S_{1,1}$ result for the CRLH leaky wave antenna.

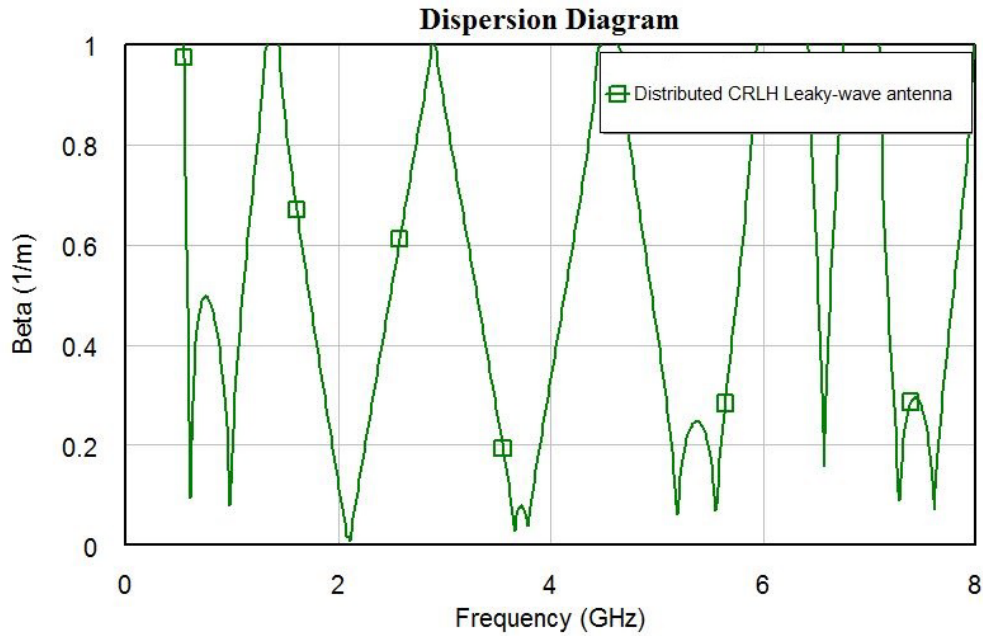


Figure 4-14: Dispersion diagram for the distributed CRLH leaky wave antenna calculated using CST's $S_{1,1}$ results.

It is observed, from the dispersion diagram in Figure 4-14 that both right-handed and left-handed regions are present in the diagram and the distributed CRLH leaky wave antenna has the transient frequency (f_0) of 2.21 GHz. Therefore the CST model of the distributed CRLH leaky wave antenna has CRLH behaviour. It can also be observed in Figure 4-14 that the dispersion diagram shows its periodic nature; whereas in the lumped element model, the dispersion diagram was not periodic. This is due to the periodic nature of the transmission line based designs.

4.5.4 Radiation pattern analysis

In order to complete the design of the CRLH leaky wave antenna, six CRLH unit cells were cascaded together to finalise the model. Since in leaky wave antennas directivity is proportional to radiation area and therefore to the total length ($N \times P$) of the designed structure; N in this case is the number of the unit cell and P is the length of each unit cell. Increasing the number of the unit cell (N), aggregates the physical length of the structure and therefore the directivity increases. After almost all the input power has leaked out, further increases in the length of the structure will not increase the directivity. In this design only six cascaded unit cells have been considered, which resulted in a good directivity of the overall structure. The designed cascaded CRLH leaky wave antenna is shown in Figure 4-15.

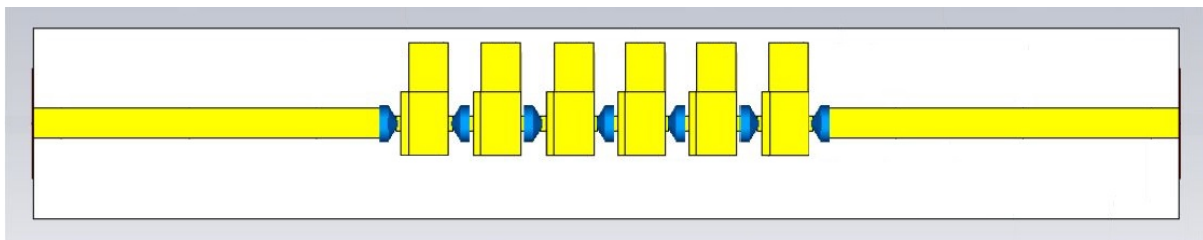


Figure 4-15: Cascaded CRLH leaky wave antenna ($N = 6$).

As described earlier, using the CRLH metamaterial in the design of the leaky wave antenna enables continuous beam scanning by changing the frequency from the left-handed region to the right handed region. The backward to forward beam scanning of the structure in Figure 4-15 has been illustrated in Figure 4-16 (A) to (D) by setting the frequency to 1.8 GHz, 1.9 GHz, 2.0 GHz and 2.2 GHz respectively. The radiation patterns in Figure 4-

16 were simulated from one waveguide port CRLH based leaky wave antenna structure of Figure 4-15, when excited with the Gaussian signal.

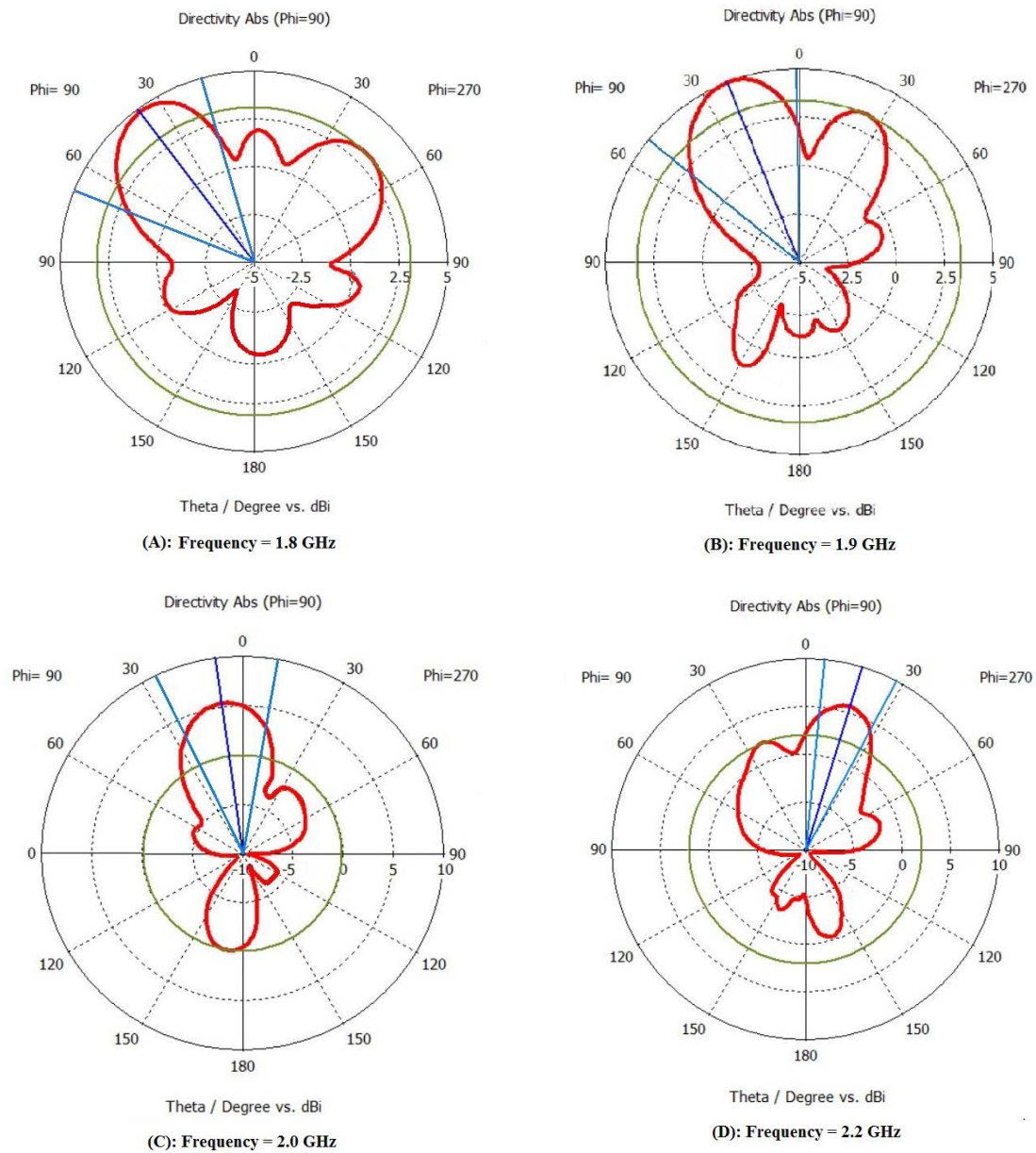


Figure 4-16: Polar representation of CRLH leaky wave antenna's radiation pattern for four different frequencies. (Note that there are different dBi scales between backward radiation sections A, B and the forward radiation sections C and D, in order to display the full detail of each plot).

It is seen in Figure 4-16 that as the frequency increases from the left-handed frequency region in part (A) to the right-handed region in part (D), the direction of the main radiation lobe varies from backward radiation in part (A) and (B) with main lobe direction of -37° and -21° respectively, to near broadside radiation at 2 GHz in part (C), with the main lobe direction of -7° and finally to forward radiation with the main lobe direction of 20° at 2.2 GHz.

4.6 Conclusion

In this chapter, the design procedure of the linear and nonlinear CRLH structure was described. The originality of this work is in the use of nonlinear CRLH, by replacing the left-handed capacitor with the varactor diode and using the quasi-lumped approach to design the distributed structure. The use of the quasi-lumped approach in this work resulted in a simple physical structure. In this work nonlinear analysis was performed using the circuit simulator to establish that the harmonic generation would occur. To establish the basic essential radiation properties, EM simulation was then applied to the linear version of the structure using an EM simulator by exciting the input port at the harmonic frequency. The radiation pattern analysis in this work indicates that the designed cascaded CRLH leaky wave antenna has relatively good directivity (6 dBi). Finally the analysis of the radiation patterns reveals that the designed structure is able to perform the backward to forward beam scanning by changing the operating frequency from the left-handed to the right-handed frequency region, without using the sophisticated biasing circuit needed when designing a conventional leaky wave antenna. The limitation of this work is that injecting the harmonic frequencies at the input port may result in different radiation properties from injecting the harmonic currents at

the point in the nonlinear structure at which the harmonic currents are generated. In the next chapter of this thesis, a novel method of injecting harmonic currents generated within the nonlinear structure has been developed, in order to analyse the EM properties of the nonlinear structures at harmonic frequencies when excited with the fundamental frequency.

References

- [1] D. Yuandan and T. Itoh, "Metamaterial-Based Antennas," *Proceedings of the IEEE*, vol. 100, pp. 2271-2285, 2012.
- [2] C. Caloz and T. Itoh, *Electromagnetic Metamaterials: Transmission Line Theory and Microwave Applications*: Wiley, 2006.
- [3] C. Caloz, T. Itoh, and A. Rennings, "CRLH metamaterial leaky-wave and resonant antennas," *Antennas and Propagation Magazine, IEEE*, vol. 50, pp. 25-39, 2008.
- [4] V. G. Veselago, "The Electrodynamics of Substances with Simultaneously Negative Values of ϵ and μ ," *Soviet Physics Uspekhi*, vol. 10 (4), pp. 509–514, 1968.
- [5] C. Caloz and T. Itoh, "Novel microwave devices and structures based on the transmission line approach of meta-materials," in *Microwave Symposium Digest, 2003 IEEE MTT-S International*, 2003, pp. 195-198 vol.1.
- [6] A. Lai, T. Itoh, and C. Caloz, "Composite right/left-handed transmission line metamaterials," *Microwave Magazine, IEEE*, vol. 5, pp. 34-50, 2004.
- [7] L. Liu, C. Caloz, and T. Itoh. (2002, Dominant mode leaky-wave antenna with backfire-to-endfire scanning capability. *Electronics Letters* 38(23), 1414-1416. Available: http://digital-library.theiet.org/content/journals/10.1049/el_20020977
- [8] S. Deng, X. Han, X. Qin, and S. Huang, "Subsurface crack propagation under rolling contact fatigue in bearing ring," *Science China Technological Sciences*, vol. 56, pp. 2422-2432, 2013/10/01 2013.
- [9] Z. Wang, Y. Feng, B. Zhu, J. Zhao, and T. Jiang, "Dark Schrödinger solitons and harmonic generation in left-handed nonlinear transmission line," *Journal of Applied Physics*, vol. 107, pp. -, 2010.

- [10] A. M. Belyantsev and A. B. Kozyrev, "RF oscillation generated by an electromagnetic shock wave in coupled transmission lines with anomalous and normal dispersion," *Technical Physics*, vol. 46, pp. 864-867, 2001/07/01 2001.
- [11] A. B. Kozyrev, "The structure of a shock electromagnetic wave synchronous with several waves propagating in coupled transmission lines with different types of dispersion," *Technical Physics*, vol. 47, pp. 272-274, 2002/02/01 2002.
- [12] A. M. Belyantsev and A. B. Kozyrev, "Reversed Doppler effect under reflection from a shock electromagnetic wave," *Technical Physics*, vol. 47, pp. 1477-1480, 2002/11/01 2002.
- [13] C.-H. Lee, J. Lee, D.-S. Woo, and K.-W. Kim, "Design of a composite right/left-handed transmission line unit-cell for a U-shaped mushroom ZOR antenna based on left-handed metamaterials," *Journal of the Korean Physical Society*, vol. 61, pp. 1633-1635, 2012/11/01 2012.
- [14] D. M. Pozar, *Microwave Engineering*, 4th ed.: Wiley Global Education, 2011.
- [15] H. X. Xu, G. M. Wang, M. Q. Qi, and Z. M. Xu, "Theoretical and experimental study of the backward-wave radiation using resonant-type metamaterial transmission lines," *Journal of Applied Physics*, vol. 112, pp. -, 2012.
- [16] J. G. Park and C. Y. Kim, "Analysis and design of the CRLH SICL unit cell using effective parameters," *IEICE Electronics Express*, vol. 11, pp. 20131000-20131000, 2014.

5 COMBINING HARMONIC BALANCE AND EM ANALYSIS FOR DESIGN AND OPTIMISATION OF NONLINEAR ACTIVE ANTENNAS

5.1 Introduction

Harmonic balance simulation is an efficient, flexible and yet accurate method for steady state analysis of both linear and nonlinear microwave circuits. Harmonic balance uses a mixed domain technique for calculating a steady state solution of a nonlinear circuit by dividing the circuit into linear and nonlinear subsections. The linear section is analysed using the frequency domain analysis; whereas the nonlinear subsection is analysed in time domain and the result is converted to frequency domain using a Fourier transform [1] by an iterative process, a self-consistent set of complex currents at all of the harmonic frequencies is arrived at. There is plenty of Computer Aided Design (CAD) software capable of harmonic balance simulation. The problem to which the harmonic balance application proposed in this work responds is the use of advanced EM simulation features in linear parts, including the antenna

radiation pattern at harmonic frequency. A novel approach is proposed in this chapter which enables harmonic balance simulation on microwave circuits of different structures to be combined with full electromagnetic simulators. Thus the full EM simulation features of packages widely used for antenna design, such as CST STUDIO SUITE and High Frequency Structural Simulator (HFSS) can be combined with high performance circuit simulators such as Microwave Office and the Advanced Design System (ADS).

5.2 Proposed harmonic balance simulation

In the proposed harmonic balance simulation technique first the microwave circuit is divided into the linear and nonlinear sections. The linear section is designed and simulated using the EM simulation features of CST STUDIO SUITE, in order to find the S-parameters of the linear parts in the frequency range that includes the harmonic used further in the simulation. The generated S-parameters are then imported into the AWR Design Environment and combined with the nonlinear section to build up the original circuit. This schematic is then simulated to generate the harmonics of the fundamental frequency. These harmonics are generated due to the existence of nonlinear parts in the circuit. The circuit is then analysed to find the voltage and current at the intersection points of the nonlinear and linear parts. The calculated complex current and voltage is recorded, in order to be reintroduced to the linear parts in CST to perform full wave analyses on the complex microwave circuit. The proposed algorithm integrates two very accurate and comprehensive pieces of simulation software that allow the users to perform the harmonic balance simulation on a variety of circuit structures, including active and passive elements and periodic structures. Figure 5.1 visualises the proposed harmonic balance simulation technique.

In order to clarify the proposed method, a 3 GHz frequency tripler patch antenna has been designed and analysed to serve as an example of this technique. This example has been used to demonstrate the proposed harmonic balance simulation technique and therefore a relatively low frequency basic microwave structure has been selected. The proposed technique is also capable of analysing more complex and higher frequency microwave structures. In this example first a patch antenna has been designed to radiate at 3 GHz. The patch is fed with a 1 GHz signal by the inset feed line. This signal travels through the antenna to reach the patch's second port which is connected to the Schottky diode. The properly biased Schottky diode is then excited to generate the third harmonic that is fed back to the patch antenna. The generated 3 GHz signal excited the antenna and produced the radiation. The design and simulation of the 3 GHz frequency tripler patch antenna is described in detail in the following sections. Further in this chapter, the proposed harmonic balance simulation technique was used to investigate the radiation pattern and frequency scanning feature of a unit cell of the NL-CRLH frequency doubler LWA developed earlier in chapter 4.

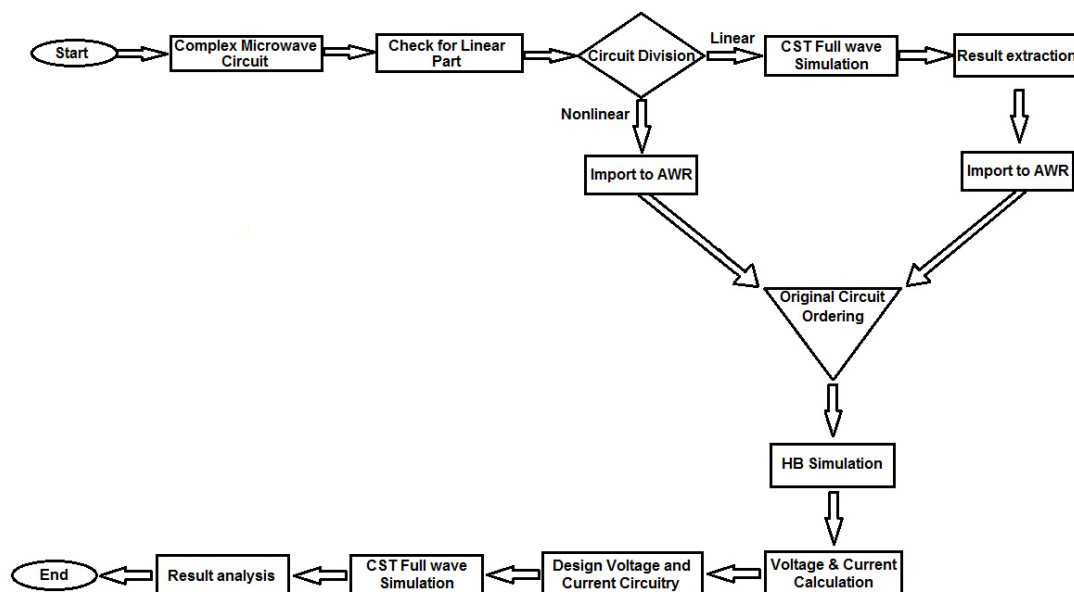


Figure 5-1: Proposed harmonic balance simulation technique.

5.3 Patch antenna design and simulation

In this section, the designed patch antenna is briefly investigated by reviewing the required patch antenna specifications. The patch antenna is designed by following the design procedure reviewed in section 2.7.2. The simulation results are reviewed to make sure the required performance of the patch antenna has been met. The parameters of the patch antenna designed in this work are shown in Figure 5-2.

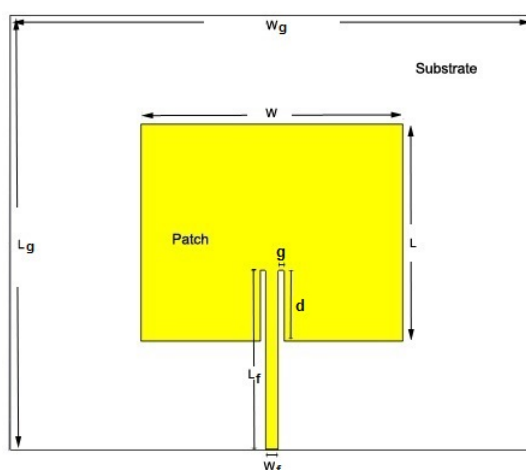


Figure 5-2: Geometry of microstrip patch antenna with inset feed.

5.3.1 Patch antenna specifications

In order to start designing the patch antenna, first a suitable substrate needs to be selected. To find the suitable substrate special attention needs to be paid to the following parameters:

- **Substrate Dielectric Constant (ϵ_r):** a higher dielectric constant would normally result in a smaller resonant structure but at the same time lower the antenna gain.

On the other hand a smaller dielectric constant will result in higher fringing effect and therefore higher antenna gain but a bigger resonant structure [2].

- **Substrate Height (h):** using a thicker substrate results in the increase of the input impedance bandwidth, radiated power and at the same time reduces the resonator loss [2].
- **Frequency of Radiation (f_0):** when selecting the substrate, the radiating frequency of the antenna must be considered to be within the effective frequency range of the substrate.

In this design RT Duroid 5880 is used as a substrate. This is selected due to its low dissipation factor, constant and fairly low dielectric constant over the wide range of frequency and also its ease of shape and cut. This substrate has the relative permittivity $\epsilon_r = 2.2$ and the height of $h = 0.787 \text{ mm}$.

The dimensions and substrate information for the designed 3 GHz microstrip patch antenna can be found in Table 5-1.

Table 5-1: 3 GHz rectangular patch antenna design parameters.

Parameters	Value	Description
f_0	3 GHz	Radiation frequency
ϵ_r	2.2	Substrate (RT Duroid 5880) dielectric constant
h	0.787 mm	Height of the substrate
W	39.5 mm	Width of patch
L	33.35 mm	Length of patch
t	0.035 mm	Patch (copper) thickness
W_f	2.38 mm	Width of feed-line
L_f	29.07 mm	Length of feed-line
d	12.4 mm	Inset feed distance from the edge of patch
g	1 mm	Gap between patch and feed-line

5.3.2 Patch antenna result analysis

Based on the design procedure explained earlier in section 2.7.2, the patch antenna was designed and simulated using CST DESIGN STUDIO software. The parameters in Table 5-1 have been optimised to achieve optimum return loss $S_{1,1}$ (Figure 5-4) and realised gain at 3 GHz. The designed patch antenna using the CST simulator is illustrated in Figure 5-3.

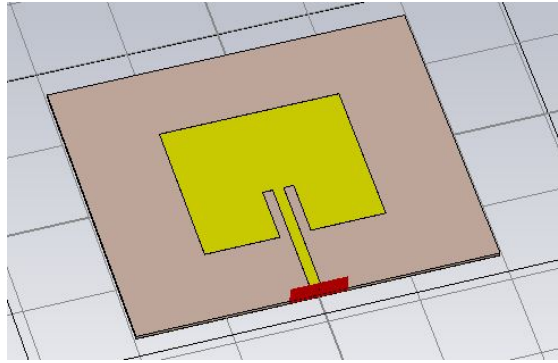


Figure 5-3: Simulated microstrip patch antenna using CST.

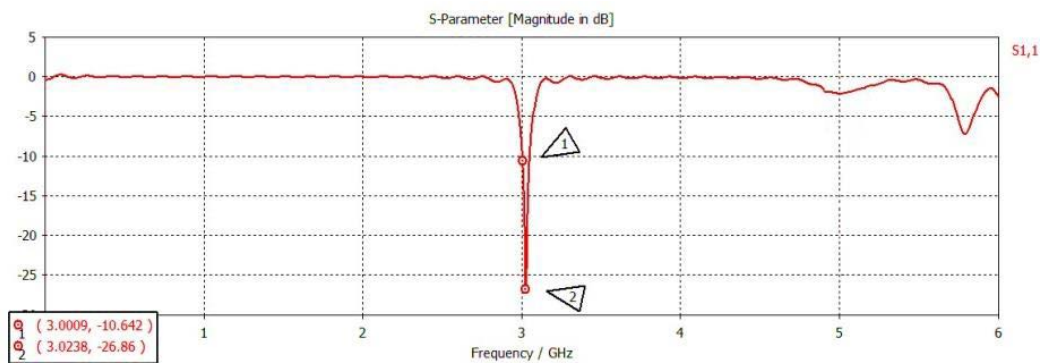


Figure 5-4: Return loss for designed patch antenna.

The two-dimensional realised gain and three-dimensional directivity pattern of the simulated patch antenna at 3 GHz can be seen in Figures 5-5 and 5-6 respectively. These results indicate that the designed patch antenna has the realised gain of 5.85 dB with the main lobe direction perpendicular to the patch surface and the main lobe directivity magnitude of 8.14 dBi; which are in agreement with the theoretical expectation from a microstrip patch antenna.

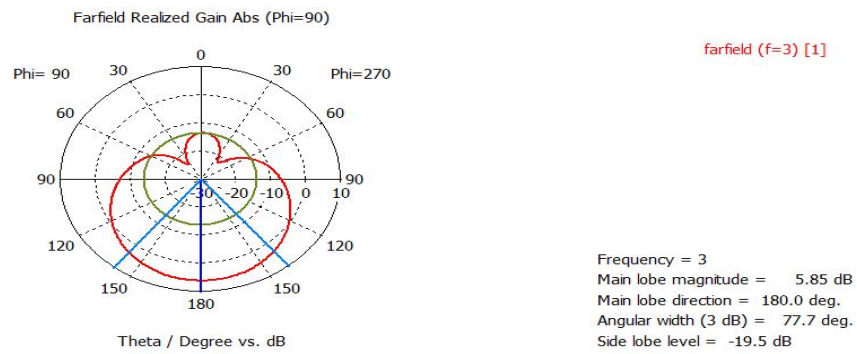


Figure 5-5: Patch antenna realised gain 2-D view.

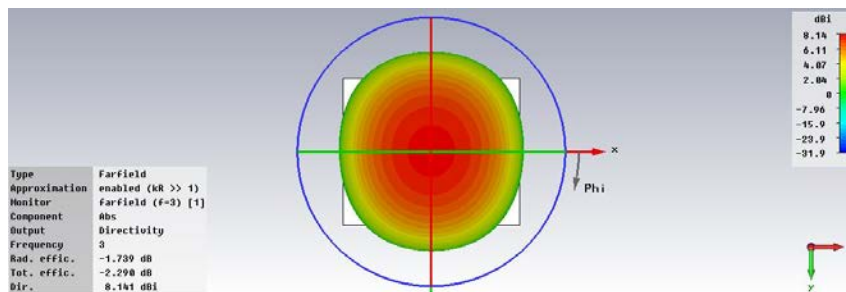


Figure 5-6: Patch antenna directivity 3-D view.

5.4 Frequency tripler patch antenna design

The frequency multiplier, or to be more specific the frequency tripler effect, can be integrated into the patch antenna by the inclusion of a Schottky diode in the patch structure. Figure 5-7 illustrates the prototype of the frequency tripler patch antenna.

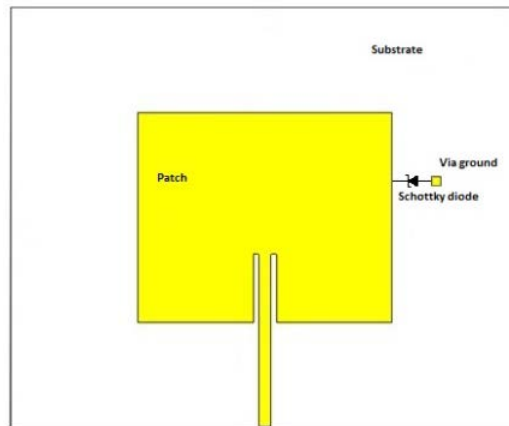


Figure 5-7: Frequency tripler patch antenna prototype.

As can be seen in Figure 5-7, in order to attach the anode of the Schottky diode to the ground, a via to ground is added in the close distance to the patch surface. Adding the via to ground and the ports to connect the Schottky diode ends to the patch and via to ground surfaces, changes the designed patch antenna's realised gain, power pattern direction and magnitude, as can be seen in Figure 5-8.

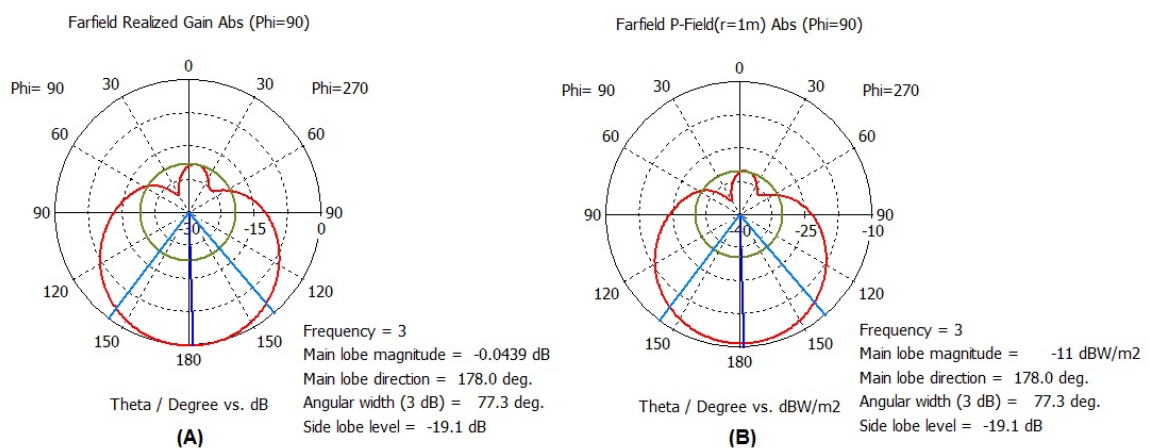


Figure 5-8: The effect of adding via to ground and Schottky diode connection ports on (A) realised gain and (B) power pattern.

5.4.1 Frequency tripler design

The frequency tripler effect is added to the antenna structure by including a Schottky diode. The operating frequency range and capacitance of the diode at the required frequency must be checked against the design specifications. For this design, a Skyworks SMS7621-079 Schottky diode was selected; it operates between DC and 12 GHz. The data sheet for this diode is provided in the appendix.

It is important to mention that the current varies along the patch length; therefore, the location where the Schottky diode is attached to the patch antenna plays a vital role in determining the power of the generated third harmonic. Hence, selecting a suitable point for the Schottky diode to connect to the patch is an important factor in the design; and determines the power of the generated third harmonic that needs to feed back to the structure.

5.4.2 Idler design

The frequency multiplier designed in this work uses the Schottky diode for harmonic generation. Having rectifying Schottky diode in the designed network, resulted in the conducting of a square wave current. This involves generating a series of harmonic currents that need to flow. Without having an idler circuit, these harmonics cannot flow and will force the Schottky diode to reverse bias itself to the point that the harmonic currents do not need to flow. Therefore the idlers are needed to establish the voltage and current waveform appropriately, to maximise the multiplication power at the required harmonic and to allow the other harmonic currents to flow [3]. In order to overcome the design limitation explained above idler circuits need to be included in the frequency tripler design. This can be achieved by designing a short circuit tuned at the fundamental and second harmonics before the load.

An open circuit is also needed at the fundamental frequency in the source side, to make sure that it rejects all the frequencies except the fundamental, to reach the Schottky diode. A schematic design of the frequency tripler is shown in Figure 5-9.

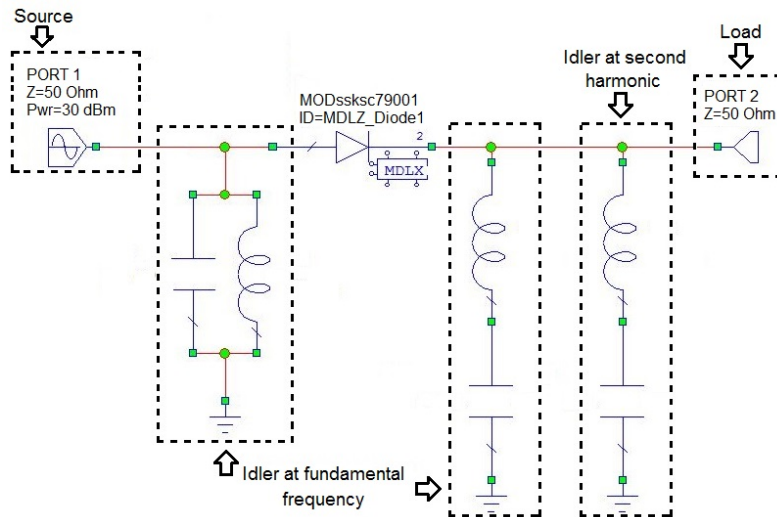


Figure 5-9: Simple frequency tripler with idler circuit.

In order to indicate the effect of an idler circuit, the circuit level demonstration was performed on the generic frequency tripler for two different conditions: one with the idler and another without the idler circuit. Figure 5-10 indicates the harmonic power level when there is no idler attached to the Schottky diode and Figure 5-11 indicates the harmonic power level of the same Schottky diode when the idlers are included.

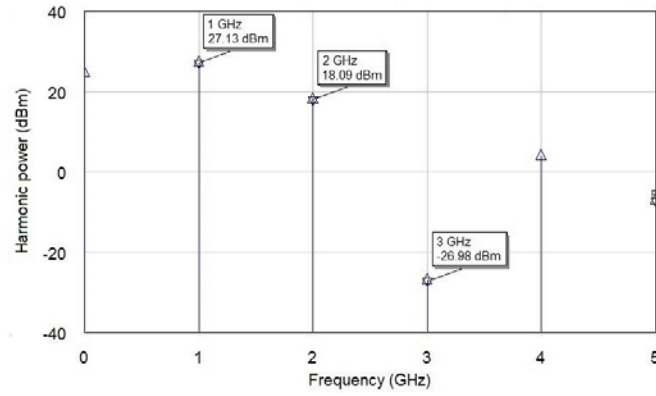


Figure 5-10: Power spectrum analysis for Schottky diode without the inclusion of idlers.

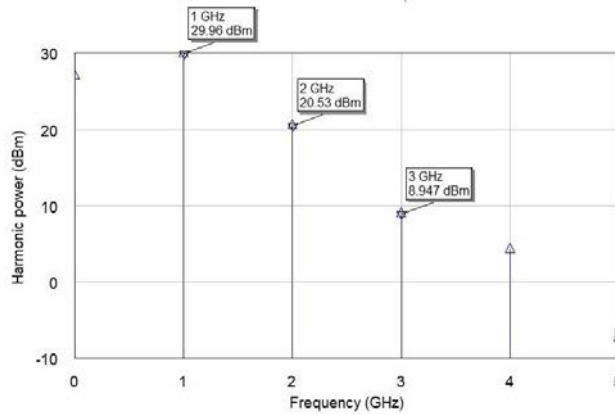


Figure 5-11: Power spectrum analysis for Schottky diode with idlers.

As can be seen in Figures 5-10 and 5-11, the inclusion of idlers at the fundamental and second harmonics improved the power spectrum level in the third harmonic by 35.9 dB. This improvement results in the generation of a much higher third harmonic power level which will be needed to excite the patch. Therefore the inclusion of the idlers has a great effect not only on the performance of the frequency tripler, but also on the overall design of the frequency tripler patch antenna.

5.4.3 Feed line resonator design

Another factor which could improve the generated third harmonic power in the circuit after the idler is the inclusion of the feed line resonator. The designed feed line resonator includes series and shunt resonators at the fundamental and third harmonics, in order to allow the fundamental frequency to pass to the patch and reject the third harmonic to avoid dissipation in the source impedance. The designed feed line resonator is shown in Figure 5-12. The return loss and the insertion loss of the feed line resonator are shown in Figure 5-13.

In order to find the best location for the feed line resonator to preserve the maximum third harmonic frequency in the circuit, a network of transmission lines with equal lengths, one negative and the other positive, were used on either side of the feed line resonator to move the resonator along the feed line, as can be seen in Figure 5-14. The best location was then selected by tuning the length of the transmission line in order to achieve the maximum radiation pattern.

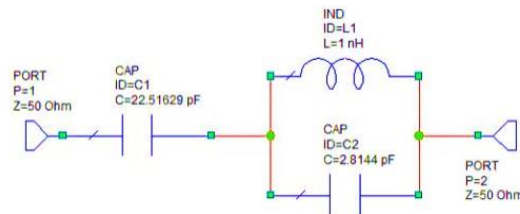


Figure 5-12: Feed line resonator design schematic.

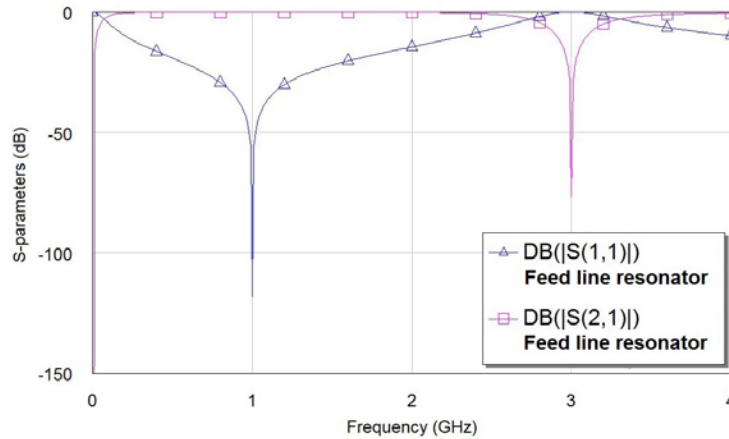


Figure 5-13: Feed line resonator S-parameter characteristics.

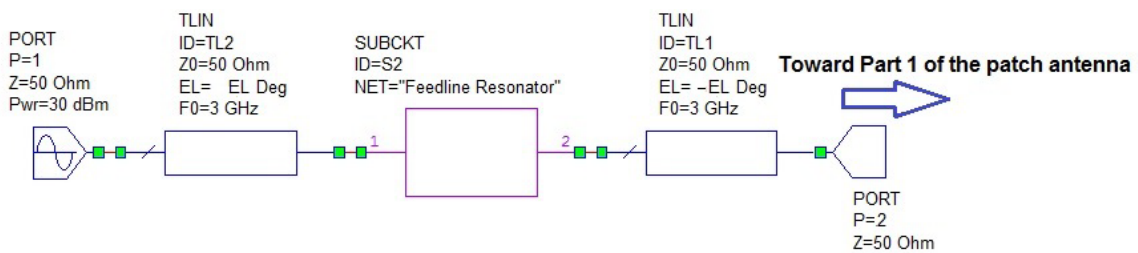
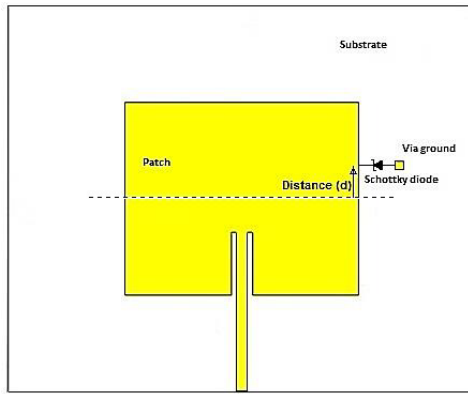


Figure 5-14: Feed line network configuration to ensure the best location for the feed line resonator.

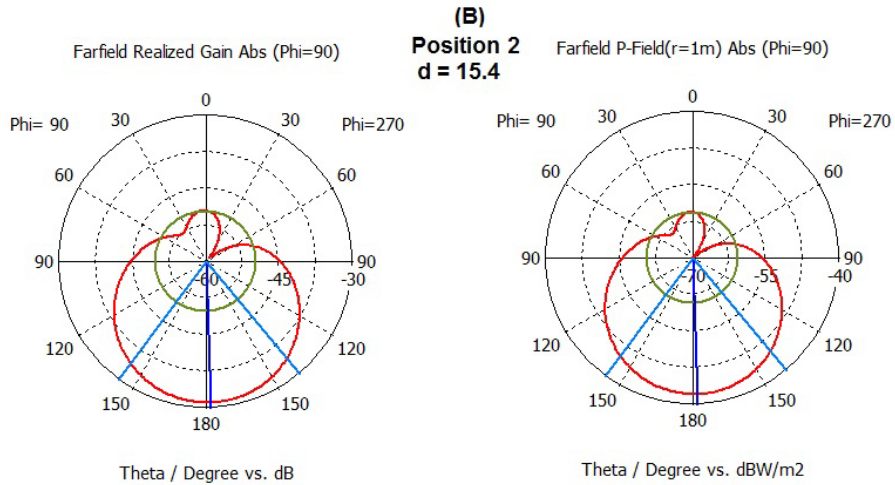
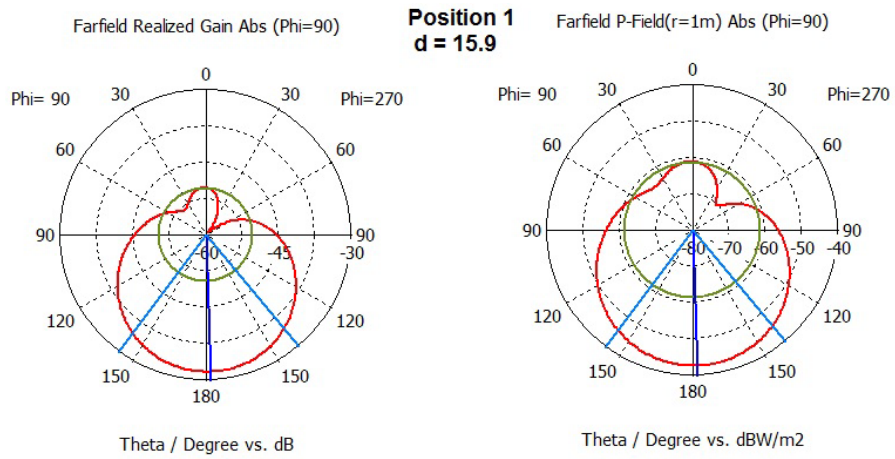
5.4.4 Schottky diode location

As mentioned earlier in this chapter, since the current varies across the length of the patch, therefore finding an optimum position for the Schottky diode where it is able to generate the maximum third harmonic power is an important step in the design of the frequency tripler patch antenna.

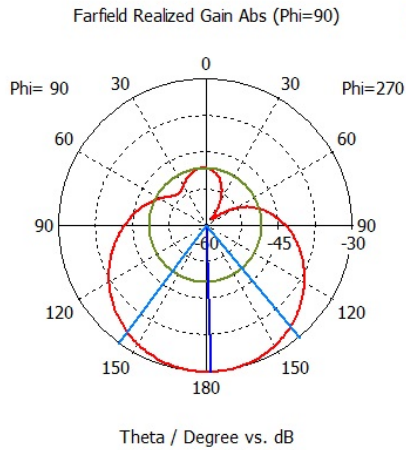
The optimum position for the diode was found through a series of numerical harmonic balance simulations as described below. The competing factors determining the optimum position include: The amplitude of the voltage at the fundamental frequency, which needs to be high, in order to generate a large current at third harmonics through the diode's nonlinear characteristic; The patch impedance at third harmonic, which will depend upon the position, and which needs to be optimised for third harmonic power transfer to the patch; The patch impedances at other harmonic frequencies, which need to create the appropriate idler effects, allowing currents to flow as required by the harmonic balance conditions, but dissipating minimal power. An arbitrary location along the patch edge was first selected. The design process was then used to determine the realised gain for the designed frequency tripler patch antenna. This method was repeated for twelve different locations of the Schottky diode along the patch length. Figure 5.15 illustrates the realised gain and power field pattern for different locations of the Schottky diode. Table 5-2 summarises the corresponding magnitude of the realised gain and power pattern in the main lobe for the different diode locations along the length of the patch antenna. After calculating these values, a fourth order polynomial curve fitting technique was employed to find the best location for the Schottky diode. Figure 5-16 represents the calculated magnitude of realised gain and power. The curve is fitted to find the location for the optimum position of the Schottky diode. Comparing the calculated location from Figure 5-16 (a) and (b), indicates that the best location of the Schottky diode is consistent whether it has been calculated from the magnitude of the realised gain, or from the magnitude of the power pattern. The calculated optimum position for the Schottky diode is used for the further simulation and analysis explained in the following sections.



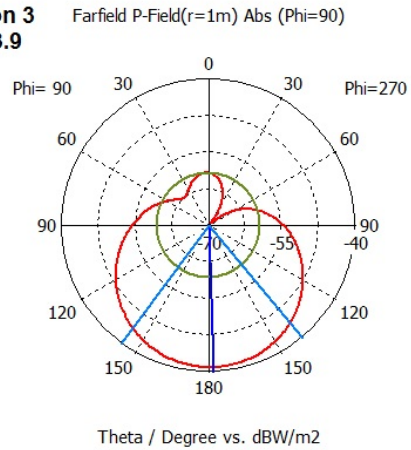
(A)



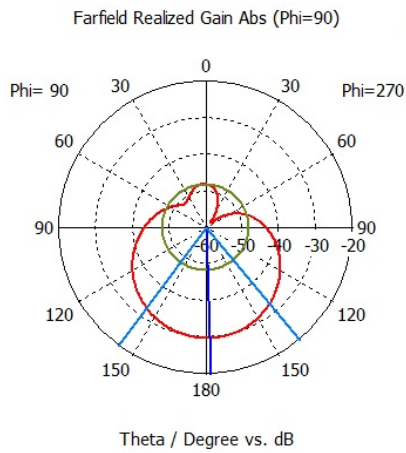
(C)



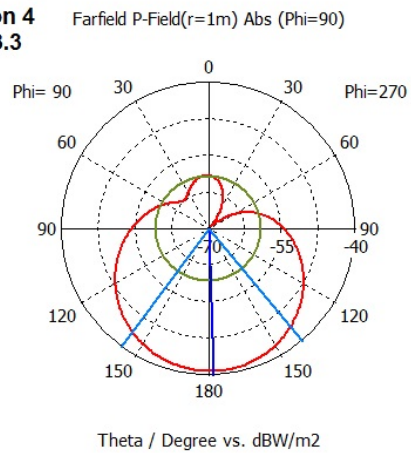
Position 3
d = 13.9



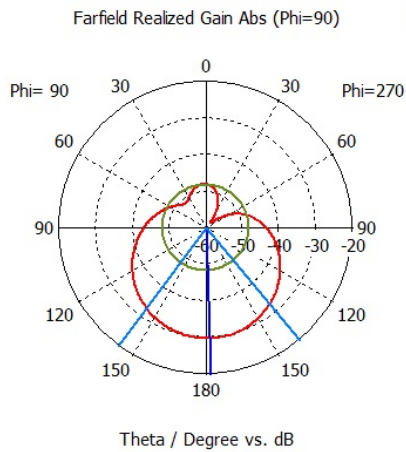
(D)



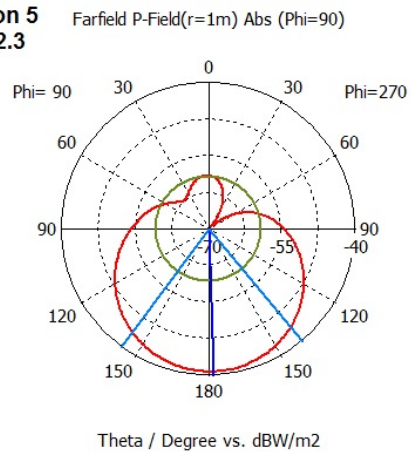
Position 4
d = 13.3



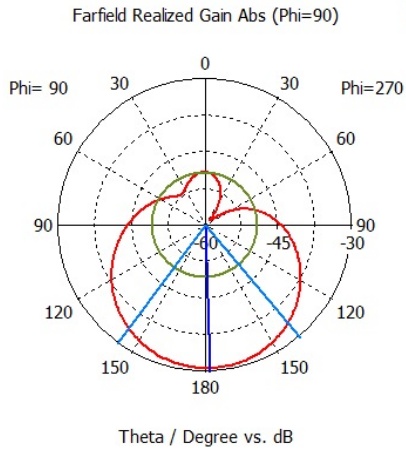
(E)



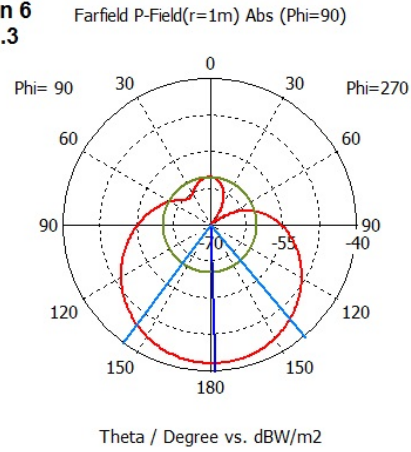
Position 5
d = 12.3



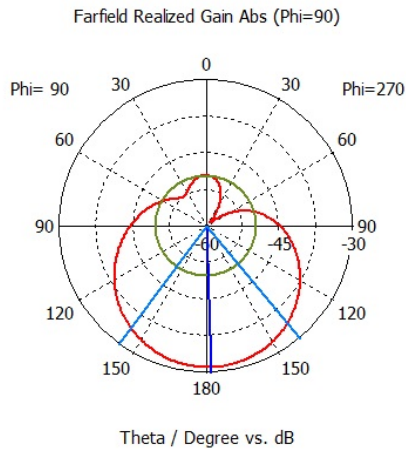
(F)



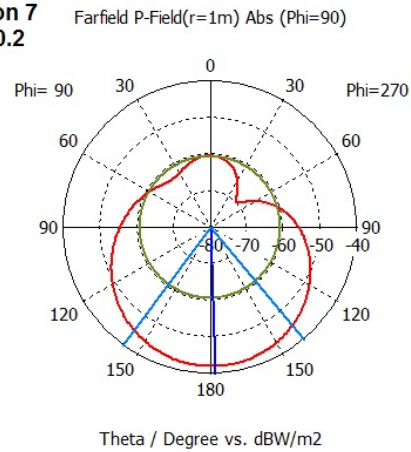
Position 6
d = 11.3



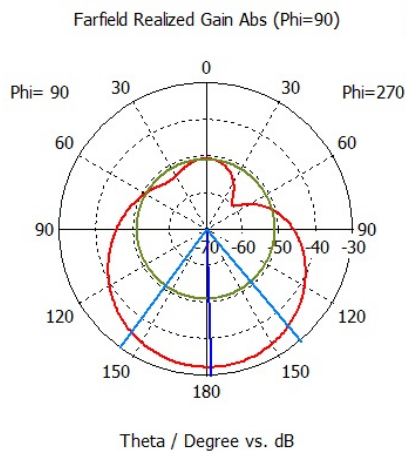
(G)



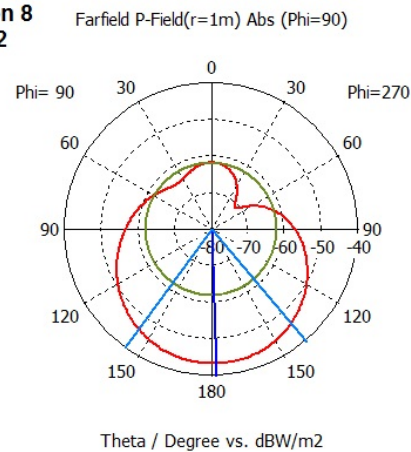
Position 7
d = 10.2



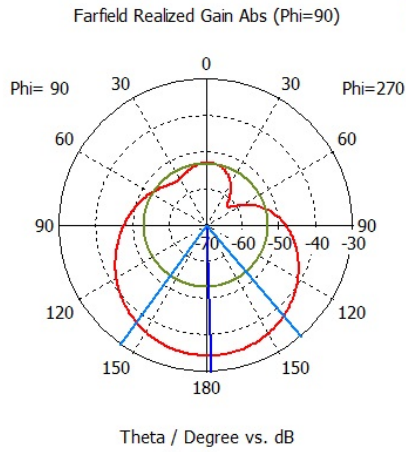
(H)



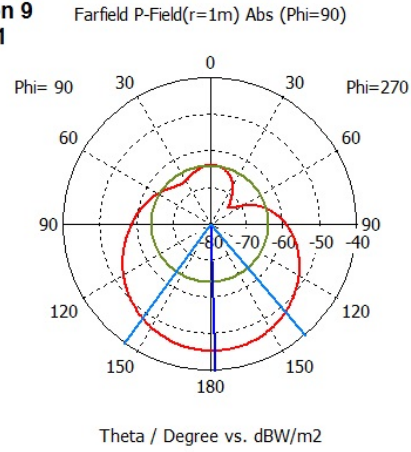
Position 8
d = 8.2



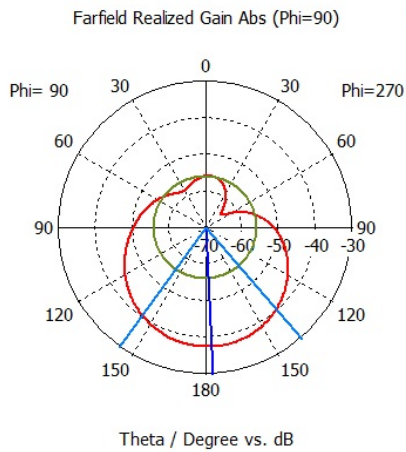
(I)



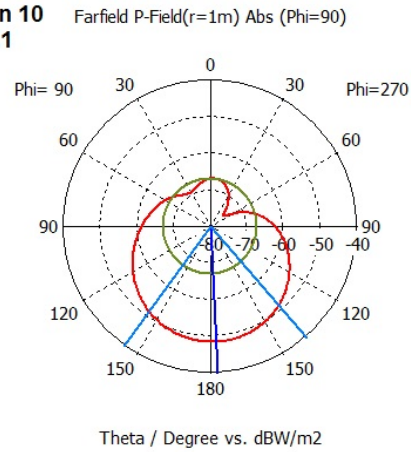
Position 9
d = 6.1



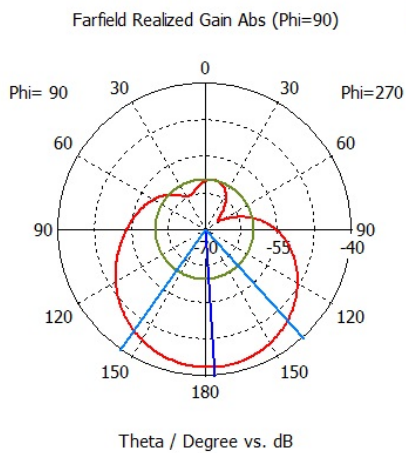
(J)



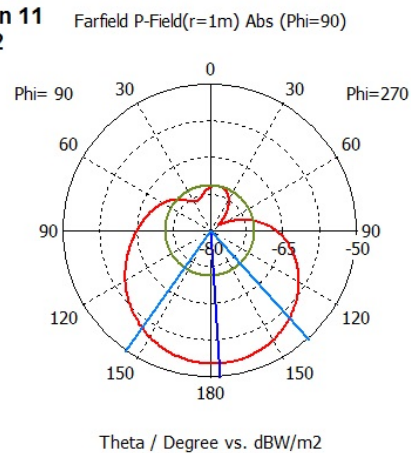
Position 10
d = 4.1



(K)



Position 11
d = 2



(L)

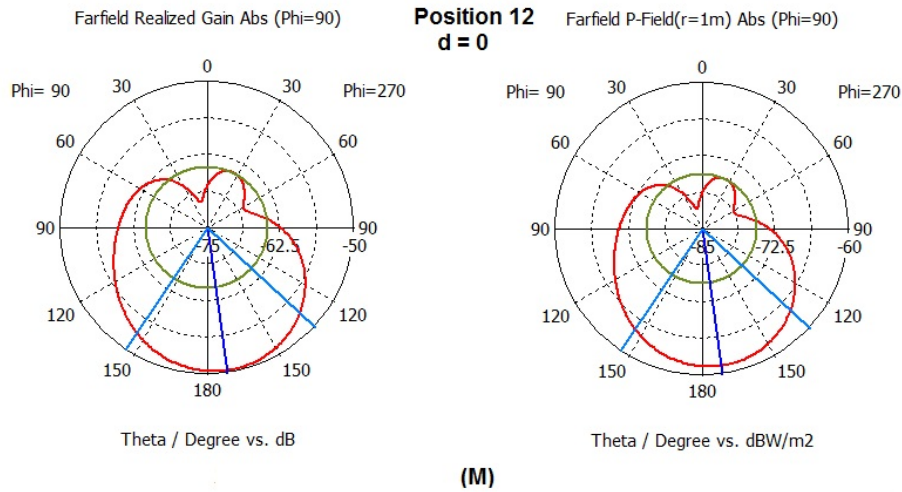


Figure 5-15: Realised gain and power field pattern of the frequency tripler patch antenna for different positions of the Schottky diode.

Table 5-2: Measured realised gain and power corresponding to different Schottky diode locations.

Distance (mm)	15.9	15.4	13.9	13.3	12.3	11.3	10.2	8.2	6.1	4.1	2	0
Realised Gain (dB)	-31.9	-31.3	-30.1	-30	-29.9	-30.8	-31	-32.5	-34.6	-37.7	-41.9	-50.6
Power (dBW/m ²)	-42.9	-42.3	-41.1	-41	-40.9	-41.8	-42.2	-43.5	-45.6	-48.7	-52.9	-61.6

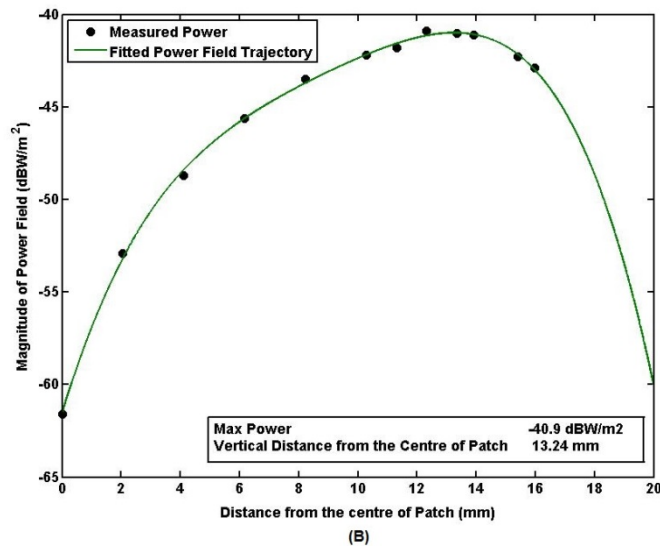
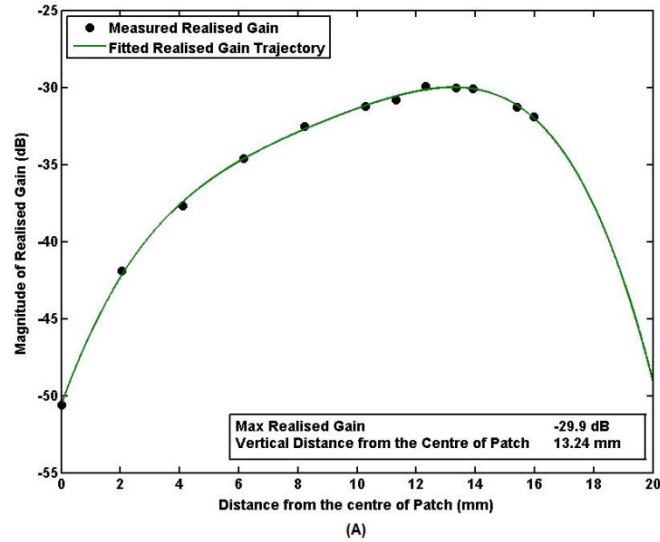


Figure 5-16: Measured and fitted trajectory for (A) realised gain and (B) power field.

5.5 Harmonic balance simulation

The proposed harmonic balance simulation technique can now be applied to the designed frequency tripler patch antenna by following the steps summarised in Figure 5-1.

In the first step, the nonlinear part, the Schottky diode in this example, needs to be de-embedded and the remaining parts are simulated using the CST software to find the S-

parameters. Figure 5-17 presents the frequency tripler patch antenna sections which are being simulated in this step. The generated S-parameters file is then imported to AWR to combine with the nonlinear parts. The circuit consists of the S-parameter file which represents the linear part of the circuit, the Schottky diode, idlers circuitry and feed line resonator. The circuit arrangement for the simulation in AWR is shown in Figure 5-18. It can be seen in Figure 5-17 and 5-18 that port 1 is where the 1 GHz signal entered the designed microstrip feedline; port 2 is the intersection of the via to ground and the Schottky diode; and port 3 is the intersection of the Schottky diode and the patch antenna. The circuit in Figure 5-18 is then simulated in order to measure the third harmonic current generated by the Schottky diode at port 1 and port 3. It should be also noted that the Schottky diodes used in this chapter's simulation are all biased (0.1 V) using an ideal bias tee. Table 5-3 presents current magnitudes and phases for the third harmonics for port 1 and 3.

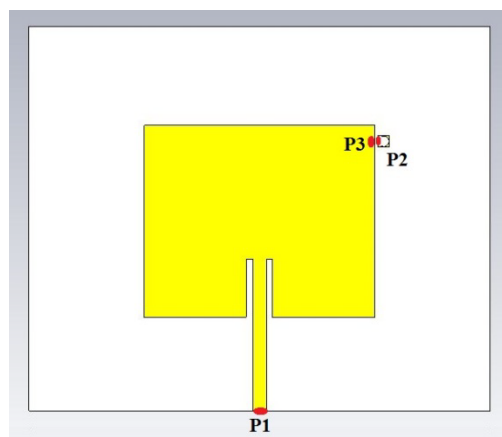


Figure 5-17: Frequency tripler patch antenna without Schottky diode.

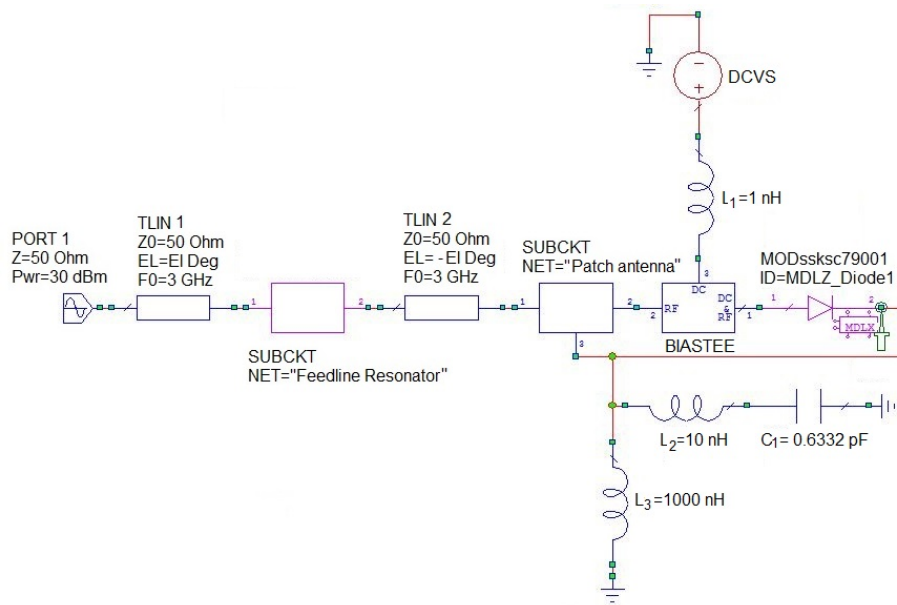


Figure 5-18: AWR Microwave Office circuit arrangement.

Table 5-3: Complex current generated at the third harmonic at port 1 and 3.

Frequency (GHz)	$ I(\text{SUBCKT.S1}@1,3) $ (mA)	$\text{Ang}(I(\text{SUBCKT.S1}@1,3))$ (Deg)	$ I(\text{SUBCKT.S1}@3,3) $ (mA)	$\text{Ang}(I(\text{SUBCKT.S1}@3,3))$ (Deg)
1	6.3509	-82.534	3.7237	80.324

In the next step, the calculated currents are generated and injected into the designed patch antenna in CST. In order to generate these currents, a network of linear voltage controlled current sources (VCCS) and a 100 Ω transmission line to generate the phase difference required between the currents are used. The transmission line is selected to be 100 Ω to match the series 100 Ω resistor and to ensure that the parallel combination of generators is matched to 50 Ω .

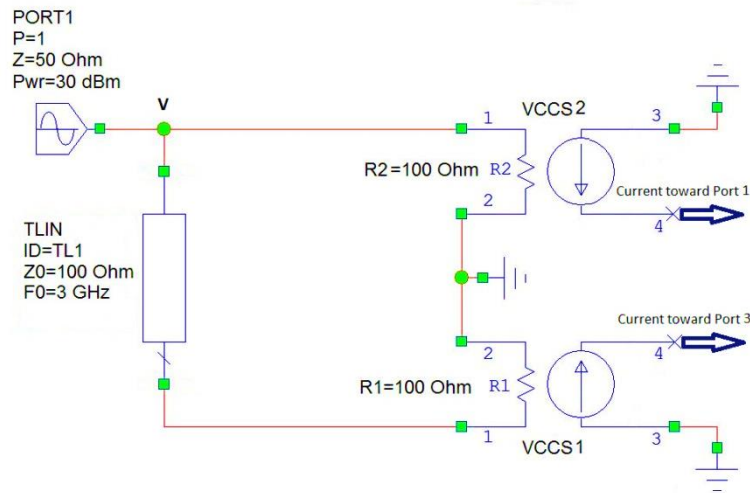


Figure 5-19: Proposed current network schematic.

Figure 5-19 illustrates the schematic of the network needed to drive the required currents into the patch antenna. To design this feeding network using voltage controlled current sources, as the name suggests, the output currents of the VCCS are functions of the voltage across the input ports and the transconductance of the VCCS, as can be seen in Equation 5-1. On the other hand voltage (V) in Equation 5-1 is calculated as it is connected to the 50 Ω port with 30 dBm power, using Equation 5-2, as can be seen below.

$$g_m = \frac{I_{out}}{V} \quad 5-1$$

$$P = \frac{V^2}{R} \quad 5-2$$

$$V = \sqrt{50}$$

Having found the voltage and using the set of known currents measured in AWR (Table 5-3) the transconductance (g_m) of the voltage controlled current sources is calculated. The transconductance values are presented in Table 5-4. Once the current magnitudes are known, the required phase difference between the two currents is determined by setting the lengths of the matched transmission lines inside the network using TXline in AWR Microwave Office.

Table 5-4: Transconductance (g_m) value of the voltage controlled current sources .

Voltage Controlled Current Sources (VCCS)	VCCS 1	VCCS 2
Transconductance (g_m)	0.5395×10^{-3}	0.9073×10^{-3}

The designed network to enforce the required third harmonic currents is then combined with the patch antenna. The combined structure is shown in Figure 5-20. This structure is then simulated to analyse the radiation and power pattern of the frequency tripler patch antenna.

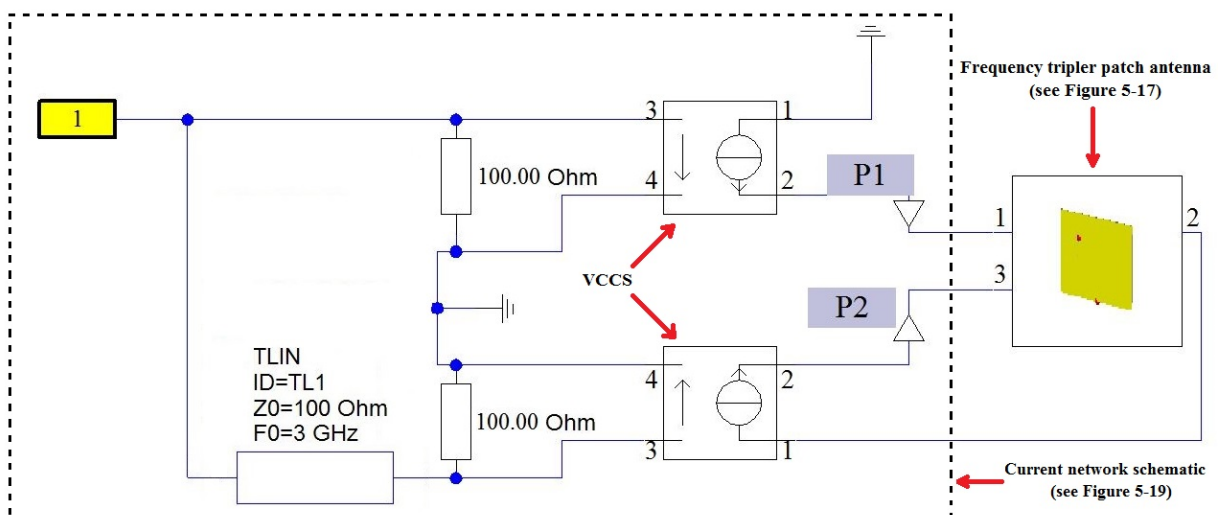


Figure 5-20: Circuit configuration for generating the required current into the designed frequency tripler patch antenna.

The magnitude of the injected currents at ports 1 and 3 have been measured at points P1 and P2 (Figure 5-20). The measured currents are shown in Figure 5-21. Comparing the results in Figure 5-21 and Table 5-3 verifies that the currents injected into the structure are in agreement with the harmonic currents in Table 5-3.

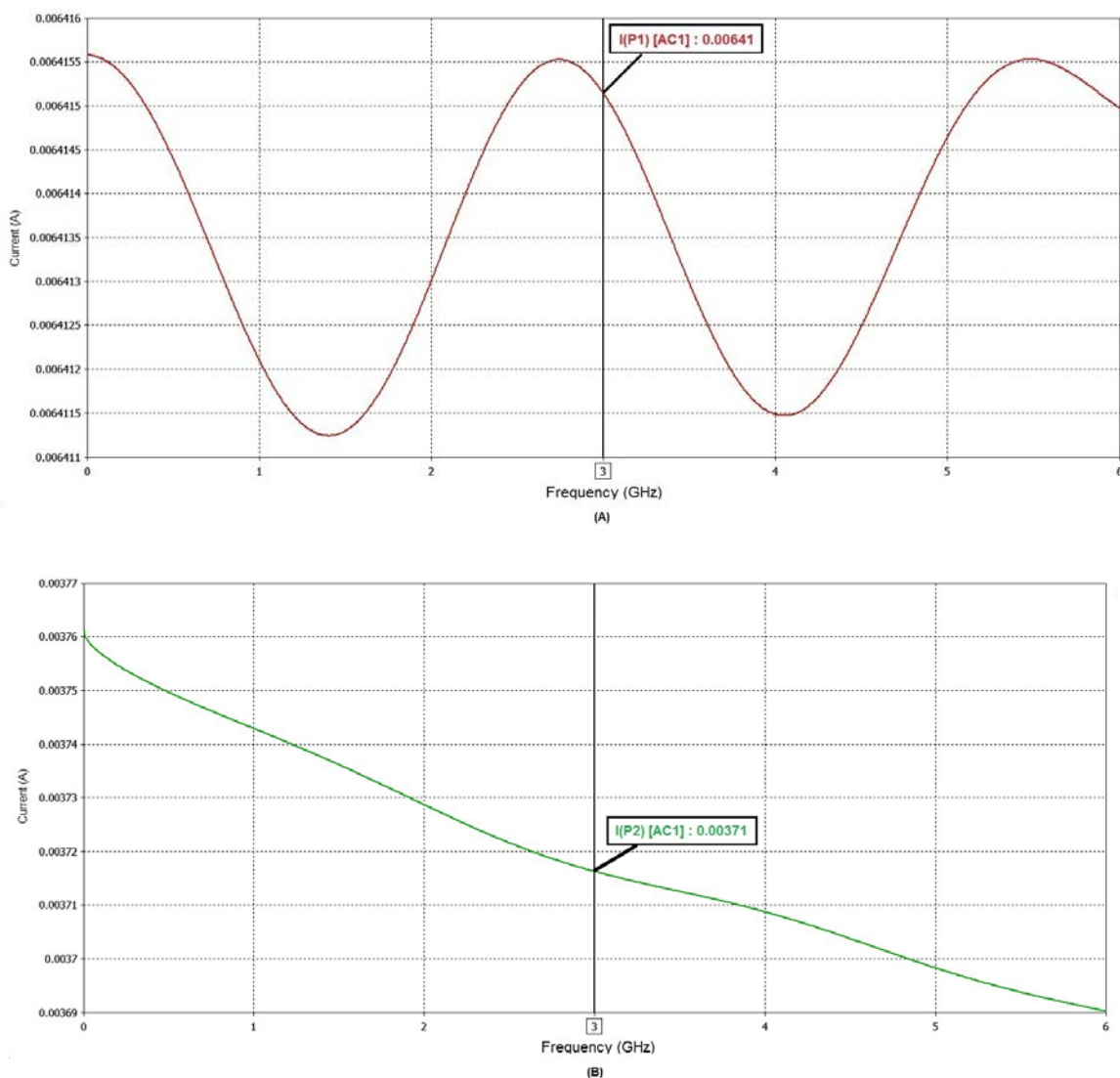


Figure 5-21: Enforced currents (A) measured at the input feed line port; (B) measured at the intersection of the Schottky diode and patch antenna.

After enforcing the required currents into the design, the circuit is now ready to perform full EM simulation at 3 GHz. The integrated circuit is now analysed for the realised gain and power pattern using CST STUDIO SUITE. Figure 5-22 indicates a two-dimensional view of the realised gain and power pattern for the designed integrated nonlinear frequency tripler patch antenna. Analysing Figures 5-22 indicates that an integrated nonlinear frequency tripler patch antenna has similar radiation and power pattern as that expected from a patch antenna (Figure 5-5), with a small deviation in the main lobe direction; which, as was explained earlier in section 5.4, is due to the inclusion of the via to ground at a short distance from the patch surface (Figure 5-8). It is important to mention that the low magnitude of the realised gain and power field that can be seen in Figure 5-22 is due to the low third harmonic power generated by the Schottky diode to excite the patch antenna. Figure 5-23 indicates that the input power fed to the Schottky diode at 1 GHz is 18.13 dBm and the generated third harmonic power is -11.34 dBm . The 29.64 dBm conversion loss in the Schottky diode is expected, as it was calculated previously in section 5.4.2 Figure 5-11. It is shown in Figure 5-11 that the conversion loss is 21.053 dBm , where the Schottky diode was excited by 30 dBm ; whereas in the designed frequency tripler patch antenna, the Schottky diode was excited with much lower fundamental frequency power and hence expected to introduce a higher conversion factor. Therefore, by taking the effect of the Schottky diode conversion loss into account when analysing the magnitude of the realised gain and power field, it can be seen that the theoretical expectation of the patch antenna has been satisfied.

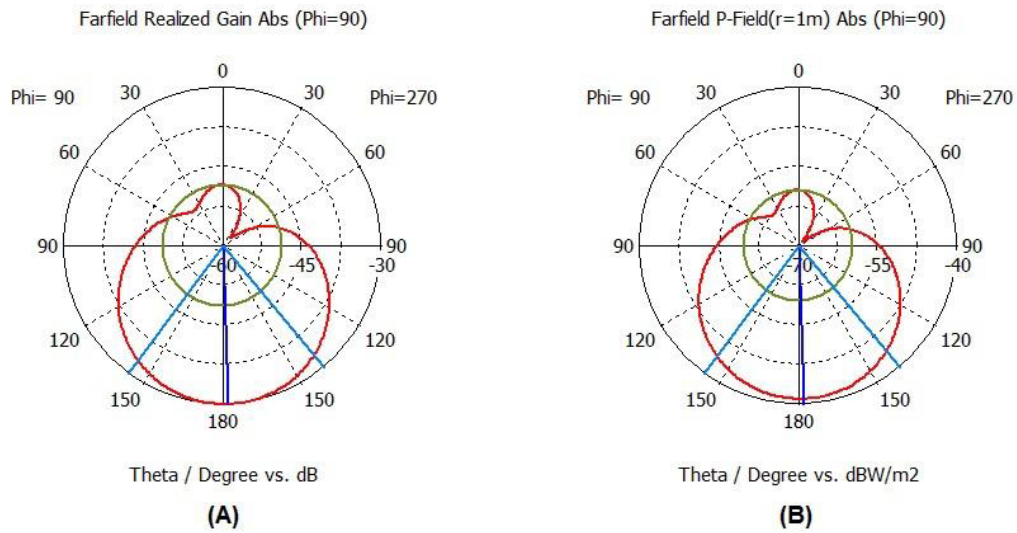


Figure 5-22: (A) 2-D realised gain and (B) power pattern of the integrated nonlinear frequency tripler patch antenna.

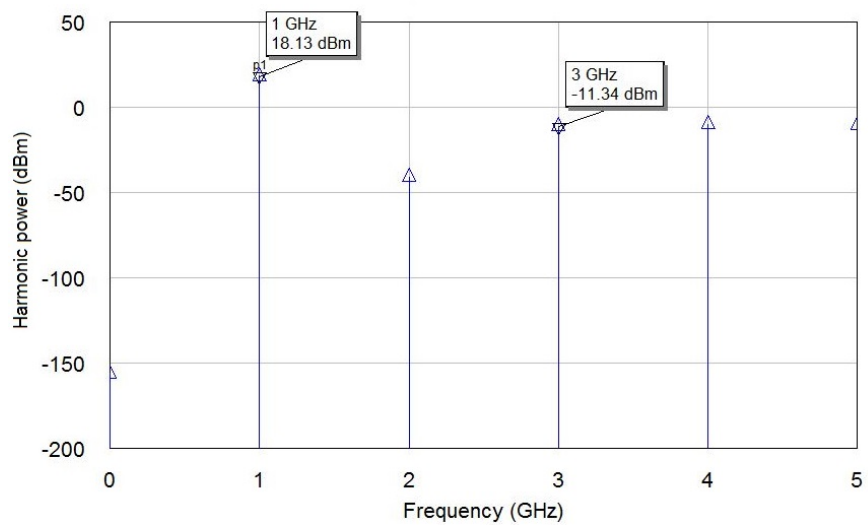


Figure 5-23: Power of the harmonics generated by the Schottky diode in the frequency tripler patch antenna.

5.6 Harmonic Balanced Analysis of the NL-CRLH Leaky Wave Antenna

In this section, the proposed method of combining harmonic balance and the EM analysis is deployed to investigate the designed NL-CRLH leaky wave antenna in section 4.4. This is done by following the steps summarised in Figure 5-1.

In the first step, the nonlinear parts, the varactor diodes in this design, were removed from the distributed NL-CRLH leaky wave antenna. The remaining parts of the model were simulated using the CST MICROWAVE STUDIO package to find the S-parameters. The NL-CRLH leaky wave antenna sections which are being simulated in this step are presented in Figure 5-24. The design procedure of the distributed NL-CRLH can be found in section 4-5. The dimensions of the distributed structure elements are listed in Table 4-3. The generated S-parameter is then imported to AWR Design Environment to combine with the nonlinear section of the NL-CRLH leaky wave antenna. Figure 5-25 is the circuit arrangement of the NL-CRLH leaky wave antenna in the AWR Design Environment. This circuit consists of the S-parameter file which represents the linear parts of the design, the varactors and idlers circuitry. The parallel LC idler before each varactor acts as a narrow passband filter ensuring that the fundamental frequency (*e.g* 1.1 GHz for the broadside radiation) will reach the varactors. In order to make sure that the biasing current is not short circuited to ground due to this circuit arrangement a large capacitor is placed in series with the parallel network. The series LC branch after each varactor in Figure 5-25 represents the idler at the third harmonic frequency. This idler suppresses any third harmonic frequency generated by the varactors. The “Varactor” SUBCKT between ports 3, 4 and ports 5, 6 of the “CRLH” SUBCKT in Figure 5-25, represents the varactor model. In this design SKYWORKS “SMV1232” varactor was used. The Spice model and capacitance vs. voltage curve of this varactor can be seen in

Figure 5-26 and 5-27 respectively. It should be noted that in Figure 5-24 and 5-25, port 1 is where the fundamental frequency signal entered the designed NL-CRLH leaky wave antenna; ports 3 and 4 are the intersection of the anode and cathode of the first varactor with the distributed NL-CRLH leaky wave antenna and port 5 and 6 corresponds to the intersections of the second varactor respectively; port 2 is the exit port of this unit cell. The power of the harmonic generated by the varactors within the circuit arrangement of Figure 5-25 is demonstrated in Figure 5-28. The circuit in Figure 5-25 is then simulated in order to measure the second harmonic generated by the varactor diodes at all ports. Table 5-5 presents current magnitudes and phases for the second harmonics for three different frequencies. The selected frequencies enabled the demonstration of backward to forward, including the broadside beam scanning by changing the operating frequency from the left-handed (0.8 GHz) to right-handed (1.5 GHz) frequency region.

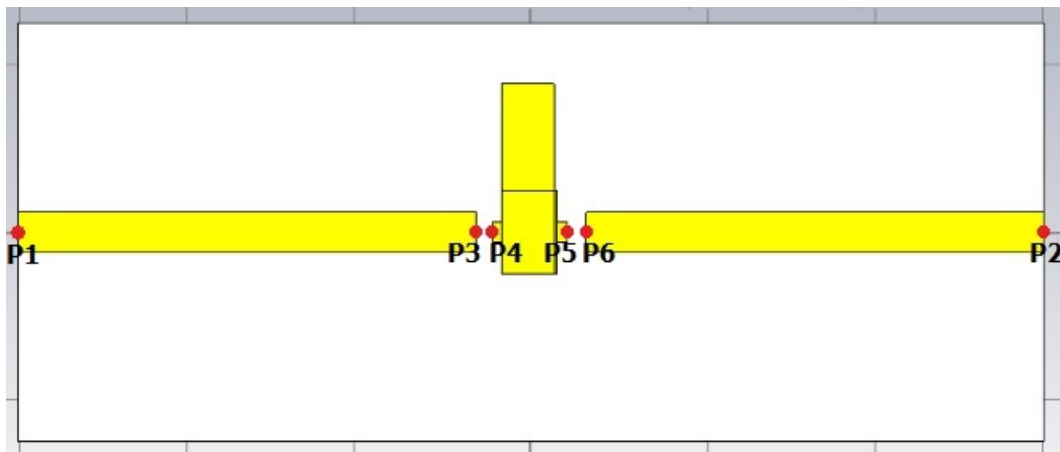


Figure 5-24: NL-CRLH leaky wave antenna structure without varactor diodes.

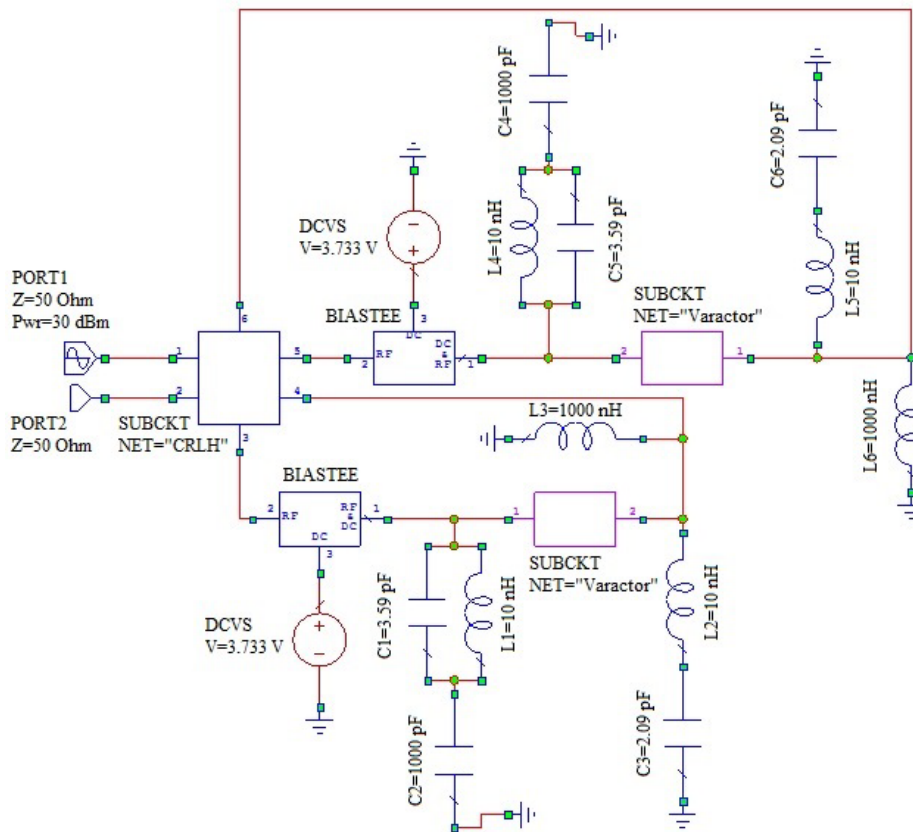


Figure 5-25: AWR Microwave Office arrangement of the NL-CRLH leaky wave antenna.

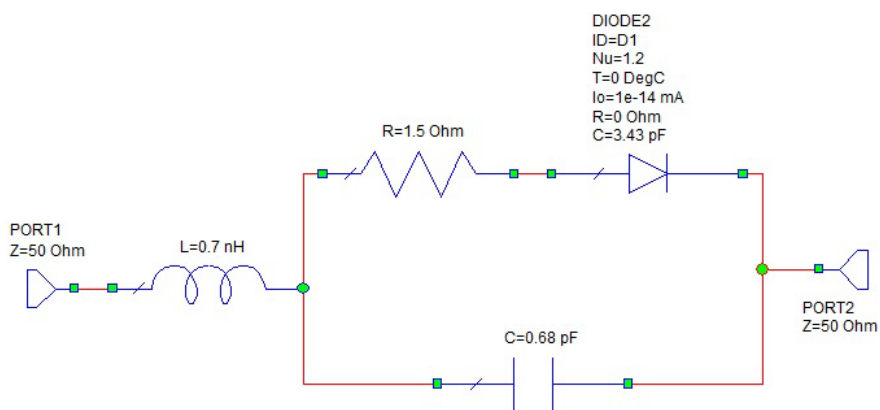


Figure 5-26: Spice model for SKYWORKS SMV 1232 varactor.

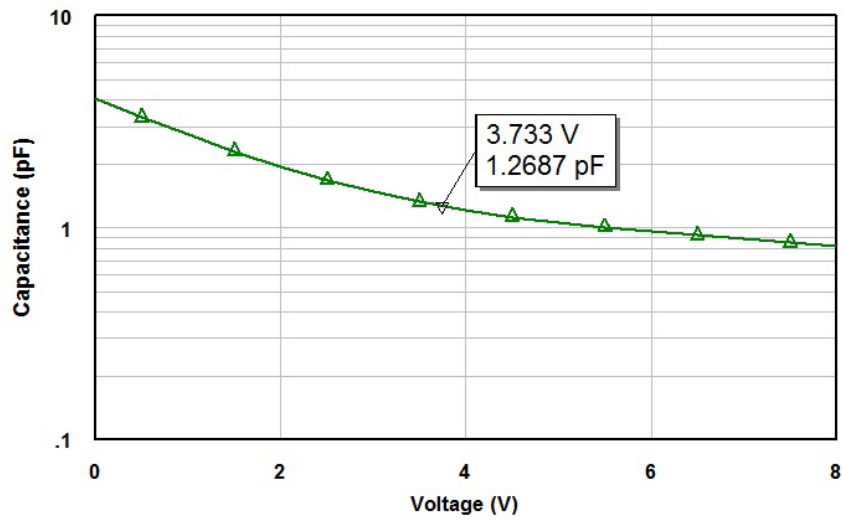


Figure 5-27: Capacitance vs. Voltage plot to investigate the required biasing voltage.

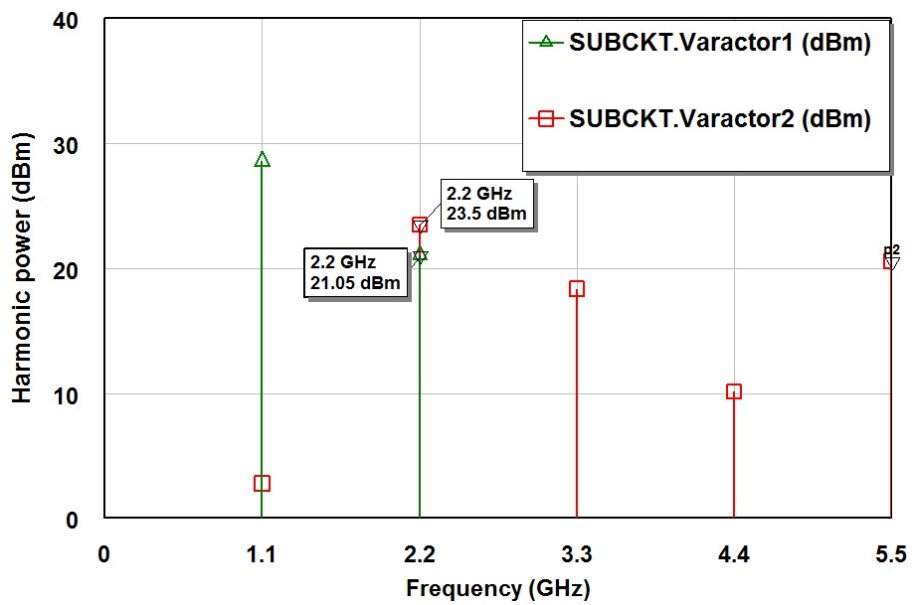


Figure 5-28: Power of the harmonics generated by the varactor diodes in the NL_CRLH leaky wave antenna (Figure 2-25).

Table 5-5: Complex current generated at the second harmonic at port 1 to 6.

Frequency (GHz)	0.8	1.1	1.5
$ I(CRLH@1, 2) $ (mA)	33.50	45.75	1.23
$Ang(I(CRLH@1, 2))$ (Deg)	110.6	70.79	36.14
$ I(CRLH@2, 2) $ (mA)	44.54	86.77	21.96
$Ang(I(CRLH@2, 2))$ (Deg)	-5.01	138.22	133.79
$ I(CRLH@3, 2) $ (mA)	34.63	47.71	1.15
$Ang(I(CRLH@3, 2))$ (Deg)	76.15	93.43	116.58
$ I(CRLH@4, 2) $ (mA)	87.89	139.92	25.71
$Ang(I(CRLH@4, 2))$ (Deg)	-37.71	-18.92	-9.12
$ I(CRLH@5, 2) $ (mA)	76.72	58.33	6.63
$Ang(I(CRLH@5, 2))$ (Deg)	159.88	-150.13	159.12
$ I(CRLH@6, 2) $ (mA)	43.98	90.74	22.47
$Ang(I(CRLH@6, 2))$ (Deg)	-38.41	159.57	-131.58

In the next step, the measured currents in all ports are generated and injected into the designed NL-CRLH structure (see Figure 5-24) at the corresponding ports in CST DESIGN STUDIO. In order to generate these currents, a network of linear voltage controlled current sources (VCCS) and 300Ω transmission lines to generate the phase difference required between the currents is used. The transmission lines are selected to be 300Ω to match the series 300Ω resistor at each current branch and to ensure that the parallel combination of the

generators is matched to 50Ω . Figure 5-29 illustrates the schematic of the network needed to drive the required currents into NL-CRLH leaky wave antenna ports. To design this feeding network using VCCSs, the output currents of the VCCS are functions of the voltage across the input ports and the transconductance (g_m) of the VCCS. Having found the voltage (using Equation 5-1 and 5-2) and using the set of known currents measured in AWR (Table 5-5) the transconductance of the VCCSs is calculated. These values are presented in Table 5-6. Having set the current magnitudes, the required phase difference between the currents for each port and port 1 is determined by setting the lengths of the matched transmission lines inside the network using TXline in AWR Microwave Office.

Table 5-6: Transconductance value of the voltage controlled current sources.

Frequency (GHz)	0.8	1.1	1.5
$g_m @ P1 (S)$	4.73×10^{-3}	6.47×10^{-3}	0.17×10^{-3}
$g_m @ P2 (S)$	6.3×10^{-3}	12.27×10^{-3}	3.1×10^{-3}
$g_m @ P3 (S)$	4.9×10^{-3}	6.74×10^{-3}	0.16×10^{-3}
$g_m @ P4 (S)$	12.43×10^{-3}	19.79×10^{-3}	3.64×10^{-3}
$g_m @ P5 (S)$	10.85×10^{-3}	8.25×10^{-3}	0.94×10^{-3}
$g_m @ P6 (S)$	6.22×10^{-3}	12.83×10^{-3}	3.18×10^{-3}

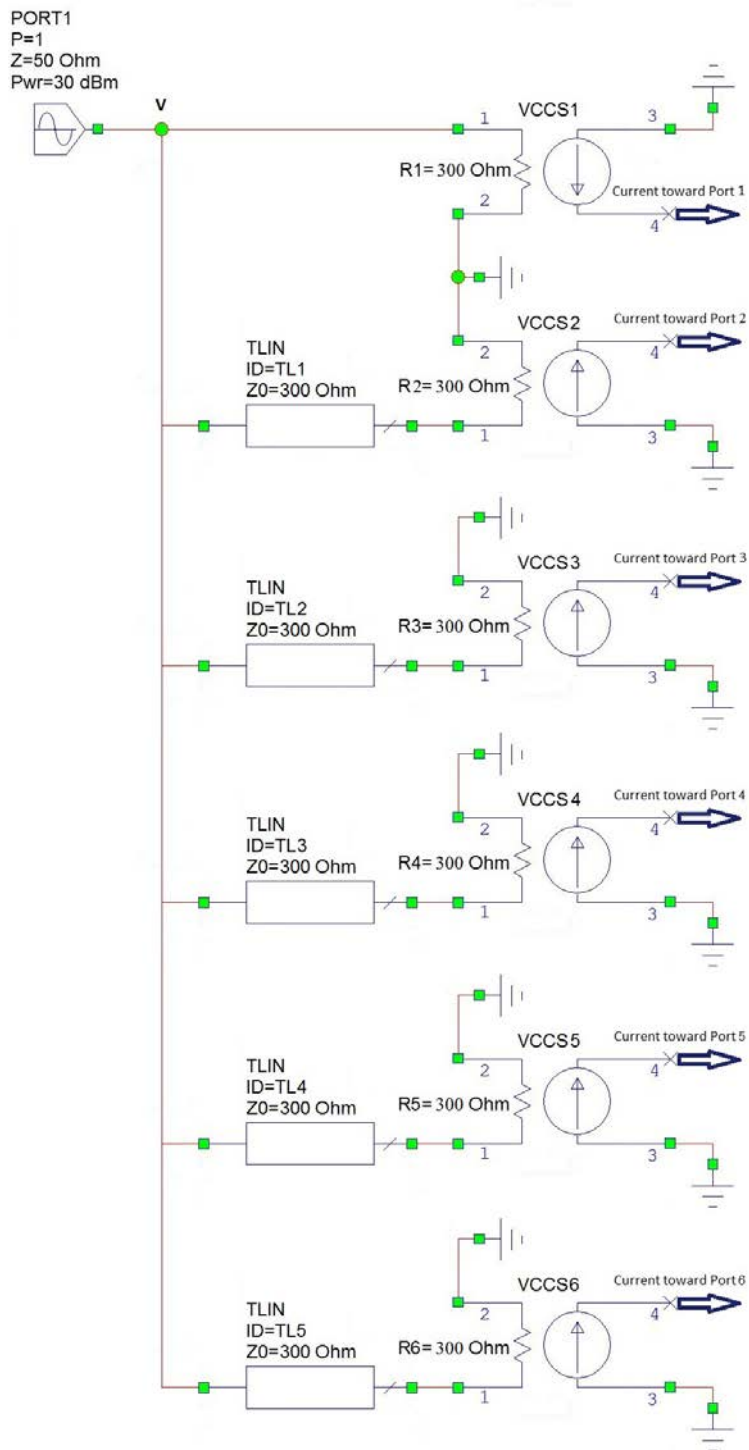


Figure 5-29: Current network schematic for current generation at the second harmonic to be injected to the NL-CRLH leaky wave antenna ports.

The designed network to enforce the required second harmonic currents is then combined with the NL-CRLH leaky wave antenna. The combined structure is shown in Figure 5-30. This structure is then simulated to analyse the radiation pattern of the NL-CRLH frequency doubler leaky wave antenna. The magnitudes of the injected currents at ports 1 to 6 have been measured at points P1 to P6 (Figure 5-30) and verified with the results in Table 5-5.

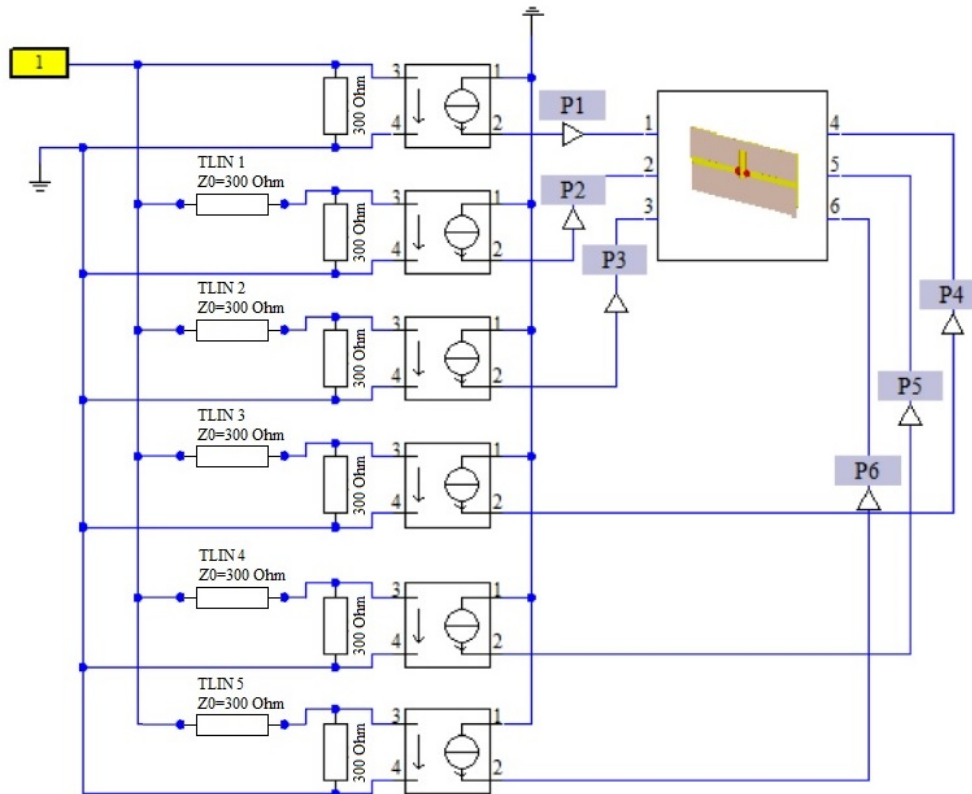


Figure 5-30: Circuit configuration for injecting the required current into the NL-CRLH leaky wave antenna structure.

After enforcing the required currents into the design, the circuit is now ready to perform the full EM simulation at the required second harmonic frequency. In this work, in order to demonstrate the backward, broadside and forward radiation of the designed NL-CRLH frequency doubler structure, the excitation frequency at port 1 is selected to be 0.8 GHz ,

1.1 GHz and finally 1.5 GHz which give rise to 1.6 GHz, 2.2 GHz and 3 GHz second harmonic that lie in left handed region, transient frequency and right handed region of the designed NL-CRLH structure respectively (see Figure 4-10 for the dispersion diagram of the designed structure). The integrated circuit (Figure 5-30) is now analysed for the realised gain using CST STUDIO SUITE. The backward to forward beam scanning of the designed integrated NL-CRLH frequency doubler LWA has been illustrated in Figure 5-31 (A) to (C) by setting the excitation frequency at port 1 to 0.8 GHz, 1.1 GHz and 1.5 GHz respectively.

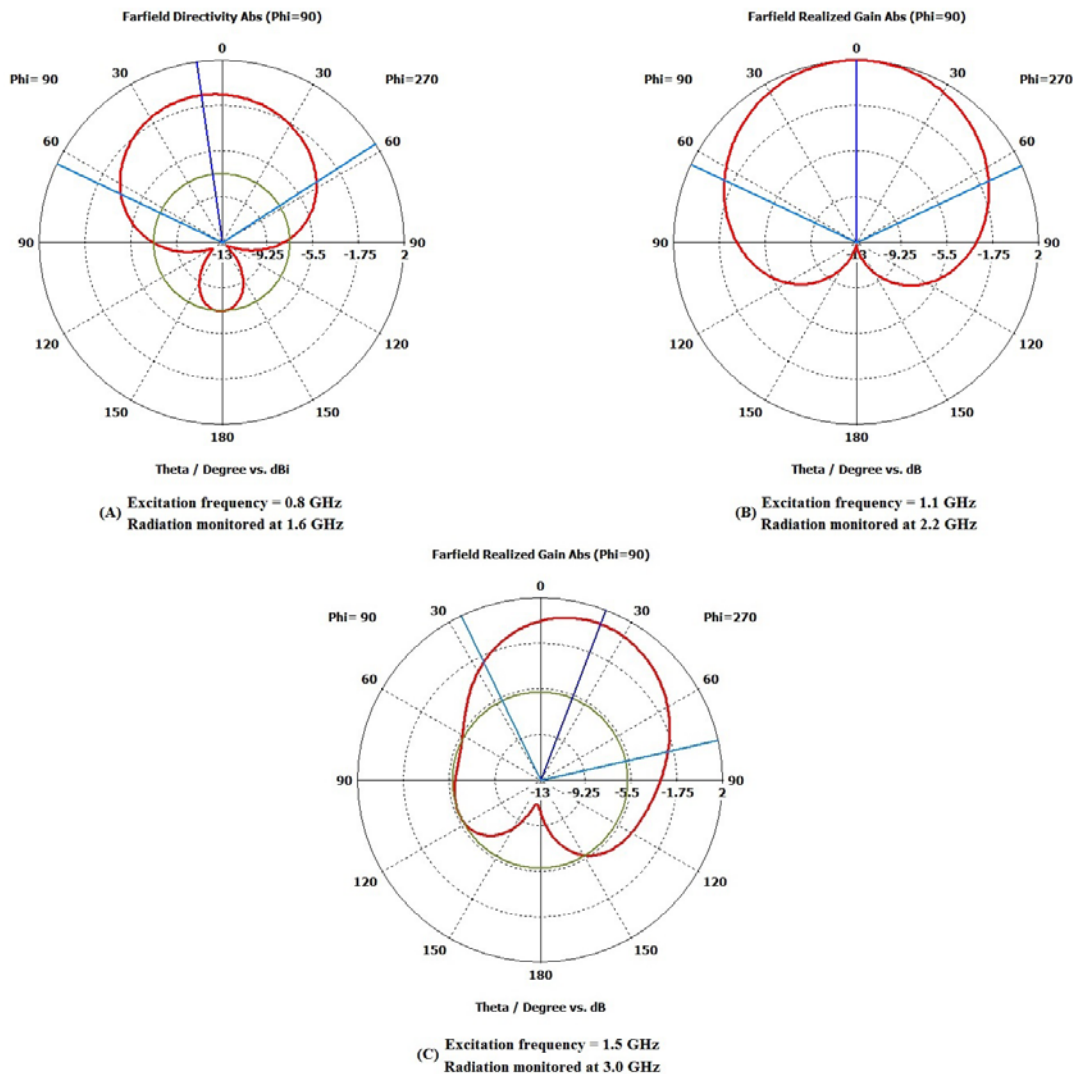


Figure 5-31: Polar representation of NL-CRLH frequency doubler LWA's radiation pattern for three different frequencies.

It is seen in Figure 5-31 that as the frequency increases from the left-handed frequency region in part (A) to the right-handed frequency region in part (C), the direction of the main radiation lobe varies from backward radiation in Part (A) with the main lobe direction of -10° , to broadside radiation at 2.2 GHz in part (B) and finally to forward radiation with the main lobe direction of 21° at 3 GHz . It is important to mention that, although in this work the proposed harmonic balance simulation technique was only applied to a single unit cell of NL-CRLH Frequency doubler LWA, the proposed technique is capable of analysing the multi-unit cell structure. In order to fully investigate the NL-CRLH frequency doubler LWA unit cell, the phase difference between fundamental current entering the first varactor (P3) and exiting from the unit cell (P6) needs to be measured, to make sure that the adjacent unit cells can be placed at appropriate distances to achieve the required beam direction and maximum directivity from the NL-CRLH leaky wave antenna array. For instance, if the LWA array designed requires radiating at the broadside, to find the distance between the adjacent cells first the phase difference between the input fundamental currents (1.1 GHz) at P3 and the fundamental current exiting P6 (Figure 5-25) has to be calculated. Table 5-7 indicates the phase of the fundamental currents at P3 and P6. After finding the phase difference between these two ports ($\Delta\theta$), since the frequency doubling structure needed to radiate at the broadside, therefore the distance between the neighbouring cells needs to be 180° . This is achieved by placing a $50\ \Omega$ transmission line at the fundamental frequency (1.1 GHz) with the electrical length (EL) of the difference between $\Delta\theta$ and 180° between each cell. Any arbitrary radiation direction other than broadside radiation, can be established by following the standard array design procedures such as reference [4].

Table 5-7: Phase of the currents at port 3 and 6 of NL-CRLH leaky wave antenna (Figure 5-25) at the fundamental frequency (1.1 GHz).

Frequency (GHz)	$Ang(I(CRLH@3,1))$ (Deg)	$Ang(I(CRLH@6,1))$ (Deg)
1.1	-9.59	-93.46

$$|\Delta\theta| = 83.87^\circ$$

$$EL = 96.13^\circ$$

5.7 Conclusion

In this chapter a new application of a harmonic balance simulation technique has been proposed. This new application enables harmonic balance simulation to combine with EM analysis for nonlinear antenna design on complex structures with radiating elements. In this method, the circuit is divided into linear and nonlinear sub sections. The linear section is first analysed using CST DESIGN STUDIO. This section is then combined with the nonlinear part to find the currents in the required harmonics using AWR Microwave Office. These currents are then reintroduced into the linear section to perform full EM simulation. In order to fully clarify the proposed technique, a nonlinear frequency tripler patch antenna has been designed and analysed using the proposed method. Further in this chapter, the proposed technique was applied on the single unit cell of the NL-CRLH frequency doubler LWA designed earlier in chapter 4 and the radiation pattern of this structure has been studied at different frequencies.

References

- [1] J. W. Bandler, R. M. Biernacki, and S. H. Chen, "Harmonic balance simulation and optimization of nonlinear circuits," in *Circuits and Systems, 1992. ISCAS '92. Proceedings., 1992 IEEE International Symposium on*, 1992, pp. 85-88 vol.1.
- [2] R. Garg, P. Bhartia, I. Bahl, and A. Ittipiboon, *Microstrip antennas design handbook*: Artech House, 2001.
- [3] S. A. Maas, *The RF and Microwave Circuit Design Cookbook*: Artech House, 1998.
- [4] C. A. Balanis, *Antenna Theory: Analysis and Design*, 3rd ed.: Wiley-Interscience, 2005.

6 CONCLUSIONS AND FUTURE WORK

6.1 Conclusions

This thesis describes research on the nonlinear analysis of optical and microwave sources. It shows and describes an integrated VCSEL model capable of accurately modelling intrinsic characteristics, as well as the parasitic and matching network effects on the VCSEL's behaviour. Further in this thesis, a nonlinear frequency doubler CRLH-LWA is designed. This design works as a frequency doubler within the structure, which is capable of radiation, from backfire to endfire and through broadside by varying the feeding frequency. The limitations of the CAD software to conveniently combine the analysis of distributed nonlinear circuits with advanced EM analysis, to find the radiation pattern at the harmonic frequencies generated within the structure motivated the research to find a new and original method of combining harmonic balance and EM analysis, for the design of nonlinear active antennas.

Parameters of the proposed integrated VCSEL equivalent circuit model were calculated using the set of analytical equations derived in this thesis. The 1300 nm intrinsic VCSEL parameters are taken from the literature. The proposed model is capable of predicting the relative intensity noise and junction noise spectrum using current, voltage and cross spectral density of the intrinsic noise source. Furthermore, the model is used to simulate the dynamic

and small signal responses of the VCSEL used in this thesis. The results of the proposed model are in good agreement with VCSEL behaviour reported in the literature.

The intention of the proposed nonlinear frequency doubler CRLH was to operate in the terahertz frequency region, where the harmonic frequency generation is favourable because of the difficulty of fundamental terahertz source generation. However, due to the complexity involved in the EM analysis of the second harmonic generated within structure, the proposed nonlinear CRLH antenna was designed in a lower frequency region. The simple and novel distributed structure of the nonlinear frequency doubler CRLH-LWA proposed in this thesis was achieved by using the quasi-lumped element approach. The radiation pattern analysis indicates a seamless transition from backward to forward radiation including broadside radiation by increasing the operating frequency.

The proposed method of combining the harmonic balance and the EM analysis for the nonlinear active antenna presented in Chapter 5 provides a novel solution for EM analysis of designs where the harmonic frequencies are generated within the structure. This method was examined for analysing the radiation pattern of the nonlinear patch antenna. The patch antenna which is designed to radiate at the third harmonic is excited by the fundamental frequency. The fundamental frequency is used by a Schottky diode within the structure to generate the third harmonic. The generated third harmonic is then fed back to the patch structure to start the radiation. The radiation pattern achieved by using this method is in good agreement with the expected patterns from this type of structure. Finally the proposed method of combining the harmonic balance and the EM analysis was applied on a unit cell of the NL-CRLH frequency doubler LWA, designed earlier in chapter 4. The radiation pattern of this structure was investigated for three different excitation frequencies in order to prove the beam scanning property of the designed NL-CRLH frequency doubler LWA by varying the excitation frequency from left-handed to transient and right-handed frequency regions.

6.1.1 Integrated Vertical Cavity Surface Emitting Laser model based on transmission line modelling

In Chapter 3, an accurate intrinsic equivalent VCSEL model was proposed by using the VCSEL rate equation and taking into account the effect of the VCSEL Langevin noise sources. Different characteristics of the VCSEL were analysed by simulating the proposed intrinsic VCSEL model. These characteristics include: intrinsic VCSEL transient behaviour; direct modulation response; and small signal characteristics. The small signal characteristics include: input impedance ($Z(\omega)$); photon modulation transfer function ($H(\omega)$); junction voltage noise spectrum ($\overline{v_1^2}/\Delta f$); and the relative intensity noise ($RIN(\omega)/\Delta f$). Further to the optical characteristics of the VCSEL, electrical aspects of the modelling such as electrical parasitics were also considered in the proposed VCSEL model, by including both parasitics arising from the VCSEL chip and packaging. Furthermore, in this work the effect of the matching network was also considered by including an L-matching network in the proposed integrated VCSEL model. It was observed from the simulation of the proposed integrated VCSEL model that the matching network improves the direct modulation response by 3 dB.

On the other hand, due to the inherent practical limitations of the lumped-elements in high frequency regions, a distributed equivalent variant of the proposed integrated VCSEL model was also developed in this work. The proposed distributed model of the VCSEL is based on transmission line modelling, where each element in the lumped-element model was replaced by a microstrip line with a specific dimension using a quasi-lumped method. The proposed distributed VCSEL model has an application for microwave signal generation such as harmonic generation by frequency switching.

6.1.2 Non-Linear Composite Right/Left Handed (NL-CRLH) frequency doubler leaky wave antenna design

In Chapter 4, the design procedure of the linear and nonlinear CRLH structure was described. The novelty in this work is the use of nonlinear CRLH, by replacing the left-handed capacitor with the varactor diode; and also a quasi-lumped approach to design the distributed structure. Using the quasi-lumped approach in this work resulted in a simple physical structure. Nonlinear analysis was performed using the circuit simulator to establish that the harmonic generation would occur. To establish the basic essential radiation properties, EM simulation was then applied to the linear version of the structure, using an EM simulator by exciting the input port at the harmonic frequency. The radiation pattern analysis in this work indicates that the designed cascaded CRLH leaky wave antenna has relatively good directivity (6 dBi). Finally, the analysis of the radiation patterns reveals that the designed structure is able to perform backward to forward beam scanning by changing the operating frequency from the left-handed to the right-handed frequency region, without using the sophisticated biasing circuitry needed when designing a conventional leaky wave antenna. The limitation of this work is that injecting the harmonic frequencies at the input port, may result in different radiation properties from injecting the harmonic currents at the point in the nonlinear structure at which the harmonic currents are generated. In Chapter 5, a new method of injecting harmonic currents generated within the nonlinear structure has been developed in order to analyse the EM properties of the nonlinear structures at harmonic frequencies when excited at the fundamental frequency.

6.1.3 Combining harmonic balance and EM analysis for design and optimisation of non-linear active antennas

In Chapter 5, a new application for the harmonic balance simulation technique was proposed. This new application enables harmonic balance simulation to combine with EM analysis for nonlinear antenna design on complex structures with radiating elements. In order to perform the proposed method the circuit is divided into linear and nonlinear sub sections. The linear section is first analysed using CST DESIGN STUDIO. The linear section is then combined with the nonlinear part to find the currents at the required harmonics using AWR Microwave Office. These currents are then reintroduced into the linear section to perform full EM simulation. In order to fully clarify the proposed technique, a nonlinear frequency tripler patch antenna has been designed and analysed using the proposed method. Further in this chapter, the proposed technique was applied on the single unit cell of the NL-CRLH frequency doubler LWA designed earlier in Chapter 4 and the radiation pattern of this structure has been studied at different frequencies.

6.2 Suggestions for possible future work

This thesis focuses on the nonlinear analysis of optical and microwave sources. In the field of nonlinear optical source analysis, the proposed integrated VCSEL model can be further developed by the inclusion of the thermal related parameters in the model. The VCSEL operations are typically thermal dependent. This is due to the use of DBR layers in their structure to maximise the optical amplifications in their small active region. In the field of nonlinear analysis of microwave sources, possible future works on the proposed nonlinear frequency doubler CRLH-LWA could be on the fabrication and measurement of the designed structure either as a single unit cell or an array. The developed structure can be also further

analysed in the millimetre wavelength region, as the harmonic generation is necessary in this region due to the difficulties of acquiring the fundamental frequency sources. A summary of the possible areas for further research in the field of this thesis is as follows:

1. The realisation of thermal behaviour of the VCSELs in the proposed integrated model. This can be done by using the thermal dependent rate equation in the derivation of the proposed model.
2. The proposed VCSEL model has applications in microwave signal generation. As an example, the harmonic generation by frequency switching of the VCSEL can be investigated using the proposed distributed VCSEL model.
3. Fabrication and measurement of the designed nonlinear frequency doubler CRLH-LWA structure either as a unit cell or an array.
4. Investigation of the proposed nonlinear frequency doubler CRLH-LWA in the millimetre wavelength regions. This may need redesigning and considerable size adjustments of the designed structure.

Appendix

A. Components Data Sheets

Skyworks SMV1430



DATA SHEET

SMV1405 to SMV1430 Series: Plastic Packaged Abrupt Junction Tuning Varactors

Applications

- High-Q resonators in wireless system VCOs
- High volume commercial systems

Features

- High Q
- Low series resistance for low phase noise
- Packages rated MSL1, 260 °C per JEDEC J-STD-020



Description





The SMV1405 to SMV1430 group of silicon abrupt junction varactor diodes is designed for use in voltage controlled oscillators (VCOs) requiring tight capacitance tolerances. The low resistance of these varactors makes them appropriate for high-Q resonators in wireless system VCOs to frequencies above 10 GHz. This family of varactors is characterized for capacitance over temperature.

Table 1 describes the various packages and markings of the SMV1405 to SMV1430 group of varactors.



Skyworks Green™ products are compliant with all applicable legislation and are halogen-free. For additional information, refer to *Skyworks Definition of Green™*, document number SQ04-0074.

Table 1. Packaging and Marking

			
Single	Single	Common Cathode	Single
SC-79 Green™	SOT-23	SOT-23	SOD-882 Green™
SMV1405-079LF Marking: Cathode			SMV1405-040LF Marking: 5
	SMV1408-001LF Green™ Marking: DV1		SMV1408-040LF Marking: DV
SMV1413-079LF Marking: Cathode	SMV1413-001LF Green™ Marking: ER1	SMV1413-004LF Green™ Marking: ER3	
			SMV1430-040LF Marking: 7
$L_s = 0.7 \text{ nH}$	$L_s = 1.5 \text{ nH}$	$L_s = 1.5 \text{ nH}$	$L_s = 0.45 \text{ nH}$



The Pb-free symbol or "LF" in the part number denotes a lead-free, RoHS-compliant package unless otherwise noted as Green™. Tin/lead (Sn/Pb) packaging is not recommended for new designs.

Electrical and Mechanical Specifications

The absolute maximum ratings of the SMV1405 to SMV1430 varactors are provided in Table 2. Electrical specifications are provided in Table 3. Typical capacitance values are listed in Table 4. Typical performance characteristics of the SMV1405 to SMV1430 varactors are illustrated in Figures 1, 2, and 3.

The SPICE model for the SMV1405 to SMV1430 varactors is shown in Figure 4, and the associated model parameters are provided in Table 5.

Package dimensions are shown in Figures 5 to 9 (odd numbers), and tape and reel dimensions are provided in Figures 6 to 10 (even numbers).

Package and Handling Information

Instructions on the shipping container label regarding exposure to moisture after the container seal is broken must be followed. Otherwise, problems related to moisture absorption may occur when the part is subjected to high temperature during solder assembly.

The SMV1405 to SMV1430 series of varactors are rated to Moisture Sensitivity Level 1 (MSL1) at 260 °C. They can be used for lead or lead-free soldering. For additional information, refer to the Skyworks Application Note, *Solder Reflow Information*, document number 200164.

Care must be taken when attaching this product, whether it is done manually or in a production solder reflow environment. Production quantities of this product are shipped in a standard tape and reel format.

Table 2. SMV1405 to SMV1430 Series Absolute Maximum Ratings (Note 1)

Parameter	Symbol	Minimum	Maximum	Units
Reverse voltage	V_R		30	V
Forward current	I_F		20	mA
Power dissipation	P_D		250	mW
Operating temperature	T_{OP}	-55	+125	°C
Storage temperature	T_{STG}	-55	+150	°C

Note 1: Exposure to maximum rating conditions for extended periods may reduce device reliability. There is no damage to device with only one parameter set at the limit and all other parameters set at or below their nominal value. Exceeding any of the limits listed here may result in permanent damage to the device.

CAUTION: Although this device is designed to be as robust as possible, electrostatic discharge (ESD) can damage this device. This device must be protected at all times from ESD. Static charges may easily produce potentials of several kilovolts on the human body or equipment, which can discharge without detection. Industry-standard ESD precautions should be used at all times.

Table 3. SMV1405 to SMV1430 Series Electrical Specifications (Note 1)
($T_{OP} = 25\text{ °C}$, Unless Otherwise Noted)

Part Number	CT @ 0.5 V (pF)	CT @ 1 V (pF)	CT @ 4 V (pF)		$\frac{CT @ 0 V}{CT @ 30 V}$ (Ratio)	RS @ 4 V, 500 MHz (Ω)	Q @ 4 V, 50 MHz
	Typ.	Typ.	Min.	Max.	Min	Max.	Typ.
SMV1405	2.1	1.80	1.21	1.45	4.1	0.80	3200
SMV1408	3.4	2.90	1.71	2.11	4.1	0.60	2900
SMV1413	7.4	6.40	3.64	4.42	4.2	0.35	2400
SMV1430	1.01	0.88	0.46	0.70	3.8	3.15	1680

Note 1: Performance is guaranteed only under the conditions listed in this table.

Reverse voltage V_R ($I_R = 10\ \mu\text{A}$) = 30 V minimum

Reverse current I_R ($V_R = 24\text{ V}$) = 20 nA maximum

Total capacitance shown was measured in the SOT-23 single configuration with a typical case capacitance of 0.13 pF. The total capacitance may differ slightly for other packages/configurations.

Table 4. Capacitance vs Reverse Voltage (Note 1)

V _R (V)	C _T (pF)			
	SMV1405	SMV1408	SMV1413	SMV1430
0	2.67	4.08	9.24	1.24
0.5	2.12	3.36	7.39	1.01
1.0	1.84	2.94	6.37	0.88
1.5	1.70	2.60	5.71	0.80
2.0	1.55	2.38	5.22	0.74
2.5	1.44	2.24	4.85	0.68
3.0	1.34	2.08	4.55	0.65
4.0	1.25	1.88	4.10	0.60
5.0	1.17	1.72	3.77	0.56
10.0	0.95	1.28	2.85	0.44
20.0	0.77	1.01	2.12	0.35
30.0	0.63	0.95	1.77	0.31

Note 1: Total capacitance shown was measured in the SOT-23 single configuration with a typical case capacitance of 0.13 pF. The total capacitance may differ slightly for other packages/configurations.

Typical Performance Characteristics

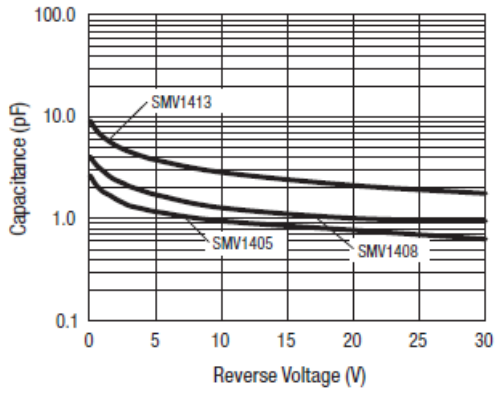


Figure 1. Capacitance vs Reverse Voltage

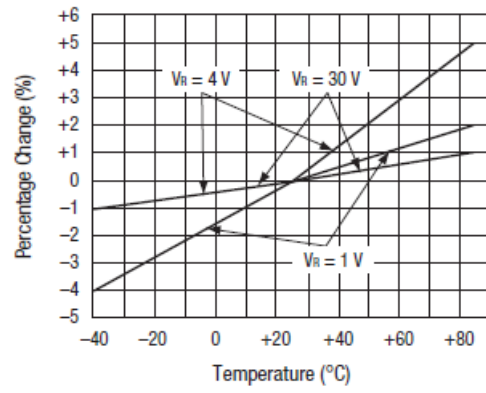


Figure 2. Relative Capacitance Change vs Temperature

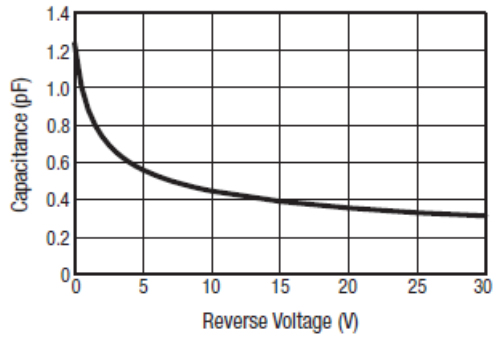


Figure 3. Capacitance vs Reverse Voltage (SMV1430)

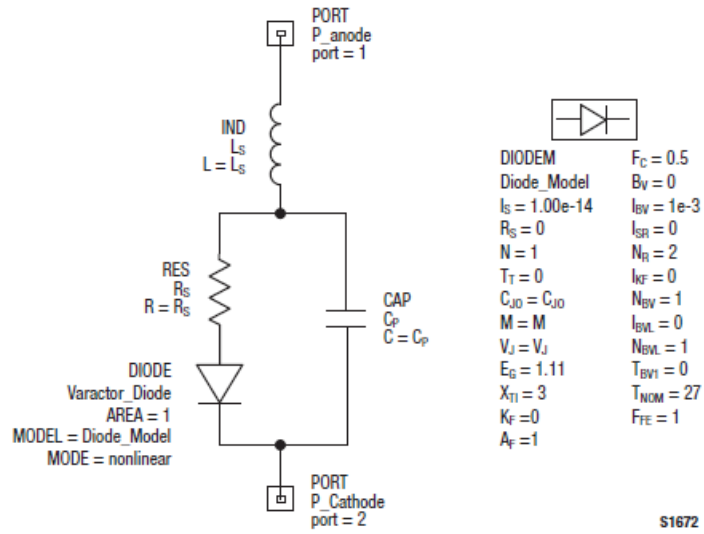


Figure 4. SPICE Model

Table 5. SPICE Model Parameters (Note 1)

Part Number	C _{J0} (pF)	V _J (V)	M	C _P (pF)	R _S (Ω)
SMV1405	2.37	0.77	0.5	0.29	0.80
SMV1408	3.89	0.92	0.5	0.21	0.60
SMV1413	8.92	0.87	0.5	0.30	0.35
SMV1430	1.11	0.86	0.5	0.13	3.15

Note 1: Values extracted from measured performance.
 For package inductance, L_s , refer to Table 1.
 For more details, refer to the Skyworks Application Note, *Varactor SPICE Model for Approved RF VCO Applications*, document number 200315.

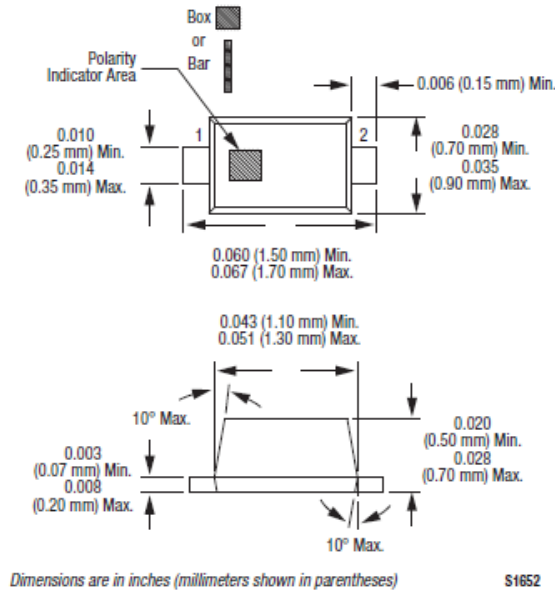


Figure 5. SC-79 Package Dimensions

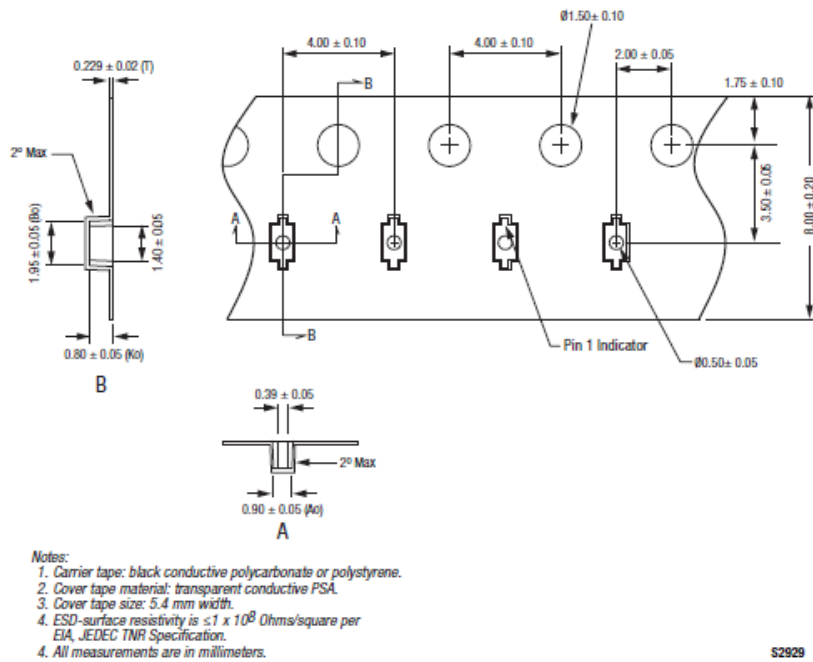
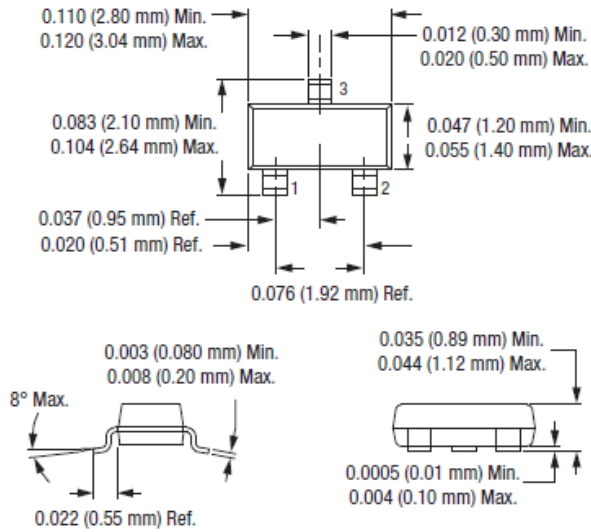


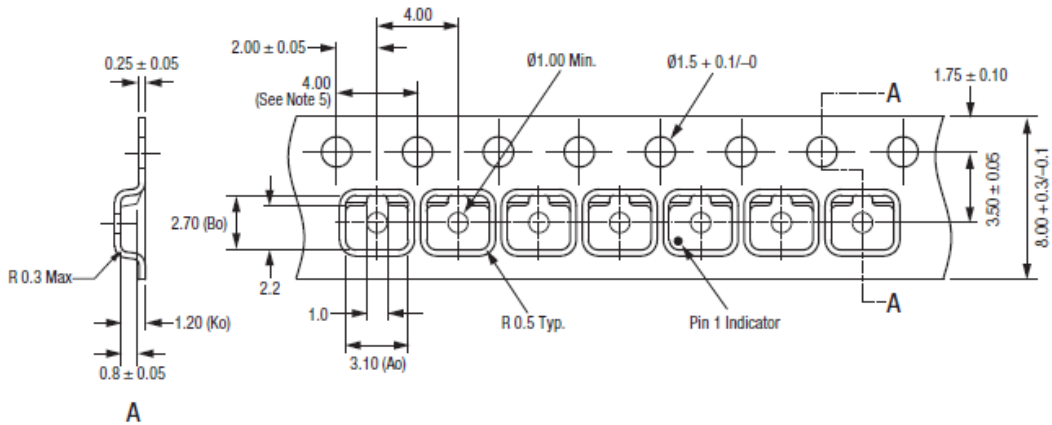
Figure 6. SC-79 Tape and Reel Dimensions

DATA SHEET • SMV1405 TO SMV1430 VARACTORS



Dimensions are in inches (millimeters shown in parentheses) **S1389**

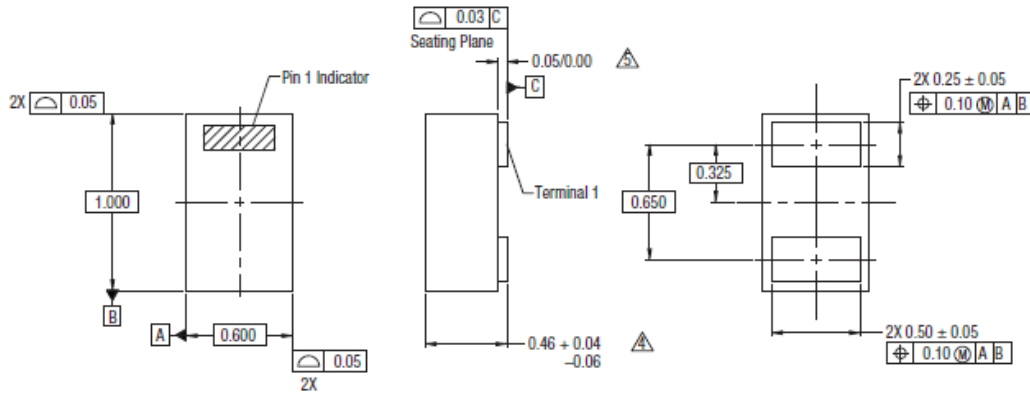
Figure 7. SOT-23 Package Dimensions



- Notes:
1. Carrier tape: black conductive polycarbonate.
 2. Cover tape material: transparent conductive PSA.
 3. Cover tape size: 5.40 mm width.
 4. Tolerance: ±0.10 mm.
 5. Ten sprocket hole pitch cumulative tolerance: ±0.2 mm.
 6. All measurements are in millimeters.

S1684b

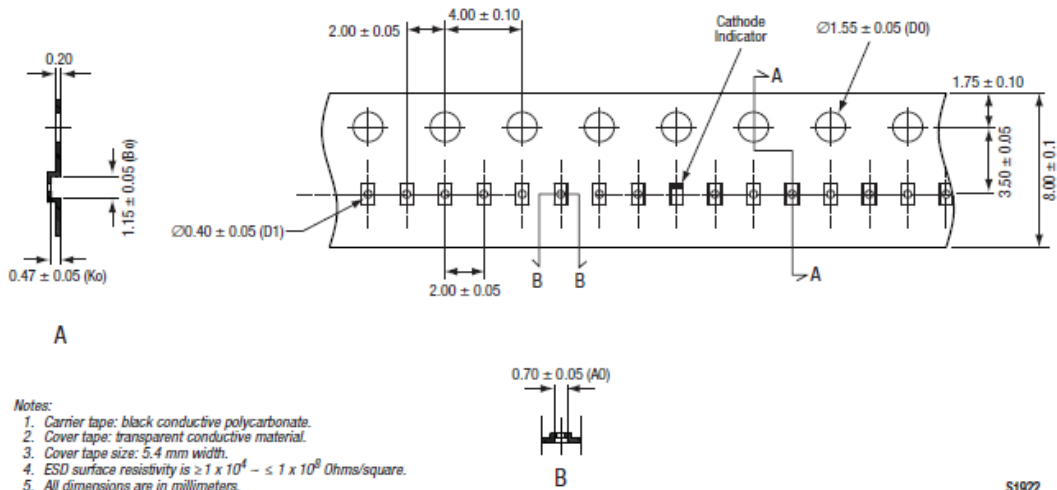
Figure 8. SOT-23 Tape and Reel Dimensions



- NOTES:
1. All measurements are in millimeters.
 2. Dimensions and tolerances according to ASME Y14.5M-1994.
 3. These packages are used principally for discrete devices.
 4. This dimension includes stand-off height and package body thickness, but does not include attached features, e.g., external heatsink or chip capacitors. An integral heatslug is not considered an attached feature.
 5. This dimension is primarily terminal plating, but does not include small metal protrusion.

Y1410

Figure 9. SOD-882 Package Dimensions



- Notes:
1. Carrier tape: black conductive polycarbonate.
 2. Cover tape: transparent conductive material.
 3. Cover tape size: 5.4 mm width.
 4. ESD surface resistivity is $\geq 1 \times 10^4 - \leq 1 \times 10^8$ Ohms/square.
 5. All dimensions are in millimeters.

S1922

Figure 10. SOD-882 Tape and Reel Dimensions



DATA SHEET

Surface Mount Mixer and Detector Schottky Diodes

Applications

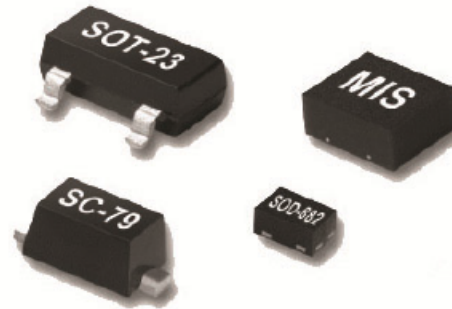
- Sensitive RF and microwave detector circuits
- Sampling and mixer circuits
- High-volume wireless
- WiFi and mobile
- Low-noise receivers in high-sensitivity ID tags
- Radio designs

Features

- Tight parameter distribution
- Available as singles, pairs, and dual pairs
- Packages rated MSL1, 260 °C per JEDEC J-STD-020



Skyworks Green™ products are compliant with all applicable legislation and are halogen-free. For additional information, refer to *Skyworks Definition of Green™*, document number SQ04-0074.




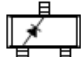




Description


These low-cost, surface mountable, plastic packaged silicon mixer Schottky diodes are designed for RF and microwave mixers and detectors. They include low barrier diodes and zero-bias detectors that combine Skyworks advanced semiconductor technology with low-cost packaging techniques. All diodes are 100 percent DC tested and deliver tight parameter distribution, which minimizes performance variability.

These diodes are available in SOD-882, SC-79, SOT-23, and Molded Interconnect System (MIS) packages. Wiring configurations include singles, common cathode, series pairs, unconnected pairs, and dual series pairs. They may be used at frequencies up to 24 GHz.

Table 1 describes the various packages and marking of the mixer and detector Schottky diodes.

Table 1. Schottky Diode Packaging and Marking

					
Single	Single	Series Pair	Reverse Series Pair	Unconnected Pair	Single
SC-79 Green™	SOT-23	SOT-23	SOT-23	MIS Green™	SOD-882 Green™
	SMS7621-001 Marking: SH1	◆ SMS7621-005 Marking: SH2	◆ SMS7621-006 Marking: SH8	SMS7621-517 Marking: H Pb-Free	
◆ SMS7621-079LF Marking: Cathode	SMS7621-001LF Green™ Marking: XH1	◆ SMS7621-005LF Green™ Marking: XH2	◆ SMS7621-006LF Green™ Marking: XH8		SMS7621-040LF Marking: E
		SMS7630-005 Marking: SD2	◆ SMS7630-006 Marking: SD8		
◆ SMS7630-079LF Marking: Anode		SMS7630-005LF Green™ Marking: XD2	◆ SMS7630-006LF Green™ Marking: XD8		SMS7630-040LF Marking: P
$L_s = 0.7 \text{ nH}$	$L_s = 1.5 \text{ nH}$	$L_s = 1.5 \text{ nH}$	$L_s = 1.5 \text{ nH}$	$L_s = 0.6 \text{ nH}$	$L_s = 0.45 \text{ nH}$

 The Pb-free symbol or "LF" in the part number denotes a lead-free, RoHS-compliant package unless otherwise noted as Green™. Tin/lead (Sn/Pb) packaging is not recommended for new designs.

Electrical and Mechanical Specifications

The absolute maximum ratings of the mixer and detector Schottky diodes are provided in Table 2. Electrical specifications are provided in Tables 3 and 4. The associated SPICE model parameters are provided in Table 5. A typical detector schematic diagram is shown in Figure 1.

Typical performance characteristics are illustrated in Figures 2 and 3. Package dimensions are shown in Figures 4 to 10 (even numbers), and tape and reel dimensions are provided in Figures 5 to 11 (odd numbers).

Package and Handling Information

Instructions on the shipping container label regarding exposure to moisture after the container seal is broken must be followed. Otherwise, problems related to moisture absorption may occur when the part is subjected to high temperature during solder assembly.

The mixer and detector Schottky diodes are rated to Moisture Sensitivity Level 1 (MSL1) at 260 °C for 5 seconds. They can be used for lead or lead-free soldering. For additional information, refer to the Skyworks Application Note, *Solder Reflow Information*, document number 200164.

Care must be taken when attaching this product, whether it is done manually or in a production solder reflow environment. Production quantities of this product are shipped in a standard tape and reel format.

Table 2. Absolute Maximum Ratings (Note 1)

Parameter	Symbol	Minimum	Maximum	Units
Reverse voltage	V_R		Rated V_B	V
Forward current, steady state	I_F		50	mA
Power dissipation	P_D		75	mW
Storage temperature	T_{STG}	-65	+150	°C
Operating temperature	T_A	-65	+150	°C
Junction temperature	T_J		+150	°C

Note 1: Exposure to maximum rating conditions for extended periods may reduce device reliability. There is no damage to device with only one parameter set at the limit and all other parameters set at or below their nominal value. Exceeding any of the limits listed here may result in permanent damage to the device.

CAUTION: Although this device is designed to be as robust as possible, electrostatic discharge (ESD) can damage this device. This device must be protected at all times from ESD. Static charges may easily produce potentials of several kilovolts on the human body or equipment, which can discharge without detection. Industry-standard ESD precautions should be used at all times.

Table 3. Electrical Specifications (Note 1)
($T_A = +25$ °C Per Junction, Unless Otherwise Noted)

Part Number	Barrier	Minimum V_B @ 10 μ A (V)	Typical C_T @ 0 V (pF)	V_F @ 1 mA (mV)	Maximum Pair Configuration ΔV_F @ 1 mA (mV)	Maximum R_T (Note 2) (Ω)
SMS7621 series	Low	2	0.25	260 to 320	10	18 @ 5 mA

Note 1: Performance is guaranteed only under the conditions listed in this table.

Note 2: R_T is the slope resistance.

DATA SHEET • MIXER AND DETECTOR SCHOTTKY DIODES

Table 4. Electrical Specifications (Note 1)
(T_A = +25 °C Per Junction, Unless Otherwise Noted)

Part Number	Minimum V _B @ 100 μA (V)	Typical C _T @ 0.15 V (pF)	V _F @ 0.1 mA (mV)	V _F @ 1 mA (mV)	Maximum Pair Configuration ΔV _F @ 1 mA (mV)	Typical R _V (Ω)
SMS7630 series	1	0.3	60 to 120	135 to 240	10	5000

Note 1: Performance is guaranteed only under the conditions listed in this table.

Table 5. SPICE Model Parameters (Per Junction)

Parameter	Units	SMS7621 Series	SMS7630 Series
I _S	A	4E-8	5E-6
R _S	Ω	12	20
N	–	1.05	1.05
T _T	sec	1E-11	1E-11
C _{J0}	pF	0.1	0.14
M	–	0.35	0.40
E _G	eV	0.69	0.69
X _{TI}	–	2	2
F _C	–	0.5	0.5
B _V	V	3	2
I _{BV}	A	1E-5	1E-4
V _J	V	0.51	0.34

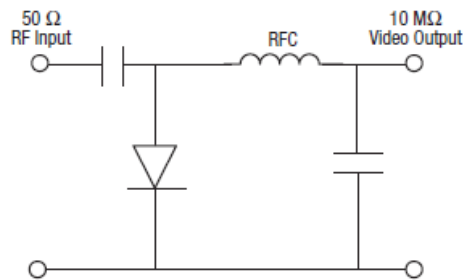


Figure 1. Typical Detector Circuit

Typical Performance Characteristics

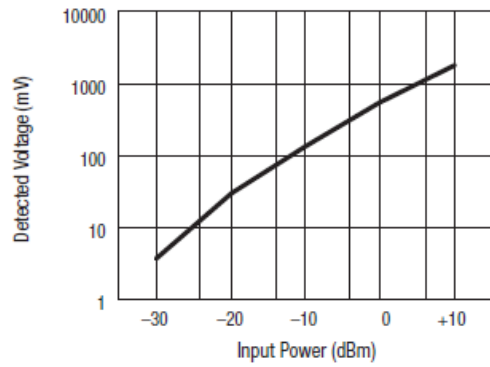


Figure 2. Typical Detector Characteristics @ 1.8 GHz

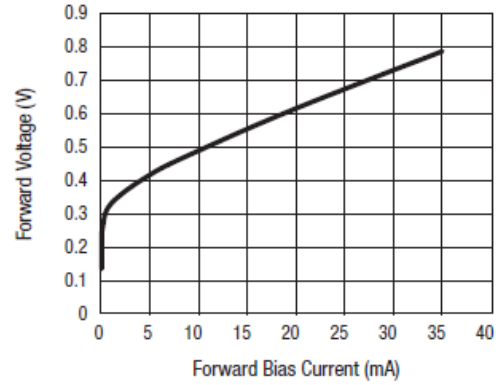
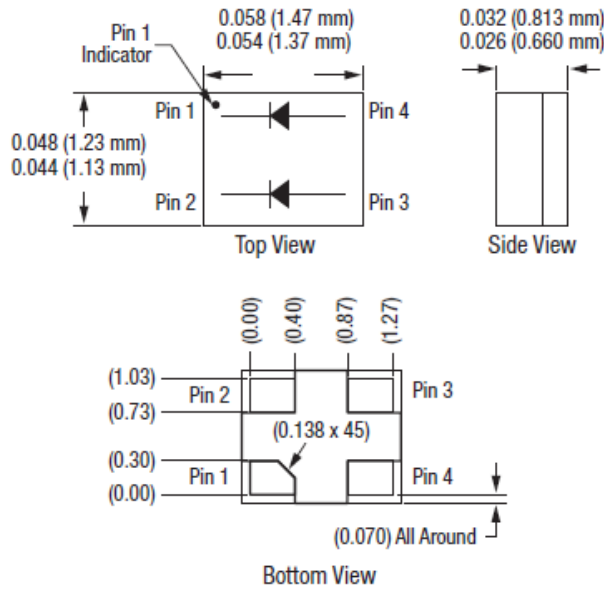


Figure 3. SMS7621 Forward Voltage vs Forward Bias Current

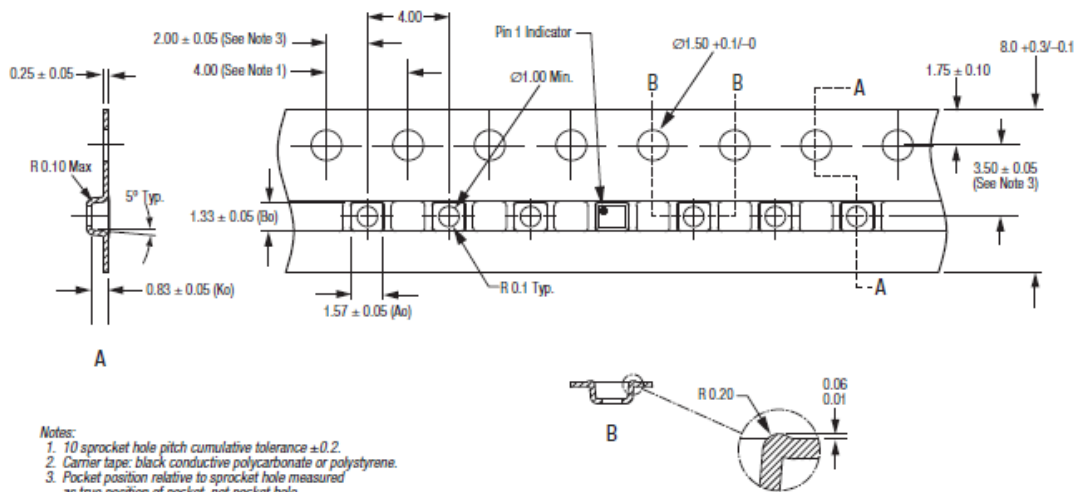
DATA SHEET • MIXER AND DETECTOR SCHOTTKY DIODES



Dimensions are in inches (millimeters shown in parentheses)

S1833

Figure 4. MIS Package Dimension Drawing

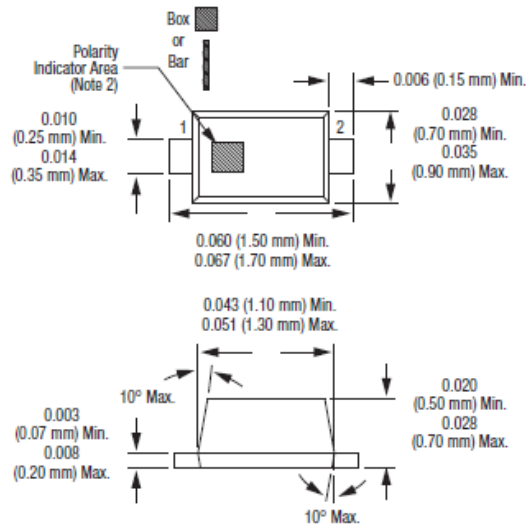


Notes:

1. 10 sprocket hole pitch cumulative tolerance ± 0.2 .
2. Carrier tape: black conductive polycarbonate or polystyrene.
3. Pocket position relative to sprocket hole measured as true position of pocket, not pocket hole.
4. ESD-surface resistivity is $\leq 1 \times 10^9$ Ohms/square per EIA, JEDEC TNR Specification.
5. Cover tape material: transparent conductive PSA with 5.4 mm width.
6. All measurements are in millimeters.

S2928

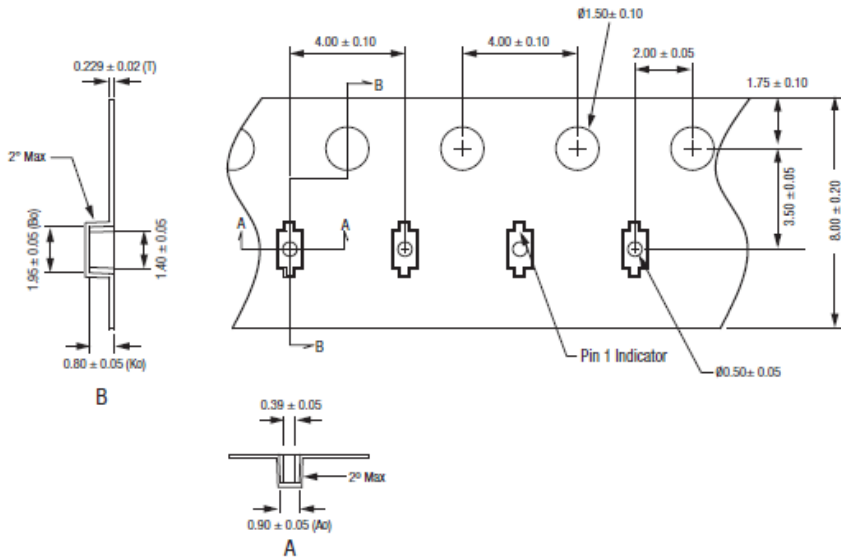
Figure 5. MIS Tape and Reel Dimensions



Notes:
 1. Dimensions are in inches (millimeters shown in parentheses).
 2. Cathode indicator for SMS7621-079LF
 Anode indicator for SMS7630-079LF

S1652a

Figure 6. SC-79 Package Dimension Drawing

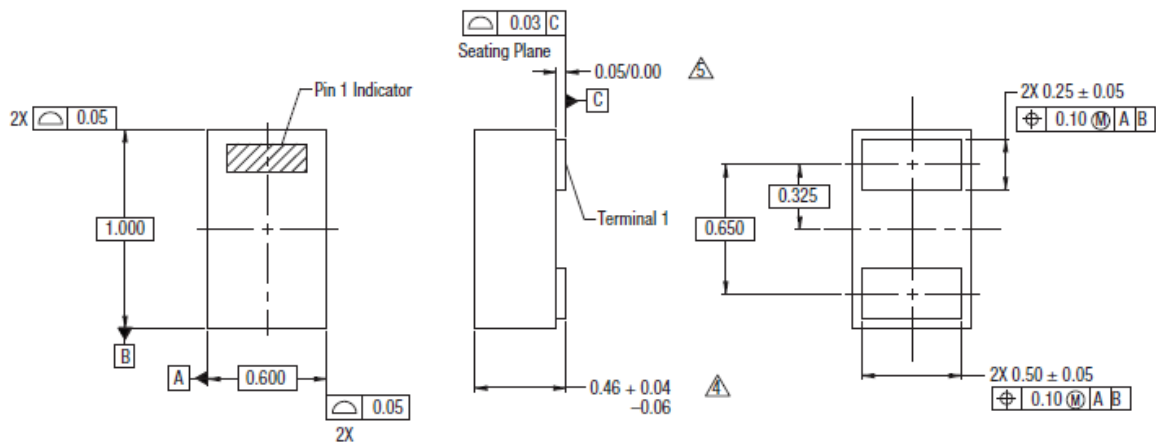


Notes:
 1. Carrier tape: black conductive polycarbonate or polystyrene.
 2. Cover tape material: transparent conductive PSA.
 3. Cover tape size: 5.4 mm width.
 4. ESD-surface resistivity is $\leq 1 \times 10^8$ Ohms/square per EIA, JEDEC TNR Specification.
 5. All measurements are in millimeters.

S2929

Figure 7. SC-79 Tape and Reel Dimensions

DATA SHEET • MIXER AND DETECTOR SCHOTTKY DIODES

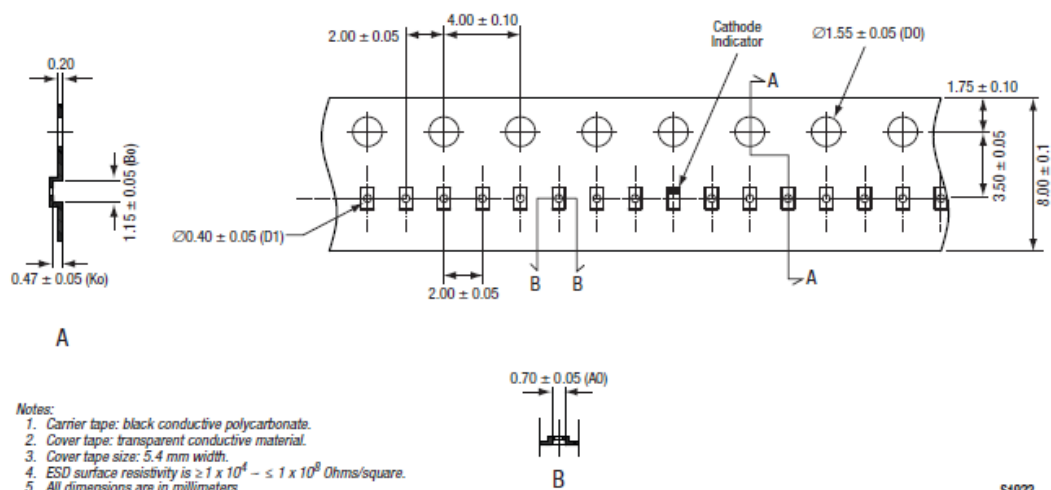


NOTES:

1. All measurements are in millimeters.
2. Dimensions and tolerances according to ASME Y14.5M-1994.
3. These packages are used principally for discrete devices.
4. This dimension includes stand-off height and package body thickness, but does not include attached features, e.g., external heatsink or chip capacitors. An integral heatslug is not considered an attached feature.
5. This dimension is primarily terminal plating, but does not include small metal protrusion.

Y1410

Figure 8. SOD-882 Package Dimension Drawing

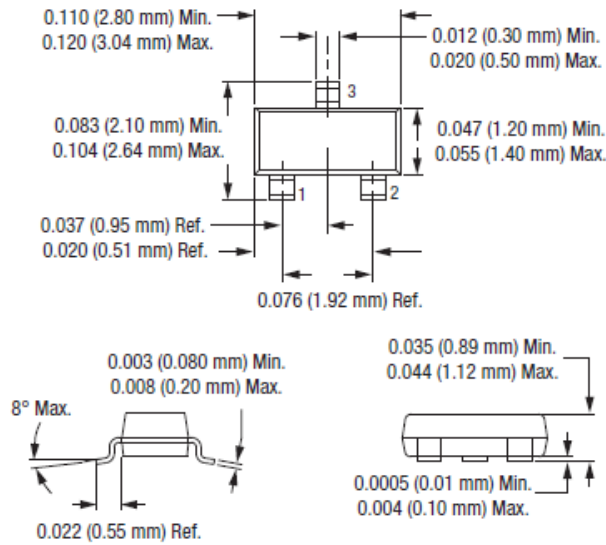


Notes:

1. Carrier tape: black conductive polycarbonate.
2. Cover tape: transparent conductive material.
3. Cover tape size: 5.4 mm width.
4. ESD surface resistivity is $\geq 1 \times 10^4 - \leq 1 \times 10^8$ Ohms/square.
5. All dimensions are in millimeters.

S1922

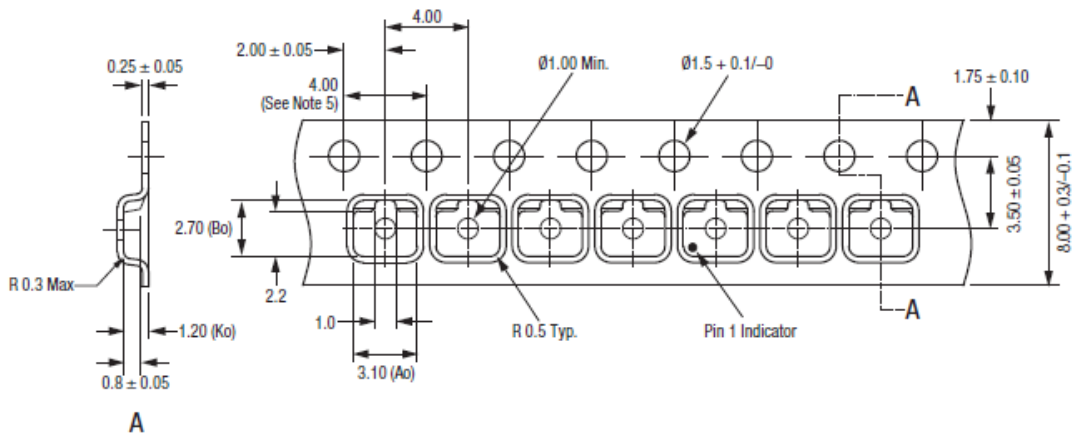
Figure 9. SOD-882 Tape and Reel Dimensions



Dimensions are in inches (millimeters shown in parentheses)

S1389

Figure 10. SOT-23 Package Dimension Drawing



Notes:

1. Carrier tape: black conductive polycarbonate.
2. Cover tape material: transparent conductive PSA.
3. Cover tape size: 5.40 mm width.
4. Tolerance: ± 0.10 mm.
5. Ten sprocket hole pitch cumulative tolerances: ± 0.2 mm.
6. All measurements are in millimeters.

S1684b

Figure 11. SOT-23 Tape and Reel Dimensions

B. Microwave Simulation Software

This section provides the manual for OrCAD EE (PSpice) Designer, that offers a transient and time domain analysis environment for VCSEL modelling; and National Instruments (NI) AWR Design Environment and Computer Simulation Technology (CST) STUDIO SUITE used in this thesis for the simulations of the microwave structures.

B.1 OrCAD EE (PSpice) Designer

The OrCAD EE (PSpice) Designer is the popular general purpose lumped circuit simulator package that includes OrCAD PSpice and OrCAD Capture. Detailed information about this software can be found on the company's website [1]. OrCAD PSpice is used in this research; it enables the DC, AC and transient analysis of the required circuitry. During this research the student version of PSpice 9.1 is used.

OrCAD PSpice manual

In order to work with OrCAD PSpice, first the designed circuit should be constructed in this software. OrCAD PSpice offers an extensive library of electrical elements. This library can be reached under the “Draw” menu by selecting “Get New Part” as illustrated in Figure B-1. To analyse the constructed circuit the required analysis should be setup. The “Setup” can be found under Analysis menu in the PSpice Schematics window. This is shown in Figure B-2.

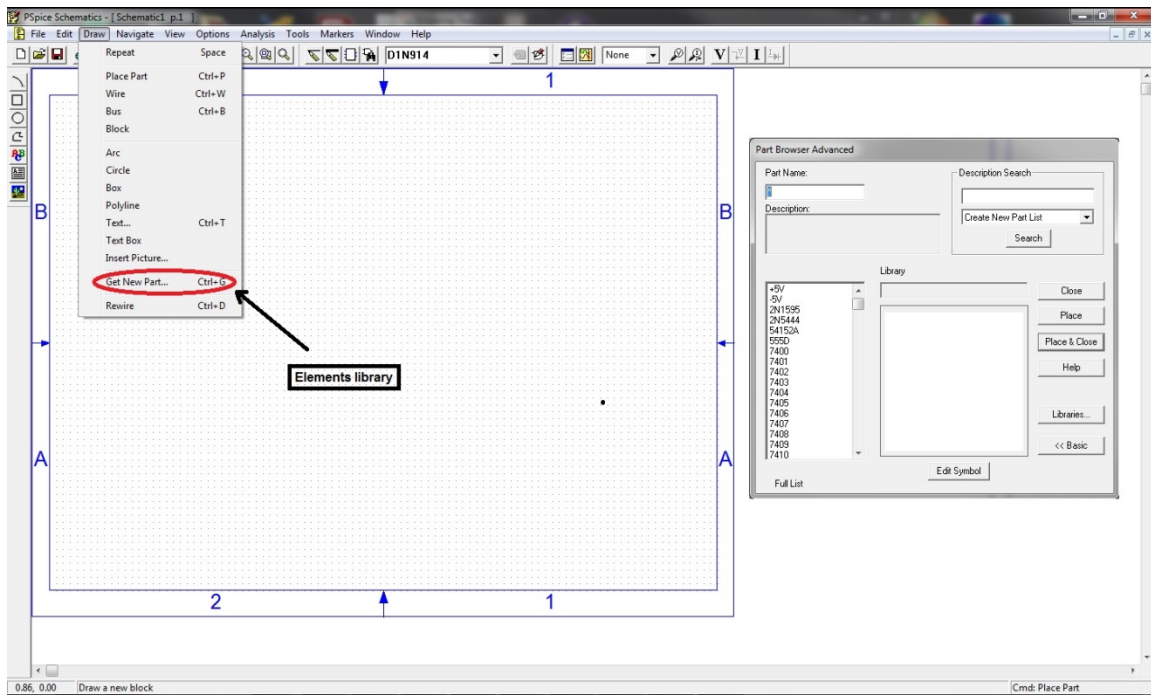


Figure B-1: OrCAD PSpice advanced part browser.

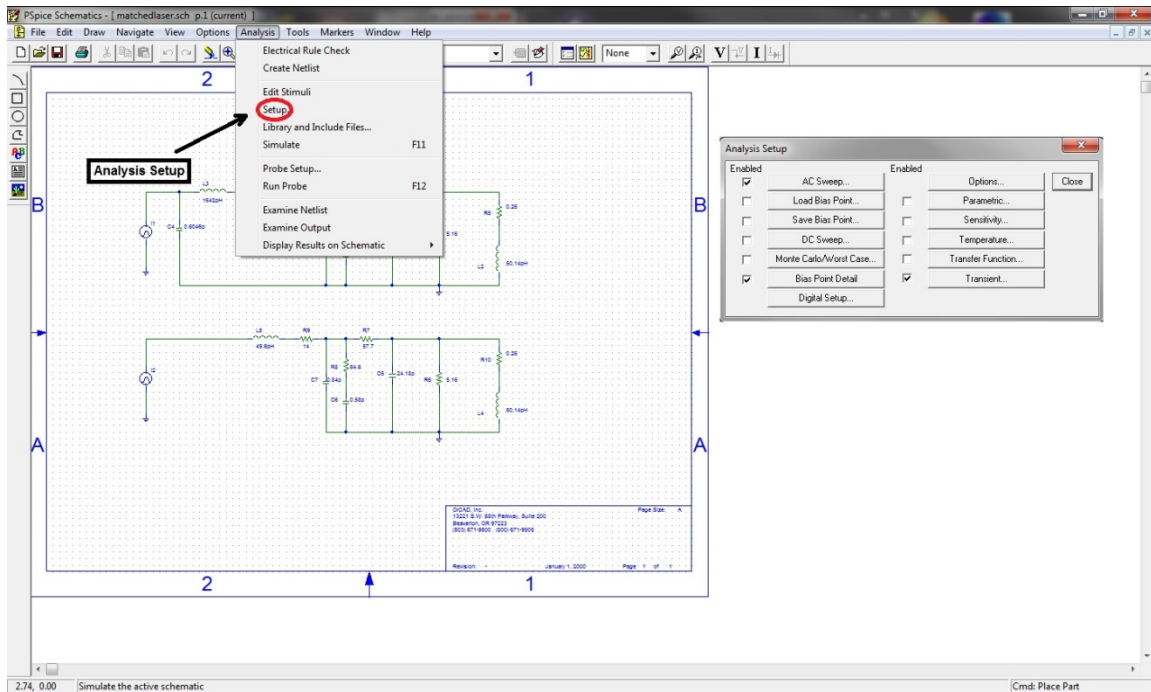


Figure B-2: OrCAD PSpice analysis setup.

B.2 National Instruments AWR Design Environment

NI AWR Design Environment is the software composed of Microwave Office and Analog Office for circuit simulation; Visual System Simulator for system simulation; and AXIEM and Analyst for electromagnetic analysis. Microwave Office is used in this research. Microwave Office is capable of: schematic design, linear and nonlinear circuit analysis, simulation, optimisation etc. Further information about the software can be found on the company's website [2]. During this research, versions 2012 and 2013 of the NI AWR Design Environment were used.

NI AWR Design Environment manual

One of the benefits of using NI AWR Microwave Office is its user friendly interface. In this work the nonlinear circuit simulator and the optimisation tool of this software were mainly used. In order to use these tools, first the global variables that include the elements' units and the frequency range used in the simulation should be setup. These setups can be done through the "Project Options" window. "Project Options" can be found under the "Options" menu of Microwave Office. Figure B-3 illustrates the "Global Units" and "Frequency" tabs within the "Project Options". The next step after setting up the required global variables is to open a new schematic. New schematics can be added by right clicking on the "Circuit Schematics" folder on the left side of the Microwave Office window and selecting "New Schematic". Now the elements of the design should be added to the schematic to build up the structure. The circuit elements can be found under the "Elements" tab on the bottom left corner of Microwave Office. Figure B-4 indicates the location of the "New Schematics" and the "Elements" within Microwave Office.

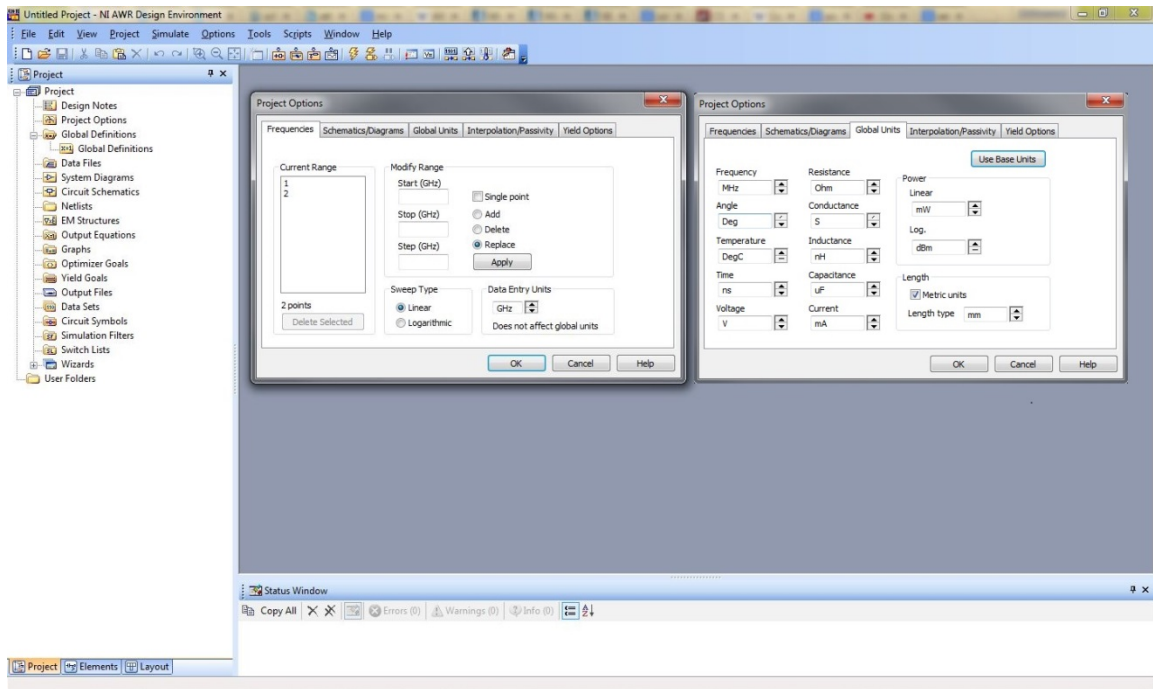


Figure B-3: Microwave Office "Project Options" menu.

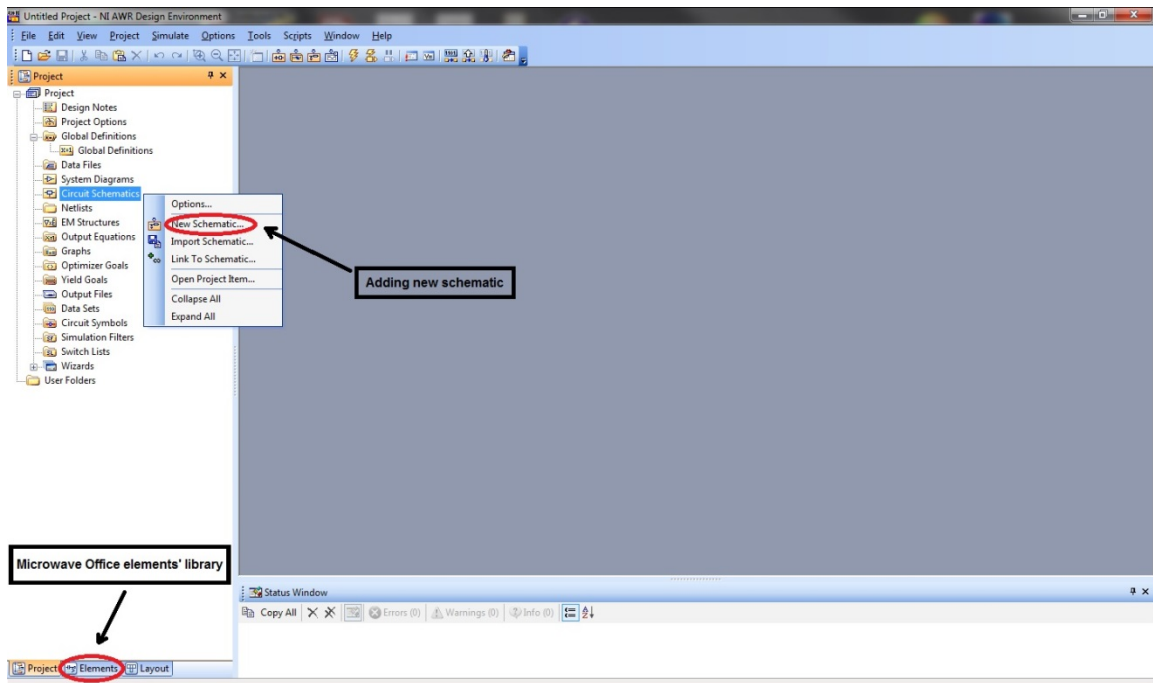


Figure B-4: Microwave Office "New Schematic" and "Elements" location.

Microwave Office provides a wide range of analysis including S-parameter analysis. After setting up the required elements of the structure, then the simulation and analysis of the results can take place. Figure B-5 indicates the “Analyze” button under the “Simulate” menu.

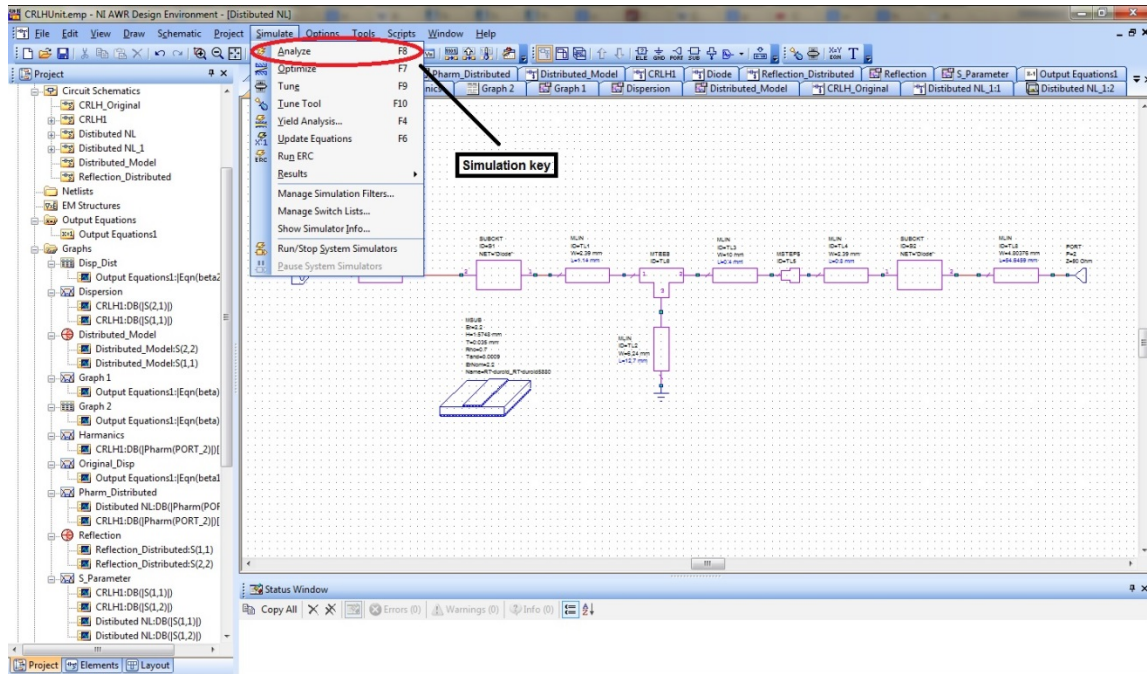


Figure B-5: Microwave Office simulation.

In the majority of cases the designed circuit needs to be optimised to achieve the required specification from the design. Microwave Office provides a real time optimisation tool as illustrated in Figure B-6.

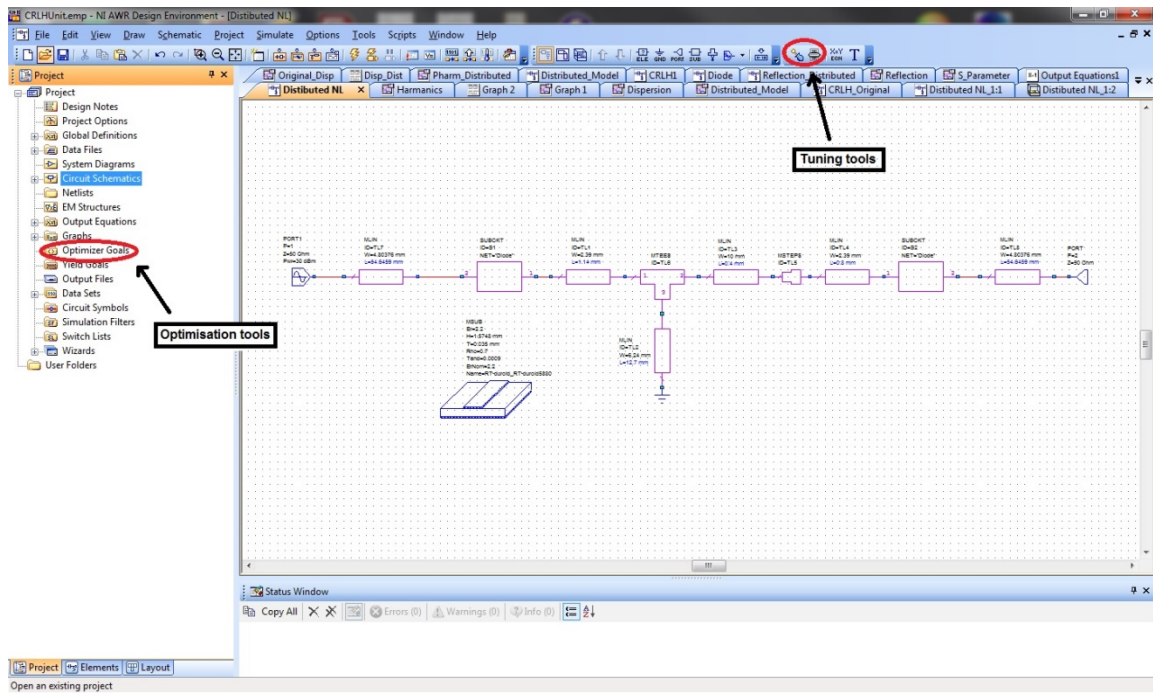


Figure B-6: Microwave Office optimisation and tuning tools.

B.3 CST STUDIO SUITE

CST STUDIO SUITE is a 3-D full wave electromagnetic simulator which contains a number of interconnected products including: CST MICROWAVE STUDIO (CST MWS) dedicated for high frequency 3-D simulations; CST DESIGN STUDIO (CST DS) for schematic design of the electromagnetic systems etc. For detailed information about the range of CST STUDIO SUITE products readers are referred to the company's website [3]. CST MWS includes three simulation tools, eigenmode solver, time domain solver and frequency domain solver to fit the needs of the specific applications. Time domain solver is used in this research; it is capable of generating results including the structure's S-parameters and far field radiation patterns for antennas. CST MWS versions 2012, 2013 and 2014 are used during the period of this research.

CST MICROWAVE STUDIO manual

CST MWS provides different templates for the possible structures analysed in this software. Therefore the first step in simulating a structure in CST is to select an appropriate CST template. These templates help to specify the basic condition for the simulation of the different structures. Figure B-7 indicated the template window of the CST MWS. The required complex 3-D structure is designed in CST MWS using the basic 3-D shape and the Boolean operations such as subtraction, trim, addition and intersect provided within the software, as shown in figure B-8.

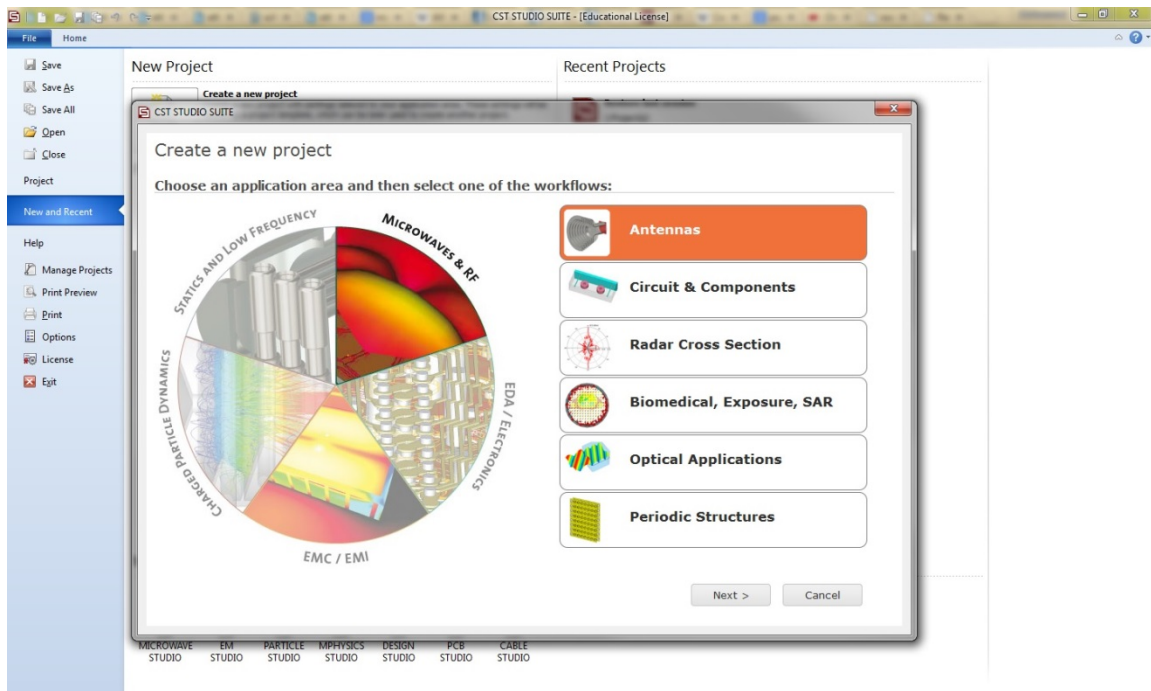


Figure B-7: CST MWS templates.

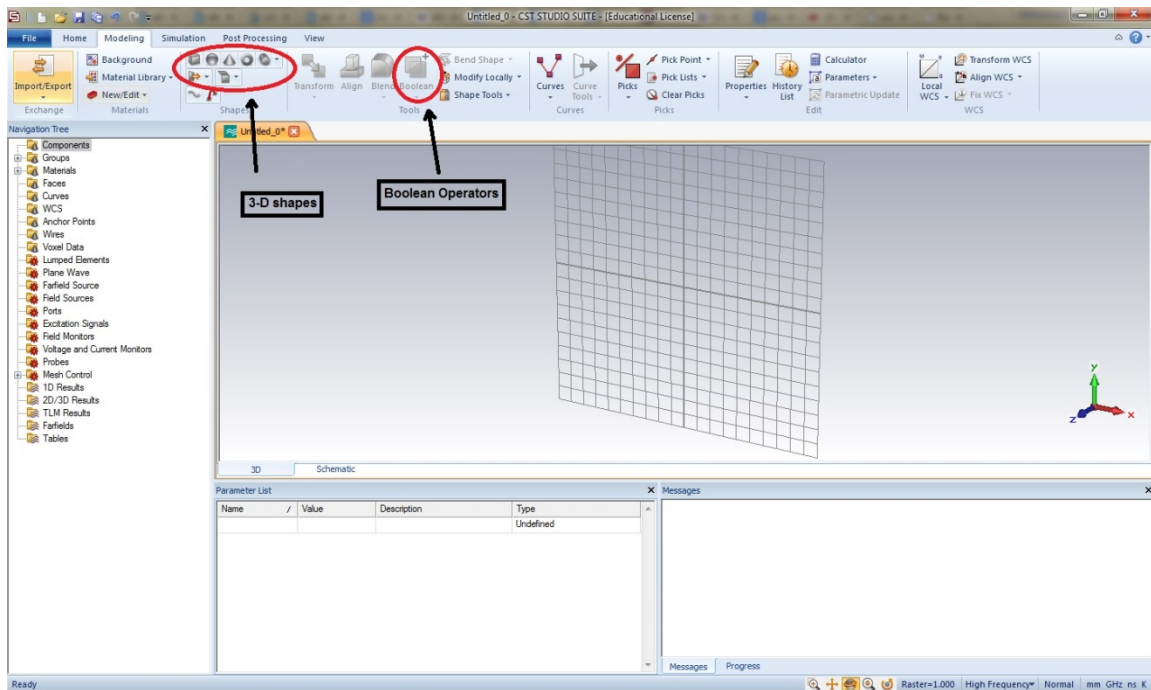


Figure B-8: CST MWS window indicating the available 3-D shapes and the possible Boolean operators.

References

- [1] O. C. D. Systems. (2014, 20 May). *OrCAD EE (PSpice) Designer*. Available: http://www.orcad.com/sites/orcad/files/resources/files/OrCAD_EE_PSpice_Designer_DS_Final.pdf
- [2] N. Instruments. (20/05/2015). *Microwave Office*. Available: <http://www.awrcorp.com/products/microwave-office>
- [3] C.-C. S. Technology. (2014, 20May). *CST STUDIO SUITE*. Available: <https://www.cst.com/Products/CSTS2>